Morphological Influences on the Photocatalytic Activity of a $CsTaWO_6$ Model System

Dissertation

zur Erlangung des akademischen Grades

„Doctor rerum naturalium“

– Dr. rer. nat. –

eingereicht am Fachbereich

Biologie und Chemie

der

Justus-Liebig-Universität Gießen

von

Tobias Weller, M. Sc.

Gießen, im Februar 2017

1. Gutachter und Betreuer:	Dr. Roland Marschall
2. Gutachter:	Prof. Dr. Bernd Smarsly
Prüfer:	Prof. Dr. Siegfried Schindler
Prüfer:	Prof. Dr. Richard Göttlich

Declaration

The present thesis was prepared in the period of 15th January 2014 – 14th January 2017 at the Institute of Physical Chemistry of the Justus-Liebig-University Giessen under the supervision and guidance of Dr. Roland Marschall.

I declare:

The present thesis was prepared by myself and without illicit help from others. Any citations being included literally, by adaptation from literature or personal communications, have been marked appropriately. The principles of best practice in academia, as documented in the respective charter of the Justus-Liebig-University, have been applied in all investigations constituting this thesis.

Ich erkläre:

Ich habe die vorgelegte Dissertation selbständig und ohne unerlaubte fremde Hilfe und nur mit den Hilfen angefertigt, die ich in der Dissertation angegeben habe. Alle Textstellen, die wörtlich oder sinngemäß aus veröffentlichten Schriften entnommen sind, und alle Angaben, die auf mündlichen Auskünften beruhen, sind als solche kenntlich gemacht. Bei den von mir durchgeführten und in der Dissertation erwähnten Untersuchungen habe ich die Grundsätze guter wissenschaftlicher Praxis, wie sie in der „Satzung der Justus-Liebig-Universität Gießen zur Sicherung guter wissenschaftlicher Praxis“ niedergelegt sind, eingehalten.

Gießen, den 24. Februar 2017

_____

Tobias Weller

Danksagung

Zuallererst möchte ich meinem Doktorvater, Dr. Roland Marschall, dafür danken, dass er mir die Möglichkeit gegeben hat, in seiner Nachwuchsgruppe zu promovieren. Daneben danke ich ihm vor allem auch für die Ermöglichung meiner Forschungsaufenthalte und Konferenzen im Ausland, die mir nicht nur wissenschaftlich sehr viel gebracht haben. Durch sie konnte ich ein wenig die weite Welt entdecken. Außerdem danke ich ihm dafür, dass er es geschafft hat, mir auch bei Rückschlägen immer wieder den Spaß an der Forschung zurückzubringen.

Mein besonderer Dank gilt zudem Prof. Dr. Bernd Smarsly, in dessen Arbeitsgruppe ich seit nunmehr fast sechs Jahren bereits vor meiner Promotion meine Bachelor- und Masterarbeit anfertigen durfte und der freundlicherweise das Zweitgutachten übernimmt.

Den Gastgebern meiner Forschungsaufenthalte möchte ich insbesondere Danken; dazu zählen Prof. Dr. Igor Djerdj sowie Dr. Suraj Mal, beide damals am Institut Rudjer Boskovic in Zagreb, Prof. Dr. Lianzhou Wang und dessen gesamter Arbeitsgruppe von der University of Queensland in Brisbane sowie Prof. Dr. Dominik Eder, Dr. Alexey Cherevan, Dr. Paul Gebhardt, Leonie Deilmann und allen anderen aus der Arbeitsgruppe Eder an der Technischen Universität Wien. Gerne denke ich an den einen oder anderen Wein in Wien oder Wodka in St. Petersburg zurück.

Von meiner „Heimat-Universität“ Gießen möchte ich mich zunächst bei allen bedanken, die mir bei all den unterschiedlichen Messmethoden geholfen haben, mir beigebracht oder teils sogar netterweise für mich gemessen haben:

- Aus dem I. Physikalischen Institut: Prof. Dr. Detlev Hofmann, Jan Philipps und David Specht für EPR-Messungen.
- Aus der AG Janek: Dr. Klaus Peppler und Dr. Boris Mogwitz für Hilfe bei REM und EDX-Messungen, Carsten Fiedler für die Mitbenutzung seines Büchis, Dr. Bjoern Luerßen und Dr. Dominik Weber für Hilfe bei XRD-Messungen und Dr. Joachim Sann für das Messen diverser Proben in der XPS und deren Auswertung.
- Aus der AG Wickleder: Anne Schulze und Günter Koch für deren Einweisung ins TEM und ihre Geduld dabei, sowie Dr. Christian Logemann für allerlei Hilfe, wenn die Technik im Labor mal wieder nicht so wollte wie der Doktorand. Außerdem Hubert Wörner für die Anfertigung von allerlei Messungen an der TGA.

- Aus der Organischen Chemie: Dr. Dennis Gerbig und Brigitte Weinl-Boulakhrouf für die Aufnahme von IR-Spektren.
- Aus unserer eigenen Arbeitsgruppe: Rüdiger Ellinghaus und Felix Badaczweski für ihre Messungen an der Physisorption und vor allem Rüdiger für die Hilfe bei deren Auswertung. Dr. Christian Suchomski danke ich für die Einweisung und viele nützliche Tipps beim Messen und Interpretieren von Raman-Spektren und auch bei anderen Fragen rund um z. B. mesoporöse Materialien. Morten Weiß möchte ich für DLS-Messungen und die tägliche Hilfe im Labor meinen Dank aussprechen.

Zudem möchte ich auch den Bachelor- und Master-Studenten danken, die ich über die Jahre betreuen durfte: Patrick Kirsten, Patrick Esch, Christopher Simon sowie Lukas Specht, der viel zum Gelingen der Größenvariation der Nanopartikel beigetragen hat.

Allen aus der Feinmechanischen Werkstatt sowie der Glasbläserei, insbesondere Harry Heidt und Anja Beneckenstein, möchte ich meinen herzlichen Dank für die Hilfe bei der Umsetzung von allerlei Basteleien aussprechen.

Der Deutschen Forschungsgesellschaft (DFG) und dem Deutschen Akademischen Austauschdienst (DAAD) möchte ich für die Finanzierung meine Stelle als wissenschaftlicher Mitarbeiter im Rahmen des Emmy-Noether-Programms beziehungsweise für die finanzielle Unterstützung bei der Ermöglichung meines Forschungsaufenthaltes in Australien danken.

Insbesondere möchte ich meinen MaWi-„Weggefährten“ Pascal Vöpel, Christoph Seitz und Rafael Meinusch danken, mit denen ich mich seit nunmehr acht Jahren durch den Uni-Alltag kämpfe, und vielen anderen aus unserer Arbeitsgruppe: Meinen Altbau-Bürokollegen Maren, Yunpei, Zewei und Rüdiger, meinen Neubau-Bürokollegen Kristin, Natalia und Calin, sowie meinen Korrekturlesern Morten, Giuli, Jana, Maren, Pascal, Christoph, Kristin und Rüdiger und natürlich auch allen anderen aus unserer Arbeitsgruppe für die tolle Arbeitsatmosphäre. Es hat immer sehr viel Spaß gemacht mit euch zu arbeiten oder etwas zu unternehmen.

Zu guter Letzt möchte ich meinen Eltern für die Unterstützung über all die Jahre danken und meiner Freundin Stefanie dafür, dass sie mich auch im größten Stress ertragen und unterstützt hat.

Table of content

Abstract

In the present work, the influence of different morphologies on the photocatalytic activity of a semiconducting transition metal oxide was investigated. The quaternary photocatalyst caesium tantalum tungstate ($CsTaWO_6$) was therefore used as a model system. This compound exhibits a number of advantages compared to other photocatalysts such as titanium dioxide (TiO_2) due to its crystallization in just one cubic crystal structure and its beneficial band positions for the test reaction of photocatalytic hydrogen generation. $CsTaWO_6$ was nanostructured *via* hydrothermal and sol-gel processes to investigate the influence of surface area, crystallinity and pore sizes on the photocatalytic activity. It was possible to synthesize single crystal $CsTaWO_6$ nanoparticles with different crystallite sizes and mesoporous materials with a number of pore sizes, pore ordering and resulting surface areas. When looking at the photocatalytic hydrogen evolution of all the investigated samples, it could be shown that an increase in surface area does not correlate with an increase in activity. In fact, the optimum crystallite size was found to be the most important aspect in nanostructured photocatalyst, whereas for $CsTaWO_6$ this optimum lies at 12 to 13 nm. Furthermore, it could be shown that larger pores lead to an enhanced hydrogen production in mesoporous photocatalysts. In general, a decrease of the synthesis temperature resulted in an increase in the defect concentration (estimated from strain parameters) and therefore a lower activity. The optimum morphology for the $CsTaWO_6$ system was found to be a mesoporous material with large pores (up to 40 nm), thin pore walls and an optimum crystallite size of approximately 12 nm.

Kurzfassung

In der vorliegenden Arbeit wurde der Einfluss unterschiedlicher Morphologie auf die photokatalytische Aktivität eines halbleitenden Übergangsmetalloxids untersucht. Dazu wurde der quaternäre Photokatalysator Cäsiumtantalwolframat ($CsTaWO_6$) als Modellsystem verwendet. Diese Verbindung besitzt gegenüber anderen Photokatalysatoren wie Titandioxid (TiO_2) den Vorteil, dass es nur in einer einzigen, kubischen Kristallstruktur kristallisiert und zudem über Bandpositionen verfügt, die für die Testreaktion der photokatalytischen Wasserstoffproduktion optimal liegen. $CsTaWO_6$ wurde über Hydrothermal- und Sol-Gel-Synthesen nanostrukturiert, um den Einfluss von Oberfläche sowie Kristallit- und Porengröße auf die photokatalytische Aktivität zu überprüfen. Dabei konnten einkristalline $CsTaWO_6$-Nanopartikel in unterschiedlichen Kristallitgrößen hergestellt werden, sowie mesoporöse Materialien mit einer Reihe von Porengrößen, Porenordnung und daraus resultierenden Oberflächen. Bei Betrachtung der photokatalytischen Wasserstoffentwicklung aller präparierten Proben konnte gezeigt werden, dass eine Oberflächenvergrößerung nicht mit einer Vergrößerung der Aktivität korreliert. Vielmehr kann die optimale Kristallitgröße als wichtigster Aspekt in nanostrukturierten Photokatalysatoren angesehen werden, wobei dieser Wert im Falle des $CsTaWO_6$ bei 12 bis 13 nm liegt. Zudem konnte herausgefunden werden, dass große Poren in mesoporösen Photokatalysatoren zu einer verbesserten Wasserstoffentwicklung beitragen. Die Abhängigkeit der Synthesetemperatur auf die Aktivität wurde auf die steigende Defektkonzentration mit sinkender Temperatur zurückgeführt, wobei mit dieser auch die photokatalytische Wasserstoffproduktion abnahm. Als optimale Morphologie konnte für $CsTaWO_6$ ein mesoporöses Material mit großen Poren (bis 40 nm), dünnen Porenwänden und Kristallitgrößen um das für $CsTaWO_6$ gefundene Optimum von 12 nm bestimmt werden.

1 Introduction

1.1 Motivation

One of the biggest challenges for society in the following decades will be a proper energy supply alongside a simultaneous reduction of fossil fuel utilization. Besides the economical aspect of increasing prices with a decreasing availability of fossil fuels, the ecological point of view is getting more and more important, especially with regard to changes in the environment and extraordinary weather phenomena due to the ongoing global warming.[1,2] Scientists all over the world have worked and are still working on a sustainable energy supply with renewable energies such as wind, solar, biomass and geothermal energy.[3] However, these comparably new technologies are restricted regarding their possible contribution to the worldwide energy consumption due to less or only local availabilities (biomass, geothermal energy) or limited time frames of usage over day and year (solar, wind).[4] Even though the energy provided by the sun is a few orders of magnitude higher than the overall power consumed on earth,[5] the limited time frames are a strongly limiting and detaining argument against a further development of renewable energies.

One possibility to overcome the issue of energy storage is the direct conversion of solar energy into chemical compounds, such as hydrogen *via* electrochemical photolysis/ photocatalysis.[6–10] The light-driven direct splitting of water into its elements hydrogen and oxygen on a semiconductor surface was first published by Fujishima and Honda in 1972.[11] Since that time, many work groups have worked in this field and published their results on different photocatalytically active materials. Up to now, the most investigated photocatalyst is titanium dioxide (TiO_2) in all its different polymorphs;[12–14] the same material as used in the first publication on this research field by Fujishima and Honda.

Similar to normal catalytically driven reactions, photocatalysis was also assumed as strongly dependent on surface area and therefore the morphology of the photocatalyst.[8,15] A number of structuration techniques were used to prepare photocatalytically active materials with increasing surface area,[16–19] differently formed pores inside the material,[20] pore ordering[21–23] and crystallite sizes,[24,25] as the latter was also predicted to have a strong influence on the photocatalytic performance. However, clearly systematic studies on just one material to get the best comparability of results were still missing. This is due to the fact that TiO_2 as the most

investigated compound has the disadvantage of phase conversion when decreasing its crystallite size (from rutile to anatase) or increasing the calcination temperature above 600 °C (phase transformation from anatase to rutile).[26] Furthermore, TiO_2 exists in a number of different additional phases such as brookite or the (more rarely) Bronze phase or even just in an amorphous phase for very small crystallites.[24] The changing phases lead to different electronic properties of the semiconducting material and therefore less comparable materials.[27,28] Besides TiO_2, no material was investigated intensively enough to draw conclusions about the relationship between morphology and activity.

In this work, the defect-pyrochlore structured compound caesium tantalum tungstate ($CsTaWO_6$) was used as a model system to investigate the relationship between morphology, surface area and crystallite size on the corresponding photocatalytic activity. $CsTaWO_6$ was reported as a highly active material for photocatalytic water splitting even without any co-catalyst by Ikeda *et al*. in 2008.[29] Further investigations by Schwertmann *et al*. demonstrated a wet-chemistry synthesis method, the so-called 'citrate route', for the preparation of $CsTaWO_6$ with a comparably high surface area of up to 4 $m^2 g^{-1}$.[30,31] Doping experiments with nitrogen and sulfur resulted in a band gap narrowing from 3.6 eV in the pure $CsTaWO_6$ material into the visible light range with around 2.3 eV.[32,33] Nevertheless, no synthesis for a nanostructured $CsTaWO_6$ was reported so far. The advantages when doing nanostructuring experiments on $CsTaWO_6$ is the existence of just one phase for this compound (a defect-pyrochlore structure), thus causing no impurities when varying the crystallite sizes or pore wall thicknesses in the material, and its excellent band positions with enough overpotential for the hydrogen evolution.

In this work, different synthetic routes for the preparation of nanostructured $CsTaWO_6$, namely nanoparticles[34] and mesoporous materials,[35] will be shown and characterized in detail, especially regarding the influence of the morphology on the photocatalytic activity. The syntheses will be adapted even for other defect-pyrochlore structured materials. Finally, conclusions will be drawn to give an instruction of how to prepare a well-active photocatalyst. These summarized requirements should be generally valid for all other kinds of photocatalytic materials.

1.2 Structure of this work

In the next Chapter (no. 2), the theoretical background of the necessity of energy storage and the advantages and disadvantages of hydrogen as an energy carrier will be discussed as well as the basic principles of heterogeneous photocatalysis. Transition metal oxides such as $CsTaWO_6$ as a photocatalyst will be introduced and principles of nanostructuring techniques on the example of nanoparticle preparation and soft-templating approaches with block copolymers will be described.

The two subsequent parts (Chapters 3 and 4) will depict the different experimental approaches in detail, including the chemicals used, the exact synthesis conditions, and the applied characterization techniques. In the latter part, the most important methods for the characterization of nanostructured photocatalysts, namely X-ray diffraction (including Rietveld refinement), nitrogen physisorption and the photocatalytic setups will be explained in more detail.

Chapter 5 includes the main part of this work, in which all the results of preliminary experiments, nanostructured $CsTaWO_6$ materials, mesoporous materials, continuative experiments for other defect-pyrochlore structured compounds and the discussion of the obtained findings will be presented. It will start with the defect-pyrochlore structured nanoparticles together with a short outlook on continuative experiments for a further usage of these nanoparticles to prepare *e.g.* nanofibers *via* electrospinning. The results of the $CsTaWO_6$ nanoparticles have been already published in *Nano Energy* in 2017.[34] Afterwards, the results on mesoporous $CsTaWO_6$ will be shown, and the formation mechanism in this special case of a sol-gel synthesis will be described in detail. Mesoporous materials prepared with P123 as porogen using a climatic chamber for the controlled drying process will be discussed first and have been published in *Advanced Energy Materials* in 2016.[35] A more advanced drying process on a heating plate with a glass dome for a more defined atmosphere and circulation control was further used to get an ordered mesoporous $CsTaWO_6$ with the ISO polymer as porogen. In continuative experiments of the mesoporous defect-pyrochlore structured materials, this technique will be applied for other polymers such as P123 and PIB-PEO as well as for another compound, namely P123-derived mesoporous $KTaWO_6$.

In the last three Chapters (6, 7 and 8) of the main part of this work, the results on the relation between morphology and photocatalytic activity will be highlighted and summarized

to give an explanation on how nanostructuring influences the performance of a photocatalyst. A short outlook will finish this part.

Attached to the main part, all used references are listed and an itemization of publications, conference contributions and research visits of the author of this work is presented.

2 Theoretical background

2.1 Challenges in future energy supply

Nowadays, the existence of global warming is mostly indisputable, especially by scientific researchers. The reason for the ongoing warm-up of the atmosphere lies in the rising amount of greenhouse gases in the earth's atmosphere caused by human being, mainly by burning of fossil fuels, deforestation and intensive animal breeding.[36] All these processes lead to the output of greenhouse gases such as carbon dioxide (CO_2) or methane (CH_4), whereas the former is assumed to have most contribution on global warming (~ 60 %).[1]

The direct relation between an increase in the average temperature on earth and the amount of greenhouse gases in atmosphere can be seen in long-term measurements of average temperatures. Such measurements were done by meteorologists and other scientist since the middle of the 19th century and from recording atmospheric CO_2 since ~ 1950, *e.g.* at Mauna Loa, Hawaii (Figure 2.1a).[2,37,38] More data of the CO_2 amount of former years are available from arctic ice core samples.[36]

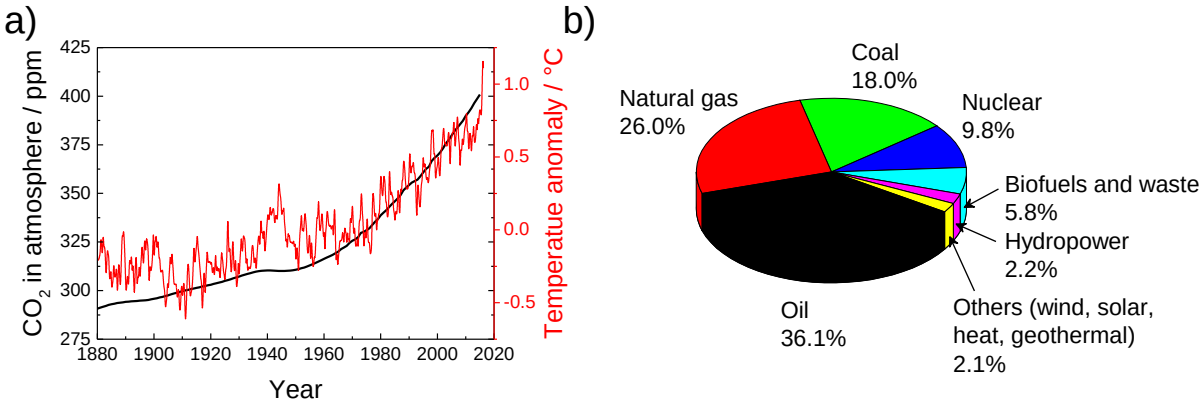

Figure 2.1: a) The direct relation between CO_2 concentration in atmosphere and raise in the average temperature, here shown as a temperature anomaly, both parameters measured at Mauna Loa, Hawaii, USA;[2,37,38] b) worldwide total energy supply by fuel in 2014.[39]

Such a strong increase of the average temperature on earth can cause a number of serious problems, such as rising sea levels due to defrosting of arctic ice and therefore flooding of low-lying regions, expansion of unlivable desert regions and missing rainfall, leading to a shortage of drinking water and massive problems in agriculture.[36] Due to these facts, the global community has declared to keep global warming below 2 °C.[40] As it can be seen in Figure 2.1a,

the average temperature raised dramatically in the last 40 years and it is questionable whether it is possible to reach this ambitious goal.

Focus has to lie on the prevention of further burning of high amounts of fossil fuels, as it is the case nowadays. Figure 2.1b shows the total energy supply by fuel worldwide in 2014,[39] indicating that around 90 % of the world's energy is received from fossil fuels (oil, natural gas, coal) or nuclear power, with the latter having the big problem of radioactive waste. Besides the climate-damaging properties of all fossil fuels, there is also the disadvantage of their natural limitation, which will lead to shrinkage of easily accessible resources.[41] This will cause a stepwise increase of the prices of fossil fuels. Thus, finding new ways to gain a sustainable energy supply are unavoidable (Figure 2.2).

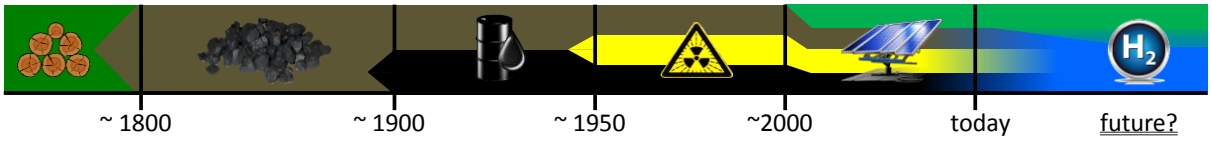

Figure 2.2: Illustrated timeline of mainly used energy sources of humankind over the last centuries. Starting from wood and other biomass, coal was used with the beginning of the industrial revolution. In the 20th century, oil became most important, while nuclear power came up after World War II. Around turn of the millennium, renewable energies rose up. In future, more renewable energies have to be used and possibly hydrogen for energy storage.

An almost limitless alternative energy source is our sun, which provides the earth with free energy the whole year. The sun energy can be used either directly in photovoltaic cells and solar thermal collectors or indirectly *via* wind, wave power or tidal power.[3] The average solar irradiation I_{SC} coming to the earth can be estimated *via* the Stefan-Boltzmann law[42] and the inverse-square law, leading to the following equation:

$$I_{SC} = \sigma \cdot T_{Sun}^4 \cdot \left(\frac{4\pi R_{sun}}{4\pi D_{S\text{-}E}}\right)^2 = 1364 \text{ W m}^{-2}, \text{ whereas} \qquad (2.1)$$

$\sigma = 5.670 \cdot 10^{-8}$ W m^{-2} K^{-4}

$T_{Sun} = 5772$ K

$R_{Sun} = 6.963 \cdot 10^{8}$ m

$D_{S\text{-}E} = 1.496 \cdot 10^{11}$ m

σ is known as the Stefan-Boltzmann constant,[43] T_{Sun} and R_{Sun} are the temperature on the surface of the sun[44] and the radius of the sun,[45] respectively, and $D_{S\text{-}E}$ is the average distance between sun and earth,[46] also known as astronomical unit (au).

The estimated value for I_{SC} fits quite well with the average solar irradiation measured in experiment, which is slightly lower with an exact value of 1360.8 W m^{-2}.[4] In 2014, the average power consumption of mankind on earth was 12.3 TW (or $1.1 \cdot 10^5$ TWh per year).[39] Assuming the radius of the earth r_E to be $6.371 \cdot 10^6$ m (radius of a sphere of same volume as the earth[47]), the solar power on earth reaches a value of $1.74 \cdot 10^{17}$W or $1.74 \cdot 10^5$ TW. That means sun provides around 14,000 times more energy than needed for all civilizing energy-consuming processes of mankind (transport, electricity, industry, mobility *etc*.) and therefore could be the favorite future energy supply.

However, solar energy has some remarkable disadvantages, too. First, the above-mentioned value for I_{SC} is only valid if the incoming radiation is exactly perpendicular to the earth's surface, which is in fact never the case for regions north of the Tropic of Cancer or south of the Tropic of Capricorn. Depending on the thickness of atmosphere that has to be passed through by sun light, a parameter "air mass coefficient" (AM) can be defined as a function of the angle *z* between incoming radiation and the ground:[48]

$$\mathrm{AM} \approx \frac{1}{\cos(z)} \tag{2.2}$$

A value of AM = 1 (or just AM1) describes the case of a perpendicular incoming radiation, therefore passing through a length of just one atmosphere, AM = 1.5 (AM1.5) passing through a length of 1.5 atmospheres and so on. Longer distances through the earth's atmosphere lead to a stronger absorption and scattering of the radiation. At AM1, the above shown value of 1360.8 W m^{-2} passes, whereas for AM1.5 just 1360.8 W m^{-2}/1.5 = 907.2 W m^{-2} can be used. Figure 2.3a illustrates the strong dependence of the incoming radiation on the angle between sun irradiation and the ground on the example of Berlin, Germany. Berlin is located north of the Tropic of Cancer; thus, even at midsummer, AM is 1.14 and the solar irradiation I_{SC} is approximately 1194 W m^{-2} on midday. Midsummer is the longest day of the year on the northern hemisphere; consequently, the overall solar energy per square meter on this day of around 12 kWh is also the highest value. On midwinter, the shortest day of the year, the overall solar energy per square meter is just approximately 1.5 kWh. Furthermore, all these values are valid for cloudless days, which is not the case over the whole year.

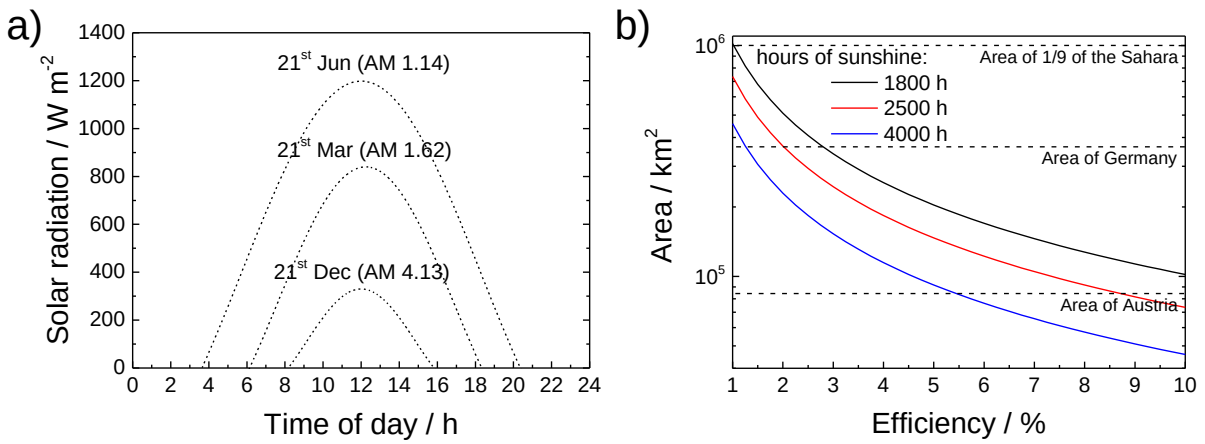

Figure 2.3: a) Simulated daily sun irradiation in Berlin, Germany (52° 31′ 20″ N, 13° 21′ 58″ E),[49] at midsummer, midwinter and beginning of spring.[50] Air mass values result from Equation (2.2) with a latitude of 52.5° for the beginning of spring, 52.5 − 23.5° = 29.0° at midsummer and 52.5 + 23.5° = 76° at midwinter (due to the earth axial tilt of 23.5°). A sinusoidal function was used for simulation inspired by the model of Khatib and Elmenreich.[51] DST (daylight saving time) was neglected. b) Land consumption to provide the whole EU-28 with solar energy, depending on the efficiency of the sun light usage and three different sunshine occurrences (1800 h ≈ Middle Europe, 2500 h ≈ Southern Europe, 4000 h ≈ Northern Africa). Dotted lines show areas of different countries; for simplification, an average solar radiation of 1000 W m^{-2} was assumed.

These considerations lead to the following conclusion: first, regions on earth that are closer to the equator are more suitable for the use of sun light due to their lower AM value and in consequence more irradiation over the whole year. Furthermore, territories with less cloudy days are beneficial also due to more hours of sunshine per year. Figure 2.3b shows the required area to provide the whole European Union with renewable, green energy as a function of efficiency of conversion and the hours of sunshine per year. 1800 h is a typical value in Germany, 2500 h can be used in Spain and a high value of around 4000 h of sunshine can be reached in closed to the equator lying, rarely clouded regions like some parts of the Sahara or Australia. This means, for example at an efficiency of 10 % (which is a low value for photovoltaic cells, but a rather high value for energy-to-fuel photocatalytic processes such as CO_2 reduction or water splitting), at a sunny place like Western Sahara, an area corresponding to the size of Switzerland (~ 41000 km^2) would be needed to collect enough solar energy to power the whole European Union.

When looking at artificial methods to use solar energy, most techniques require semiconductors to generate electron-hole pairs, which can be further used to generate electrical power (photovoltaic cells) or to perform redox reactions (photocatalysis). For a detailed discussion of semiconductors and photocatalysis, see Chapter 2.3. However, all these semiconductors offer a characteristic band gap and can therefore only use solar light with an equal or higher energy than this band gap. The effective solar radiation is shown in Figure 2.4 and, before passing the earth's atmosphere (AM0), resembling the radiation of a blackbody with the temperature of the sun's surface. In experiments, most time a value for AM of 1.5 is adopted to simulate realistic condition like *e.g.* in Middle Europe. It can be seen that the total intensity of the radiation after passing 1.5 atmospheres is slightly decreased due to absorption and reflection. Characteristic bands can be seen especially in the IR region due to vibrational and rotational modes of H_2O and CO_2. The absorption in this part of the spectra makes CO_2 to a greenhouse gas, while the main components of our atmosphere (N_2, O_2, Ar) do not absorb in the IR region.

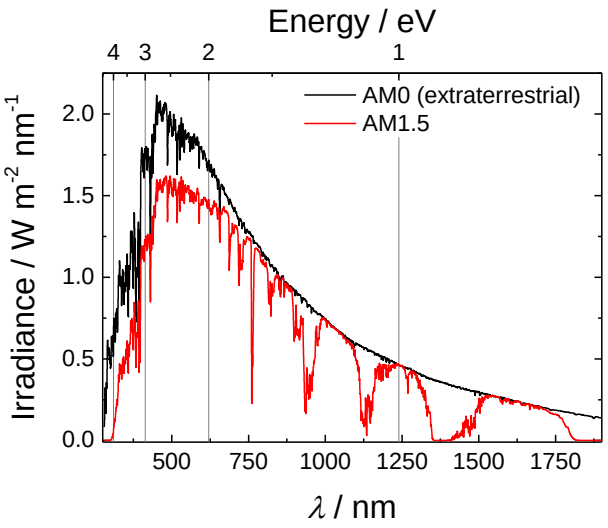

Figure 2.4: Solar radiation spectrum on top of the earth's atmosphere (AM0, black), which is nearly identical to the spectrum of a black body with 5772 K (T_{Sun}) and the solar radiation spectrum on sea level after passing 1.5 atmospheres (AM1.5, red). The differences mainly occur from sun light absorption by IR active species like H_2O and CO_2 (explanation of the greenhouse effect).[52]

If solar energy is used by semiconductors as sun light converters, it can be imagined that depending on the band gap of the semiconductor, only a part of the sunlight can be used. For example, with band gaps of 3.6 eV ($CsTaWO_6$),[30] 3.2 eV (TiO_2, anatase)[6] and 1.1 eV (Si),[53] 3.2, 6.6 or 76.9 % of the overall solar irradiation can be used, respectively. To perform overall

water splitting for a chemical energy storage in hydrogen, an energy of 1.23 eV is required,[11] resulting in around 71 % of the sun light being potentially usable for this reaction (for more details, see Chapter 2.3.1).

2.2 Energy storage

As it was shown in Figure 2.3a, the solar radiation changes extensively with daytime, leading to zero radiation at night and a maximum at midday, and with the time of the year. Therefore, it is not only necessary to store energy during sunshine periods for a consumption at night, but also for cloudy days and long periods with less irradiation in winter months. So there is a strong necessity to store energy in an easily storable way, *e.g.* chemical compounds.[54] Other forms of energy storage like batteries based on electrochemistry can only store small amounts of energy (see Figure 2.5) and are only suitable for use in portable or mobile devices, *e.g.* electric cars. Mechanical energy storage like in pumped hydroelectric energy storage can be very destructive for the environment, expensive and is also not able to store enough energy.[55] Energy storage in chemical compounds can provide several advantages:

1) comparably high energy densities and therefore high amounts of storable energy (Figure 2.5),
2) easy to transport,[54]
3) existing infrastructure for liquid and gaseous fuels (from today's oil and natural gas applications),[55]
4) and the applicability of chemical compounds as educts in *e.g.* chemical industry.[55,56]

An interesting way to directly convert sun energy in chemical energy is photocatalysis on semiconducting materials (see Chapter 2.3).[57–59] In general, all uphill reactions, which means endergonic reactions and therefore a higher energetic product(s) compared to the educt(s), are suitable to store energy.[60] Examples for such reactions are CO_2 reduction to methanol (CH_3OH)[61] or methane (CH_4)[62,63] or water splitting into its elements, hydrogen and oxygen.[7,64] The former reaction has the advantage of producing chemical compounds that are directly usable in *e.g.* combustion engines and the existence of an infrastructure for transportation. Disadvantages are, if used in combustion engines, the low efficiencies compared to *e.g.* fuel cells based on electrochemical reactions instead of just thermally combustion of fuels. Such fuel cells are by now well investigated[55,65] and first examples of fuel cell cars are commercially

available.[66] In most fuel cells, hydrogen together with oxygen from air is converted back to water, which makes it a very clean reaction with just pure water as product. The required hydrogen could come from water splitting, leading to an overall CO_2 free way of providing mobility. Furthermore, hydrogen is a very important chemical in agricultural and chemical industries, especially in the well-known Haber-Bosch process (generation of ammonia from nitrogen and hydrogen) for the production of fertilizers.[67]

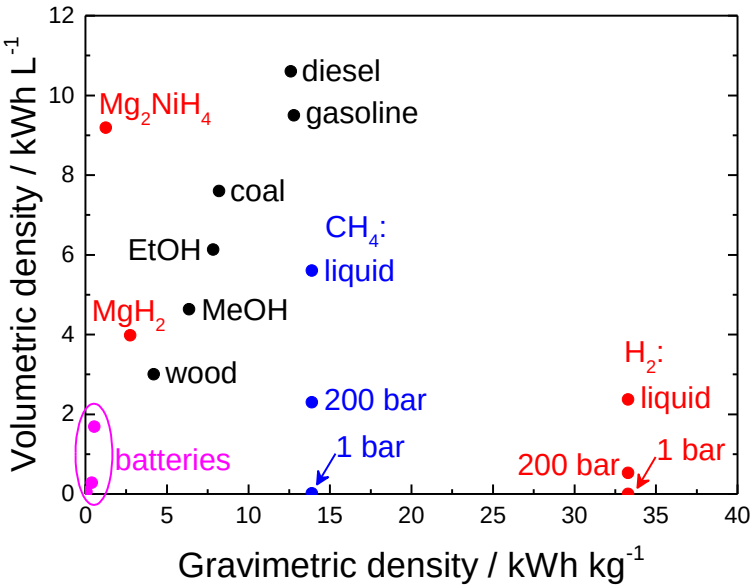

Figure 2.5: Gravimetric and volumetric energy densities for different solid, liquid and gaseous fuels; red: hydrogen storage; blue: methane storage; black: other (fossil) fuels; purple: batteries.[68–70]

Hydrogen exhibits a very high gravimetric energy density because it is the lightest element (Figure 2.5, marked red). On the other hand, as it is gaseous under ambient conditions, the volumetric energy density is very low.[68–70] Thus, for an economic use of hydrogen, the gas has to be compressed or even liquefied, which reduces the potential size of a tank for transportation or storage by two to three orders of magnitude. But even as a liquid, hydrogen has still a low volumetric density compared to *e.g.* liquid methane or presently used fuels such as gasoline or diesel. This strong disadvantage can be overcome in two different ways: either the storage in metal hydrides as it is shown in Figure 2.5 for MgH_2 or Mg_2NiH_4,[68] which also has the advantage of being more protected against burning, or the formation of hydrocarbons by the reaction of CO_2 with H_2, having again the advantage of a possible use of the existing infrastructure for fossil fuels.[55] A combination of all of these strategies could lead to the storage of nearly unlimited amounts of energy in chemical compounds. Scientists even dream

of an economy based on the use of hydrogen instead of fossil fuels, called a hydrogen-based economy.[5,61,64,69,71] A possible way to run several energy-consuming applications in a hydrogen-based economy is illustrated in Figure 2.6.

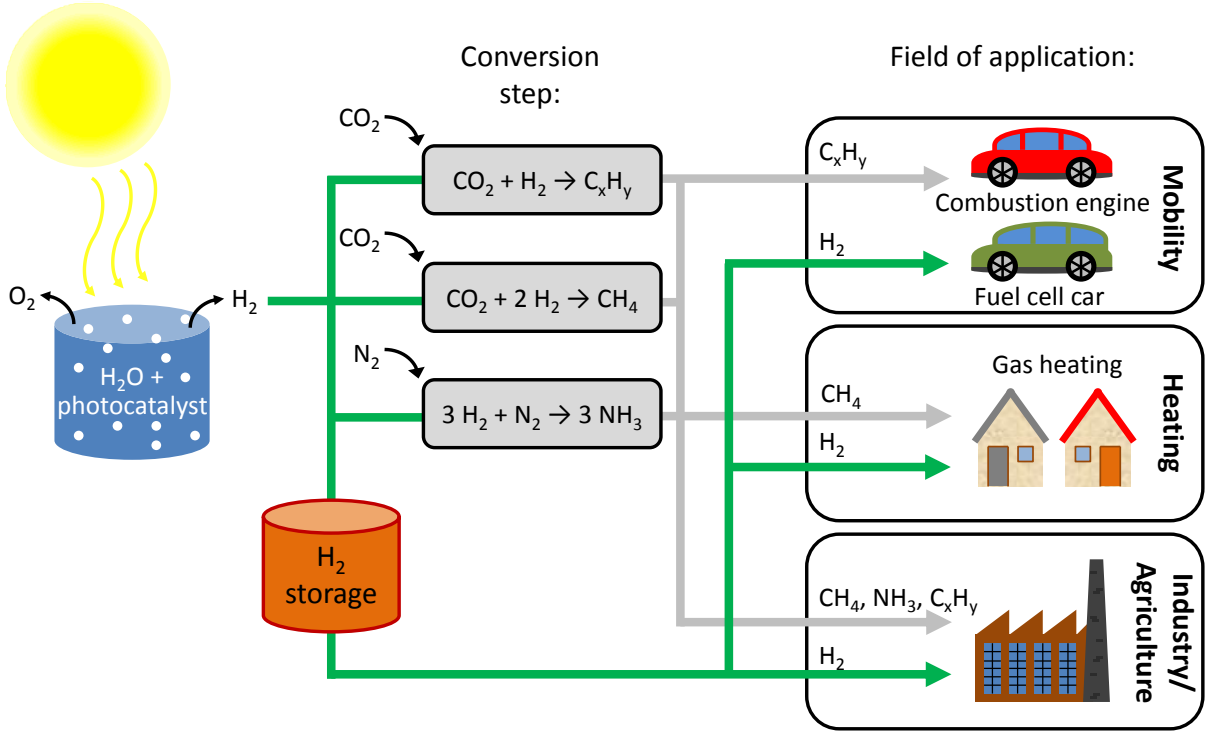

Figure 2.6: Scheme of a possible prospective hydrogen-based economy:[56] hydrogen is produced *via* photocatalysis and either stored or directly consumed, for example in fuel cell cars or industry (*e.g.* blast furnaces with hydrogen instead of coke[72,73]), or further converted into chemicals (*e.g.* ammonia, synthetic natural gas (Sabatier process[62,74])) or other organic hydrogen carriers.[75]

2.3 Photocatalysis

Compared to electrolysis of water into its elements *via* for example electricity from photovoltaic cells,[65,76,77] a more efficient way could be the direct photocatalytic splitting of water on a semiconductor surface. In general, photocatalysis can be explained as a process in which a chemical reaction occurs faster and/or can only occur due to the presence of light (photons) as a catalyst.[9,60] Endergonic chemical reactions taking advantage of photocatalysis for energy storage purposes are also known as "uphill reactions",[57,60] and include processes like the photocatalytic splitting of water into hydrogen and oxygen[7,64] or the photocatalytic reduction of CO_2 to CH_4 to store energy in chemical compounds.[62,63]

Like in all catalytic processes, photocatalysis can also be divided into homogenous and heterogeneous photocatalysis, whereas the former consists of educt(s) and photocatalyst in the same phase (generally aqueous) and the latter of two different phases.[9,78] In this work, the focus will lie on heterogeneous photocatalysis with a solid, semiconducting photocatalyst and liquid educts, that are converted into gaseous or solvated, energetically higher products.

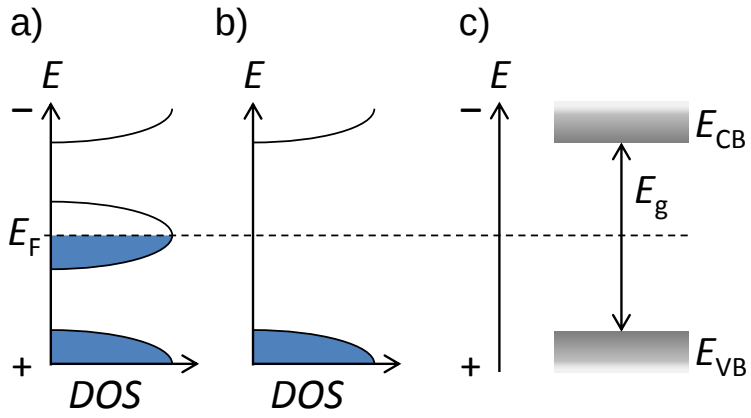

Figure 2.7: Band structure of a) a metal and b) a semiconductor; blue color indicates occupied states, the dashed line marks the position of the Fermi level E_F and c) shows a simplified picture of an intrinsic semiconductor, illustrating the most important parameters E_{CB} (conduction band), E_{VB} (valence band) and E_g (band gap).

To fundamentally understand the mechanism in a heterogeneous photocatalytic reaction, some basics about semiconductor physics need to be considered. Figure 2.7 shows the differences between metallic conductors and semiconductors. It can be seen that in semiconductors, the main characteristics are the position of the valence band (E_{VB}), which consists of fully occupied energetic ground states, the conduction band (E_{CB}), which comprises

all empty states, and the energy difference between the two bands, known as the band gap E_g.[79] Materials with a band gap above ~ 4 eV are insulators. In between the band gap, the so-called Fermi level E_F is situated which is the energy level with an occupation probability of ½.[60]

Semiconductors can be divided into three different types: intrinsic, p-type and n-type semiconductors (Figure 2.8).[80] Intrinsic semiconductors show the behavior already illustrated in Figure 2.7b with a Fermi level exactly in the middle of the band gap. Pristine silicon is an example for an intrinsic semiconductor.[60] A lot of (transition) metal oxides do not show such a behavior; they are either p- or n-type semiconductors. A small group of oxides are p-type semiconductors due to a cation-deficiency and thus are hole-conductors.[81] A bigger group shows n-type behavior, resulting from anion-deficiency, which leads to electron conductors. Examples for both types of semiconductors are copper(II) oxide (CuO) with high content of Cu(I), leading to a p-type behavior and for the more common n-type semiconductors TiO_2 or WO_3, where oxygen vacancies lead to a partial reduction of metal ions, *e.g.* Ti(+IV) to Ti(+III) or W(+VI) to W(+V). Due to the additional states near the valence band edge (p-type) or conduction band (n-type) edge, the Fermi level E_F is strongly shifted towards the valence or reduction band, respectively (Figure 2.8b and c).

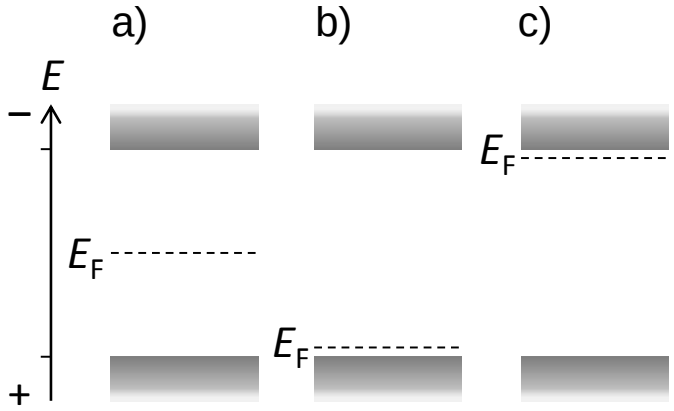

Figure 2.8: Differences in the Fermi level of a) an intrinsic semiconductor (*e.g.*, pure Si),[80] b) a p-type semiconductor (CuO, $CaFe_2O_4$)[8] and c) a n-type semiconductor (most transition metal oxides, *e.g.*: TiO_2, WO_3, Ta_2O_5, $CsTaWO_6$).[8,60]

By shining light on a semiconducting material, an electron from the valence band can be excited into the conduction band, if the energy of the photon is at least as high as the band gap energy E_g. At this state, there are an electron in the conduction band of the semiconductor e^-_{CB} and a hole h^+_{VB} at the electrons former place in the valence band (Figure 2.10a).[8,57]

Apart from the value of the band gap itself, another characteristic feature has a strong influence on the charge carrier lifetimes: the simplified schemes (Figure 2.7-Figure 2.10) do not represent the detailed electronic structure of the conduction and valence band. When having a closer look into the electronic structure of the bands (Figure 2.9), one is able to see that there are direct or indirect transitions possible, depending on the positions of the valence band maximum and the conduction band minimum.[82] The so-called *k*-vector describes the periodicity of the lattice of a crystal (in reciprocal space). In direct semiconductors, a direct transition leads to the formation of an electron-hole pair at the same *k*-value, thus having a high probability of recombination. In indirect semiconductors, an indirect transition occurs and the change in *k*-value is carried out by phonon excitation. Due to the higher complexity of this process, light absorption is weaker than in a direct semiconductor,[83] but separation of the charges is much more efficient. Thus, indirect semiconductors are beneficial if charge separation is required, *e.g.* in photovoltaics and photocatalysts.

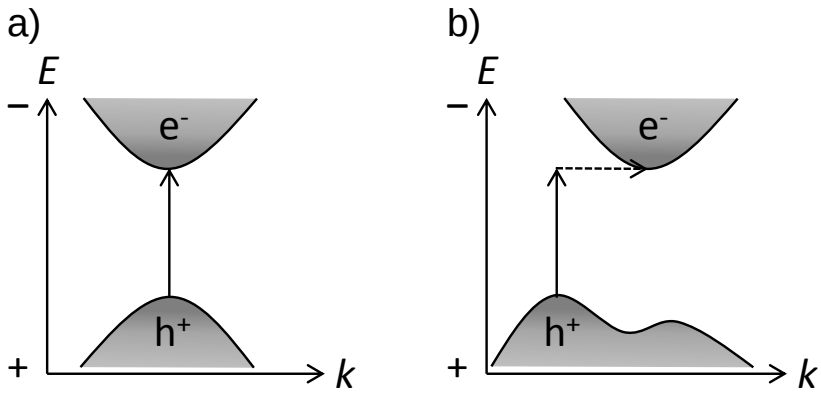

Figure 2.9: Illustration of a) a direct and b) an indirect semiconductor. The *k* value represents different periodical points of the crystal lattice.

The two generated charge carriers inside the semiconductor, namely the electron e^-_{CB} in the conduction band and the hole h^+_{VB} in the valence band, can now perform the catalytic reactions. As they are generated by a photon, the process is called a 'photocatalytic reaction'. Electrons can reduce an electron accepting educt (A), while holes can oxidize an electron donating educt (D, Figure 2.10a). During the process of water splitting, protons are reduced to hydrogen and water is oxidized to oxygen (Figure 2.10b).[64] When talking about specific reactions, the required valence and conduction band positions of a semiconductor can be defined by the oxidation and reduction potential of both half reactions. For overall water

splitting, the electrochemical potential for the hydrogen evolution reaction (HER) is at 0 V (at pH = 0) due to the definition of the standard hydrogen electrode (SHE), and the electrochemical potential for the oxygen evolution reaction (OER) is at +1.23 V *vs*. SHE, leading to a theoretical minimum band gap of 1.23 eV a semiconductor needs to have to perform this reaction.[8,64,84,85] The band positions have to enclose the HER and OER potential to proceed the overall water splitting reaction, thus the conduction band has to be more negative than the HER potential and the valence band more positive than the OER potential. Due to the necessity of an overpotential for both half reactions, in reality the minimum value increases to around 2 eV.[86] The overall water splitting, as well as other possible redox reactions on a photocatalyst, will be discussed in detail in the next chapter.

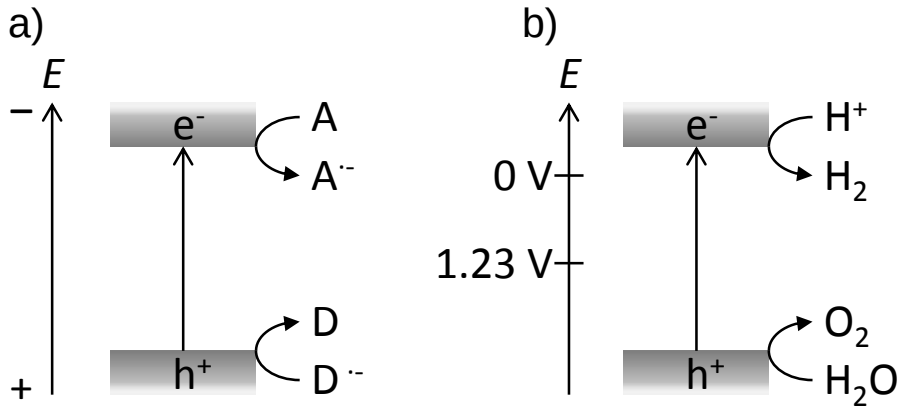

Figure 2.10: a) Principles of photocatalytic reactions on a semiconductor surface. Electrons promote the reduction, holes the oxidation half reaction, whereas an electron acceptor (A) is reduced and an electron donor (D) is oxidized. b) Example of a photocatalytic redox reaction, here overall water splitting into its elements.

2.3.1 Heterogeneous photocatalysis

As discussed above, the electrons and holes generated in a semiconductor due to the irradiation with light can be used for the reduction and oxidation half reactions, respectively, of a redox reaction.

$$2\ h\nu \rightarrow 2\ e^-_{CB} + 2\ h^+_{VB} \tag{2.3}$$

In overall water splitting, the half reactions are the oxidation of water into oxygen and protons

$$H_2O_{(l)} + 2\ h^+_{VB} \rightarrow \frac{1}{2}\ O_{2(g)} + 2\ H^+_{(aq)} \tag{2.4}$$

and the reduction of protons to hydrogen

$$2\ H^{+}_{(aq)} + 2\ e^{-}_{CB} \rightarrow H_{2(g)} \tag{2.5}$$

which leads to the reaction for the overall water splitting:[9,57,64,84]

$$2\ h\nu + H_2O_{(l)} \rightarrow \frac{1}{2}O_{2(g)} + H_{2(g)}; \qquad \Delta G^0 = +237\ \text{kJ mol}^{-1} \tag{2.6}$$

Therefore, two photons with a minimum energy of

$$E = h\nu = \frac{237\ \text{kJ mol}^{-1} / (N_A \cdot e)}{2} = 1.23\ \text{eV} \tag{2.7}$$

have to be provided to decompose one molecule of water. This means, a semiconductor needs a minimum band gap of 1.23 eV to generate electron-hole pairs suitable for water splitting. Ohmic losses and kinetic hindering lower the driving force for the reaction, leading to a much higher required band gap for an efficient photocatalyst of around 2 eV.[87,88]

However, pure photocatalytic semiconductors show a very low activity for the overall water splitting. For instance, the most prominent photocatalyst material TiO_2 does not show water splitting activity if no modifications are made.[28,89] A major drawback is the recombination of excited electron-hole pairs, which leads to heating of the photocatalyst instead of performing redox reactions. Several mechanisms, which can lead to recombination, are summarized in Figure 2.11. After the excitation of an electron-hole pair, the charge carriers are energetically separated, but spatially still very close together (Figure 2.11a). This is especially the case in direct semiconductors, whereas in indirect semiconductors they are at two different positions of the unit cell (see Figure 2.9). Going to bigger particles, the formation of a depletion zone causes a band bending, leading to a separation of electrons and holes.[63,90,91] In the case of a n-type semiconductor (Figure 2.11b), this band bending leads to a strong driving force for the holes to migrate to the surface of the photocatalyst particle, which is at the same time the interface between photocatalyst and electrolyte. It is therefore an easy way to separate electrons and holes and avoid recombination in bigger particles. But such a band bending does not occur in smaller crystallites (below 100 nm). Thus, due to the generally smaller crystallite sizes, all nanostructuring (see Chapter 2.5) lack the intrinsic driving force for charge carrier migration.[60,92]

During the migration of charge carriers to the surface, several mechanisms can lead to recombination processes, for instance:

- surface recombination, because of the surface being the largest defect of a nanocrystal (Figure 2.11c)[24,64]
- bulk recombination at point defects (Figure 2.11d) or at grain boundaries (Figure 2.11e) [24,64,90]
- recombination due to limited diffusion lengths of the charge carriers (Figure 2.11f). The diffusion length is different for both charge carriers (electrons and holes) and depends on the material.[86,93] In general, smaller particles should lead to less recombination, in this case due to smaller diffusion path ways to the surface, which is contrary to the process explained for Figure 2.11b.[94]

The defects mentioned above will be summarized as 'strain' in some parts of this work, because it is hard to distinguish between the different types of defects in most characterization techniques, for example in in X-ray diffraction and refined X-ray data.

Nanostructured materials often require lower annealing temperatures during synthesis, leading to more grain boundaries, and show a higher number of defects due to the higher surface area, leading to increased surface recombination.

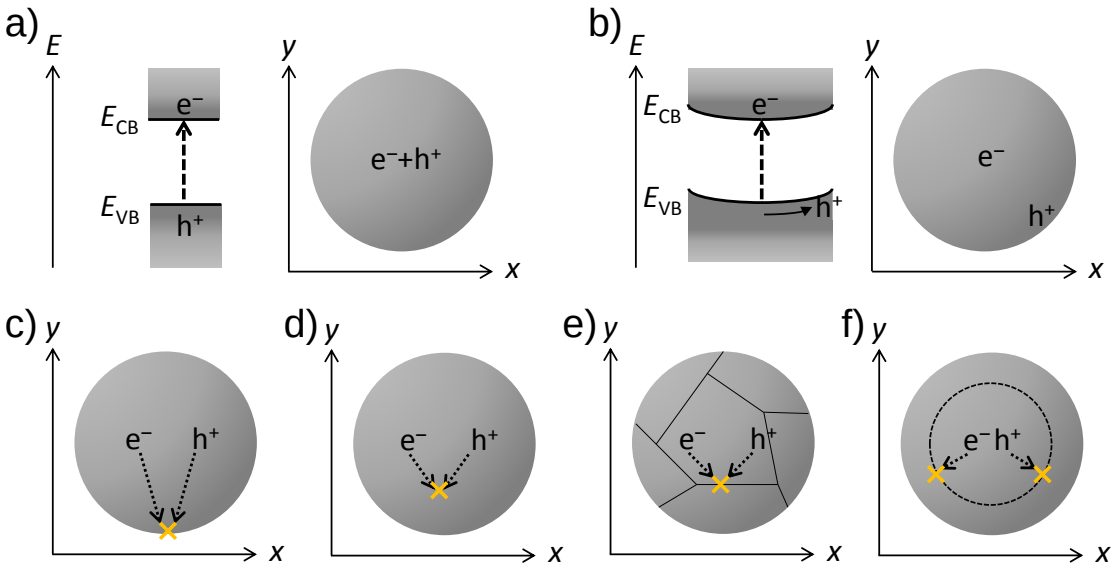

Figure 2.11: Excitation of an electron-hole pair in a) a particle in the nanometer scale (≤ 50 nm) and b) a bigger particle (≥ 100 nm, here for an-type semiconductor), shown from the energetic and spatial point of view and c-f) different possible recombination processes: c) surface recombination, d) bulk recombination, e) recombination at grain boundaries and f) influence of diffusion length.[24,64,86,90,93]

There are several ways to avoid these recombination processes and therefore enhance the photocatalytic activity of a semiconductor:

1) loading with co-catalysts[54,95,96]
2) usage of sacrificial agents[97–99]
3) combination of multiple photocatalyst with different band positions/band gaps (*e.g.* Z-scheme)[41,58]

The latter case 3) is a very powerful tool to enhance photocatalytic reactions. For instance, the photocatalytic activity of TiO_2 is strongly enhanced if two different phases of titania are present, usually anatase and rutile with slightly different band positions due to the different crystal phases. The most prominent example is the rutile/anatase composition P25,[100] often used as a reference material to estimate the activity of a TiO_2 photocatalyst (sometimes even if the photocatalyst is phase-pure and therefore hard to compare with a two-phase P25 material; see Chapter 2.5.4). Other prominent examples are CdS/TiO_2[101] or CdS/ZnO.[102]

Here, focus will be put on case 1) and 2) to avoid effects of charge separation due to different phases, that could affect the photocatalytic activity in a way that would prevent distinguishing from influences of the phases and morphologies. The idea behind the use of both co-catalysts and sacrificial agents will be explained in the next chapter.

2.3.2 Co-catalysts and sacrificial agents

To avoid recombination, a faster separation of the charge carriers and/or a fast consumption of at least one of the charge carriers is necessary. A faster separation can be realized by the deposition of a so called co-catalyst, which is a metal, metal oxide or even a more complex material that accumulates the electrons or holes on its surface (Figure 2.12a).[95] Prominent examples of such co-catalysts for the reduction half reaction are metals like Pt, Rh, or Au, metal oxides like NiO, Co_3O_4 or core-shell materials like Rh on Cr_2O_3 and for the oxidation half reaction metal oxides like IrO_2 or Co-species with phosphate (CoPi).[57,95] Here, the focus will lie on metallic co-catalysts for the reduction half reaction, that is the hydrogen evolution reaction in the photocatalytic hydrogen generation. For the oxidation half reaction, a sacrificial agent will be used whose purpose will be explained later.

Co-catalysts for the hydrogen evolution reaction have to fulfill several requirements: first of all, it is beneficial if the precursor is water-soluble in this case, which enables the

photodeposition of the co-catalyst as a consequence. Photodeposition means the light-induced *in-situ* deposition from an aqueous solution due to the reduction of the metal ions on the photocatalyst, exactly at the position where the electrons reach its surface. Typical examples for photodeposition are nanoparticles of Pt(0) from an aqueous $H_3Pt(+III)Cl_6$ solution (Pt-TiO_2)[103] or Rh(0) from $Na_3Rh(+III)Cl_6$ (Rh-$CsTaWO_6$).[30] The advantages of this technique are the small particle sizes of the co-catalyst, the good distribution over the whole photocatalyst, and the easy handling of the deposition. Alternatively, the pure metal co-catalyst can be grinded with the photocatalyst (*e.g.* Au nanoparticles) or the co-catalyst deposition can be carried out *via* an impregnation or deposition-precipitation process. All of these techniques normally lead to a diminished activity compared to photodeposition.[104] In all cases, a Schottky contact between metal particles and semiconducting photocatalyst is formed.[8]

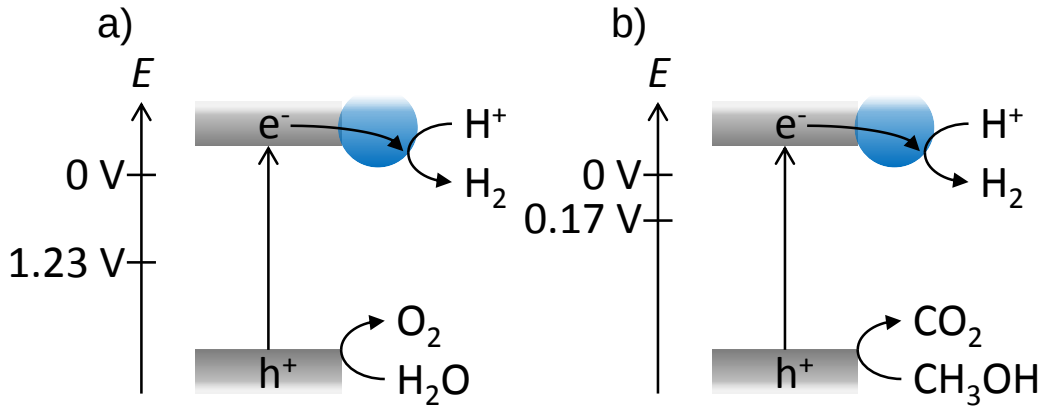

Figure 2.12: a) Illustration of the effect of a co-catalyst for the reduction half reaction and b) the combination of co-catalyst for the reduction plus methanol as sacrificial agent for the oxidation half reaction.

For the oxidation half reaction, the challenging step in overall water splitting is the accumulation of four holes at one site of the photocatalyst to generate one molecule of oxygen (Equation (2.4)). To avoid this limiting step, sacrificial agents can be used, mostly organic molecules such as alcohols or organic pollutants (Figure 2.12b). The latter makes it possible to generate hydrogen on the reduction site and degrade pollutants on the oxidation site at the same time, making it also a very interesting application of photocatalysis for water treatment. The most prominent example for a sacrificial agent is the oxidation of methanol to CO_2:

$$CH_3OH_{(l)} \rightarrow HCHO_{(g)} + H_{2(g)} \quad (2.8)$$

$$HCHO_{(g)} + H_2O_{(l)} \rightarrow HCO_2H_{(l)} + H_{2(g)} \quad (2.9)$$

$$HCO_2H_{(l)} \rightarrow CO_{2(g)} + H_{2(g)} \quad (2.10)$$

with the overall reaction being:[97]

$$CH_3OH_{(l)} + H_2O_{(l)} \rightarrow CO_{2(g)} + 3\ H_{2(g)}; \qquad \Delta G^0 = +16\ \text{kJ mol}^{-1} \quad (2.11)$$

The Gibbs free energy (ΔG^0) for this reaction is much smaller compared to +237 kJ mol^{-1} for the overall water splitting (Equation (2.6)). This reaction is called 'photocatalytic hydrogen production', whereas hydrogen is detected and the amount of evolved gas is given in mol/mmol/µmol. The generated CO_2 is often not detected, either because of non-useful detection techniques or just due to its partial solubility in water.[105] The formation of carbonic acid or carbonates binds CO_2 inside the solution to some extent, making it impossible to quantitatively detect CO_2 in the gas phase.

A combination of both co-catalyst and sacrificial agent is shown in Figure 2.12b: when choosing a suitable co-catalyst with a Fermi level lower than the one of the photocatalyst, electrons are transferred to the metallic co-catalyst due to a Schottky contact between semiconductor photocatalyst and the co-catalyst.[8] At the valence band, holes are consumed for methanol oxidation quickly. Both techniques lead to a very efficient separation of charge carriers and therefore enhanced photocatalytic activity.

2.4 Transition metal oxides in photocatalysis

2.4.1 Transition metal oxides: General aspects

The band gaps and band positions of different transition metal oxides are shown in Figure 2.13. It can be seen that all valence bands occur from the oxygen O 2p orbitals, while the conduction bands are composed of the corresponding transition metal d-orbitals.[106] TiO_2, Nb_2O_5 and Ta_2O_5 can theoretically produce hydrogen because the conduction band is more negative than the proton reduction potential (0 V at pH = 0), while the overpotential for TiO_2 is comparably low. WO_3 cannot evolve hydrogen, because of the more positive conduction band minimum. The principle of anion doping is shown for Ta_2O_5, where the introduction of N 2p orbitals lead to a decrease in band gap.

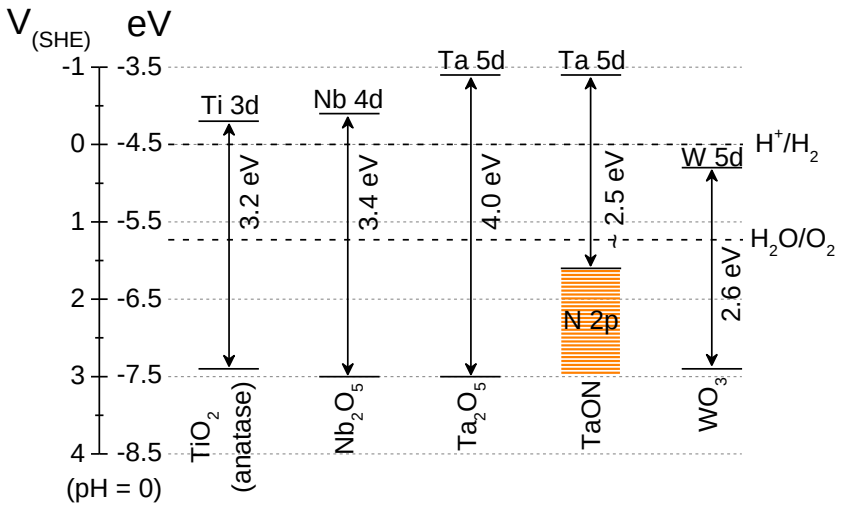

Figure 2.13: Origin of band positions in some transition metal oxides, also showing the change in the band gap in Ta_2O_5 due to nitrogen doping to $Ta_2O_{5-x}N_y$ or up to TaON, resulting in a visible light active photocatalyst.[8,107]

The more complex quaternary transition metal oxide $CsTaWO_6$ used in this work will be presented more detailed in the following subsection.

2.4.2 Defect-pyrochlore structured materials

The defect-pyrochlore structure can be generally described as a modification of the well-known pyrochlore structure with the general formula $A_2B_2O_6Y$ (*e.g.* $(Na,Ca)_2Nb_2O_6(OH,F)$.[107–109] Removing a combination of A and Y ions leads to a wide variation of different defect-pyrochlore structures with the general formula $A_{2-x}B_2O_6Y_x$ (x = 0–1).[109,110] Ikeda *et al.*[29] reported some defect-pyrochlore structured materials as highly active photocatalysts even for overall water splitting without any co-catalyst.

These materials were described with the formula $ABB'O_6$, where A consists of an alkali metal in the oxidation state +I and B and B' are transition metals with oxidation states of +V and +VI, respectively (Figure 2.14). In detail, Ikeda *et al*. investigated materials with A = Rb, Cs, B = Nb, Ta and B' = W.[29] Later on, Schwertmann *et al*. extended this range of materials by the compound $CsTaMoO_6$, which was reported as a highly active photocatalyst for the oxygen evolution reaction (OER).[31]

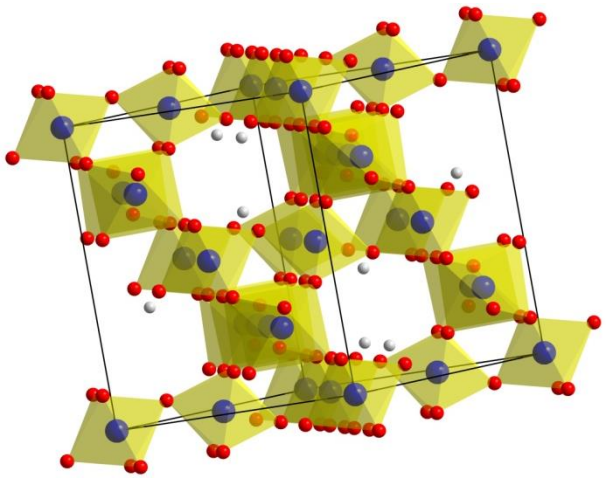

Figure 2.14: Unit cell of the defect-pyrochlore structure with the general formula $ABB'O_6$ with *e.g.* A = K, Rb, Cs (grey), B = Nb, Ta and B' = Mo, W (both blue) and O (red).

Figure 2.15 shows a set of defect-pyrochlore structured transition metal oxides, their band positions and band gaps related to the standard potentials of the hydrogen and oxygen evolution reaction (HER and OER, respectively) in volt and the vacuum level in electronvolt. The small differences in band positions between $CsTaWO_6$ and $CsNbWO_6$ result from the less negative potential of the Nb 4d compared to the Ta 5d orbitals (see also Figure 2.13). The small contribution of the Nb 4d and Ta 5d to the conduction band arise from the convolution of Nb/Ta and W d-orbitals. Usually, the conduction band minimum in defect-pyrochlore structured tungstate materials is supposed to be formed by W 5d, with contributions of the corresponding second transition metal oxide (Figure 2.16).[111,112]

A reduction of the large band gap in the $CsTaWO_6$ material of around 3.6 eV can be done by substitution of tungsten with molybdenum, leading to a band gap of around 2.9 eV.[31] However, this compound is only active for the oxygen evolution reaction due to the more positive conduction band position, caused by the introduced Mo 4d states. A suitable technique to synthesize a visible light-active defect-pyrochlore structured material for hydrogen production is doping with nitrogen, sulfur or tin, as it will be explained in the next Chapter 2.4.3 in detail. Introducing fully occupied s-orbitals leads to a shift of the valence band minimum to more negative potentials, while the conduction band stays unaffected, leading to a decreased band gap of around 2.3−2.4 eV.[32]

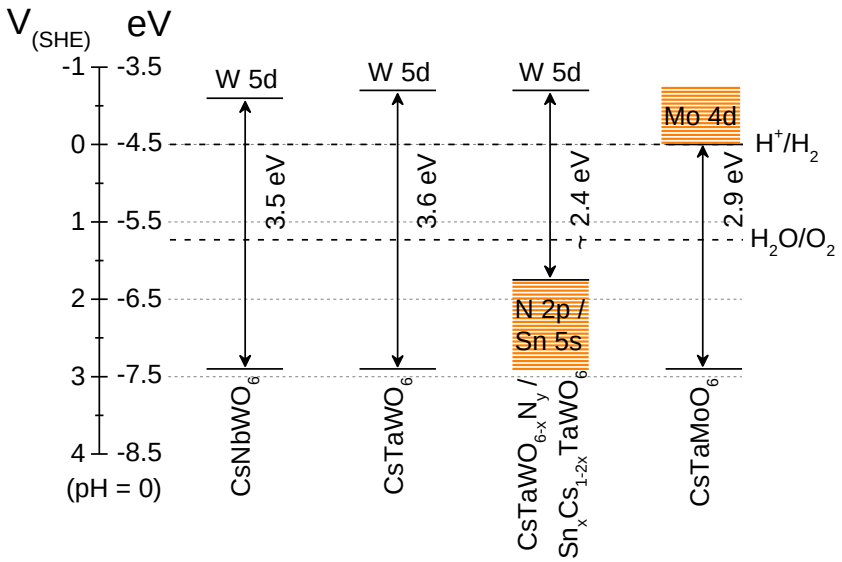

Figure 2.15: Band positions relative to the normal hydrogen electrode (SHE), the vacuum level and corresponding band gaps of different defect-pyrochlore structured materials.[8,31,32]

This work focusses on $CsTaWO_6$ and its photocatalytic activity in hydrogen production from a water/methanol solution. The exact crystallographic parameters of $CsTaWO_6$ are shown in Table 2.1. The lattice constant of the cubic defect-pyrochlore structured $CsTaWO_6$ is a = 10.3768 Å.[32] Band positions of the pure, N- and Sn-doped material are shown in Figure 2.15 and the origin of the conduction and valence band is shown in Figure 2.16. The indirect character of the band gap (as described in Figure 2.9) is also illustrated.

Table 2.1: Crystallographic parameters of the defect-pyrochlore structured $CsTaWO_6$ (JCPDS reference card no. 25-0233).

Element	Position			Wyckoff position	Site occupation factor
	x	*y*	*z*		
Cs	0.375	0.375	0.375	8b	1.0
Ta	0.000	0.000	0.000	16c	0.5
W	0.000	0.000	0.000	16c	0.5
O	0.318	0.125	0.125	48f	1.0

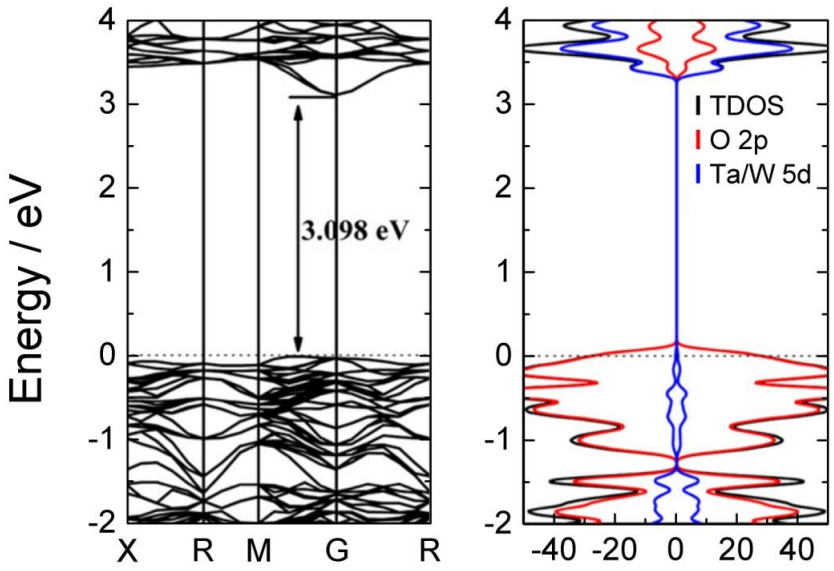

Figure 2.16: a) Calculated electronic band structure of $CsTaWO_6$ as a function of the wave vector *k*, representing different periodical points of the crystal lattice in reciprocal space (shown on the *x*-axis). The indirect nature of the band gap of $CsTaWO_6$ becomes visible, even if the energetic differences between direct and indirect transition are very weak. b) Calculated density of states, showing the origin of the valence and conduction band.[111]

2.4.3 Doping of transition metal oxides for visible light absorption

As it was shown for transition metal oxides and $CsTaWO_6$ in particular, the band gap of these materials is far too large for an efficient photocatalytic behavior under visible light irradiation (*e.g.*, $CsTaWO_6$ can only absorb around 3.2 % of sun spectrum; see Chapter 2.1). Therefore, reducing the band gap is necessary for the use in applications to take advantage of typical transition metal oxide properties, namely their stability under a wide range of conditions (UV light, aqueous media, radical species). To decrease the band gap, additional energy states have to be inserted between conduction and valence band. In the case of $CsTaWO_6$, these states should be more negative compared to the valence band (O 2p orbitals). When consulting the periodic table of elements, a first idea of an element with these properties would be nitrogen due to its lower electronegativity compared to oxygen, leading to a weaker binding of electrons in the N 2p states of the N^{3-} anion.[107] For same reasons, S 3p orbitals of S^{2-} should behave similarly. In fact, both N-doped and N/S-co-doped $CsTaWO_6$ were already reported by Mukherji *et al.*[32] and Marschall *et al.*,[33] respectively. Anion doping takes place at the 48f Wyckoff position by substituting one oxygen by one sulfur atom or three oxygen atoms by two nitrogen atoms, or as Kröger-Vink-notation:

$$2\ O_O^x + 2\ S_{(g)} \rightarrow 2\ S_O^x + O_{2(g)} \tag{2.12}$$

$$3\ O_O^x + 2\ NH_{3(g)} \rightarrow 2\ N_O^{'} + V_O^{\bullet\bullet} + 3\ H_2O_{(g)} \tag{2.13}$$

These substitutions lead to the illustrated changes in band gap (Figure 2.15). Equation (2.12) shows a simplified assumption of monoatomic sulfur in the gas phase (whereas gaseous sulfur has a number of different allotropes in fact).[113] Both doping strategies show some remarkable disadvantages. These are, in the case of nitrogen, the formation of oxygen vacancies, which can be overcome in principal by co-doping with fluorine (from F_2,[114] HF[115] or PTFE[116]):

$$2\ O_O^x + NH_{3(g)} + HF_{(g)} \rightarrow N_O^{'} + F_O^{\bullet} + 2\ H_2O_{(g)} \tag{2.14}$$

Additionally, for N-doping as well as for S-doping, high temperatures are needed; for nitrogen to decompose the ammonia gas and therefore to allow substitution of oxygen and for sulfur to melt and further evaporate the solid sulfur precursor. Heating has to be carried out with an inert carrier gas to avoid instantaneous reoxidation, but under these conditions,

a reduction and therefore the initiation of defects can easily occur, leading to a defect-rich material. Typical temperatures are 550 °C for N-doping and 650 °C for S-doping,[32] which can lead to a destruction of the morphology in the case of nanostructured $CsTaWO_6$. Furthermore, the N and S atoms can be introduced into the material not only by substitution, but also on interstitial places in the lattice. Thus, a full substitution cannot be considered and the formula of the *e.g.* N-doped $CsTaWO_6$ is more likely $CsTaWO_{6-x}N_y$ due to this reason (Figure 2.15).

Another strategy for band gap reduction can be the insertion of elements with the outer shell being fully occupied $5s^2$ orbitals, such as Sb^{3+}, Sn^{2+} and In^{+}. For defect-pyrochlore structured materials ($KTaWO_6$), it was recently found in our group that the substitution of Cs^{+} by Sn^{2+} (Equation (2.15)) leads to the highest increase in absorption and photocatalytic activity.[117]

$$2\ Cs_{Cs}^{x} + Sn_{(l)}^{2+} \rightarrow Sn_{Cs}^{\bullet} + V_{Cs}^{'} + 2\ Cs_{(l)}^{+} \qquad (2.15)$$

2.5 Nanostructuring

2.5.1 Nanostructured photocatalysts – Advantages and disadvantages

In general, heterogeneous catalysis is assumed to be a surface dependent process, which means the larger the surface, the better the performance of a catalyst.[8] The activity of a heterogeneous catalyst, *e.g.* catalytic converters in automobiles or iron catalysts in the Haber-Bosch process, increases with its surface area.[118] However, heterogeneous photocatalysis seems to be a much more complex process. First of all, heterogeneous photocatalysis is not only a process at the surface of the photocatalyst, but also in the bulk of the material due to the required generation of charge carriers inside the material that have to migrate to the surface to perform redox reactions. These charge carriers recombine after a certain diffusion length or at defects, that can be either inside the bulk (site defects, Frenkel defects, *etc*.) or at the surface.[24,64,86,90,93] The usually lower synthesis temperatures for materials with a high surface area also contribute to a higher number of unhealed defects (or strain). Therefore, in fact a higher surface area leads to a higher number of possible sites for the photocatalytic redox reactions, but acts as a defect at the same time. These opposing effects make it difficult to find the best morphology for a heterogeneous photocatalyst.

Additionally, bulk properties, which are beneficial for a high activity, such as band-bending at the interface between photocatalyst and the electrolyte (*e.g.* water), normally leading to an enhanced charge separation and forcing them to the surface of the photocatalyst, do not occur in crystallites smaller than approximately 100 nm.[60]

In general, the following requirements for an effective photocatalyst can be assumed:

- high crystallinity,
- short diffusion ways,
- high surface area to increase the catalytic activity,
- overpotential large enough for hydrogen and oxygen production.

To find the optimum between high crystallinity, small crystallite sizes and therefore short diffusion ways and maintaining a high surface area simultaneously, is the main challenge in these studies on the enhancement of photocatalytic activity. Different morphologies that could be beneficial in photocatalysis, are illustrated in Figure 2.17. Mesoporous materials would lead to a high surface area (Figure 2.17a), while ordered porosity could have further advantages due to very homogenous pore wall thicknesses and an improved transportation of the electrolyte through the highly ordered pore channels (Figure 2.17b). Beside a high surface area, nanoparticles could have a good dispersibility in the electrolyte because of their smaller particle size (Figure 2.17c).

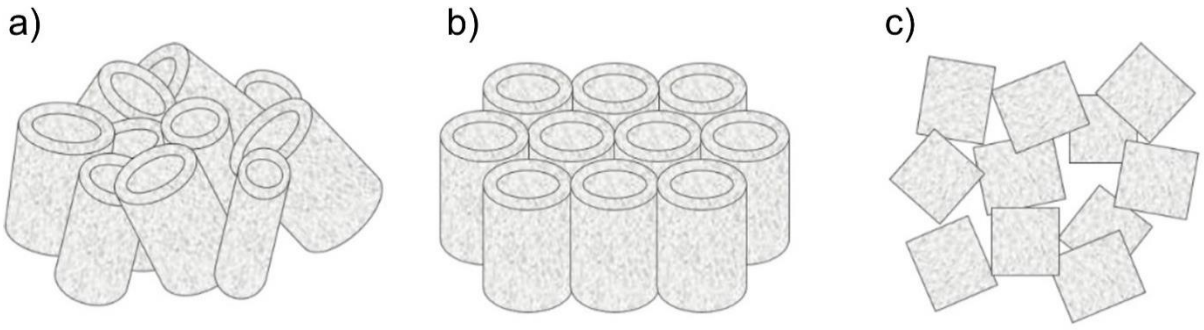

Figure 2.17: Illustration of different nanostructure morphologies: a) non-ordered porous materials, b) ordered porous materials and c) nanoparticles.[119]

Many contradictory results have been published during the last years about the influence of surface area and morphology on the photocatalytic activity. A few examples for transition metal oxides shall be discussed here. Grewe *et al*. published results on P123-derived ordered mesoporous Ta_2O_5 (108 $m^2\ g^{-1}$) and compared it to a commercially available, non-porous

Ta_2O_5 (1 $m^2 g^{-1}$) reference. A 108 times higher surface area just led to 1.5 times higher photocatalytic hydrogen production from water/methanol.[120] On the other hand, Cherevan *et al*. prepared the same compound, also with an ordered mesoporosity, and found out, that their material had a rise in hydrogen generation activity by 15 times compared to a reference material, while the surface area increased by a factor of 15 (34 $m^2 g^{-1}$ for mesoporous Ta_2O_5, 2 $m^2 g^{-1}$ for a non-porous sol-gel reference).[22] The differences in their findings could be due to one of the following reasons: the different ordering and pore sizes of both materials (around 3 nm worm-like pores *vs*. > 20 nm gyroidal pores, respectively) or the higher calcination temperature and therefore a higher crystallinity of the latter one (amorphous (T_{calc} = 550 °C) *vs*. highly crystalline pore walls (T_{calc} = 700 °C)). Actually, Guo *et al*. showed a strong influence of the calcination temperature on the photocatalytic performance for mesoporous Ta_2O_5. A higher calcination temperature (700 °C or higher) led to a 22 times higher photocatalytic hydrogen production compared to amorphous materials (500 °C and 650 °C), although the surface area strongly decreased with increasing temperature.[121] Unfortunately, the average pore size of the material also increased with increasing temperature, making it therefore very hard to clarify which parameter had the larger influence on the activity of the photocatalyst.

Other researchers did comparable studies especially for the most widely used photocatalyst TiO_2, but this compound has on more disadvantage when heated up, namely its phase transformation from anatase to rutile at around 600 °C,[26] generating one more parameter, that varies during temperature and morphology studies. Furthermore, phase pure TiO_2 in any crystallite phase is often compared to a standard, commercially available TiO_2 such as P25, consisting of anatase and rutile, and thus cannot be consulted as a comparable reference (see also Chapter 2.5.4).

Unlike surface area and morphology, studies on the influence of the optimum crystallite size on the photocatalytic activity are rarely available. In theory, there should be such an optimum in the crystallite size, mainly depending on the diffusion length *D* of the minority charge carriers in the investigated material. Assuming spherical particles, the optimum should be a crystallite size of around two times the diffusion length *D* (Figure 2.18b), whereby all generated charge carriers can migrate to the surface and perform electrochemical reactions theoretically. Slightly different crystallite sizes should lead to lower photocatalytic activities:

in case of $D > 2\,L$ (Figure 2.18a) due to recombination of excited charge carriers on their diffusion path through the surface. For $D < 2\,L$ (Figure 2.18c), the decrease in activity arises from either an increase in strain/defects based on the higher surface-to-volume ratio (surface as defect, see Figure 2.11c), the higher strain in decreasing crystallites and therefore higher number of defects in general, or due to changing electronic properties (quantum size effect) and therefore a higher band gap energy.

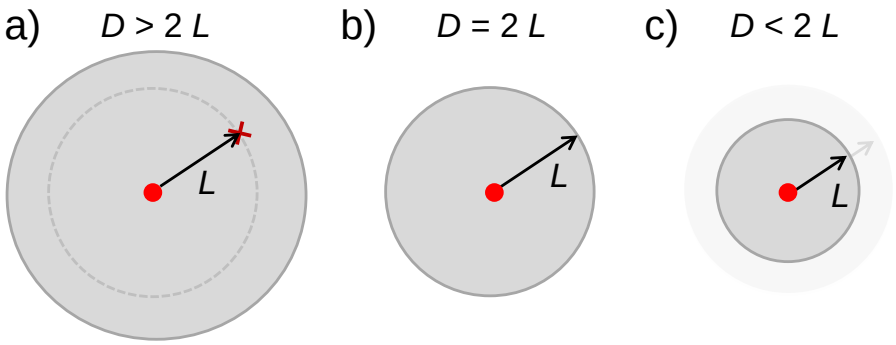

Figure 2.18: Illustration of the optimum particle size in photocatalysis: a) particle with a size bigger than two times the diffusion length of the charge carrier (red point), which thus recombines inside the particle, b) optimum particle size with $D = 2\,L$ and c) smaller particle size than two times the diffusion length.

2.5.2 Nanoparticle preparation: Hydrothermal synthesis

In this work, the preparation of nanoparticles was performed in a hydrothermal synthesis process. Commonly, a hydrothermal synthesis can be described as a special case of solvothermal synthesis with an aqueous solution as solvent. Suitable precursors are dissolved in this solution and the preparation is performed in an enclosed, sealed vessel such as an autoclave or a hydrothermal bomb at temperatures above the boiling point of water (> 100 °C), leading to a high pressure inside the vessel.[122] Water shows a number of particular properties at these conditions, *e.g.* a much lower density and viscosity, leading to a good transport of the precursors inside the reaction solution and a decrease in the dielectric constant.[123] The latter induces a complete change in the solubility of many precursors, which results in a much better dissolution compared to that in water under normal conditions. The hydrothermal synthesis shown in this thesis (see Chapter 3.2.1 for experimental details and Chapter 5.1 for results) is an adaption of the sol-gel synthesis (citrate route) of $CsTaWO_6$ by Schwertmann *et al.*[30] The precursors for the hydrothermal synthesis of the $CsTaWO_6$ product

are the same. Nevertheless, the complexing agents, which are necessary for dissolving the precursor educts in the citrate route in water and normal pressure, can be neglected in the hydrothermal synthesis due to the above-mentioned special conditions in the closed vessel. The only additive that is necessary for the successful preparation of defect-pyrochlore structured nanoparticles is a basic nitrogen atom containing molecule such as ammonia or urea, which in both cases acts as a kind of complexing agent due to the free electron pair at the nitrogen atom. The advantages of the hydrothermal synthesis are the formation of the product at much lower temperatures and the prevention of organic complexing agents that are hard to remove after the reaction. The additives in the hydrothermal synthesis, namely ammonia and urea, can be removed easily with water after the synthesis, leading to a completely phase pure material without any organic residues.

2.5.3 Preparation of mesoporous materials

There are two major techniques for the preparation of mesoporous materials, namely hard- and soft-templating.[124–127] In hard-templating approaches, a mesoporous template, *e.g.* a silica or carbon scaffold, is infiltrated with a precursor solution and after the formation of the targeted compound (*e.g.* by sol-gel processes and crystallization) inside the pores of the scaffold, the template is removed by etching (in the case of silica) or calcination (in the case of mesoporous carbon). A negative of the template can be obtained. Such a hard-templating synthesis was performed parallel to this thesis for $CsTaWO_6$ by Weiss *et al*.[128] The disadvantages of this technique can be an incomplete removal of the template or an incomplete infiltration of the precursor solution and therefore an imperfect negative of the template.[129] Additionally, some precursors can react with the silica or carbon matrix to form silicates or carbides.[130]

These disadvantages can be overcome by the second prominent templating technique: soft-templating. In soft-templating, a structure directing agent is kept inside a precursor solution, either an ionic or non-ionic surfactant, which forms a template due to micelle formation.[131–133] A multitude of different pore sizes, pore geometries and pore ordering can be obtained by the choice of different surfactants.[124,127] Prominent and often used examples of structure directing ionic surfactants are CTAB, and polymers as non-ionic surfactants.[131] The latter exhibit a wide range of chain lengths, chain sequences and number of different chains,

all having influence on the solubility, micelle formation, size and geometry, and the stability of the polymer under heat treatment.

After dissolving precursors and surfactant, micelle formation has to occur under controlled conditions to form the desired structure.[133] Afterwards, the solution is dried at a certain temperature,[134,135] usually followed by a calcination step to remove the surfactant and to get the crystal phase and a high crystallinity of the product at the same time.[124,131,136]

These steps are described in detail in the following chapters, beginning with the potentials of the soft-templating technique in preparation of mesoporous transition metal oxides (2.5.3.1) and followed by a short introduction into micelle formation with special attention to the used polymers (2.5.3.2). It ends up with an explanation of the EISA (2.5.3.3) and the sol-gel process for the preparation of transition metal oxides from soluble precursors (2.5.3.4).

2.5.3.1 Mesoporous transition metal oxides *via* soft-templating

All of the introduced binary transition metal oxides in Chapter 2.4 have already been produced with a mesoporous morphology using the soft-templating approach. A few of them, leading to different pore sizes with different polymers and synthesis procedures, are listed in Table 2.2.[20–22,120,121,137–139]

Table 2.2: Examples of different mesoporous transition metal oxides and their synthesis routes.

Compound	Polymer	Precursor	Solvent	S_{BET} / $m^2\ g^{-1}$	D_p / nm	Ref.
TiO_2	PI-*b*-PEO	$TiCl_4$, $Ti(O^iPr)_4$	THF	30	30	137
TiO_2	P123	$TiCl_4$, $Ti(O^iPr)_4$	EtOH	135	3.5	138
TiO_2	polyethylene glycol dodecyl ether	$Ti(OBu)_4$	*n*-BuOH, H_2O, HAc, Acac, CH_3CN	20–61	7–20	20
WO_3	PI-*b*-PEO	WCl_6	chloroform	56	23	21
WO_3	PEO-*b*-PS	WCl_6	THF	121	11	139
Ta_2O_5	P123	$Ta(OEt)_5$	EtOH	102	4	120
Ta_2O_5	P123	$TaCl_5$	EtOH	41	12	121
Ta_2O_5	ISO	$Ta(OEt)_5$	THF	32	30	22

S_{BET} = BET surface area, D_P = average pore diameter from physisorption

Starting from these literature results, a synthesis strategy for mesoporous $CsTaWO_6$ should be developed in this work on the basis of caesium carbonate, tantalum chloride and tungsten chloride as precursors due to their rather good solubility in ethanol.[121,140] Different polymers were used, namely Pluronic P123 and the ISO polymer, dissolved in ethanol and/or THF. The features of these two polymers are explained in the next chapter. Another block copolymer, PIB-PEO, will be also introduced shortly.

2.5.3.2 A short introduction to block copolymers

For the self-assembling of micelles in an aqueous or alcoholic solution to generate the later pores, a polymer has to consist of hydrophilic and hydrophobic parts. Normally, such non-ionic surfactants have two or three blocks, consequently called diblock and triblock copolymers, respectively. In this work, the diblock copolymer Pluronic P123 and the triblock copolymer ISO were used. Pluronic P123 is a commercially available polymer (*BASF*) of the composition $(PEO)_{20}(PPO)_{70}(PEO)_{20}$, with the hydrophobic propylene oxide (PPO) block embedded by two sequences of the hydrophilic polyethylene oxide (PEO) block. With the general formula $(PEO)_n(PPO)_m(PEO)_n$, a whole group of diblock copolymers can be described, all of the Pluronic family (see Figure 2.19a). [127,141,142] Depending on the chain lengths, these polymers are either liquid (L), paste-like (P) or solid (F) and can assemble differently, *e.g.* as spherical micelles or lamellar structures, depending on the size of the head group (hydrophilic part).

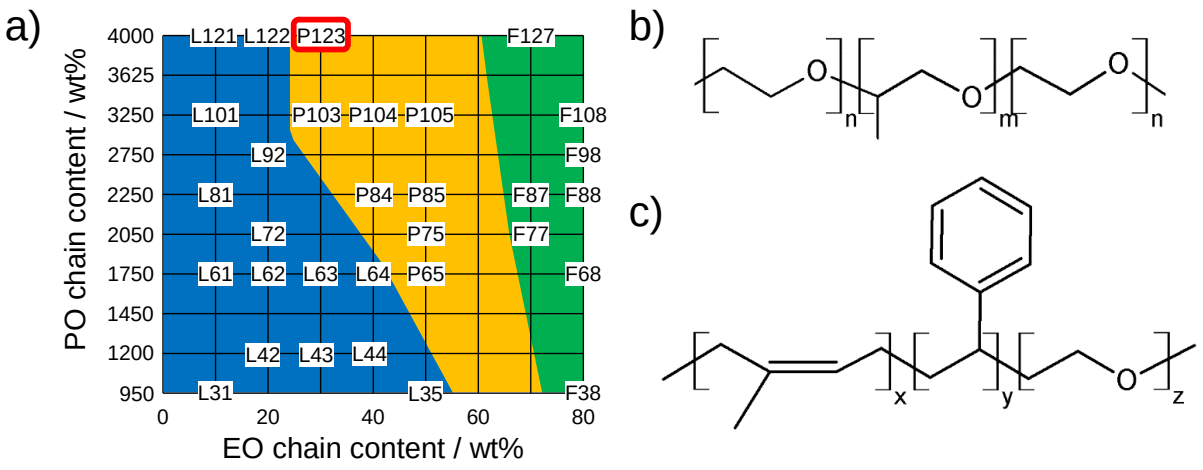

Figure 2.19: a) The 'Pluronic grid',[127,141,142] an illustration of the different available polymers of the general formula $(PEO)_n(PPO)_m(PEO)_n$ and their physical properties: L (or blue): liquid, P (or orange): paste-like, F (or green): solid. The in this work used Pluronic P123 is highlighted in red. b) Structural formula of Pluronic $(PEO)_n(PPO)_m(PEO)_n$ and c) of the ISO polymer $(PI)_x(PS)_y(PEO)_z$.[22] In this work, ISO with a composition of approximately $(PI)_{330}(PS)_{520}(PEO)_{70}$ was used.

The ISO terpolymer consists of three different blocks with the composition $(PI)_x(PS)_y(PEO)_z$ (Figure 2.19c), with PEO being once again the hydrophilic part and polyisoprene (PI) and polystyrene (PS) the hydrophobic chains.[143–146] In theory, under the used polar solvents EtOH and THF, the formed micelles should lead to pores with a size of around 5 and 30 nm for P123 and ISO, respectively.[22,121,146]

The pore size and geometry directly depends on the size of the micelles and therefore the used polymer. Other parameters that can influence the pores are the drying conditions, the solvent and thus *e.g.* a possible swelling of the micelles and hence their growing, consequently causing a growing of the pores in the final structure.[145,147–149] In the case of the ISO polymer, the addition of inorganic hydrophilic precursors leads to a swelling of the hydrophilic part of the polymer (PEO), causing an aging of the polymer.[22,145] The mass ratio of the hydrophilic side chain increases and the positon in the phase diagram is shifted towards the PEO side. Varying this parameter can lead to a number of possible pore geometries, especially spherical cubically ordered pores and non-ordered pores. This special property makes it an interesting tool to investigate different pore geometries, all obtained at similar reaction conditions (Figure 2.20).[144,150]

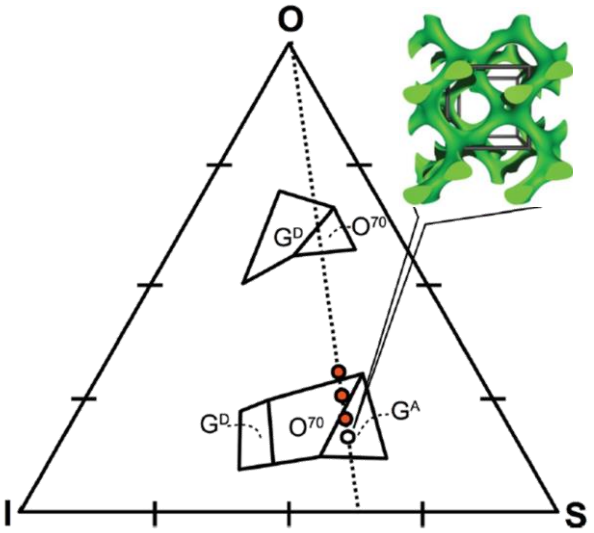

Figure 2.20: Phase diagram of the ISO block copolymer. The dashed line indicates the different pore orders that are possible with the used polymer due to the swelling of the hydrophilic "O" part (PEO) after the addition of hydrophilic precursor.[150] The marked region with G^A belongs to the alternating gyroid pore geometry.

Besides the two already mentioned block copolymers P123 and ISO, another polymer, namely the diblock copolymer PIB-PEO, was used in some continuative experiments in Chapter 5.2.5.2. PEO acts once again as the hydrophilic chain of the polymer, PIB (polyisobutylene) as the hydrophobic part. PIB-PEO plays a negligible role in this work; detailed information about this polymer and the resulting pore morphology can be found in literature.[151–153] The average pore size for the polymer with the composition PIB_{50}-PEO_{45} should lie in the range of 10–15 nm.[153]

2.5.3.3 EISA process

The spontaneous formation of the micelles from a solution of dissolved polymer chains is known as the 'evaporation induced self-assembling' (EISA).[131,133] As it was described above, the polymer can assemble in different arrangements, *e.g.* spherical, cylindrical or lamellar. In Figure 2.21, the formation of spherical pores is shown. This mechanism takes place for P123 as well as for the ISO polymer.

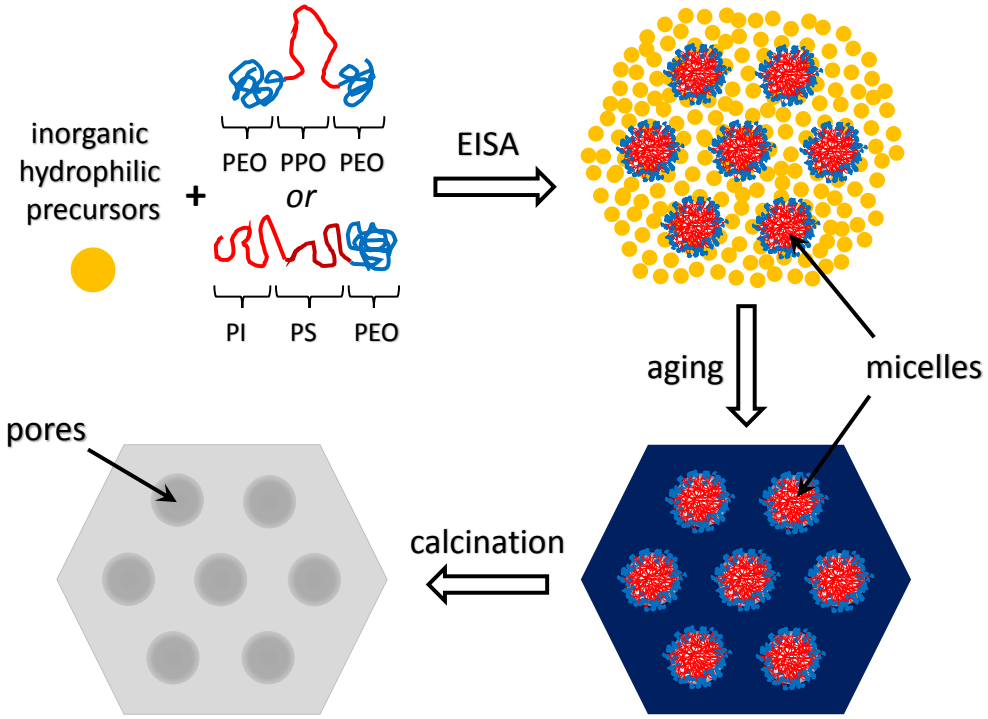

Figure 2.21: Illustration of the evaporation-induced self-assembling (EISA) of polymers and the formation of a mesoporous oxide: during evaporation of the solvent, polymer micelles are formed (here: spherical, as it is the case for P123 and ISO under the used conditions). After an additional aging step, the sol-gel transition is completed and the micelles are embedded in the matrix. The oxide is formed after a calcination step and the polymer is removed, leaving pores inside the oxide powder.[131,154]

In a first step, the solvent is slowly evaporated under controlled conditions (in best case, with temperature and humidity control).[131,154] During this step, a critical micelle concentration is reached at which the polymer starts to assemble, with hydrophobic tails away from the polar solvent and hydrophilic PEO chains in the direction of the solvent and the hydrophilic precursor.[155,156] The inorganic precursors themselves form a wet gel (due to the sol-gel process, see Chapter 2.5.3.4), still including solvent molecules. Furthermore, the inorganic hydrophilic precursors are also incorporated in the hydrophilic part of the polymer. After further aging, the precursors condensate and the solvents are evaporated completely. The polymer micelles are now incorporated in a solid composite, at best in an ordered manner. In a last step, the sample is usually calcined at an appropriate temperature to get the desired crystal phase and at the same removing the polymer completely.[124,131,136] In the end, a highly porous powder can be obtained.

Most literature about polymer-derived transition metal oxides is based on binary compounds (*e.g.* TiO_2, Ta_2O_5, WO_3; see Table 2.2); examples for more complex oxides are very rare.[157–161] Challenging aspects in the preparation of complex phases like defect-pyrochlore structured $CsTaWO_6$ are the interaction between the different precursors and their diverse solubility and sol-gel transition behavior, all together leading to a synthesis difficult to control. Results can be either the formation of undesired by-phases, phase separation, or simply a less porous or non-porous material due to ripening processes or phase transformations on the way to the desired phase.

2.5.3.4 Principles of sol-gel processes

During the evaporation of the solvent in the EISA process, the precursors undergo different formation processes, especially sol-gel processes. In a first step, a sol is formed, consisting of small nanoparticles in solution, which further proceed condensation to form a wet gel of interconnected particles. After complete removal of the solvent, a solid gel is received.[162–164] Nowadays, the mechanisms of aqueous sol-gel processes are well known, especially for very fundamental reactions like the formation of SiO_2.[163] In principle, a suitable precursor such as tetraethyl orthosilicate (TEOS, $Si(OC_2H_5)_4$) or tetramethyl orthosilicate (TMOS, $Si(OCH_3)_4$) is dissolved in a mixture of water and alcohol (*e.g.* ethanol). The initiated reaction is based on two major steps: the partial hydrolysis of the precursor to

$$Si(OR)_4 + x\ H_2O \rightarrow Si(OR)_{1-x}(OH)_x + x\ HR, \text{ with R = } e.g.\ CH_3 \text{ or } C_2H_5 \qquad (2.16)$$

followed by the condensation to $(OR,OH)_3Si–O–Si(OR,OH)_3$ under the release of H_2O and further condensation steps, resulting in the final gel.[162–165]

This mechanism is based on the hydrolysis and therefore takes place in aqueous solutions under water elimination. For non-aqueous solutions, the whole process is very similar, even if it is not as much investigated as for the sol-gel process in aqueous solution. Here, the source for oxygen to form an oxide material comes from the solvent or from the organic part of the precursor. The non-aqueous synthesis reported in this thesis (Chapter 3.2.2) for the formation of mesoporous semiconducting oxides is based on chloride precursors, dissolved in EtOH. Therefore, only the formation of an oxide material from chlorides in alcohol will be described here. The first step is once again the hydrolysis, taking place immediately after bringing chlorides and alcohol together:[166–168]

$$MCl_x + y\ ROH \rightarrow (RO)_yMCl_{x-y} + y\ HCl \tag{2.17}$$

with M = Ta, W. Here, the oxygen source is the hydroxy group of the alcohol. The elimination of the alcohol leads to the hydrolysis of the chloride precursor and the release of hydrochloric acid. The second step is the condensation reaction, described in the following equation:

$$MCl_x+(RO)_yMCl_{x-y} \rightarrow Cl_{x-1}M\text{-}O\text{-}MCl_{x-y}(RO)_{y-1} + RCl \tag{2.18}$$

Besides this general synthesis procedure, the reaction was investigated in literature for tungsten chloride (WCl_6) dissolved in ethanol (EtOH, C_2H_5OH).[165,169,170] It could be seen that especially the hydrolysis step is strongly dependent on the ratio of EtOH to WCl_6.[169] At a molar ratio of 1:1, $W(OC_2H_5OH)Cl_5$ is formed, but about half of this compound decomposes to $WOCl_4$ and C_2H_5Cl. At higher amounts of EtOH, the reaction proceeds and the product above a ratio of around 10:1 has an average composition around $W(OC_2H_5OH)_{3.5}Cl_{2.5}$. In our experiments, the molar ratio of EtOH to WCl_6 is around 100:1 (see Table 3.8 and Table 3.9). At such a high excess of ethanol, another reaction can occur, forming pentavalent tungsten:

$$W(+VI)Cl_6 + 2\ C_2H_5OH \rightarrow W(+V)Cl_3(OC_2H_5)_2 + 2\ HCl + \frac{1}{2}Cl_2 \tag{2.19}$$

This interesting behavior was confirmed in literature *via* elemental analysis and EPR of the reaction solution.[169] So in general it is possible to get stable compounds with pentavalent tungsten in non-aqueous sol-gel processes. This will be important when looking at the exact formation mechanism for the mesoporous $CsTaWO_6$. The other precursor for this compound,

namely Cs_2CO_3 and $TaCl_5$, take place in the sol-gel process as follows: Cs_2CO_3 does not undergo any sol-gel process; only an anion exchange takes place, resulting in CsCl from the high excess of chloride from $TaCl_5$ and WCl_6, released during their sol-gel transitions. $TaCl_5$ itself undergoes the same reactions as shown in Equations (2.17) and (2.18), so the hydrolysis and condensation in an alcoholic environment. The exact mechanism for the whole reaction of Cs_2CO_3, $TaCl_5$ and WCl_6 is even more complicated and will be explained in detail in Chapter 5.2.2.

2.5.4 How to choose a reference material for nanostructured materials

The selection of a suitable reference material is quite important for a subsequent evaluation of the enhancement of photocatalytic activity by nanostructuring. Choosing a commercially purchasable standard material has the advantage of a good comparability to the results of other groups due to the availability of getting the same material from the same provider. On the other hand, disadvantages occur due to *e.g.* a missing full characterization of the material and the mostly unknown synthesis procedure for the materials and therefore possible by-phases, that are not taken into account. A prominent example for such a commercially available material is P25 provided by *Evonik*, which is a TiO_2 powder mainly consisting of the two phases anatase (~ 70−85 %) and rutile (~ 15 %), but also amorphous TiO_2 (0−13 %).[100] Due to this changing composition and the different phases, getting new information about the influence of nanostructuring is very hard if compared to phase-pure, nanostructured TiO_2 materials (*e.g.*, TiO_2 anatase nanoparticles).[24,103,171–173] The number of phases leads to a charge separation caused by the different band positions and makes P25 a rather good photocatalyst, compared to phase-pure TiO_2 materials.[174]

For tantalum oxide, the commercially available Ta_2O_5 powder can be used as a reference material, but the missing full characterization and the high synthesis temperature make it once again hard to compare with nanostructured materials. For example, Grewe *et al*. compared the highly crystalline commercial Ta_2O_5 powder with their amorphous, ordered mesoporous Ta_2O_5 and can therefore see just minor enhancements in photocatalytic activity.[120] A more sensible way would be the production of a reference sample at the same conditions as the nanostructured materials. At this point, the influences of the nanostructuring itself (higher surface area, mesopore size *etc*.) could be observed much

better. Cherevan *et al*. used such a reference material to draw their conclusions on the influence of nanostructuring on a Ta_2O_5 photocatalyst.[22]

$CsTaWO_6$, as it is used in this work, is not available by any commercial provider. Therefore, such a comparison can be omitted. However, there are two synthesis techniques, which lead to phase-pure and already well-characterized $CsTaWO_6$ materials, namely solid-state reaction (SSR)[29,32,33] and sol-gel citrate route.[30,31] Both syntheses are used in this work to prepare reference materials and rank the results of the photocatalytic measurements. Furthermore, at the beginning of this work, $CsTaWO_6$ *via* SSR and ball-milled $CsTaWO_6$ *via* citrate route were still the most active configuration of this compound; thus, a comparison shows if the new synthesis routes lead to any advantages in the photocatalytic performance. In the case of $CsTaWO_6$ nanoparticles, the preparation of a reference material at the same temperatures, but with surface areas as low as for SSR or citrate route (< 1 up to 4 $m^2 g^{-1}$) is not possible. Therefore, only the above-mentioned two reference materials can be considered. For the mesoporous $CsTaWO_6$ samples, non-porous references were prepared by just excluding the polymer during the synthesis; drying and calcination steps stayed the same. Unfortunately, such syntheses do not lead to a phase-pure reference material and are thus once again hard to compare with phase-pure nanostructured materials (see Figure 5.58 in Chapter 5.2.4.2).

3 Experimental section

3.1 Used chemicals

All chemicals were used without further purification and are listed here, divided into precursor chemicals (Table 3.1), solvents, additives and acids/bases (Table 3.2), and polymers (Table 3.3), which were necessary for either nanostructuring or electrospinning. In case of the use of water for synthesis or washing (*e.g.* hydrothermal syntheses), demineralized water was used.

Table 3.1: List of precursor chemicals.

Chemical	Chemical Formula	Purity	CAS number	Producer
caesium carbonate	Cs_2CO_3	99.9 %	534-17-8	Alfa Aesar
tantalum chloride	$TaCl_5$	99 %	7721-01-9	H.C.Starck
tungsten chloride	WCl_6	99 %	13283-01-7	H.C.Starck
caesium nitrate	$CsNO_3$	99.8 %	7789-18-6	Alfa Aesar
tantalum ethoxide	$Ta(OEt)_5$	99.999 %	6074-84-6	Alfa Aesar
ammonium tungstate	$(NH_4)_{10}(W_{12}O_{41})$	99.99 %	11140-77-5	Alfa Aesar
ammonium molybdate	$(NH_4)_6(Mo_7O_{24}) \cdot 4\ H_2O$	99 %	12054-85-2	Alfa Aesar
potassium acetate	KOAc	99.98 %	127-08-2	Sigma-Aldrich
niobium ethoxide	$Nb(OEt)_5$	99.999 %	3236-82-6	Alfa Aesar
tantalum oxide	Ta_2O_5	99 %	1314-61-0	Alfa Aesar
tungsten oxide	WO_3	electronic grade	1314-35-8	H.C.Starck

Table 3.2: List of solvents, additives, acids and bases.

Chemical*	Chemical Formula	Purity	CAS number	Producer
ethanol (EtOH)	C_2H_5OH	99.9 %	64-17-5	VWR chemicals
methanol (MeOH)	CH_3OH	HPLC grade	67-56-1	VWR chemicals
tetrahydrofuran (THF)	C_4H_8O	99.5 %	109-99-9	Carl Roth
citric acid monohydrate	$C_6H_8O_7 \cdot H_2O$	99 %	5949-29-1	Alfa Aesar
ethylenediaminetetraacetic acid (EDTA)	$C_{10}H_{16}N_2O_8$	99.4 %	60-00-4	Alfa Aesar
hydrogen peroxide	H_2O_2	30 %	7722-84-1	Acros Organics
sulfuric acid	H_2SO_4	96 %	7664-93-9	Stockmeyer
hydrochloric acid	HCl	37 %	7647-01-0	Stockmeyer
nitric acid	HNO_3	60 %	7697-37-2	Stockmeyer
sodium hexachlororhodate	Na_3RhCl_6	99.999 %	14972-70-4	Aldrich
aqueous ammonia	NH_3	≥ 25 %	7664-41-7	Fluka
urea	CH_4N_2O	≥ 99.5 %	57-13-6	Sigma-Aldrich
N,N-dimethylformamide (DMF)	C_3H_7NO	99 %	68-12-2	Stockmeyer
tin(II) sulfate	$SnSO_4$	99 %	7488-55-3	Carl Roth

* in parentheses: trivial name/abbreviation

Table 3.3: List of polymers.

Short name	Long name	Chemical composition	CAS number	Producer
PEO	poly(ethylene oxide)	$(PEO)_{160}$ M_w = 10000 g mol^{-1}	25322-68-3	Sigma-Aldrich
PEO-PPO-PEO (PEO-*b*-PPO-*b*-PEO, Pluronic P123)	poly(ethylene oxide)-*b*-poly(propylene oxide)-*b*-poly(ethylene oxide)	$(PEO)_{20}(PPO)_{70}(PEO)_{20}$ M_w = 5800 g mol^{-1}	9003-11-6	Sigma-Aldrich
PIB-PEO (PIB-*b*-PEO)	poly(isobutylene)-*b*-poly(ethylene oxide)	$(PIB)_{50}(PEO)_{45}$ M_w = 5620 g mol^{-1}	–	BASF SE
ISO (PI-*b*-PS-*b*-PEO)	polyisoprene-*b*-polystyrene-*b*-poly(ethylene oxide)	$(PI)_{330}(PS)_{520}(PEO)_{70}$ M_w = 80400 g mol^{-1}	–	work group of Prof. Dr. U. Wiesner
PAN	polyacrylonitrile	$(PAN)_{2800}$ M_w = 150000 g mol^{-1}	25014-41-9	Sigma-Aldrich

The ISO polymer of this batch had a composition of approximately $(PI)_{330}(PS)_{520}(PEO)_{70}$, calculated from the investigated composition of 27.85 wt% polyisoprene (31.21 vol%), 66.87 wt% polystyrene (64.18 vol%) and 5.27 wt% poly(ethylene oxide) (4.61 vol%). The density of the used ISO polymer is 0.93 g cm^{-3}.

In this list, all the hydrophilic poly(ethylene oxide) groups got the abbreviation 'PEO' for simplification; in general, for polymers with relatively smaller molecular weights like the above-listed P123 and PEO, the term poly(ethylene glycol) (PEG) is often used.[175] This

(unofficial) rule was omitted to prevent a possible confusion of the reader due to changing names in between the text.

3.2 Preparation techniques

3.2.1 Nanoparticle preparation

Defect-pyrochlore structured nanoparticles were prepared by stepwise addition of water-soluble precursor in stoichiometric amounts in a snap-cap glass vial under stirring. After the addition of the B-cation precursor ($Nb(OEt)_5$, $Ta(OEt)_5$), only a short intermediate stirring step was performed to homogenize the solution, followed by transfer in the reaction vessel. The hydrothermal reaction was carried out in a 45 mL Teflon-lined hydrothermal synthesis autoclave (*Parr Instrument Company, Model 4744 General Purpose Acid Digestion Vessel*), filled with 17 mL of the reaction solution (40 % filling). The principle reaction steps are illustrated in Figure 3.1; detailed explanations for every compound can be found in the next subsections.

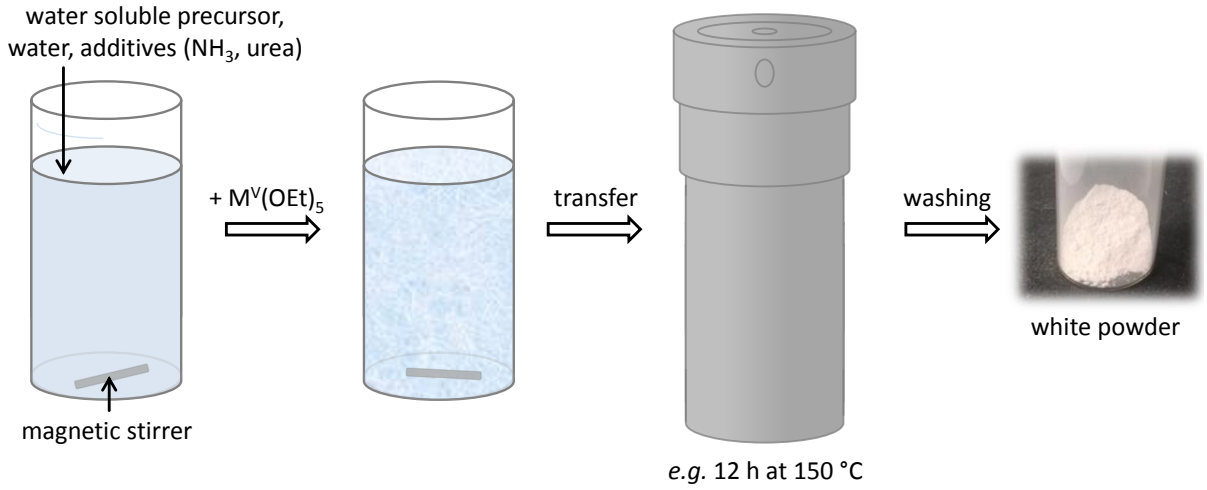

Figure 3.1: General synthesis procedure for the preparation of defect-pyrochlore structured nanoparticles *via* hydrothermal synthesis.

3.2.1.1 $CsTaWO_6$ nanoparticles

<u>$CsTaWO_6$ nanoparticles with 8–16 nm:</u> $CsNO_3$ was dissolved in different amounts of deionized water and conc. aqueous ammonia. After approximately 30 min of stirring, ammonium tungstate was added. A solution of 0.24 M $Ta(OEt)_5$ in abs. EtOH was prepared, and 2.8 mL of this solution were added to the clear precursor solution, after which it became

opaque and white in color. After another 15 min of stirring, the solution was transferred into the 45 mL autoclave and heated for several hours in a drying oven at different temperatures. The product was washed with water for several times and finally one time with ethanol. The resulting white $CsTaWO_6$ nanoparticle powder was dried at 80 °C in a drying oven.

$CsTaWO_6$ nanoparticles with 30 nm: For nanoparticles with a crystallite size of 30 nm, urea was used instead of 1 mL ammonia solution in the same molar amount (≙ 829 mg urea). Precursor amounts and synthesis procedure were similar to the ammonia-containing route described above.

Table 3.4: Precursor and ratios for the preparation of 400 mg $CsTaWO_6$ nanoparticles.

Chemical	M_W / g mol^{-1}	Amount / mol	Amount / g	Equivalent
$CsNO_3$	194.91	$6.75 \cdot 10^{-4}$	0.132	1
$Ta(OEt)_5$	406.26	$6.75 \cdot 10^{-4}$	0.274 (≙ 2.4 mL 0.24 M in EtOH)	1
$(NH_4)_{10}(W_{12}O_{41})$	3060.58	$5.40 \cdot 10^{-5}$	0.165	0.083
dissolved in a mixture of water (0 to 16.75 mL) and conc. aqueous ammonia (17 to 0.25 mL) *or* urea (829 mg)				
$CsTaWO_6$	593.69	$6.75 \cdot 10^{-4}$	0.400	1

3.2.1.2 $CsTaMoO_6$ nanoparticles

For the preparation of $CsTaMoO_6$ nanoparticles, only the precursor of the B' cation was changed to the corresponding molybdenum containing compound ammonium molybdate. Other precursors (A and B cation) stayed the same. Hydrothermal synthesis was carried out at 150 °C for different times.

Table 3.5: Precursor and ratios for the preparation of 342 mg $CsTaMoO_6$ nanoparticles.

Chemical	M_W / g mol^{-1}	Amount / mol	Amount / g	Equivalent
$CsNO_3$	194.91	$6.75 \cdot 10^{-4}$	0.132	1
$Ta(OEt)_5$	406.26	$6.75 \cdot 10^{-4}$	0.274 (≙ 2.4 mL 0.24 M in EtOH)	1
$(NH_4)_6(Mo_7O_{24}) \cdot 4\ H_2O$	1235.86	$9.65 \cdot 10^{-5}$	0.119	0.143
dissolved in a mixture of 16 mL water and 1 mL conc. aqueous ammonia				
$CsTaMoO_6$	505.79	$6.75 \cdot 10^{-4}$	0.342	1

3.2.1.3 $CsNbWO_6$ nanoparticles

Besides the variation of the B' cation (W or Mo), also the B cation was changed from Ta to Nb by changing the precursor from $Ta(OEt)_5$ to $Nb(OEt)_5$ to get the compound $CsNbWO_6$.

Table 3.6: Precursor and ratios for the preparation of 340 mg $CsNbWO_6$ nanoparticles.

Chemical	M_W / g mol^{-1}	Amount / mol	Amount / g	Equivalent
$CsNO_3$	194.91	$6.75 \cdot 10^{-4}$	0.132	1
$Nb(OEt)_5$	318.21	$6.75 \cdot 10^{-4}$	0.215 (≙ 171 µL)	1
$(NH_4)_{10}(W_{12}O_{41})$	3060.58	$5.40 \cdot 10^{-5}$	0.165	0.083
dissolved in a mixture of 16 mL water and 1 mL conc. aqueous ammonia				
$CsNbWO_6$	502.76	$6.75 \cdot 10^{-4}$	0.340	1

3.2.1.4 Continuative experiments: Microwave synthesis, nanofibers, Sn-doping

Microwave-assisted $CsTaWO_6$ nanoparticles:

The same ratio and amount of precursor as shown in Table 3.4 were dissolved in 1 mL aqueous ammonia plus 16 mL of water. 12 mL of the dispersion was poured into a 30 mL microwave vial, which correlates to a filling of 40 %. Ratios, amount of solvents and filling were identical to the hydrothermal synthesis of 13 nm $CsTaWO_6$ nanoparticles *via* hydrothermal synthesis (see Chapter 3.2.1.1). The dispersion was heated in a microwave (*Anton Paar Monowave 300*) to 150 °C as fast as possible, hold at this temperature for 90 min and cooled

down with compressed air. Afterwards, the white precipitate was washed with water for several times, one last time with ethanol and dried at 80 °C.

Electrospinning of $CsTaWO_6$/carbon fibers:

250 mg as-prepared $CsTaWO_6$ nanoparticles (L_a = 13 nm, from hydrothermal synthesis with 1 mL 25 % aqueous ammonia, 16 mL H_2O) were dispersed in a solution of 250 mg PAN in 2.5 g DMF and ultrasonicated for 20 min at 40 °C. The stable dispersion was filled in a syringe and electrospinning was carried out with a collector voltage of 13 kV and the voltage at the needle was set to 2 kV. The distance between needle and collector was 22 cm and the pump rate 0.2 mL h^{-1}. After electrospinning overnight, the as-spun fiber mat underwent a stabilization step for 1 h at 225 °C in air, followed by a carbonization step for 1 h at 800 °C under argon atmosphere (50 mL min^{-1}), in both steps with heating rates of 2 °C min^{-1}.[176]

Sn-doped $CsTaWO_6$ nanoparticles:

350 mg as-prepared $CsTaWO_6$ nanoparticles (L_a = 13 nm, from hydrothermal synthesis with 1 mL 25 % aqueous ammonia, 16 mL H_2O) were dispersed in 17.5 mL of a solution of $SnSO_4$ in water with a concentration of 7.2 mg $SnSO_4$ mL^{-1}. The dispersion changed its color from white to yellow/orange immediately. After shaking overnight, the $CsTaWO_6$ nanoparticles were centrifuged and dried (1 d experiment) or a new $SnSO_4$ solution was added. The exchange of the doping solution was repeated five times in total (7 d experiment). After the last exchange, the dispersion was shaken for three days, followed by washing with water several times and subsequent drying at 80 °C.

The same procedure was performed for a $CsTaWO_6$ reference sample, prepared *via* solid state reaction (SSR, see Chapter 3.2.3.2).

3.2.2 Mesoporous materials

3.2.2.1 Mesoporous materials prepared in a climatic chamber

Preliminary experiments: Mesoporous Ta_2O_5, WO_3 and Nb_2O_5:

For the pretests of the synthesis of mesoporous materials in a climatic chamber, $1.5 \cdot 10^{-3}$ mol of the corresponding precursor chloride (Table 3.7) was dissolved in a mixture of 0.25 g P123 and 2.5 g abs. ethanol (for $TaCl_5$, $NbCl_5$) or THF (for WCl_6) and stirred for about 2 h. This procedure was an adaption of a literature-known synthesis of P123-derived

mesoporous Ta_2O_5.[121] The solution was purred into a Petri dish (5 cm in diameter) and transferred into a climatic chamber (Vötsch VC^3 4018), set to a constant temperature of 40 °C and 50 % relative humidity. After 4 to 6 days, the resulting solid product was stabilized for 12 h at 250 °C and calcined for 30 min at differing calcination temperatures.

Table 3.7: Amount of precursor for the synthesis of mesoporous Ta_2O_5, WO_3 and Nb_2O_5.

Chemical	M_W / g mol^{-1}	**Amount / mol**	**Amount / g**
$TaCl_5$	358.21	$1.5 \cdot 10^{-3}$	0.537
WCl_6	396.56	$1.5 \cdot 10^{-3}$	0.595
$NbCl_5$	270.17	$1.5 \cdot 10^{-3}$	0.405
dissolved in 2.5 g EtOH ($TaCl_5$, $NbCl_5$) or THF (WCl_6) + 0.25 g P123			

Mesoporous $CsTaWO_6$:

For the preparation of mesoporous $CsTaWO_6$, a similar total amount of precursor ($1.25 \cdot 10^{-3}$ mol) and the same amount of polymer P123 (0.25 g) and solvent as in the pretests were used, consisting of a mixture of abs. EtOH and THF to get a good solubility of all precursors. The exact amounts can be found in Table 3.8.

Table 3.8: Exact precursor ratios for the synthesis of mesoporous $CsTaWO_6$ with P123 as porogen.

Chemical	M_W / g mol^{-1}	**Amount / mol**	**Amount / g**	**Equivalent**
Cs_2CO_3	325.82	$2.5 \cdot 10^{-4}$	0.081	0.5
$TaCl_5$	358.21	$5.0 \cdot 10^{-4}$	0.179	1
WCl_6	396.56	$5.0 \cdot 10^{-4}$	0.198	1
dissolved in 1.25 g EtOH, 1.25 g THF and 0.25 g P123				
$CsTaWO_6$	593.69	$5.0 \cdot 10^{-4}$	0.297	1

For the standard synthesis of mesoporous $CsTaWO_6$, P123 was dissolved in EtOH and THF and constantly stirred for 1 h. Cs_2CO_3 was added, stirred for around 1 h and $TaCl_5$ was added, too. Finally, WCl_6 was put into the clear solution, which became yellow-brown in color immediately. After stirring for approximately 1 h, the whole solution was poured into a Petri dish with 5 cm in diameter and transferred into a climatic chamber (Vötsch VC^3 4018), set to a constant temperature of 40 °C and 50 % relative humidity. After 4 days, the resulting dark

blue-purple solid was calcined at different temperatures for 30 min (500, 550, 600 °C), 2.5 h (450 °C) or 4 h (400 °C). Longer calcination times at lower temperatures were needed to remove more of the polymer. The different synthesis steps are illustrated in Figure 3.2.

For the synthesis of mesoporous $CsTaWO_6$ with citric acid as additive,[136] 0.315 g of $C_6H_8O_7$ monohydrate was added at the beginning of the standard synthesis to the mixture of polymer P123, EtOH, and THF. All following steps were unchanged.

For the third synthesis with inorganic acids as additive,[177] 0.125 g of 96 % H_2SO_4 and 0.35 g of 37 % HCl were added to the polymer/EtOH/THF solution at the beginning of the standard synthesis. All other steps remained the same. Heat treatment was carried out for 30 min at 550 °C under argon atmosphere (50 mL min^{-1}), followed by a calcination step for 1.5 h at 450 °C under oxygen gas flow (50 mL min^{-1}).

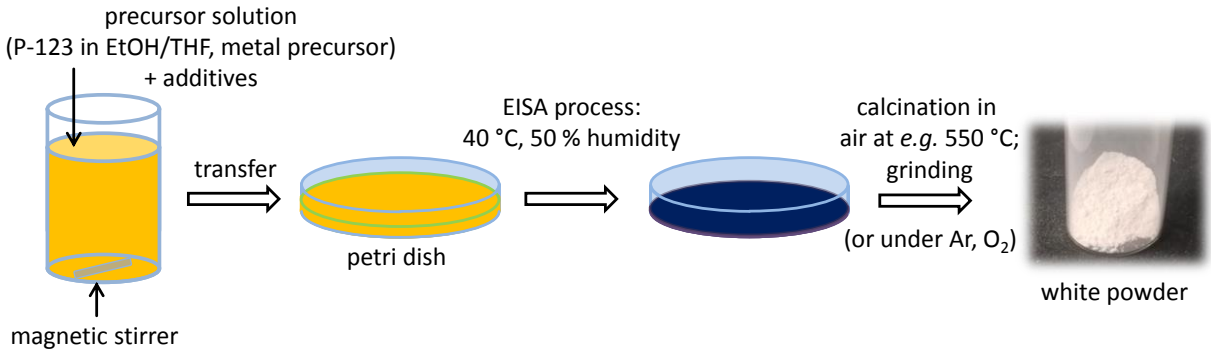

Figure 3.2: Synthesis of mesoporous $CsTaWO_6$ with P123 as porogen. Here, the EISA process was carried out in a climatic chamber.

3.2.2.2 ISO-derived Mesoporous $CsTaWO_6$ prepared on a heating plate

This synthesis strategy was used for the preparation of ISO-derived mesoporous $CsTaWO_6$ with the EISA process carried out on a heating plate instead of a climatic chamber. Precursor and solvents stayed the same as for the P123-derived mesoporous $CsTaWO_6$ with drying step in the climatic chamber (see above, Chapter 3.2.2.1). Exact ratios are listed in Table 3.9.

Here, precursor and solvents were dissolved separately; the ISO polymer in THF, and the precursor in abs. EtOH, starting with Cs_2CO_3 (Figure 3.3). After 1 h of stirring, $TaCl_5$ was added and stirred for another 1 h. Finally, WCl_6 came into the precursor solution, which immediately turned from colorless to orange/brown. The solution was stirred for another 1 h. Afterwards, 2 mL of polymer solution were merged together with a certain volume of precursor solution,

whereas the exact ratio determines the pore ordering (*e.g.*, 250 µL leads to ordered pores, 1000 µL to a non-ordered system). Each solution was stirred another 2 h and during that time turned into a dark red-blue color. Finally, it was purred into 5 mL PTFE cups and put on a heating plate under a glass dome, with a constant heating at 40 °C. Around 2 days later, the PTFE cups were transferred into a small vacuum oven for a final drying step (Büchi glass oven B-585) at 50 °C under vacuum for 24 h. The resulting pellet-like dark blue solid was calcined in air for 30 min or 1 h at 550 °C or 700 °C. A picture of the dark blue solid before the calcination step can be seen in the inset of Figure 5.29a.

Table 3.9: Exact precursor ratios for the synthesis of mesoporous $CsTaWO_6$ with ISO as porogen.

Precursor	***M*W / g mol^{-1}**	**Amount / mol**	**Amount / g**	**Equivalent**
Cs_2CO_3	325.82	$4.0 \cdot 10^{-4}$	0.130	0.5
$TaCl_5$	358.21	$8.0 \cdot 10^{-4}$	0.287	1
WCl_6	396.56	$8.0 \cdot 10^{-4}$	0.317	1
dissolved in 4.0 mL (3.2 g) EtOH				
405 mg ISO tripolymer dissolved in 11.57 g THF				

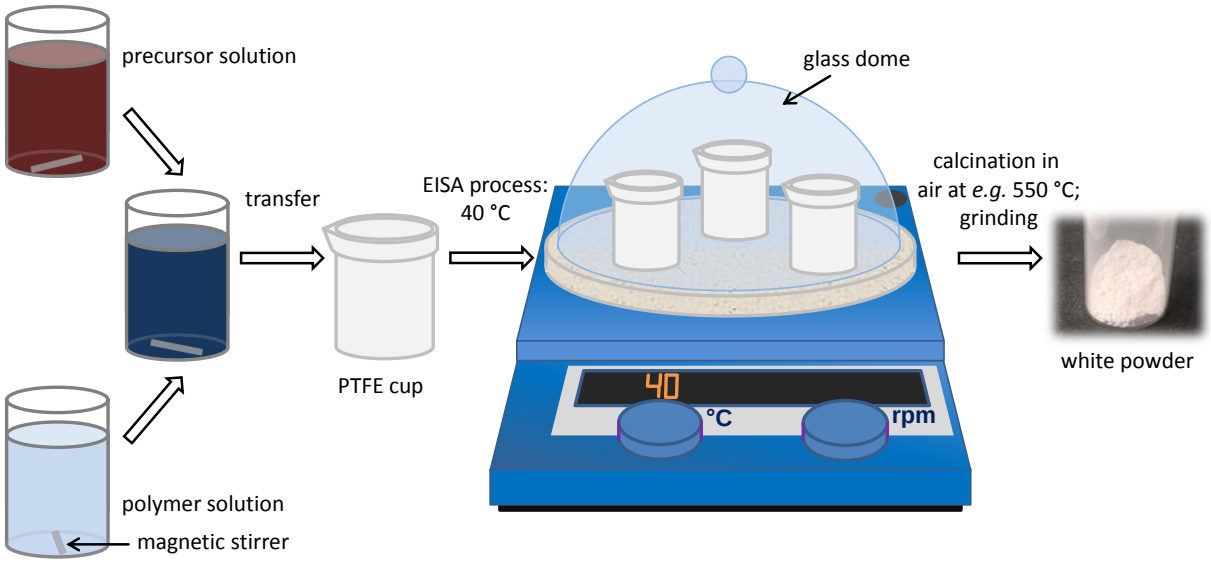

Figure 3.3: Schematic illustration of the preparation steps for the synthesis of ISO-derived mesoporous $CsTaWO_6$. The drying step performed under a glass dome leads to a very stable and high solvent vapor pressure atmosphere of the evaporating EtOH/THF solution and a stable temperature of 40 °C, representing good conditions for a control of the EISA process.

3.2.2.3 Continuative experiments: Use of other polymers and mesoporous $KTaWO_6$

Mesoporous $CsTaWO_6$ with other polymers as porogen:

The synthesis strategy for PIB-PEO-derived $CsTaWO_6$ was the same as for the ISO-derived one, described in Chapter 3.2.2.2, with a heating plate to carry out the drying process. The 405 mg of ISO polymer were replaced by 405 mg of PIB-PEO. The adjustment of the precursor-to-polymer ratio was done by changing the amount of precursor solution in the synthesis (200, 400 or 600 µL), while the polymer solution was always 2000 µL.

For the P123-derived samples prepared on the heating plate, the precursor solution stayed the same (Table 3.9), but the polymer solution was slightly changed to 1 g P123 in 5 g EtOH plus 5 g THF. All other synthesis steps were kept unchanged; precursor-to-polymer ratios were once again varied to find the best conditions.

Mesoporous $KTaWO_6$ prepared on a heating plate:

The P123-derived mesoporous $KTaWO_6$ was prepared in the same way as the P123-derived $CsTaWO_6$ (see section above), but with potassium acetate instead of caesium carbonate. Exact ratios are listed in Table 3.10. For the synthesis shown in Chapter 5.2.5.3, 1270 µL precursor and 2000 µL polymer solution was used.

Table 3.10: Exact precursor ratios for the synthesis of mesoporous $KTaWO_6$ with P123 as porogen.

Precursor	M_W / g mol^{-1}	Amount / mol	Amount / g	Equivalent
KOAc	98.15	$5.0 \cdot 10^{-4}$	0.049	1
$TaCl_5$	358.21	$5.0 \cdot 10^{-4}$	0.183	1
WCl_6	396.56	$5.0 \cdot 10^{-4}$	0.198	1
dissolved in 3.0 mL (2.5 g) EtOH				
1 g P123 dissolved in 5 g EtOH plus 5 g THF				

3.2.3 Reference materials

3.2.3.1 Citrate route

A non-porous reference material was prepared *via* sol-gel citrate route with a calcination step at 850 °C for 10 h, as described for the $CsTaWO_6$ photocatalyst in literature.[30]

3.2.3.2 Solid state synthesis

$CsTaWO_6$ was synthesized in a solid state reaction by grinding stoichiometric mixtures of Cs_2CO_3, Ta_2O_5 and WO_3, followed by calcination for 36 h at 810 °C, with one intermediate grinding step after 18 h.[32]

4 Characterization techniques

Techniques that had been most important for the characterization of the photocatalyst powders are introduced in more detail. X-ray diffraction and analysis, nitrogen physisorption and the setup for photocatalytic hydrogen generation will be described in Chapters 4.1 to 4.3. The equipment for other applied characterization methods are listed in Chapter 4.4 *et sqq*.

4.1 X-ray diffraction

Powder X-ray diffraction patterns (PXRD or XRD) were recorded on a *PANalytical X'Pert Pro* diffractometer with Bragg-Brentano geometry and a Cu K_α radiation source with a wavelength of λ = 1.5406 Å. The measurements ranged from 2 θ = 10–90° and a step size of 0.016 or 0.034°, whereas the smaller step size was chosen if Rietveld refinements were required.

The XRD patterns were investigated regarding to phase purity, crystallinity, crystallite size and lattice constants. Phase purity was determined by comparing with reference cards from the *PANalytical X'Pert HighScore Plus* software, version 3.0.5 (2012) or the *Crystallography Open Database*[178–182] (http://www.crystallography.net/cod/index.php), which had been in some cases modified *via* the software *Diamond*, version 3.2k, especially to substitute elements and/or adjust lattice constants (*e.g.* for $CsTaMoO_6$). Reference cards are quoted with their corresponding JCPDS (Joint Committee on Powder Diffraction Standards) number.

Crystallite sizes were determined *via* Scherrer equation or were received by Rietveld refinements with the free software *FullProf Program*, version 2.05 (2011). The exact procedures for both techniques are depicted in the next two chapters.

4.1.1 Scherrer equation

The classical Scherrer equation describes the relation between the full width at half maximum (FWHM) *B* of a XRD reflection *hkl* and the linear dimension of the crystallite *L*:[183,184]

$$L = \frac{K \cdot \lambda}{B \cdot \cos(\theta)}, \text{ whereas} \qquad (4.1)$$

λ = 1.5406 Å (wavelength of the radiation source Cu K_α)

θ = Bragg angle of the *hkl* reflection

K = Bragg constant (0.9-1)

Bragg calculated *K* to $2((\ln 2)/\pi)^{1/2} = 0.93$,[184] but there had been a discussion about the exact value of *K* because this value depends on the profile function used to calculate *B*.[184] Therefore, it is more suitable to convert the Bragg angle θ into the scattering vector *S via* the equation

$$S = \frac{2 \cdot \sin(\theta)}{\lambda}, \tag{4.2}$$

plotting the diffraction intensity against this scattering vector *S* and afterwards calculating the crystallite size from a simple integration of the *hkl* reflection (integral breath). The obtained values for height and area of the reflection have to be inserted into the following equation:

$$L[\text{Å}] = \frac{\text{Height of the reflection}}{\text{Area of the reflection } [\text{Å}^{-1}]} \tag{4.3}$$

The reflections that should be taken into account for the calculation of the crystallite size from Scherrer's equation have to be well separated without any overlapping with other reflections. In this work, a minimum of two different reflections were used and averaged for every value of the crystallite size from Scherrer equation.

4.1.2 Rietveld refinement

To get reliable results in Rietveld refinements, the resolution of the instruments and thus the instrumental line broadening has to be measured with a well-defined standard material. A high purity lanthanum hexaboride (LaB_6)[185] was used as a profile shape standard and the obtained values were converted into an instrumental resolution file (IRF).

For Rietveld refinements,[186,187] the peak shape was fitted with the Thompson-Cox-Hastings Pseudo-Voigt profile function[188] (convolution of Gaussian and Lorentzian functions) and the background by either a 6-coefficient polynomial background function or a linear interpolation between given points with refinable heights that is subtracted afterwards. For an exact mathematical description of the formula used in the *Fullprof* software, please have a look at the *Fullprof* manual.[189] Shortly, different parameters define the Gaussian (*U*, *V*, *W*) and Lorentzian (*X*, *Y*) part of the function and therefore the line broadening. If providing an IRF file, the parameter V and W can be fixed due to the defined line broadening from the instrument.[189]

For Rietveld refinements of defect-pyrochlore structured materials, the following sequence for parameter fitting was found to be most promising:

1. Fitting of the background (polynomial or linear interpolation), the zero offset (offset due to instrumental reasons), the lattice constant *a* and the *X* and *Y* values of the Lorentzian part of the peak shape function[190] at the same time, till reaching convergence.
2. Afterwards, the *X* and *Y* values were fixed and the Gaussian part of the peak shape function was fitted (namely *U*, *V*, *W*; just if necessary).
3. Alternating refinement of the *X*, *Y* and *U*, *V*, *W* parameters until reaching an optimum.
4. Refining the atom parameters, starting with the *x*, *y*, *z* positions of the different elements (only values with no integer fraction, like the *x* position of oxygen in $CsTaWO_6$, see Table 2.1)
5. In a last step, the Debye-Waller factors *B* for every element were refined.

All parameters were carefully examined during refinements to get reasonable results.

The *FullProf* Rietveld refinement is based on the least-square minimization to get the optimum fit and the goodness of the fit can be estimated by several so-called *R* factors.[191] The most important is the R_{wp} ("R weighted profile") factor, that makes it possible to follow the minimization of the differences between the observed and the calculated intensities. The R_{wp} value shows the least-square residual, normalized by the weighted intensities and decreases during the refinement until reaching a minimum. A more common, but less meaningful parameter is the X^2 ("Chi square") value, also called the "goodness-of-fit", which is strongly influenced by the background of the refined XRD pattern.[191] A high background leads to a small and therefore "good" value for X^2, even if the refinement of the reflections themselves can be worse. Nevertheless, the very common X^2 value is also given for every Rietveld refinement in this work.

In case of *Fullprof* Rietveld refinements for the estimation of strain in the samples, the *V* and *W* were fixed to zero and did not undergo a refinement.[189] One refinement was made to obtain crystallite size and other values (L_a, *a*, and corresponding X^2, R_{wp}), one without refining *V* and *W* for the strain parameter. The obtained parameter for the dimension of strain gives no physical interpretation; it is just a phenomenological treatment of line broadening[189] and

can be related to structural defects, but hardly to the exact nature of the defect (disorder, vacancies, dislocations *etc*.).[192] The obtained strain parameter from Rietveld refinements corresponds to 25 % of the strain defined by Stokes and Wilson[193] and represents the upper limit of the strain.[192] It is calculated by the part of line-broadening in XRD that does not appear from crystallite size and instrumental broadening.

Other strain characterization techniques such as Williamson-Hall plots[192,194,195] led to less accurate results due to the low number of easily separable reflections in the cubic defect-pyrochlore structured $CsTaWO_6$. The strong line-broadening at high diffraction angles can be hardly determined by hand; therefore, the overall refinement of the XRD patterns with Rietveld gave more reliable values for the strain parameter.

4.1.3 SAXS measurements

Small-angle X-ray scattering (SAXS) was performed on a *Bruker AXS Nanostar* with a *Vantec 2000 area detector* and a Cu K_α radiation source (λ = 1.5406 Å) at the Vienna University of Technology. These measurements resulted in 2D patterns, which were integrated around the beam center to obtain a plot of intensity against scattering vector q, whereas q is defined as $q = 4\pi\sin\theta/\lambda$, with θ = scattering angle and λ = used X-ray wavelength.

4.2 Physisorption

In this work, nitrogen physisorption isotherms were collected at 77 K (boiling point of liquid nitrogen) using a *Quadrasorb evo Surface Area & Pore Size Analyzer* from *Quantachrome Instruments*. In principle, the exact amount of nitrogen adsorbed or desorbed on the surface of a material at a constant temperature and different pressures is measured volumetrically.[196] Two branches are recorded: one at increasing pressure and therefore the adsorption of nitrogen and one at decreasing pressure where nitrogen is desorbed again. This technique provides several useful information, such as surface area, pore volume and pore size distribution of a material.[197] In porous materials, one can estimate the size of the pores from the increase of adsorbed nitrogen. Smaller pores are already filled at smaller relative pressures p/p_0 (micropores), medium pores (mesopores) at higher pressure and so on.

Isotherms of different shapes can be recorded, depending on the nature of porosity in the measured sample. In general, porosity is divided into three different size ranges (IUPAC

definition): micropores (pore size < 2 nm), mesopores (between 2 and 50 nm) and macropores (above 50 nm).[198] Figure 4.1 shows isotherms of different mesoporous materials. Type I isotherms can be observed on samples with microporosity, whereas I(a) represents a solid with narrow micropores and I(b) wider micropores up to the mesopore range (~ 2.5 nm). Type II and III are related to non-porous or macroporous materials, with monolayer formation in type II (see Chapter 4.2.1) and without monolayer formation in type III (due to weak interactions between adsorbent (solid) and adsorbate (here: N_2)). Most important for this work will be isotherms of type IV(a) or V, corresponding to mesoporous materials with and without microporosity, respectively. A hysteresis occurs for mesopores wider than 4 nm (in the case of N_2 as adsorbate); smaller pores would lead to type IV(b) isotherms. The last case, a type VI isotherm, can be observed for non-porous materials with a layer-by-layer adsorption (*e.g.*, graphitic carbon).[197]

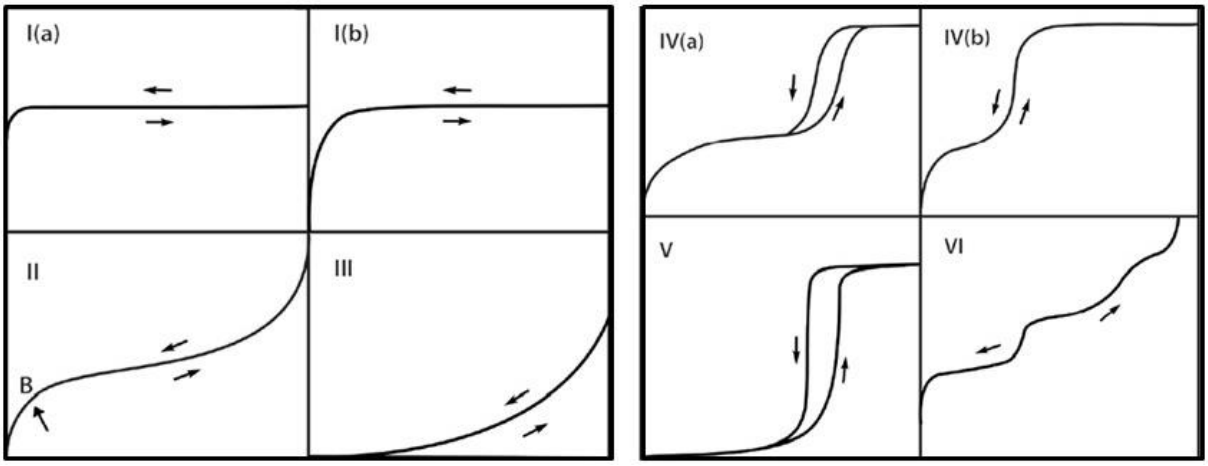

Figure 4.1: Different types of physisorption isotherms according to the IUPAC classification (adopted from Thommes *et al*.[197]).

4.2.1 Surface area determination

The most common method for calculating the surface area of a material is the BET equation (after S. Brunauer, P. H. Emmett and E. Teller).[199,200] It correlates the adsorbed volume as a function of the applied pressure p at small ratios p/p_0, whereas p_0 is the saturation pressure of the adsorbent (here: nitrogen). In this region, the gas is adsorbed in multiple layers and the required volume to cover one monolayer (V_{mono}), which is a single layer on the whole surface of the sample, can be calculated *via* the following equation:

$$\frac{p}{V\,(p_0 - p)} = \frac{1}{V_{\text{mono}} \cdot C} + \frac{C - 1}{V_{\text{mono}} \cdot C} \cdot \frac{p}{p_0} \tag{4.4}$$

When plotting the left part of the equation against p/p_0, V_{mono} for the volume of nitrogen necessary to form one monolayer and the BET constant C can be obtained. The surface area S_{BET} of the sample can be calculated by using the equation

$$S_{\text{BET}} = \frac{V_{\text{mono}} \cdot \rho_{N_2} \cdot N_A \cdot A_{N_2}}{m_s \cdot M_{N_2}} \tag{4.5}$$

whereas ρ_{N_2}, A_{N_2} and M_{N_2} are the density, the contact surface area by each molecule and the molecular weight of the liquid nitrogen (0.808 g cm^{-3}, 16.2 Å^2 and 28.013 g mol^{-1}, respectively),[201] m_s is the sample mass and N_A is Avogadro's constant.

4.2.2 Estimation of the pore size distribution

Up to now, several models can fit the adsorption or desorption branch of an isotherm. A classical method, based on macroscopic, thermodynamic assumptions, is the BJH model (E. P. Barrett, L. G. Joyner, P. P. Halenda),[202] which theoretical considerations are based on the layer-by-layer desorption of a filled cylindrical pore while decreasing the pressure. Therefore, only the desorption branch is taken into account for estimating the pore size distribution (PSD). This model is always good for a first impression of the pore size distribution, but it has some remarkable disadvantages: first of all, it underestimates the size of pores especially for mesopores smaller than approximately 10 nm by a factor of 0.2 to 0.3.[203] Furthermore, this model is only completely valid for cylindrical pores. In addition, the calculation of the pore size distribution from the desorption branch can lead to wrong values if pore blocking takes place, that means bigger pores cannot be emptied with decreasing relative pressures due to smaller necks that are still filled and therefore block the emptying process.[197,203,204]

Due to the above mentioned reasons, DFT (density functional theory) methods are nowadays mostly common, more detailed NLDFT (non-local DFT) and QSDFT (quenched solid DFT), whereas the latter one is mostly used for porous carbon and is therefore not discussed here.[203] (NL)DFT methods are based on microscopic assumptions and can therefore also be valid for very small pores.[204–206] These approaches simulate the intermolecular potentials of fluid-fluid as well as fluid-solid interactions in model pores. Because of the description on the molecular level, NLDFT methods are more reliable compared to the BJH method.[197]

Furthermore, data for the pore size distribution can be obtained from the adsorption as well as from the desorption branch, making it possible to see possible pore blocking by a comparison of both PSDs.[204]

For $CsTaWO_6$, there are no explicit models which are valid for this material in total. Thus, adsorption and desorption models for nitrogen on SiO_2 were used (for the adsorption branch: cylindrical NLDFT model, for desorption branch: cylindrical NLDFT equilibrium model). In general, the fluid-solid interactions in other oxide materials, like $CsTaWO_6$, should behave similar. The validity of these models was estimated by the fitting comparison (Figure 4.2), provided by the used analysis software *ASiQWin* version 4.0. For the P123-derived mesoporous $CsTaWO_6$, the fitting error for both NLDFT models is below 1 %, indicating a good validity for these samples (Figure 4.2a). The ISO-derived mesoporous $CsTaWO_6$ samples show a low fitting error for the NLDFT adsorption model (1.3 %), but a higher value of 3.6 % for the NLDFT equilibrium model, applied on the desorption branch (Figure 4.2b). However, main deviation can be seen at the linear part of the isotherm between around p/p_0 = 0.1−0.8. This region has no major influence on the calculation of the pore diameter D_p, which is the most important value taken from these NLDFT fittings. Therefore, the NLDFT models for SiO_2 are sufficiently valid for the estimation of median pore sizes in mesoporous $CsTaWO_6$.

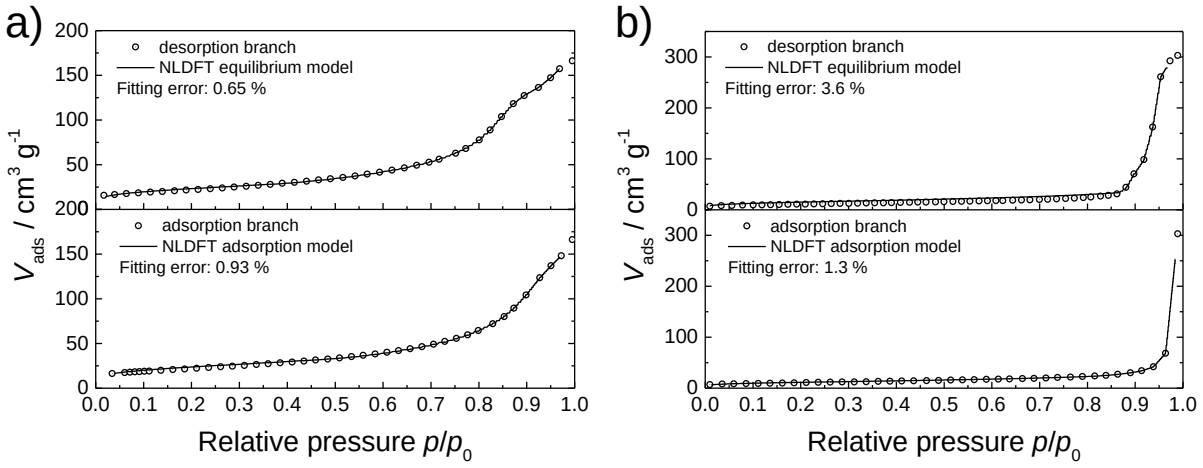

Figure 4.2: Fitting comparison for the NLDFT adsorption and equilibrium model on the isotherms of a) P123-derived mesoporous $CsTaWO_6$ with H_2SO_4/HCl additive (Chapter 5.2.3) and b) ISO-derived ordered mesoporous $CsTaWO_6$ (Chapter 5.2.4).

4.3 Photocatalytic hydrogen production

Photocatalytic activities were tested by performing photocatalytic hydrogen production experiments from a mixture of 10 vol% methanol in water. The photocatalyst is dispersed in this solution and hydrogen is produced by shining light onto the dispersion. The fundamental decomposition process of MeOH can be found in Chapter 2.3.2. In general, hydrogen and carbon dioxide is produced. Quantification of carbon dioxide is problematic due to its good solubility in water (formation of carbonic acid/carbonates). Hydrogen is detected either by gas chromatography (GC) or mass spectrometry (MS). Both techniques were used in this work and will be explained in this chapter. The decision between choosing GC or MS has to be done according to the desired reaction conditions. For instance, when using a sun simulator with comparable low intensity and therefore also small amounts of evolved hydrogen, the detection by GC is more suitable due to the better resolution. For small amounts of evolved gases, the high signal-to-noise ratio of the MS leads to difficulties in the interpretation of data. For more intense light sources like high-pressure or mid-pressure UV lamps, the amounts of evolved hydrogen are much higher and thus the use of MS becomes reasonable. The advantage of the MS is the small time interval between two measuring points of just a few seconds, leading to a big data set and a good resolved hydrogen evolution curve with many data points. In contrast, the time interval between two measurements in GC is around 30 min due to a heating step and subsequent cooling down of the column (Figure 4.3).

For both techniques (GC and MS), measurements were carried out as long as a constant rate of hydrogen was detected. In practice, this is the case after at least three measurements and therefore approximately 1.5 h for GC detection and around 30 min to 1 h for MS detection. For analyzing the results, the values of constant hydrogen production were taken and denoted as hydrogen evolution at steady state (Figure 4.3). Equations (4.6) and (4.7) were used to calculate hydrogen evolution rates (in µmol h^{-1}) from the measured value of hydrogen gas in the argon carrier gas (in %). Molecular volume of hydrogen was calculated using the ideal gas equation with a temperature of 35 °C (308.15 K) for GC (column temperature) and 20 °C (293.15 K) for MS (room temperature).

In general, the setups for photocatalytic measurements with GC or MS are very similar. After a certain time of flushing the stirred solution with argon to remove the oxygen from air, a continuous Ar flow is adjusted and the measurement is started at the same time as the lamp

is turned on. Gas flows were in all cases controlled with a *Bronckhorst* mass flow controller (MFC), stirring of the solution was carried out with a magnetic stirrer.

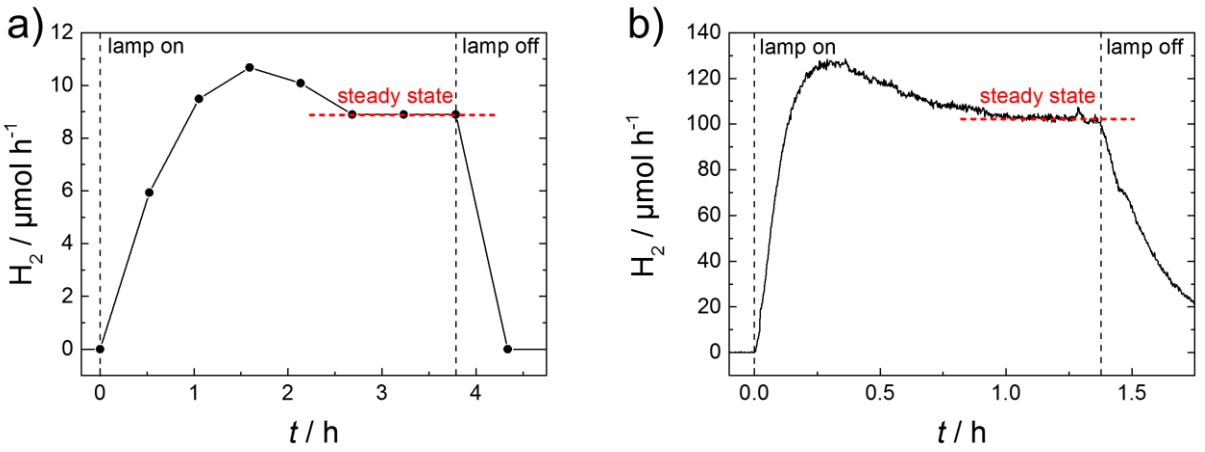

Figure 4.3: Comparison of a) hydrogen measurements with a GC under solar simulator irradiation and b) with MS under UV light for the same sample (P123-derived mesoporous $CsTaWO_6$, T_{calc} = 550 °C, prepared without additives). Estimated steady state conditions are marked with a dashed red line.

4.3.1 Hydrogen generation under sun light irradiation (GC detection)

A scheme of the photocatalytic setup for measurements with the solar simulator is shown in Figure 4.5. A solution of 20 mL MeOH as hole scavenger (see Chapter 2.3.2[103,207]) and 180 mL H_2O was prepared. Around 30 mL of this solution together with 200 mg of the photocatalyst was dispersed by using an ultrasonic bath for 10 min. The homogenous dispersion and the remaining water/methanol mixture were filled in a glass reactor with a top quartz window and a water cooling jacket, keeping the whole solution at a constant temperature of 20 °C using a thermostat (*LAUDA RP 845*). Some measurements under sun light irradiation were carried out without any co-catalyst, leading in the nanostructured materials to a strong blue coloring of the solution after irradiation (see Chapter 5.4 for detailed discussion). For the deposition of co-catalyst, rhodium was added *via* an aqueous sodium hexachlororhodate (Na_3RhCl_6, 99.999 %, Aldrich) solution. Before measurements, the whole suspension was flushed with a continuous argon (Ar 5.0) gas flow of 100 mL min^{-1} and stirred with 400 rpm. After at least one hour, the gas flow was set to 25 mL min^{-1} and the 150 W solar simulator (*Newport Oriel Sol 1A*, 1000 W m^{-2} intensity) was turned on, shinning on the dispersion trough the on-top quartz window. The incorporated AM1.5G glass filter was removed before the photocatalytic measurements to get enough UV light for the high band

gap material $CsTaWO_6$ (for detailed spectra, see Figure 4.4. Hydrogen evolution was recorded using a *Shimadzu GC-2014* gas chromatograph with a thermal conductivity detector (TCD) and a *ShinCarbon* GC column.

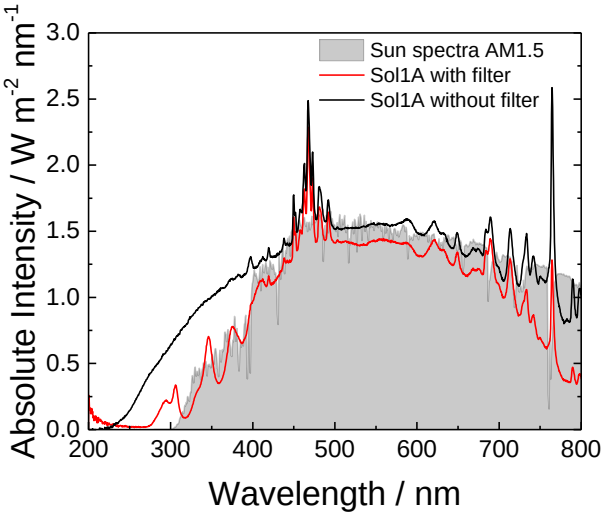

Figure 4.4: Spectra of the used *Newport Oriel Sol1A* solar simulator with and without AM1.5 filtering, and the solar spectrum with AM1.5 as reference.[52]

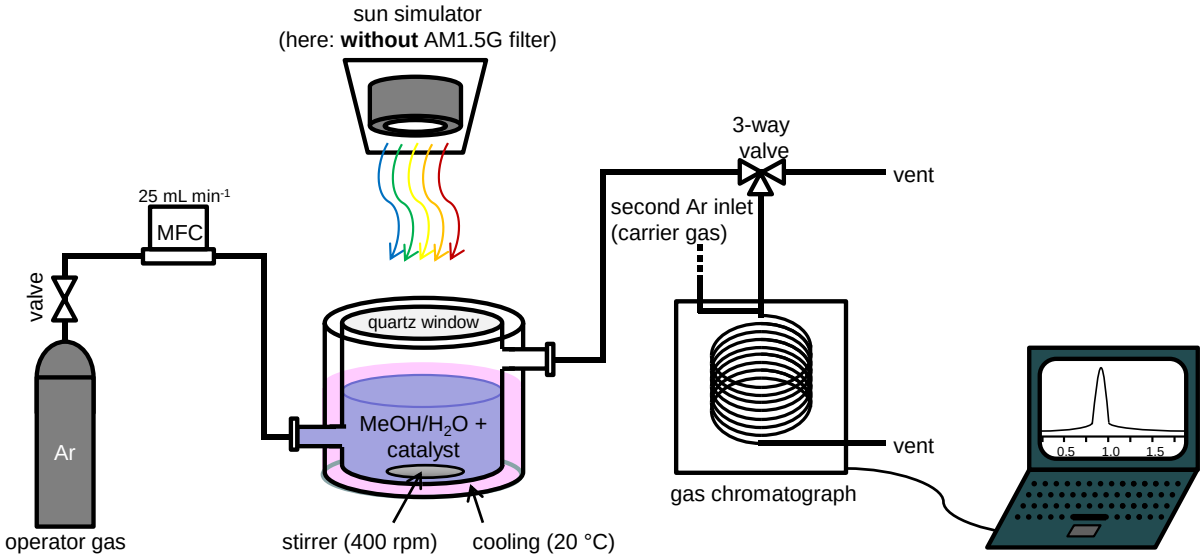

Figure 4.5: Scheme of the photocatalytic setup for the measurement of hydrogen generation under sun light irradiation and detection of the evolved gases *via* gas chromatography.

One measurement took around 30 min, whereas in the first 4 min, a sample loop with a volume of 500 µL was continuously flushed with the evolving H_2/Ar gas. Afterwards, the sample loop was closed and the embedded gas was able to release for half a minute. Then, the gas was carried by a second Ar gas flow into the column and the containing gases were

separated and detected with a TCD detector with a detector current of 30 mA. After 5.5 min, the separation of the gases was finished and the column was heated up from its constant measurement temperature of 35 °C with a heating ramp of 42.5 °C min^{-1} to 120 °C to remove possible water inside the column. The column was cooled down again after a holding time of 2 min with a rate of −10 °C min^{-1}. After this procedure, the next data point could be measured.

After getting a constant value of the evolved hydrogen gas, the measurement was interrupted by turning off the sun simulator. Another portion of Rh co-catalyst was added *via* an installed rubber sealing, and the solution was flushed with 100 mL min^{-1} Ar to remove remaining hydrogen and included air. A new measurement was started as soon as all hydrogen was flushed away, once again with an Ar flow of 25 mL min^{-1}. The evolved hydrogen rates in percent were converted into rates in µmol per hour *via* Equation (4.6).

$$H_2 \text{ rate } \left[\mu\text{mol h}^{-1}\right] = \left(\left(\frac{H_2[\%]}{100} \right) \cdot 1500 \text{ mL h}^{-1} \text{ / } 25290 \text{ mL mol}^{-1} \right) \cdot 10^6 \qquad (4.6)$$

4.3.2 Hydrogen generation under UV light irradiation (MS detection)

In principle, the setup of the hydrogen evolution from UV light irradiation, detected *via* MS (Figure 4.6), is very similar to the setup described above (Figure 4.5).

Due to the bigger size of the glass reactor for the used UV lamp (mercury intrusion lamp, *Peschl UV consulting*, *TQ 718*, 700 W, set to 350 W), a solution of 60 mL MeOH, 540 mL H_2O and 300 mg of photocatalyst was necessary. The photocatalyst was dispersed in around 30 mL of the solution, using an ultrasonic bath for 10 min. The dispersion plus the residual part of the MeOH/H_2O mixture were filled into the reactor and stirred with 200 rpm. Rh as co-catalyst was added (aqueous Na_3RhCl_6 solution). A thermostat (*LAUDA RP 845*) was used to generate a continuous water flow of 10 °C in an inner and an outer cooling circle to cool down the UV lamp and the glass reactor, respectively. To remove oxygen, the whole dispersion was flushed with Ar 5.0 for 30 min. Reactor and lamp were shielded with a metal housing. The MS (*HIDEN Analytical HPR 20 QIC R&D*) was started and after turning on the UV lamp, the evolved hydrogen gas was continuously detected (MS settings: 70 eV ionisation energy, 20 µA emission current).

After getting a constant value of the hydrogen evolution, the lamp was turned off, more Rh co-catalyst was added *via* an installed rubber sealing and the lamp was turned on again after

a complete removal of hydrogen. The evolved hydrogen rates in percent were converted into rates in µmol per hour *via* Equation (4.7).

$$H_2 \text{ rate } [\mu\text{mol h}^{-1}] = \left(\left(\frac{H_2[\%]}{100} \right) \cdot 6000 \text{ mL h}^{-1} / 24054 \text{ mL mol}^{-1} \right) \cdot 10^6 \qquad (4.7)$$

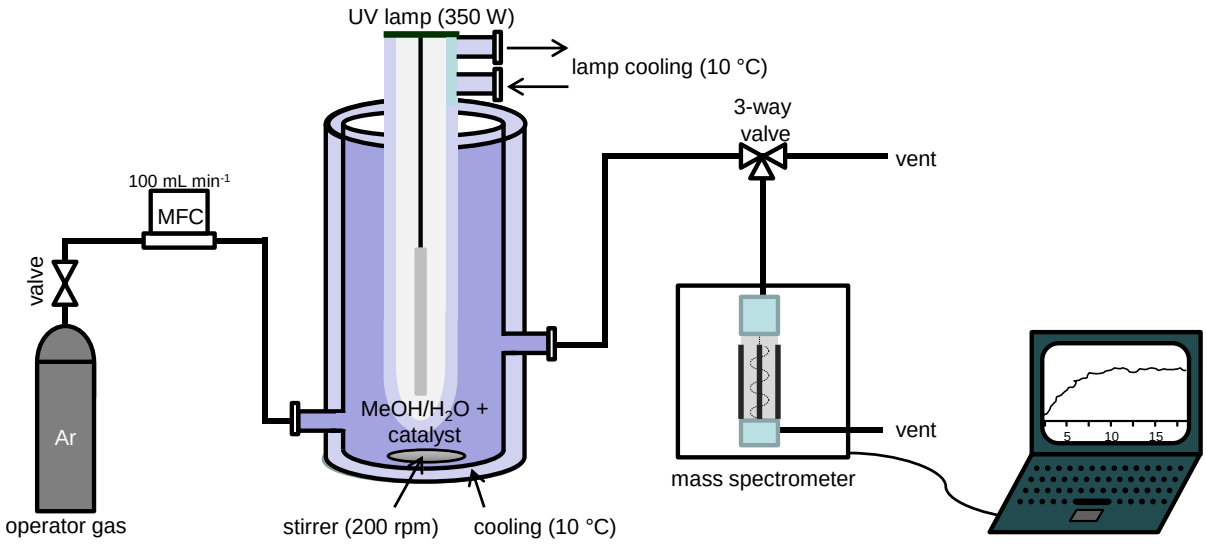

Figure 4.6: Scheme of the photocatalytic setup for the measurement of hydrogen generation under UV light irradiation and detection of the evolved gases *via* mass spectroscopy.

4.4 Raman spectroscopy

Raman spectra were obtained using a *Bruker Senterra R200-532* with a laser power of 0.2–2 mW (λ = 532 nm), 50–250 co-additions à 3–6 s and in a range of 100 to 1555 cm^{-1} with a resolution of 3–5 cm^{-1}.

4.5 Infrared spectroscopy

Fourier transformed infrared spectra (FTIR) were recorded on a *Bruker Optics Alpha* instrument in a range of 400 to 4000 cm^{-1} with a resolution of 4 cm^{-1}, using a pellet consisting of KBr and the verified sample.

4.6 UV-Vis spectroscopy

Diffuse reflectance UV-visible spectroscopy (DR-UV-Vis) was performed on a *Perkin Elmer Lambda 750 UV-Vis-NIR spectrometer* and a Praying-Mantis mirror unit, using $BaSO_4$ as a white

standard. Conversion of diffuse reflectance spectra into absorption spectra was done *via* the Kubelka-Munk function, and bang gaps were calculated from Tauc plots.[208]

4.7 Dynamic light scattering

Dynamic light scattering (DLS) was measured at a *Malvern Zetasizer ZS* to investigate the hydrodynamic radius. The samples were dissolved in a solution of 10 % methanol in water (same concentration as for photocatalytic experiments), ultrasonicated for several minutes and measured at a temperature of 25 °C, an angle of 173° and a resolution of 300 size classes.

4.8 Scanning electron microscopy and energy-dispersive X-ray spectroscopy

Scanning electron microscopy images (SEM) were received on a *Zeiss MERLIN field* em*ission scanning electron microscope* (FE-SEM) and energy-dispersive X-ray (EDX) spectra were obtained by an *Oxford Instruments energy dispersive X-ray spectroscopy analyzer* (*X-Max 50 mm*^{2}) with an accelerating voltage of 20 keV. For mesoporous materials, pore diameter and pore wall thickness were determined using the free software *ImageJ*, version 1.45s.

4.9 Transmission electron microscopy and selected area electron diffraction

Transmission electron microscopy (TEM) and selected area electron diffraction (SAED) were received on a *Philips CM30* with 300 kV acceleration voltage. Sample preparation was made on carbon-filmed copper mesh grids. For nanoparticles, the average particle sizes of at minimum thirty nanoparticles for each sample were estimated with the free software *ImageJ*, version 1.45s. For mesoporous materials, pore diameter and pore wall thickness were also determined using the free software *ImageJ.*

4.10 X-ray photoelectron microscopy

X-ray photoelectron spectroscopy (XPS) measurements were carried out at a *PHI Versaprobe II Scanning ESCA Microprobe* (*Physical Electronics*) with a monochromatized Al K_α X-ray source (beam diameter 200 µm, X-ray power 50 W). The analyzer pass energy for detail spectra was set to 23.5 eV with a step time of 50 ms and a step size of 0.2 eV. The sample was flooded with slow electrons and argon ions using the built-in ion sputter and electron guns during the measurements in order to compensate surface charging effects. Data evaluation

was done using *CasaXPS* software. For charge correction, the energy of the C 1s-line was fixed to 284.8 eV.

4.11 Thermogravimetric analysis

Thermogravimetric analyses (TGA) were obtained on a *Netzsch STA 409 PC/PG* instrument from a temperature range of 30 to 800 °C with a heating rate of 1 °C min^{-1} or 5 °C min^{-1} under synthetic air and an attached mass spectrometer detected the evolving gases.

4.12 Electron paramagnetic resonance spectroscopy

Electron paramagnetic resonance (EPR) spectra were measured on a 9.5 GHz EPR spectrometer *Bruker ESP 300E* (10 mW power, modulation amplitude 1 G, modulation frequency 100 kHz). The EPR setup was equipped with an *Oxford-He-flow cryosystem*. The measurement temperature was set to 100 K to obtain optimum signal-to-noise ratio.

5 Results and discussion

5.1 Nanoparticulate materials

Defect-pyrochlore structured nanoparticles of different composition will be shown in the next chapter. The adjustment of the nanoparticle size for $CsTaWO_6$ will be explained and the influence on the photocatalytic activity discussed carefully. Some continuative experiments, like doping and electrospinning of the materials will be presented at the end of this part.

5.1.1 $CsTaWO_6$ nanoparticles

5.1.1.1 Influence of synthesis temperature and additives

The described low-temperature hydrothermal synthesis (see Chapter 3.2.1.1) was carried out at different temperatures (Figure 5.1a). Above 100 °C, the average crystallite size (L_a) does not change remarkably with synthesis temperature and stays constant at a value of around 14−15 nm (Figure 5.1b; values for L_a from Rietveld refinements). At 100 °C or below, XRD patterns already show all desired reflections, but also a strong amorphous background, indicating that these temperatures are too low to achieve full conversion of all precursors and therefore a crystalline product in total. All syntheses above 100 °C show phase-pure and highly crystalline $CsTaWO_6$. No further additional annealing step was necessary. This reaction temperature is 400 °C lower than in the mesoporous reaction[35] (Chapter 3.2.1.4) or citrate route[30] (Chapter 3.2.3.1), and 650 °C lower than in solid state reaction (Chapter 3.2.3.2).[32,209]

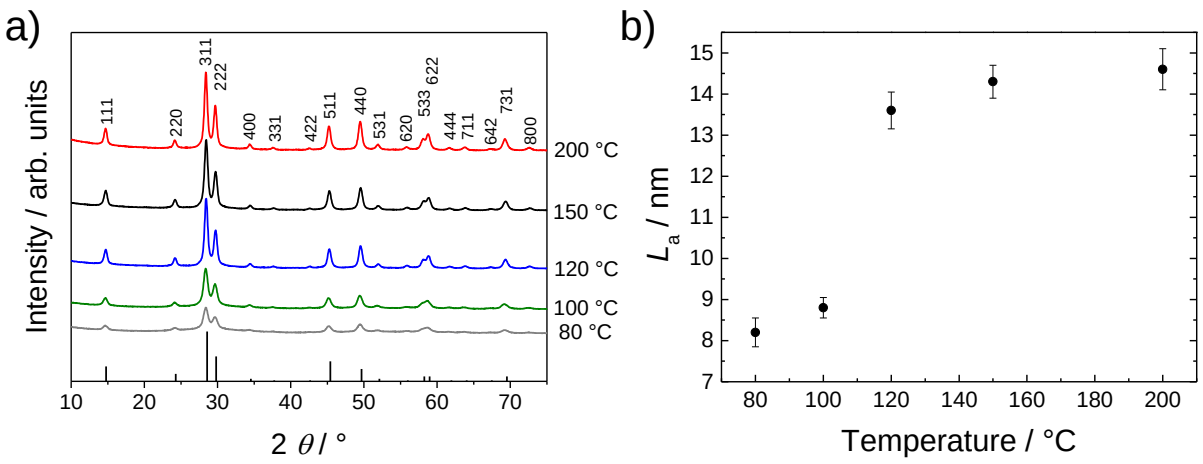

Figure 5.1: (a) XRD patterns of $CsTaWO_6$ nanoparticles synthesized for 12 h at temperatures of 80 to 200 °C with 1 mL NH_3 in the reaction solution (reference card: JCPDS 25-2033) and (b) the calculated average crystallite sizes from Rietveld refinements.

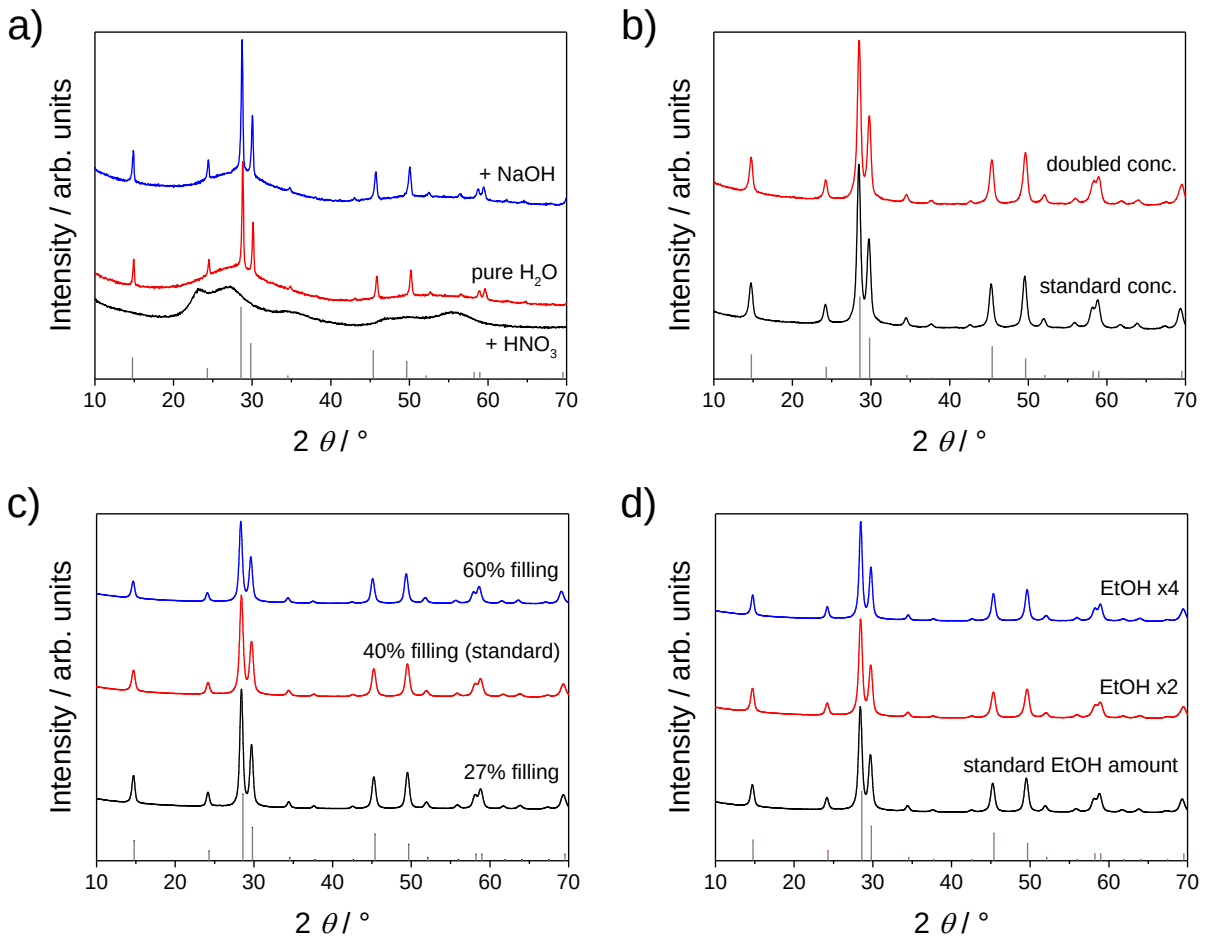

Figure 5.2: Influence of different synthesis parameters on crystal phase and crystal size of the $CsTaWO_6$ nanoparticles: a) different additives, b) doubled concentration compared to normal synthesis, c) different fillings of the autoclave and d) increased amount of EtOH in the synthesis (reference card: JCPDS 25-2033).

For a detailed investigation of the influence of the crystallite size on photocatalytic activity, the average crystallite size of the nanoparticles had to be adjusted. Changing of different parameters was carried out to investigate their influence on the average crystallite size. The precursor ratio, the autoclave filling and the amount of ethanol (from different concentrated $Ta(OEt)_5$ solutions) showed only a minor influence on the average crystallite size (Figure 5.2b-d). The use of other bases, such as NaOH (Figure 5.2a), other nitrogen containing compounds, such as HNO_3, or pure water, did not lead to the desired phase. During these experiments it could be seen that it was possible to double the amount of precursors at the beginning of the synthesis leading to a higher yield and only slightly smaller nanoparticles (Figure 5.2b). Therefore, all further syntheses were performed with this higher precursor ratio.

It was found that the crystallite size could be varied with changing the amount of additives: an increase of the amount of ammonia from 1 to 17 mL (= pure ammonia solution) leads to a stepwise decrease of the crystallite size from 16 to 8 nm. Urea as an additive resulted in large crystallites of 30 nm. The crystallite sizes were obtained from Rietveld refinements (Figure 5.3, Table 5.1) and confirmed by TEM measurements (Figure 5.6).

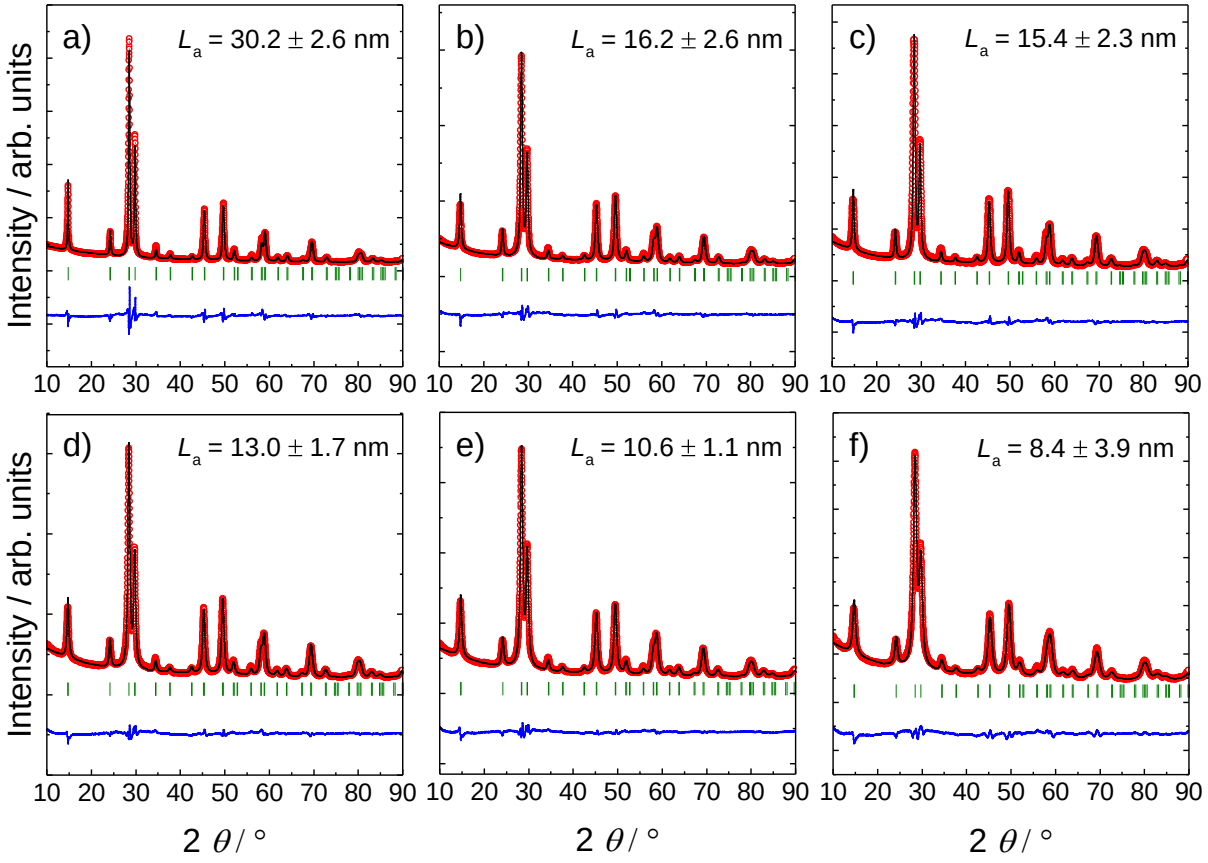

Figure 5.3: Rietveld refinements of $CsTaWO_6$ nanoparticles, synthesized with different amounts of additives: a) urea instead of NH_3, b) 0.25 mL NH_3, c) 0.50 mL NH_3, d) 1 mL NH_3, e) 6 mL NH_3 and f) 17 mL NH_3 (= pure 25 % aqueous ammonia solution), resulting in nanoparticles with average crystallite sizes of around 30 down to 8 nm, respectively.

All XRD patterns indicate phase pure $CsTaWO_6$ material, crystallized in the cubic defect-pyrochlore structure $Fd\bar{3}m$. No amorphous background is visible, evidencing a highly crystalline product. The yield in every of the six shown synthesis routes was above 80 %, resulting in around 350 mg $CsTaWO_6$ nanoparticles per batch. The values for the strain from Rietveld refinements, which are an indication for defects inside the material, are increasing with decreasing crystallite size (Table 5.1).

Table 5.1: Obtained parameters from Rietveld refinements of $CsTaWO_6$ nanoparticles.

Additive	L_a / nm	a / Å	Strain	χ^2	R_{wp} / %
urea	30.2 ± 2.6	10.3772	43.7	38.8	17.1
0.25 mL NH_3	16.2 ± 2.6	10.3903	45.6	15.7	11.0
0.50 mL NH_3	15.4 ± 2.3	10.4005	47.4	13.0	10.0
1 mL NH_3	13.0 ± 1.7	10.4044	46.8	10.1	9.4
6 mL NH_3	10.6 ± 1.1	10.4209	56.3	9.7	8.1
17 mL NH_3	8.4 ± 3.9	10.4099	55.0	9.9	12.4

L_a = average crystallite size, a = lattice constant, χ^2 = goodness of fit, R_{wp} = weighted profile R-factor

The reason for the change in the crystallite size with varying ammonia amount could be the differences in the pH or the change in pressure due to the volatile NH_3, outgassing from the solution at higher temperatures and therefore increasing the pressure (Figure 5.4).[210,211] Similar pressure dependencies were found for the hydrothermal synthesis of nanosized Fe_2O_3 particles.[212] A linear dependence can be found when plotting the crystallite size of the ammonia containing routes against the ammonia content and thus on the pH of the reaction solution, approximately (Figure 5.5a). On the other hand, urea causes only a slightly change in pressure due to its partial thermal decomposition at the reaction temperature of 150 °C into ammonia and cyanic acid.[213–215]

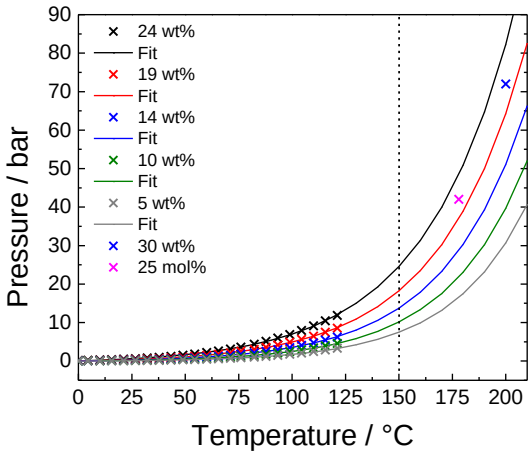

Figure 5.4: Pressure-temperature dependency of aqueous ammonia solutions with different ammonia concentrations. Dashed line indicates the temperature used in the synthesis of $CsTaWO_6$ nanoparticles (Figure 5.3). Even at highest ammonia concentrations (~ 30 wt% in water), pressure does not exceed 30 bar.[210,211] The maximum pressure for the used autoclave is 124 bar.

Interestingly, an increase of the lattice parameter *a* with decreasing crystallite size can be observed (Figure 5.5b). For the biggest crystallites, this parameter has a value of 10.3772(3) Å, which is nearly identical to the theoretical value for the bulk material (10.3768 Å).[33] Smaller crystallites exhibit larger lattice parameters. This effect can be ascribed to the quantum size effect and/or reduced ionic valencies, as it was reported for other metal oxide nanoparticles.[216–218] The different behavior of the nanoparticles with the smallest crystallite size from this tendency can be explained by the strong deviation from the average, which is also observable in TEM images (see Figure 5.6f and Figure 5.7).

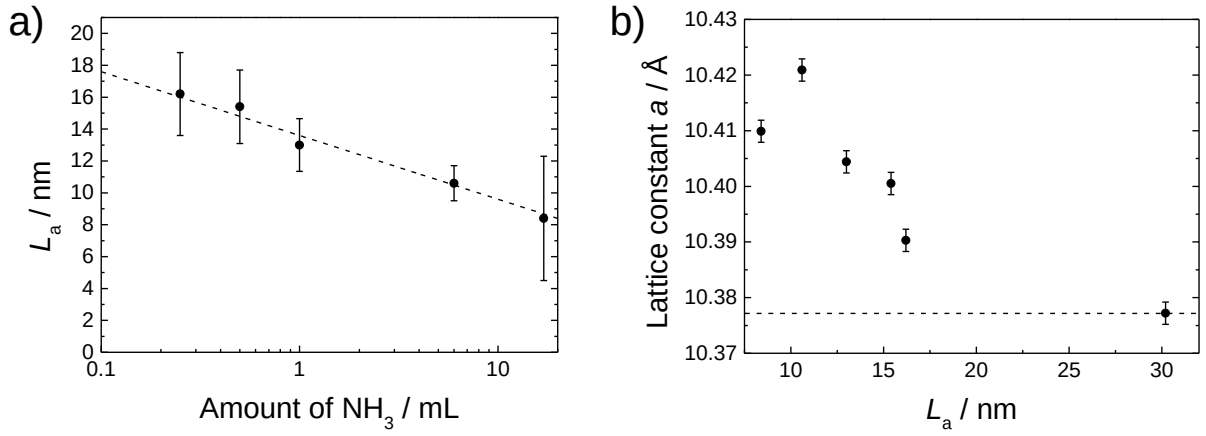

Figure 5.5: a) Crystallite size L_a *versus* the amount of ammonia and therefore the pH in hydrothermal synthesis; b) variation of the lattice parameter *a* with different $CsTaWO_6$ nanoparticle sizes (L_a and *a* from Rietveld refinements).

5.1.1.2 Morphology, surface and bulk chemistry

The morphology of the $CsTaWO_6$ nanoparticles was investigated by transmission electron microscopy (TEM, Figure 5.6). At higher magnification, lattice planes can be observed on the nanoparticles, which are prove for the high crystallinity of the material. This could be confirmed by selected area electron diffraction (SAED) (insets Figure 5.6a-f), showing Debye-Scherrer rings at the expected positions and fitting perfectly to the *d*-spacings of the defect-pyrochlore structure (JCPDS card no. 25-0233). The smallest nanoparticles (~ 8 nm) have a more spherical shape and are less uniform compared to the well-defined cubic nanoparticles of larger crystallite sizes. Nevertheless, even the smallest particles show lattice planes and rings in the SAED pattern, demonstrating a high crystallinity.

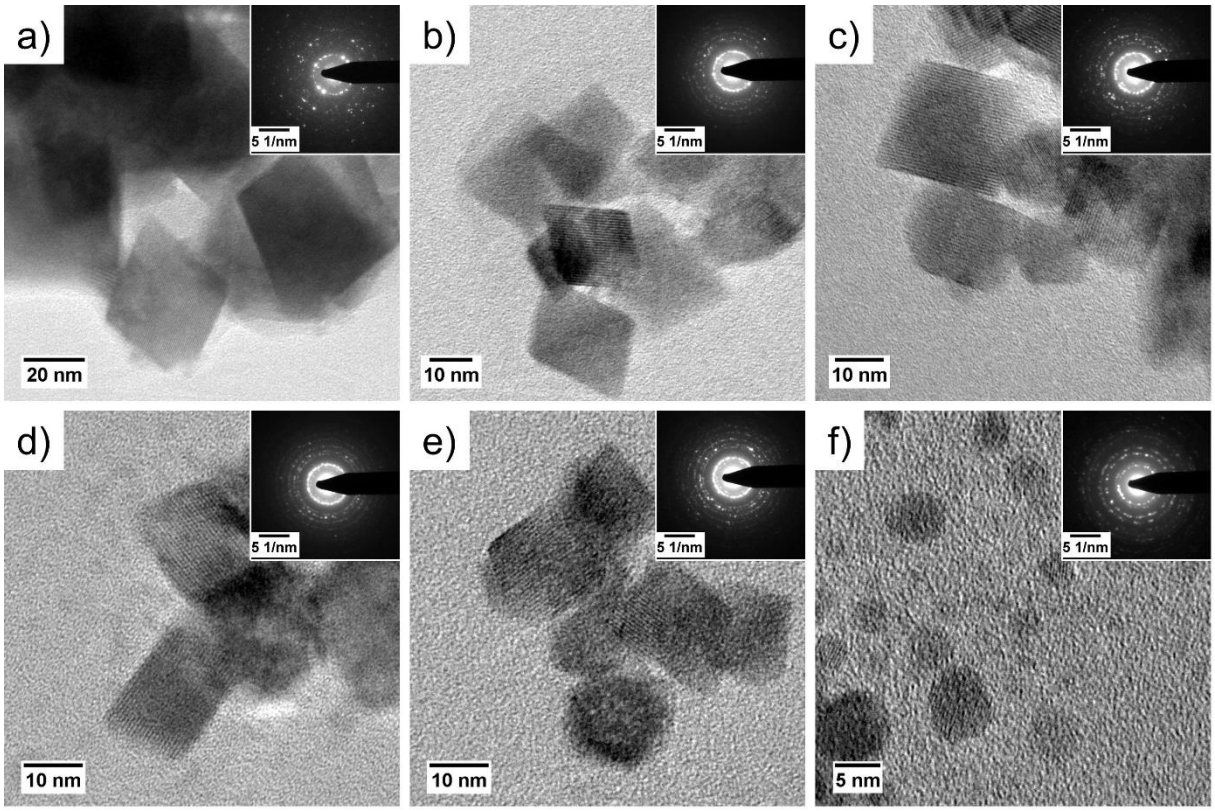

Figure 5.6: TEM images and SAED patterns (insets) of differently sized $CsTaWO_6$ nanoparticles: a) 30 nm, b) 16 nm, c) 15 nm, d) 13 nm, e) 11 nm and f) 8 nm.

Beside the calculation of the crystallite size from Rietveld refinements (Table 5.1), Scherrer's equation (*via* integral breath) was used to determine the size of the crystallites and to prove the values from Rietveld refinements, and were compared with the average particle sizes from TEM images (Figure 5.7). The values for crystallite and particle sizes are very close, indicating that every $CsTaWO_6$ nanoparticle is composed of one single crystal and thus the samples should have a comparatively high surface area.

The surface area was determined by N_2 physisorption (Figure 5.8a). The resulting surfaces are increasing with decreasing crystallite sizes from 16 $m^2 g^{-1}$ to 76 $m^2 g^{-1}$ for nanoparticle sizes of 30 nm down to 8 nm, respectively (Figure 5.8b). The theoretical surface areas for freestanding, dense cubic particles with a density of around 7 g cm^{-3} (known from Rietveld refinements and JCPDS reference card no. 25-0233) are shown as a dashed line in Figure 5.8b. The experimentally obtained surface areas are following the same trend with a small deviation in all cases due to agglomeration of nanoparticles, which slightly decreases the surface area compared to the theoretical value. The hysteresis in the N_2 physisorption measurements and the rather high pore volumes are caused by voids between the agglomerated particles known

as interparticle porosity.[118] A shifting of the hysteresis to reduced relative pressures with decreasing crystallite size can be explained by smaller voids between the smaller particles.

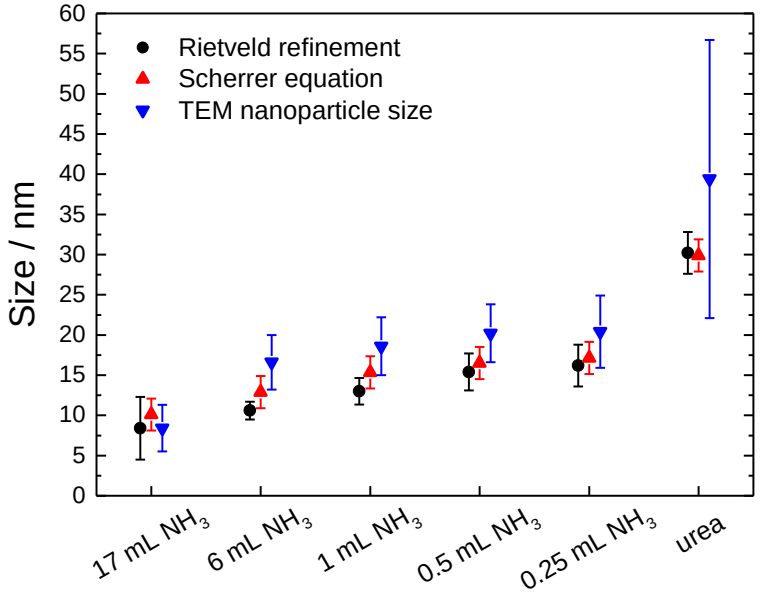

Figure 5.7: Comparison of average crystallite sizes from Rietveld refinements and Scherrer equation on the (111) and (220) reflections and the particle sizes from TEM images for the different $CsTaWO_6$ nanoparticle samples, indicated by the different amounts of additives.

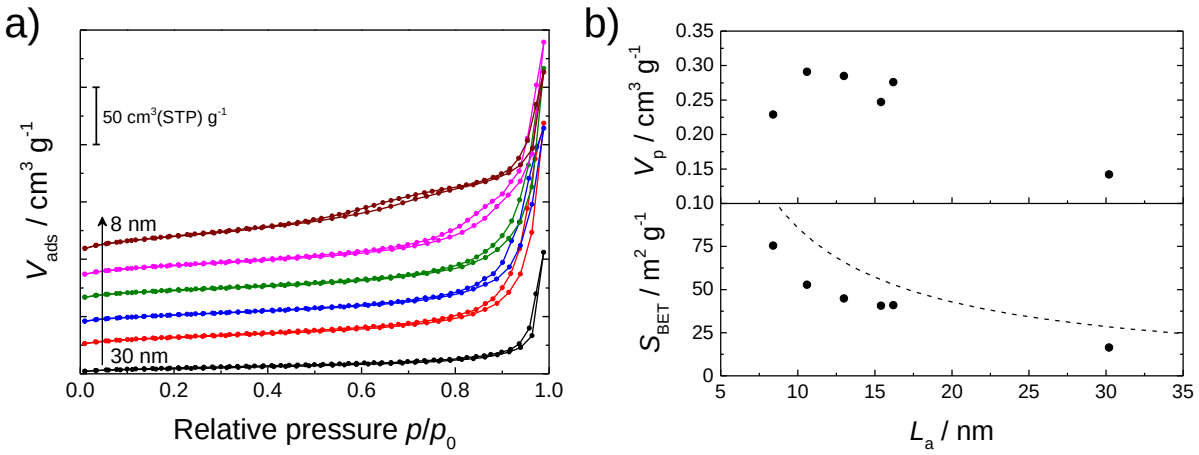

Figure 5.8: a) Nitrogen physisorption isotherms and b) respective pore volumes V_p and BET surface areas S_{BET} for $CsTaWO_6$ nanoparticles with crystallite sizes of 8 to 30 nm. The dashed line in b) indicates the theoretical surface area for free-standing nanoparticles with cubic shape.

Due to the high surface areas, the nature of the surface plays an important role for the photocatalytic activity, especially defects and residues on the surface of the nanoparticles. IR and Raman spectroscopy are both techniques to characterize the chemical nature of the

surface to see possible by-products in an amorphous state or in very small amounts, making them invisible for X-ray diffraction.

Figure 5.9 shows IR and Raman spectra for the synthesized nanoparticles. Both methods confirm the formation of phase-pure $CsTaWO_6$ without by-products or organic residues on the surface. Some weak bands in IR spectra can be seen due to nitrates from the caesium nitrate precursor (around 1410 cm^{-1}).[219] Besides these bands, IR spectroscopy evidenced only bands that can be assigned to water (~ 3400 and 1600 cm^{-1}) and a broad band below 1000 cm^{-1} with two minima due to metal-oxygen bonds in $CsTaWO_6$ (Ta–O and W–O).

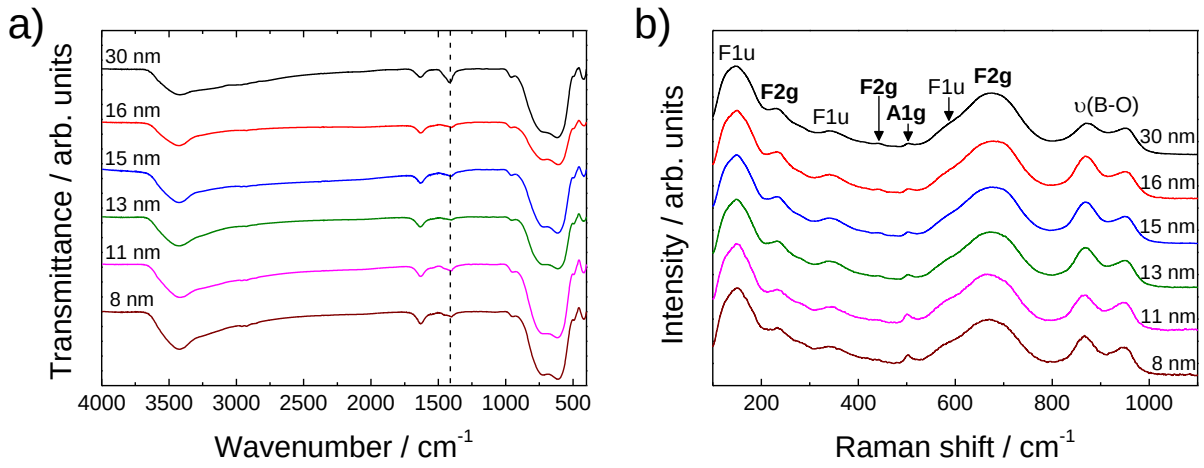

Figure 5.9: a) IR spectra and b) Raman spectra of $CsTaWO_6$ nanoparticles in the range of 8 to 30 nm. Dashed line in a) represents the position of the band from nitrate residues.

The obtained Raman spectra (Figure 5.9b) show very similar band positions and intensities for all measured samples, with nine different bands. All of them can be attributed to modes of $CsTaWO_6$, as reported in literature (Table 5.2),[220] which is once again a clear evidence for a phase-pure material. The four bold modes correspond to normally Raman-active bands; the three other bands are defect-induced, normally Raman-inactive bands that can be seen in all $CsTaWO_6$ samples. The two remaining bands at higher wavenumbers around 850 and 950 cm^{-1} can be assigned to defects due to vacancies on the B or B' site (here: Ta, W; bands denoted as *v*(B–O)). These bands are getting more pronounced with decreasing crystallite size, especially in all samples with $L_a < 30$ nm. Thus, it can be assumed that nanoparticles with smaller crystallite sizes have a slightly higher defect concentration/more vacancies on the B site, as it was already assumed by the strain parameter from Rietveld refinements (Table 5.1) However, no further differences were present, indicating the phase-purity of all samples.

Table 5.2: Experimentally obtained Raman modes, symmetries and comparison with reference values for the $CsTaWO_6$ nanoparticles, both performed at a Raman setup with a green laser (532 nm).

Number	Symmetry	Raman-active	Wavenumber / cm^{-1}	
			exp.	ref.[220]
1	F1u	No	146s	145s
2	F2g	No	240m	249m
3	F1u	No	345m	354w
4	F2g	Yes	444vw	445w
5	A1g	Yes	498w	476vw
6	F1u	No	586m	594m
7	F2g	Yes	676s	682s
8	*v*(B–O)	–	873m	869m
9	*v*(B–O)	–	952m	945m

band intensities: s = strong, m = medium, w = weak, vw =very weak

To get an insight into even very low amounts of light compounds or other precursor residues and additives on the surface, TG-MS measurements were performed. Figure 5.10a shows the mass change during heating and the derivation of the mass change for two different samples with the highest and the lowest amount of ammonia in the synthesis.

Only very low decrements of both sample masses between 3 to 5 % can be detected up to a temperature of 800 °C. The MS data in Figure 5.10b specify the exact mass-to-charge ratios *m*/*z* of the evolved fragments. The sample with the lower amount of ammonia loses only water and/or ammonia during heating, whereas both *m*/*z* ratios could belong two both compounds, a clear correlation is difficult. The sample with the higher amount of ammonia loses these two fragments, but also small amounts of nitrogen oxide (*m*/*z* = 30) and carbon dioxide (*m*/*z* = 44). The former one is due to residual nitrate from the caesium nitrate precursor, while the latter one comes from very small amounts of organic waste on the particle surface. In both samples, the main mass loss is below 200 °C and corresponds to the evaporation of ammonia and water from the synthesis and/or the washing process after the synthesis. However, both samples show only weak amounts of residues, indicating a very clean $CsTaWO_6$ nanoparticle surface.

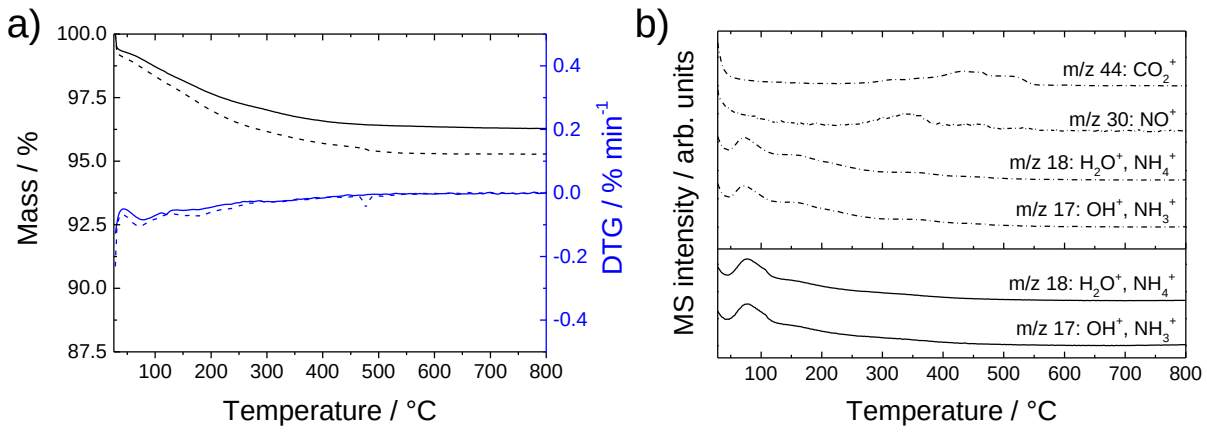

Figure 5.10: a) TG and DTG data and b) corresponding MS data in a temperature range from 30 °C up to 800 °C for two $CsTaWO_6$ nanoparticle samples prepared with the lowest and highest amount of ammonia: 0.25 mL NH_3 (L_a = 16 nm; solid lines) and 17 mL NH_3 (L_a = 8 nm; dashed lines).

After the investigation of the surface chemistry, the bulk composition of the nanoparticles was investigated with EDX. For small nanoparticles, EDX can provide an elemental composition because the penetration length is large enough to analyze a number of nanoparticles. The ratio of Cs : Ta : W was found to be 1:~1.35:1 with an error of approximately ± 2 at% (Figure 5.11). The aberration from the ideal 1:1:1 composition in $CsTaWO_6$ can be explained by the imperfect conversion of the precursor. The residual precursors caesium nitrate and ammonium metatungstate can be easily removed during the washing process after the synthesis, whereas the tantalum precursor $Ta(OEt)_5$ has already reacted with water to form an amorphous tantalum oxide (similar to the hydrolysis shown in Equation (2.16) for $Si(OR)_4$). This compound is insoluble in water and cannot be detected by Raman or IR spectroscopy, XRD and TG-MS, but leads to the slightly higher ratio of tantalum in the final product. However, the small amounts of amorphous tantalum oxide do not lead to any negative effects in the photocatalytic performance due to the high bandgap of this material of around 4 eV.[8] In fact, this amount of lower active material could even lead to an underestimation of the photocatalytic activity of the $CsTaWO_6$ nanoparticles.

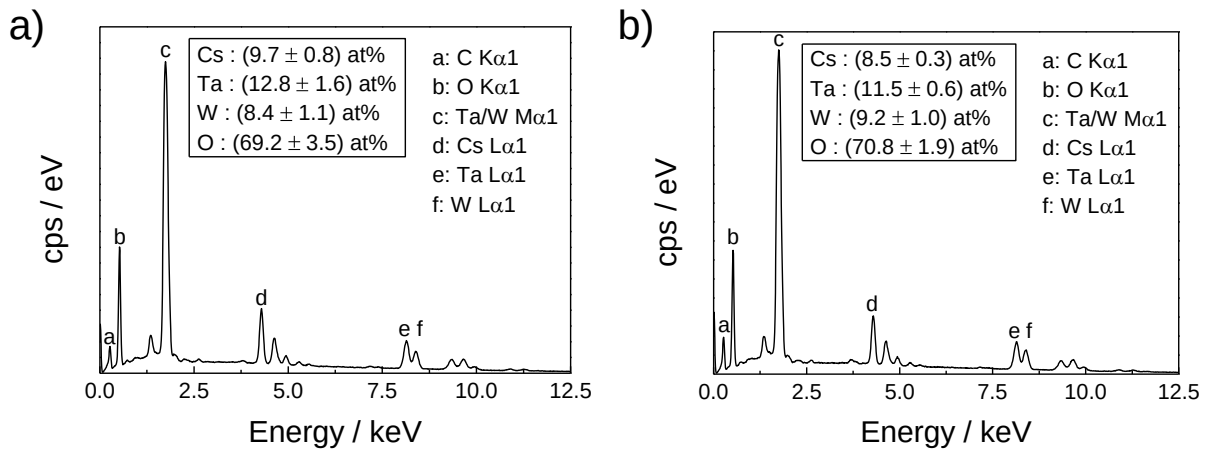

Figure 5.11: EDX analysis of smallest (8 nm, a)) and biggest (30 nm, b)) nanoparticles. Only peaks belonging to lines that were used for composition analysis are indicated.

Beside the five elements caesium, tantalum, tungsten, oxygen and a small amount of carbon from the sample holder, no further elements could be found in EDX spectra, especially no nitrogen. This means that no high number of residues due to the used ammonia or urea is left in the 8 and 30 nm nanoparticles, respectively.

5.1.1.3 Absorption behavior and dispersibility

The absorption behavior and therefore the band gaps of the semiconducting nanoparticles were investigated *via* diffuse reflectance UV-Vis spectroscopy on the nanoparticle powders (Figure 5.12a). A blue shift to lower wavelengths can be observed in the reflectance spectra of the smallest nanoparticles of 8 and 11 nm. The spectra were converted using the Kubelka-Munk function and Tauc-Plots were used to calculate the optical band gaps (E_g) (Figure 5.12b).[208]

Additionally, the calculated band gaps (E_g) were plotted against the average crystallite size (L_a) from Rietveld refinement (Table 5.1). An interesting effect can be seen, which was already predicted by Brus' model in literature.[221,222] The biggest nanoparticles have a band gap of around 3.69 eV; with decreasing crystallite size, the band gap decreases first, later on increasing dramatically. The strong blue-shift for small nanoparticles can be explained by the quantum size effect (QSE), which strongly depends on the respective material.[223–227] For example, TiO_2 nanoparticles show a QSE below 2-3 nm;[227] on the other hand, in InSb, a QSE can be observed for nanoparticles even bigger than 20 nm.[225] The decrease in the band gap for the nanoparticles of 13 and 15 nm can be described as a result of a higher number of

defects in the semiconductor with decreasing particle size, which are causing traps near the band edges and therefore a red-shift in the absorption spectra.[228] This is confirmed by the strain values from Rietveld refinements (Table 5.1). The drop of the band gap for the smallest nanoparticles of 8 nm can be explained again by the strong deviation of their crystallite sizes (Figure 5.7). It should be mentioned that this is the first observation of a quantum size effect in a quaternary semiconductor.

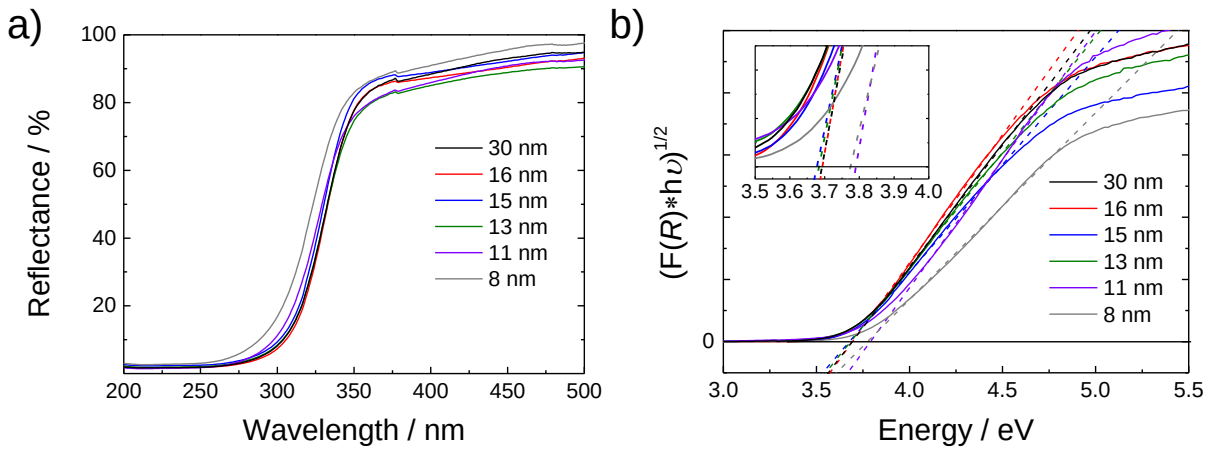

Figure 5.12: a) Diffuse reflectance UV-Vis spectra of $CsTaWO_6$ nanoparticles and b) the same spectra converted by the Kubelka-Munk function into absorption spectra and optical band gaps estimated *via* Tauc-Plots.

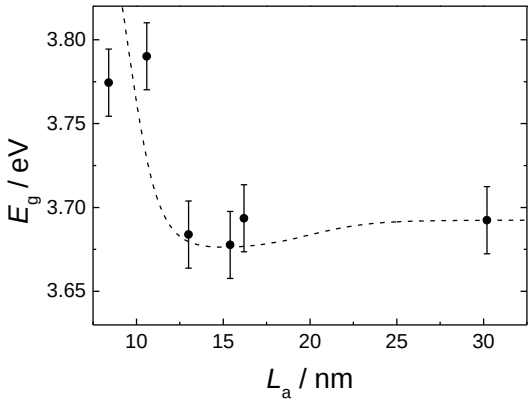

Figure 5.13: Band gaps of $CsTaWO_6$ nanoparticles *versus* the corresponding average crystallite sizes from Rietveld refinements, showing a good agreement to Brus' model.[221,222] The dashed line is just to guide the eye and is not a result of data fitting.

As another important property, the dispersibility of the photocatalyst in the used water/methanol solution for photocatalysis was measured. With dynamic light scattering (DLS), the agglomeration of the as-prepared $CsTaWO_6$ nanoparticles can be followed.

Figure 5.14 shows the hydrodynamic radii of all the investigated $CsTaWO_6$ nanoparticle samples.

The mean hydrodynamic radius for crystallite sizes of 11 to 16 nm can be found between 125 and 140 nm, while the 16 nm crystallite sample shows two maxima around 125 and 175 nm and an additionally one with a weak distribution around 330 nm. The biggest (30 nm) as well as the smallest (8 nm) nanoparticles exhibit a much larger average hydrodynamic radius with 220 and 200 nm, respectively. For the 30 nm particles, the reason for this huge difference compared to the other nanoparticles could be a stronger tendency of agglomeration for bigger particles, whereas the 8 nm particles could have a higher number concentration for the same mass of particles compared to the bigger ones and a higher diffusion coefficient,[228,229] also resulting in more agglomeration and therefore an increased hydrodynamic radius.

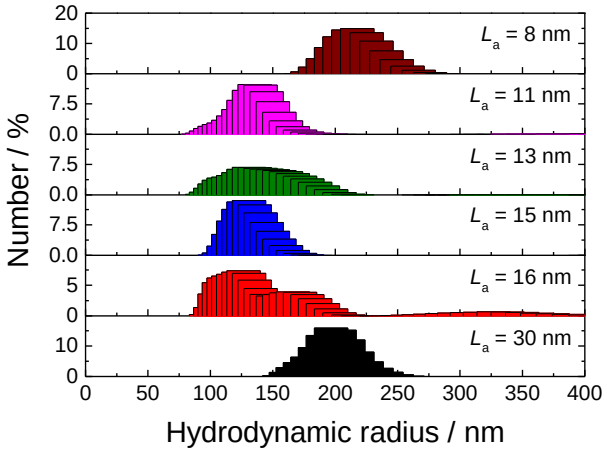

Figure 5.14: DLS measurements showing the hydrodynamic radii for $CsTaWO_6$ nanoparticles with different crystallite sizes.

5.1.1.4 Photocatalytic activity

$CsTaWO_6$ nanoparticles of many different sizes could be obtained *via* a simple hydrothermal synthesis, all having comparable morphology and properties. The influence of the crystallite size on the photocatalytic hydrogen production was investigated. Every sample was dispersed in a water/methanol mixture and stepwise loaded with Rh as co-catalyst *via* photodeposition. The resulting steady-state hydrogen evolution rates for the nanoparticles of 8 to 30 nm are given in Figure 5.15, together with the corresponding BET surface areas from N_2 physisorption.

The highest hydrogen production rate could be observed for the nanoparticles with a crystallite size of 13 nm and the smallest amount of co-catalyst (0.025 wt%). Interestingly, the photocatalytic activities do not correlate to the surface areas of the nanoparticles. All nanoparticles with sizes of 13 to 16 nm exhibit nearly the same surface areas, but lead to strong differences in activity. Furthermore, for the 8 and 11 nm samples, a higher surface area leads to smaller hydrogen evolution rates. This effect can be explained by the slightly higher band gaps for both samples (Figure 5.12), resulting in less photon absorption from the light source and a higher strain/defect concentration inside for nanoparticles (see strain parameter in Table 5.2). Additionally, the smallest nanoparticles tend to form huge agglomerates and therefore a smaller accessible surface area. Once again, the 8 nm nanoparticles seem to differ and show an increase in the hydrogen production rate compared to nanoparticles with an average crystallite size of 11 nm. This behavior can be explained again by the strong deviation of the crystallite size for this sample (Figure 5.7) and possibly due to the different shape of these particles (spherical instead of cubic, see TEM image in Figure 5.6f).

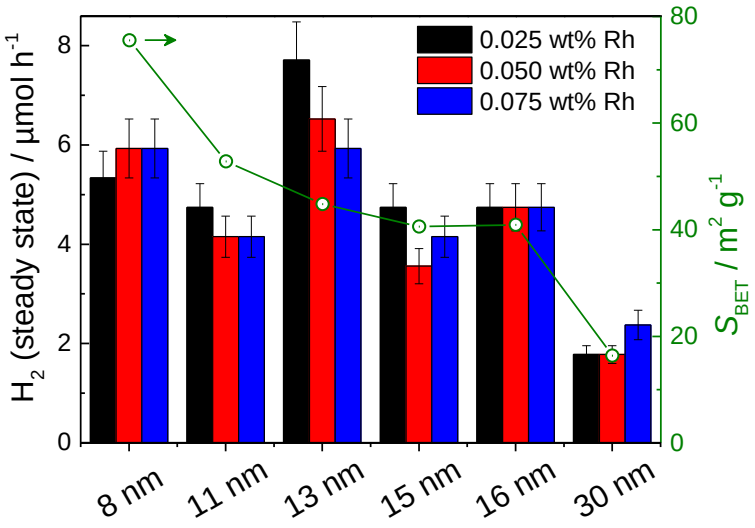

Figure 5.15: Hydrogen evolution rates for $CsTaWO_6$ nanoparticles (1 sun irradiation, without AM1.5 filtering; see Chapter 4.3.1) of different crystallite sizes with three loadings of Rh as co-catalyst. The green solid line indicates the corresponding BET surface areas.

The nanoparticles with 13 nm crystallite size showed the highest hydrogen production rates, but do not have the highest surface area or exhibit a higher agglomeration or a different shape compared to slightly smaller or bigger nanoparticles (11, 15, 16 nm). Furthermore, the strain and therefore defect concentration of these three samples is nearly identical.

Therefore, the high photocatalytic activity seems to be directly correlated to the crystallite size and one can conclude that a crystallite size of 13 nm seems to be the optimum for $CsTaWO_6$. An explanation for this finding can be the optimum trade-off between surface area and thus surface defects and the diffusion length of the charge carriers in the particular particle size, hinting to a diffusion length of the minority charge carrier of about 6-7 nm.

Interestingly, Kočí *et al*. could find a similar optimum particle size of 14 nm during their investigations on the influence of the particle size of TiO_2 on photocatalytic CO_2 reduction.[25] However, in their work, the TiO_2 phase composition changed between anatase and another semi-crystalline phase of anatase and amorphous TiO_2. Thus, a comparison with their results is difficult. Nevertheless, this could be a hint that an optimum crystallite size in this dimension could possibly be not only the best for $CsTaWO_6$, but also for other common transition metal oxide photocatalysts, such as *e.g.* Ta_2O_5 or WO_3.

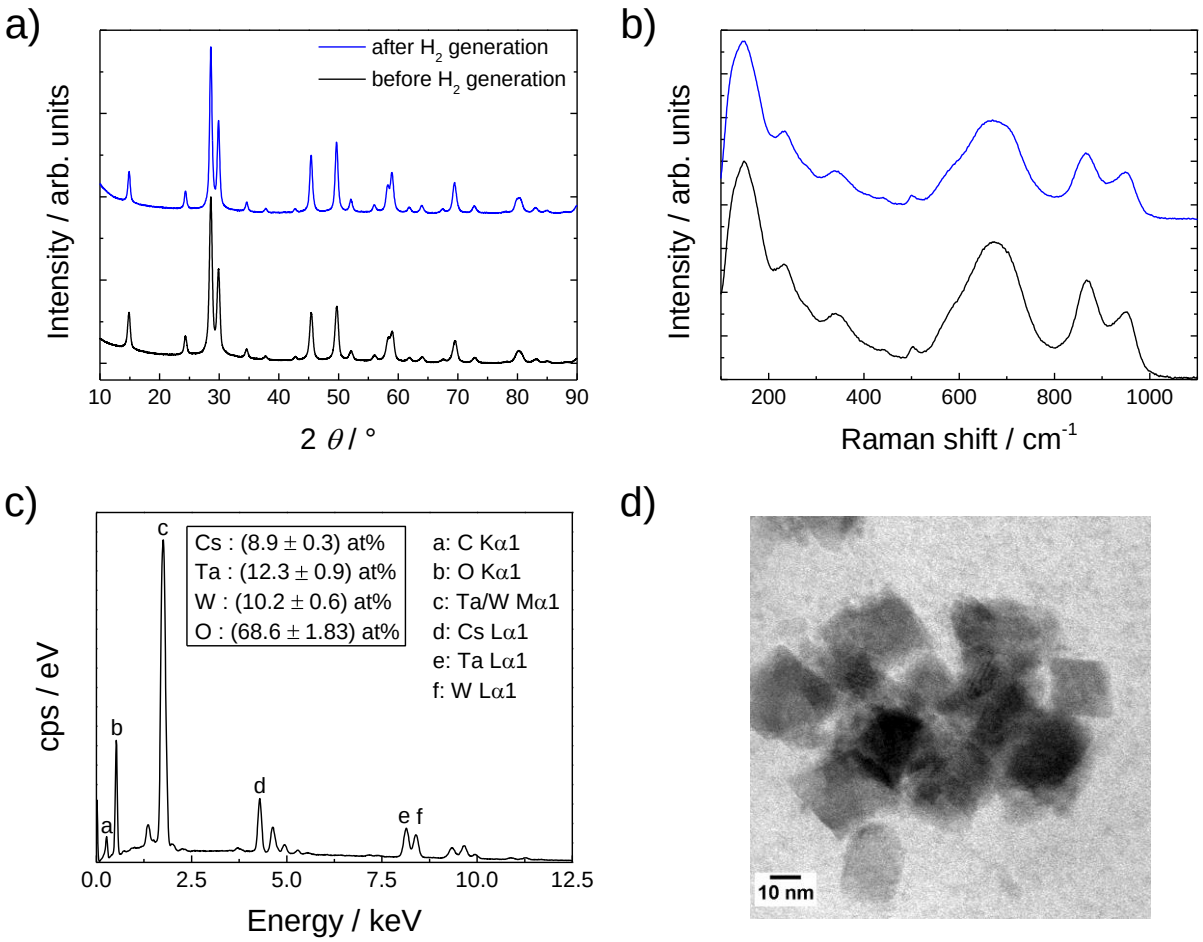

Figure 5.16: Post-catalytic characterization of 13 nm nanoparticles: a) XRD patterns and b) Raman spectra of the sample before (black) and after (red) H_2 generation; c) EDX spectrum and d) TEM image after photocatalysis.

A detailed post-catalytic characterization was carried out to investigate possible changes of the photocatalyst after hydrogen production for approximately 10 h. XRD, Raman spectroscopy, EDX analysis, TEM images (all Figure 5.16) and N_2 physisorption were measured on the sample with the highest photocatalytic activity (average crystallite size of 13 nm). All characterization techniques exhibit no remarkable changes, and a high stability of the $CsTaWO_6$ nanoparticles under the chosen conditions can be suggested. The surface area was nearly unaffected and only slightly decreased from 45 to 43 $m^2\ g^{-1}$, which is within the error range of the measurement.

5.1.2 $CsTaMoO_6$ and $CsNbWO_6$ nanoparticles

After the successful synthesis of $CsTaWO_6$ nanoparticles with the above-described strategy, the adaption of this process for other defect-pyrochlore structured materials was investigated. In a first step, the formation of $CsTaMoO_6$ *via* the same synthesis strategy as for $CsTaWO_6$ was tried, using ammonium molybdate instead of ammonium tungstate. XRD patterns of the obtained products are shown in Figure 5.17. For this compound, a synthesis time of 12 h was far too less; therefore, 48 h and 96 h were tried. After 96 h, all reflections of the $CsTaMoO_6$ JCPDS reference card no. 49-0698 can be seen and the amorphous background that is visible for the 12 and 48 h samples was clearly reduced. Maybe a higher synthesis time, but especially a slightly higher reaction temperature, could lead to a totally crystalline product.

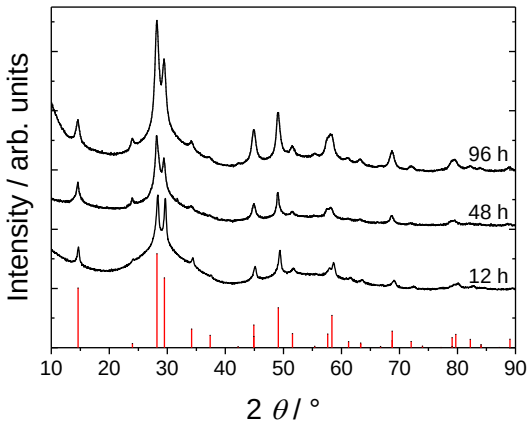

Figure 5.17: XRD patterns of $CsTaMoO_6$ nanoparticles, synthesized hydrothermally with different holding times (reference card: JCPDS 49-0698).

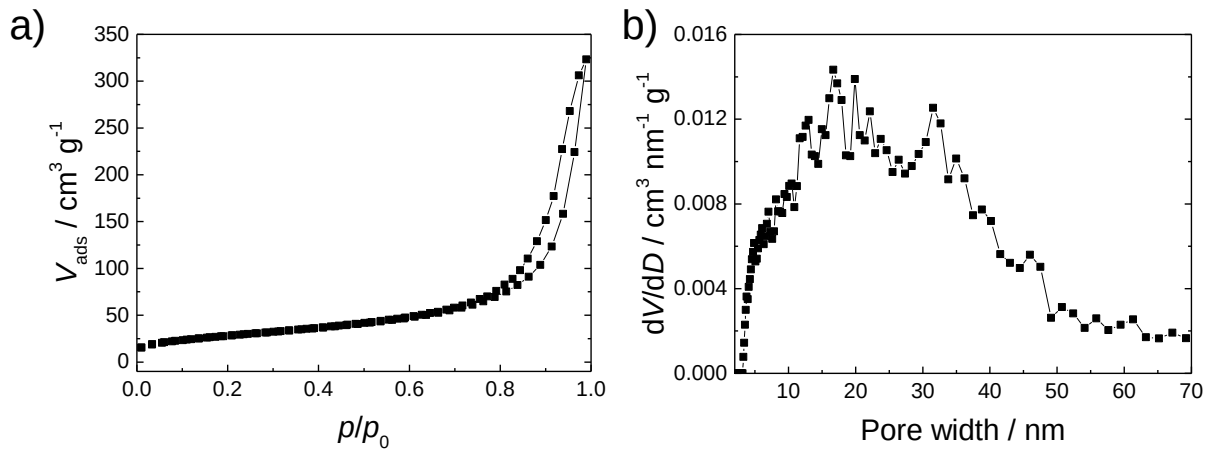

Figure 5.18: a) N_2 physisorption and b) corresponding pore size distribution from the NLDFT adsorption branch of the $CsTaMoO_6$ nanoparticles, synthesized for 96 h at 150 °C.

The N_2 physisorption isotherm of the $CsTaMoO_6$ nanoparticles is illustrated in Figure 5.18a, and the corresponding pore size distribution in Figure 5.18b. A comparably high BET surface area of 100 m^2 g^{-1} could be estimated and the broad pore size distribution results from the interparticle pores between the $CsTaMoO_6$ nanoparticles.

TEM images exhibit a crystalline product (Figure 5.19). However, the morphology of the $CsTaMoO_6$ material has more a sponge-like character than of defined nanoparticles. This geometry can explain the high surface area of the product. Therefore, the term 'nanoparticles' in this case of the $CsTaMoO_6$ material is misleading. The real morphology is more of an undefined mesoporous sponge with a high surface area. SAED ring patterns show a well crystalline material with defect-pyrochlore structure.

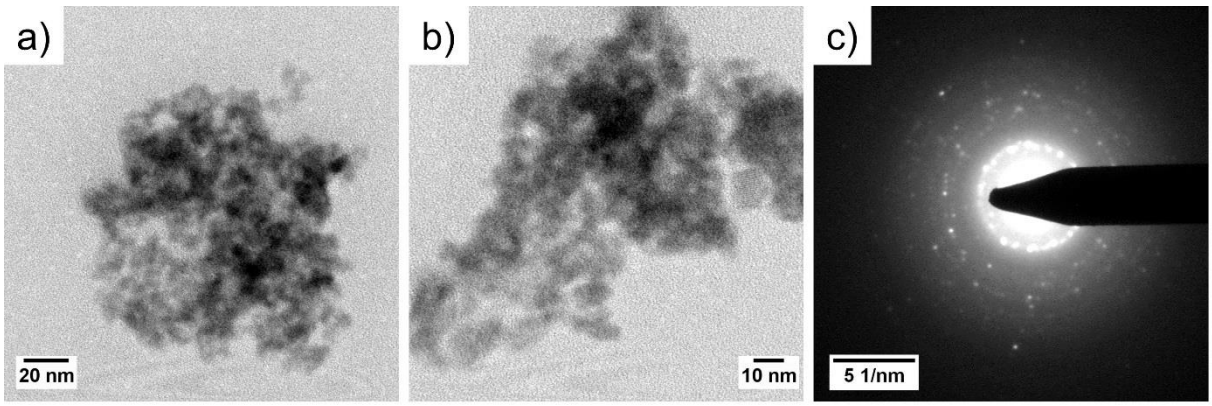

Figure 5.19: a-b) TEM images and c) SAED pattern of the $CsTaMoO_6$ nanoparticles, synthesized for 96 h at 150 °C, showing a sponge-like structure of the product.

A synthesis of $CsNbWO_6$ nanoparticles was investigated by substituting tantalum ethoxide with niobium ethoxide in the standard synthesis of the $CsTaWO_6$ nanoparticles (see Chapter 3.2.1.3). Unfortunately, no crystalline product could be obtained even after 24 h of heat treatment in the hydrothermal synthesis. Some first evidence of the formation of $CsNbWO_6$ can be seen in the reflection at around 2 θ = 28°, which has the highest intensity in the JCPDS reference card no. 49-0698 of the defect-pyrochlore structured $CsNbWO_6$.

Further experiments would be necessary to obtain a crystalline product. In particular, the synthesis temperature of 150 °C seems to be too low for this compound. In a solution of 1 mL aqueous ammonia and 16 mL of water and a filling of around 40 % in the autoclave, temperatures of 200 °C are possible, as it had been already shown in Figure 5.1. Even slightly higher temperatures should be theoretically possible in water-ammonia mixtures as it can be seen from Figure 5.4.

Besides $CsTaWO_6$ nanoparticles and $CsTaMoO_6$ sponge-like nanostructures with high surface areas, the preparation of $KTaWO_6$ nanoparticles with a high crystallinity and a surface area above 70 $m^2 g^{-1}$ was successful in our group (results not shown here).

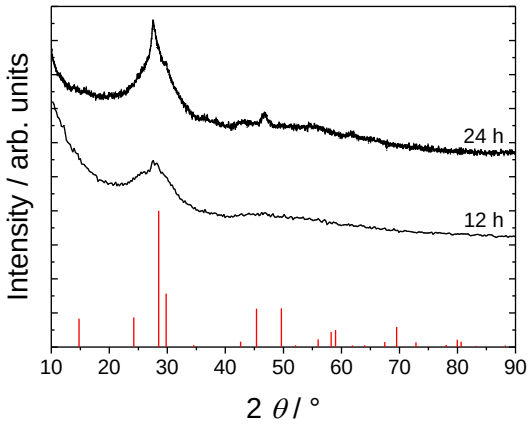

Figure 5.20: XRD patterns of the product of the synthesis route of $CsNbWO_6$ nanoparticles (see Chapter 3.2.1.3) for two different holding times of the hydrothermal step, showing just broad reflections of an amorphous powder (reference card $CsNbWO_6$: JCPDS 49-0698).

5.1.3 Continuative experiments

5.1.3.1 Microwave-assisted synthesis

Compared to the hydrothermal synthesis of $CsTaWO_6$ nanoparticles shown above, a microwave-assisted synthesis would have a number of advantages. For instance, microwave

syntheses often require lower reaction times, faster heating rates and an even more homogenous temperature profile inside the reactor.[122] Hilaire *et al*. published a microwave-assisted synthesis for WO_3 nanoparticles with a reaction time of just 10 min at a temperature of 200 °C,[230,231] whereas normal autoclave syntheses take around half an hour plus a much longer heating (5 °C min^{-1}) and cooling time.[231] Similar strategies are reported for other transition metal oxides like Ta_2O_5 and Nb_2O_5, both requiring comparably low synthesis temperatures of 220 °C and 250 °C, respectively.[232] Therefore, an adaption of these synthesis routes was investigated for the preparation of $CsTaWO_6$ nanoparticles in a microwave-assisted synthesis. Benzyl alcohol was used as solvent and $CsNO_3$, $TaCl_5$ and WCl_6 as precursor. Unfortunately, no crystalline $CsTaWO_6$ was obtained in this case (not shown here).

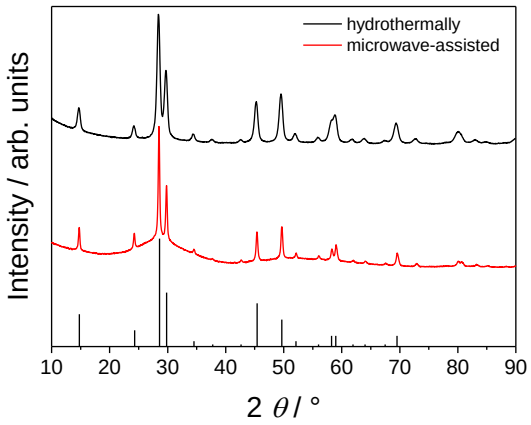

Figure 5.21: XRD pattern of the product of the microwave-assisted synthesis of $CsTaWO_6$ nanoparticles in water, compared to the hydrothermally synthesized nanoparticles. All reflections of the desired defect-pyrochlore structure can be seen (JCPDS 25-2033).

Another strategy led to the desired defect-pyrochlore structured phase, namely using the same solvent and precursor as for the hydrothermal synthesis. Caesium nitrate, ammonium tungstate and tantalum ethoxide were dissolved in 1 mL of aqueous ammonia and 16 mL of water, a microwave tube was filled to 40 % with this reaction solution and heated as fast as possible in a microwave to a temperature of 150 °C, held for 90 min and the received white powder was washed and centrifuged several times and afterwards dried at 80 °C. The XRD pattern of the product is shown in Figure 5.21. It can be seen that the reflections are sharper compared to $CsTaWO_6$ nanoparticles synthesized *via* hydrothermal synthesis. Studies about the influence of heating time, temperature and the influence of the amount of ammonia has to be done. However, the microwave-assisted synthesis leads to phase-pure $CsTaWO_6$

nanoparticles even faster than *via* hydrothermal route, while both techniques are much more economical and ecological compared to the standard synthesis *via* SSR or citrate route.

5.1.3.2 Electrospun $CsTaWO_6$-nanoparticle/carbon nanofibers

An interesting strategy for a further structuring of the $CsTaWO_6$ nanoparticles is electrospinning. With this technique, a mat of long, freestanding fibers can be produced, either by electrospinning of a precursor solution, including a polymer to adjust the viscosity or by using dispersion of as-prepared or stabilized nanoparticles in a polymer/solvent mixture with a defined viscosity. First experiments were made on electrospinning of as-prepared $CsTaWO_6$ nanoparticles with PAN as polymer and DMF as solvent. The use of PAN enables the possibility of not only having a polymer for the viscosity, but also a carbon matrix around the nanoparticles after a proper carbonization strategy (800 °C in Ar).

Figure 5.22a shows photographic images of the as-prepared white $CsTaWO_6$ nanoparticles as well as the $CsTaWO_6$/carbon nanofibers. The XRD patterns of both samples (Figure 5.22b) are nearly identical, with two small reflections of by-products in the nanofibers. The crystallite sizes L_a are identical (averaged: 13 nm), indicating no ripening process during the carbonization step.

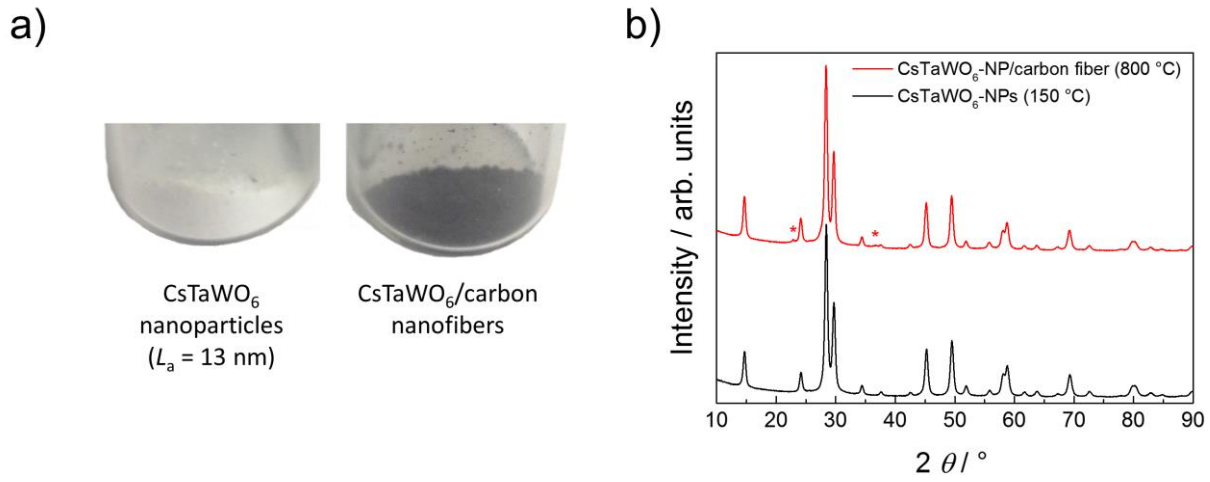

Figure 5.22: a) Photographs of the as-prepared white $CsTaWO_6$ nanoparticles and the electrospun $CsTaWO_6$-nanoparticle/carbon composite fibers and b) XRD patterns of the as-prepared $CsTaWO_6$ nanoparticles (L_a = 13 nm) and the spun fibers after heating to 800 °C in Ar, showing nearly identical patterns. The two marked reflections could occur due to formation of a by-product.

The BET surface area of the fibers is 25 $m^2 g^{-1}$, which is an evidence for the embedding of the nanoparticles into the carbon matrix, especially if compared to the 46 $m^2 g^{-1}$ of the as-prepared nanoparticles.

SEM images of the nanofibers show long fiber structures with spherical structures on their surfaces, confirming the embedded character of the nanoparticles inside the carbon fiber matrix (Figure 5.23a-b). TEM images demonstrate the good distribution of the nanoparticles inside the fibers, whereas the carbon matrix can be seen hardly due to the good transmission of the electrons through the carbon material. In Figure 5.23d, the carbon fiber matrix can be seen as two diagonals left and right of the nanoparticle line, going from the upper left to the lower right.

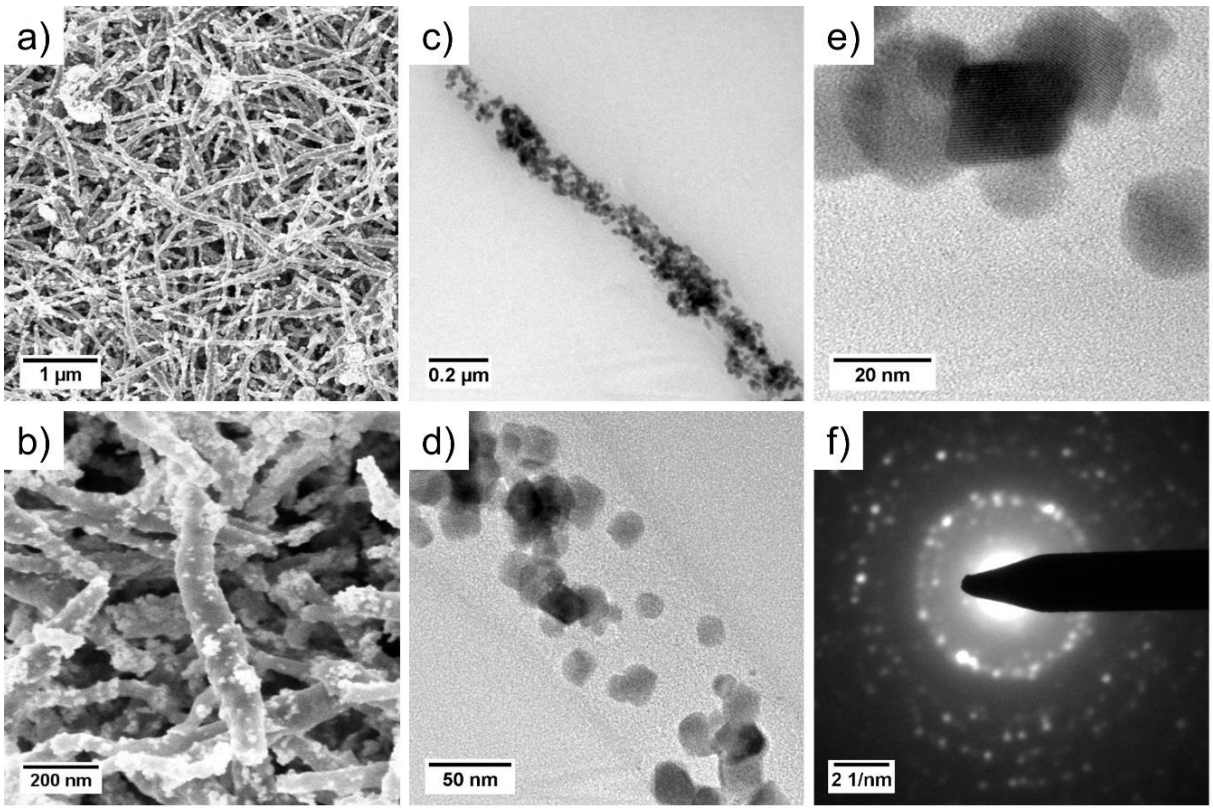

Figure 5.23: a-b) SEM image of electrospun $CsTaWO_6$-nanoparticle/carbon composite fibers, c-e) TEM images of the same sample and f) SAED pattern, showing a high crystallinity of the composite.

The idea to prepare a carbon matrix was based on the rather good electrical conductivity of this material,[233] possibly acting as a kind of co-catalyst to accumulate and separate the electrons from the holes.[234–237] However, the photocatalytic hydrogen evolution could not be increased by this strategy. Nearly no hydrogen could be detected. One reason could be the

undefined band positions of the partially nitrogen-doped carbon matrix, which could in theory lie at positions that do not enhance the hydrogen production half reaction. Most probably, the further heating of the as-prepared $CsTaWO_6$ nanoparticles to higher temperatures leads to a decomposition, as it was already slightly observable in Figure 5.22b. This assumption could be confirmed due to reference $CsTaWO_6$ nanoparticles, heated to 800 °C for 1 h in Ar and tested regarding their photocatalytic activity. No hydrogen could be detected in this reference material, too.

5.1.3.3 Sn-doped $CsTaWO_6$ nanoparticles

Due to the high surface areas and small particle size of the $CsTaWO_6$ nanoparticles, doping experiments should lead to a homogenous distribution of the doped elements, especially compared to the much bigger particles of *e.g.* SSR synthesized $CsTaWO_6$, where just a surface doping could occur. The good dispersibility of the $CsTaWO_6$ nanoparticles (Figure 5.14) enables a doping from aqueous solutions. Figure 5.24 shows first results of doping experiments, whereas it is even visible by eye that the $CsTaWO_6$ in the morphology of nanoparticles shows a better degree of doping (yellow color) compared to the SSR product (light green).

Figure 5.24: Photograph of the different undoped and Sn-doped $CsTaWO_6$ samples. From left to right: undoped $CsTaWO_6$ nanoparticles, Sn-doped $CsTaWO_6$ *via* SSR and Sn-doped $CsTaWO_6$ nanoparticles for 1 d or 7 d (rightmost).

XRD pattern and Raman spectra (Figure 5.25) does not show any changes after the doping process for the nanoparticles.

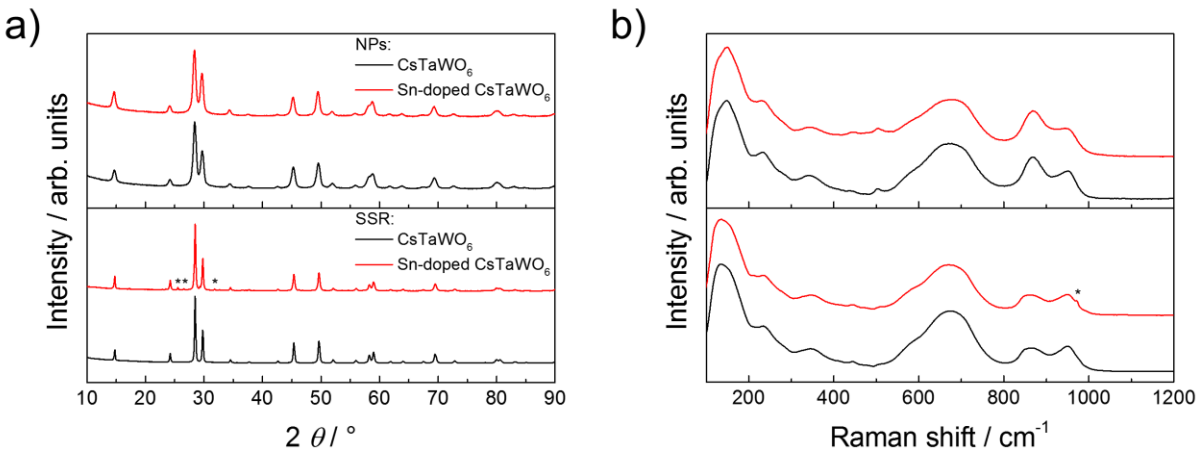

Figure 5.25: a) XRD pattern of $CsTaWO_6$ prepared *via* SSR and hydrothermally (nanoparticles, 'NP') before and after Sn-doping; b) Raman spectra of the same samples. Marked reflections in XRD and bands in Raman spectra for Sn-doped $CsTaWO_6$ *via* SSR belong to an occurred by-product.

UV-Vis spectra of the doped materials show a small shoulder at lower energies than the band gap of the pure material, indicating the doping due to the insertion of states in the band gap near the valence band. A longer doping time of 7 d with several changes of the doping solution (5 times) leads to the strongest shoulder in the UV-Vis spectra.

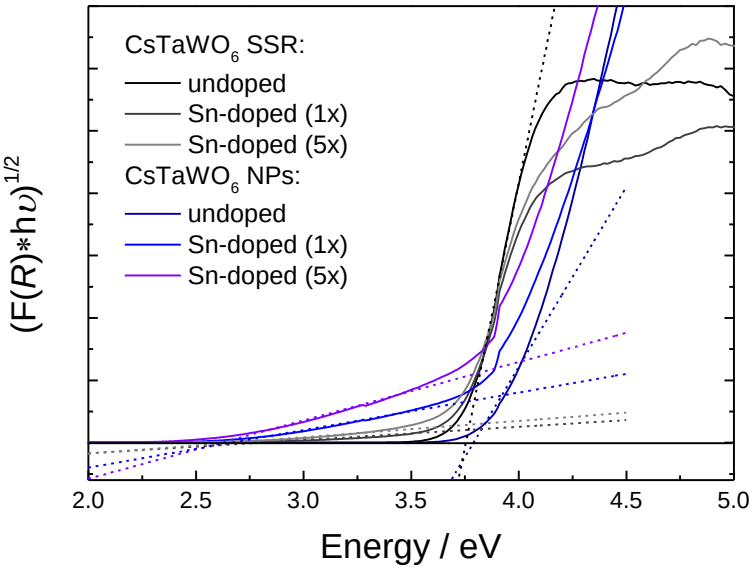

Figure 5.26: UV-Vis spectra of $CsTaWO_6$ prepared *via* SSR and hydrothermally (nanoparticles, 'NP') before and after Sn-doping for 1 d (no change of the $SnSO_4$ doping solution) or 7 d (5x change of the $SnSO_4$ doping solution).

Although the absorption edge was not completely shifted and just a shoulder occurred, the changes in band gap was estimated *via* Tauc-Plots. The obtained values for E_g are listed in

Table 5.3. A clear difference compared to the undoped materials can be seen. The color of the Sn-doped nanoparticles (Figure 5.24) and the smallest band gap of these samples are an indication for the more homogenous doping of these materials compared to the SSR materials with much bigger particle and crystallite size.

Table 5.3: Band gaps of the Sn-doped and undoped samples.

Material	**Doping**	E_g **/ eV**	**Color**
$CsTaWO_6$ *via* SSR	undoped	3.75	white
	Sn-doped (1x)	2.80	light green
	Sn-doped (5x)	2.67	light green
$CsTaWO_6$ nanoparticles	undoped	3.79	white
	Sn-doped (1x)	2.66	yellow
	Sn-doped (5x)	2.62	yellow-orange

E_g = band gap

5.2 Mesoporous transition metal oxides

5.2.1 P123-derived binary oxides as preliminary experiments

Before the synthesis of complex defect-pyrochlore structured mesoporous materials with the general formula $ABB'O_6$, some preliminary experiments were made to obtain an impression of how to synthesize such mesoporous powders in the best way (Figure 5.27). Binary oxides, namely Ta_2O_5, WO_3 and Nb_2O_5, were prepared as P123-derived mesoporous powders with synthetic routes based on the syntheses listed in Table 2.2. Calcination was performed in two steps, beginning with a stabilization step for 12 h at 250 °C as described in literature[121] and a further annealing to the desired temperature (450 to 850 °C).

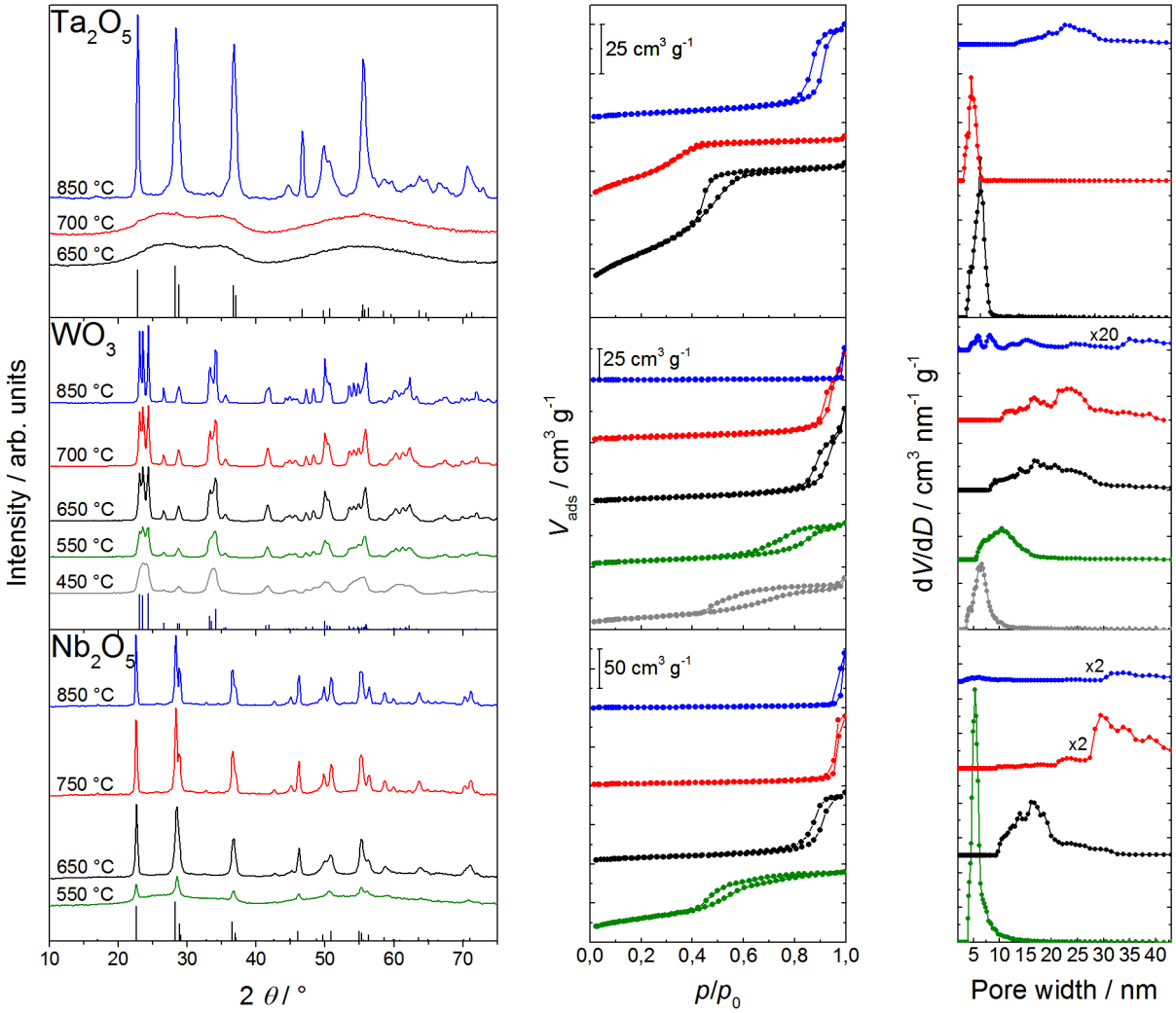

Figure 5.27: XRD patterns of P123-derived mesoporous Ta_2O_5, WO_3 and Nb_2O_5 (left), corresponding nitrogen physisorption isotherms (middle) and pore size distribution from NLDFT adsorption model (right). JCPDS reference cards: Ta_2O_5 04-9498, WO_3 43-1035, Nb_2O_5 27-1003.

Mesoporous tantalum oxide (Ta_2O_5) could be synthesized with a relatively high surface area of up to 122 $m^2 g^{-1}$ when calcined at 650 °C, but XRD patterns still show an amorphous product. Even at higher calcination temperatures (700 °C, 89 $m^2 g^{-1}$), tantalum oxide in an amorphous state was obtained. With the used holding time of 30 min, a crystalline product with orthorhombic crystal structure (JCPDS 04-3498) was received after calcination at 850 °C. However, no remarkable amount of mesopores is left after this temperature treatment, and the surface area decreased to 16 $m^2 g^{-1}$. That is the reason for the high holding times and temperatures in the literature for the preparation of crystalline mesoporous tantalum oxide, while lower temperatures lead to the formation of amorphous mesoporous Ta_2O_5.[22,120]

In contrast to Ta_2O_5, under the selected conditions tungsten oxide (WO_3) already crystallizes at comparably low temperatures[21] and a fully crystalline product with a monoclinic crystal structure (JCPDS 43-1035) can be obtained after calcination at 450 °C. At this point, the surface area is around 35 $m^2 g^{-1}$ and the average pore diameter is in the range of around 7 nm. This is an indication for a beginning collapse of the pores because P123 should lead to an average pore size of around 5 nm. Thus, the growing of the crystallites starts to destroy the pore structure, whereas at this point the polymer P123 is burned away nearly completely and cannot further stabilize the pores.[238]

Mesoporous niobium oxide (Nb_2O_5) was also prepared and showed best results at a calcination temperature of 550 °C with a surface area of 109 $m^2 g^{-1}$ and the expected average pore size of 5 nm. XRD patterns show first reflection of the Nb_2O_5 orthorhombic phase (JCPDS 27-1003), which are getting more pronounced when calcined at 650 °C. The surface area for this temperature is around 29 $m^2 g^{-1}$, once again an indicator for the collapse of the pore system. For this compound, an optimum of crystallinity, surface area and mesoporosity will probably lie in between these two temperatures (550-650 °C).

Several conclusions can be drawn from these preliminary experiments: first of all, the formation of a mesoporous $CsTaWO_6$ could be problematic due to the different calcination temperatures of the single compounds Ta_2O_5 (beginning at 700 °C) and WO_3 (beginning at 400 °C). In a worst case, the completely different crystallization temperatures could lead to a phase separation into Ta_2O_5 and WO_3 during calcination. This could result in a destruction of the pore system caused by the different growth of both co-existing phases and possibly due to the necessity of higher temperatures to form the desired $CsTaWO_6$ from these phases.

Moreover, it can be seen that the preservation of mesopores from P123-derived samples is also strongly temperature dependent, and changes between different compounds. Especially, the optimum between crystallinity and surface area/mesoporosity has to be found for each material, namely the best calcination temperature.

Table 5.4: Obtained values for P123-derived mesoporous Ta_2O_5, WO_3 and Nb_2O_5, calcined at different temperatures.

Compound	T_{calc} / °C	S_{BET} / m² g⁻¹	D_p / nm	V_p / cm³ g⁻¹
Ta_2O_5	650	122	5	0.12
	700	89	4	0.06
	850	16	16	0.07
WO_3	450	35	7	0.05
	550	19	10	0.05
	650	18	20	0.09
	700	14	23	0.09
	850	> 1	–	–
Nb_2O_5	550	109	5	0.13
	650	29	16	0.13
	750	11	30	0.09
	850	5	30	0.02

S_{BET} = BET surface area, D_p = pore diameter, V_p = pore volume.

5.2.2 Formation mechanism of mesoporous $CsTaWO_6$

5.2.2.1 Sol-gel processes in the precursor solution

Since there was no quaternary oxide photocatalyst with mesoporous morphology reported so far in literature, the formation mechanism of the mesoporous $CsTaWO_6$ was carefully investigated. In this chapter, the formation is shown on the example of the mesoporous $CsTaWO_6$ with ISO polymer as structure directing agent (Chapter 5.2.4). The same behavior (changes in color *etc*.) can be also observed in the P123-derived mesoporous $CsTaWO_6$ (Chapter 5.2.3).

The first step in synthesizing ISO-derived mesoporous $CsTaWO_6$ is the preparation of a precursor solution, starting with Cs_2CO_3 in ethanol, followed by the addition of $TaCl_5$ (for a

detailed description, see Chapter 3.2.2.2). A white powder can be obtained by drying the clear precursor solution at this point of the synthesis, resulting in the XRD pattern shown in Figure 5.28a. The reflections belong to the cubic CsCl phase, which indicates the reaction of both precursors, *e.g.* according to the following equation:

$$Cs_2CO_3 + TaCl_5 + 2\ C_2H_5OH \rightarrow 2\ CsCl + Ta(OC_2H_5)_2Cl_3 + H_2CO_3 \qquad (5.1)$$

The highly crystalline caesium chloride can be seen very easily, while the tantalum ethoxy chloride can be further condensate to an amorphous tantalum oxide, that evidently contributes together with the ISO polymer to the high background in the XRD pattern. The formed carbonic acid can decompose into CO_2 and water; the former gaseous product can leave the solution, whereas the latter one accelerates the further condensation of tantalum chloride/tantalum ethoxy chloride and later of the tungsten chloride.

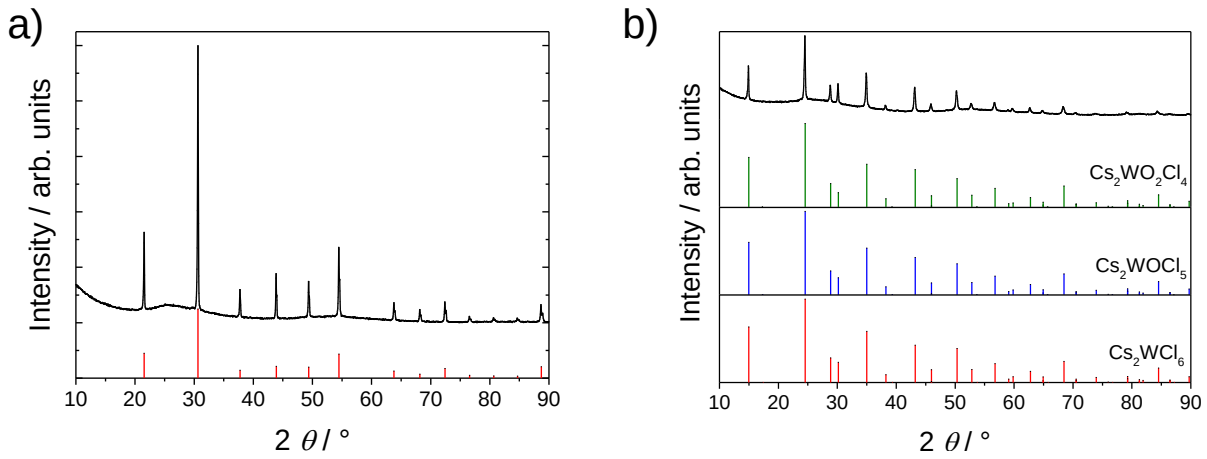

Figure 5.28: XRD patterns of a) Cs_2CO_3 plus $TaCl_5$, dissolved in EtOH, dried at 80 °C and a reference card for CsCl (JCPDS 02-2173) and b) Cs_2CO_3, $TaCl_5$ and WCl_6 (= precursor solution) dissolved in EtOH after drying. Reference cards of Cs_2WCl_6, Cs_2WOCl_5 and $Cs_2WO_2Cl_4$ are shown (JCPDS card nos. 40-9674, 18-0374 and 22-0202, respectively).

The next step is the addition of the last precursor, namely tungsten chloride. The clear solution becomes yellow immediately and gets darker with time, ending up as an orange/brown solution. Due to the high excess of ethanol as a solvent for the precursor, WCl_6 reacts according to the following equation

$$WCl_6 + 2\ C_2H_5OH \rightarrow W(OC_2H_5)_2Cl_3 + 2\ HCl + \frac{1}{2}\ Cl_2 \uparrow \qquad (5.2)$$

and further condensates with other molecules of tungsten chloride or tungsten ethoxy chloride, one example for this condensation is shown in the next equation:[169]

$$2\ W(OC_2H_5)_2Cl_3 \rightarrow Cl_2(C_2H_5O)_2W{-}O{-}W(OC_2H_5)Cl_3 + C_2H_5Cl\uparrow \qquad (5.3)$$

As it was described above, the precursor solution consists of an orange-brownish color, which can be an evidence for the presence of $WOCl_4$.[239] After drying at 40 °C on the heating plate, the solid has a dark red-blue color. The oxidation state of tungsten changes from +VI in WCl_6 into +V after hydrolysis and condensation. This oxidation state can be generally observed in a strong blue coloring (see inset Figure 5.29a). A XRD pattern of the solid is shown in Figure 5.28b. All reflections can be attributed to a cubic crystal structure with space group $Fm\bar{3}m$. From X-ray diffraction, it is not possible to obtain the exact composition of this compound, because Cs_2WCl_6, Cs_2WOCl_5 and $Cs_2WO_2Cl_4$ do all have the same crystal structure, and the changes in relative intensities are very weak (small changes of the intensities can be seen in the region $2\,\theta \approx 30°$). Even if there are some hints for the existence of tungsten in the oxidation state of +V due to the color and therefore of Cs_2WOCl_5 (which is reported as a green-blue solid), [240] a clear estimation cannot be made *via* XRD. The oxidation state +V of tungsten is theoretically possible in a stable compound and described in literature.[241–244]

A more favorable technique to determine the exact composition is EPR spectroscopy due to the different oxidation states of tungsten in the three possible compounds ($Cs_2W(+IV)Cl_6$, $Cs_2W(+V)OCl_5$ and $Cs_2W(+VI)O_2Cl_4$). In EPR, the only active species is W(+V) because of the unpaired d-electron in this oxidation state (electron configuration [Xe] $4f^{14}\ 5d^1$). The EPR spectrum of the dried precursor solution (Figure 5.29a) shows two signals in the range between 3500 and 4000 G. The stability of the here reported compound was very high; for example, the EPR measurements were made on a sample 30 days after preparation. Furthermore, after the addition of water to the product, the compound decomposed (Figure 5.29b).

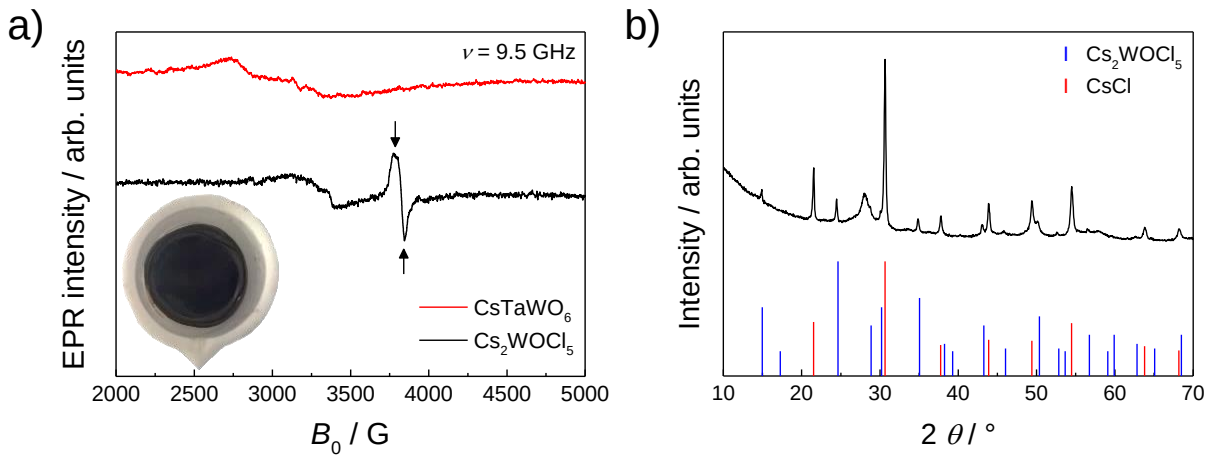

Figure 5.29: a) EPR spectrum of ISO/Cs_2WOCl_5 (black), showing the typical EPR signals for W(+V) at $g_{\parallel}$ = 1.79 and $g_{\perp}$ = 1.76,[245,246] and $CsTaWO_6$ (red) where no W(+V) can be seen.[112] The inset is showing one of the dark blue pellets in a PTFE cup after drying on a heating plate and in the vacuum oven. b) XRD pattern of the product after washing with water, showing decomposition of Cs_2WOCl_5. Reference patterns are CsCl (JCPDS 02-2173) and Cs_2WOCl_5 (JCPDS 18-0374).

The two signals can be converted into the so-called *g*-value, a dimensionless factor of the magnetic moment of the unpaired electron:

$$g = \frac{h \cdot \nu}{\mu_B \cdot B_0}, \text{ whereas} \qquad (5.4)$$

$h = 6.626 \cdot 10^{-34}$ Js

ν = frequency of the used microwave irradiation

μ_B = Bohr magneton

B_0 = magnetic flux density (in Tesla (T); 1 T = 10 kG

The two signals with $g_{\parallel}$ = 1.79 and $g_{\perp}$ = 1.76 fit perfectly to the experimentally measured and theoretically calculated values for W(+V) in the $(WOCl_5)^{2-}$ anion.[245,246] This is a strong indication for the proposed mechanism above.

The targeted compound of this synthesis is $CsTaWO_6$ and consequently, the stoichiometric ratios of the Cs, Ta and W precursors are 1:1:1. The intermediate product has the composition Cs_2WOCl_5. Therefore, at least half of the tungsten and the whole tantalum are not represented in this formula. It has been already mentioned that tantalum could be present in the form of an amorphous tantalum oxide/tantalum oxychloride before the addition of tungsten chloride, which could be also the case after the addition. Furthermore, hydrolyzed and condensated

tungsten in the form of amorphous tungsten oxide/tungsten oxychloride can be also present and tantalum could be incorporated in the Cs_2WOCl_5 structure, partially replacing tungsten of the same valence (Cs_2TaOCl_5). This would also lead to a very fine mixture of the precursor, which is beneficial for the following calcination step to form the caesium tantalum tungsten oxide. For simplification, the vacuum-dried precursor/polymer solid before calcination will be denoted as ISO/Cs_2WOCl_5 hereinafter (or P123/Cs_2WOCl_5 in the case of P123-derived materials).

5.2.2.2 Processes during calcination

Figure 5.30a shows the XRD patterns of the precursor solution after drying at 50 °C in vacuum and after the following calcination step at 550 °C. In both cases, a cubic crystal system can be observed, but the intensities and half widths of the reflections change drastically. The crystal structure of the oxychloride Cs_2WOCl_5 and the defect-pyrochlore $CsTaWO_6$ are illustrated in Figure 5.30b. The lattice parameters of both compounds are very similar, making it possible to get an easy transformation *via* oxidation and Cs_2WOCl_5 possibly acting as a host crystal. In both structures, the transition metal is six-fold octahedrally coordinated with either chlorine or oxygen. During oxidation, all residual chlorine atoms are replaced by oxygen (see also XPS measurements after calcination in Figure 5.41).

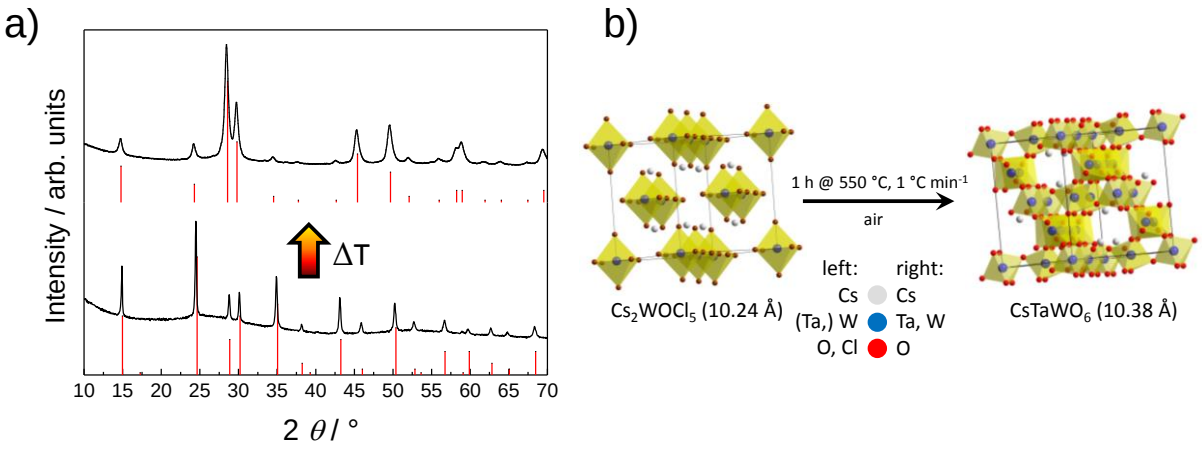

Figure 5.30: a) XRD pattern of the dried precursor solution before and after calcination and b) the crystal structure of Cs_2WOCl_5 (JCPDS 18-0374) and $CsTaWO_6$ (JCPDS 25-0233).[240]

The exact mechanism of the oxidation can be followed by *ex-situ* XRD and IR spectroscopy, both measured after heating up the dried precursor solution to the respective temperature (Figure 5.31 and Figure 5.32). A proof for the existence of W–O bonds, either in the Cs_2WOCl_5

or the amorphous gel, can be seen in the infrared spectrum of the dark blue solid before calcination, which includes a band a 957 cm^{-1} that can be attributed to the stretching mode of W–O in Cs_2WOCl_5.[247,248]

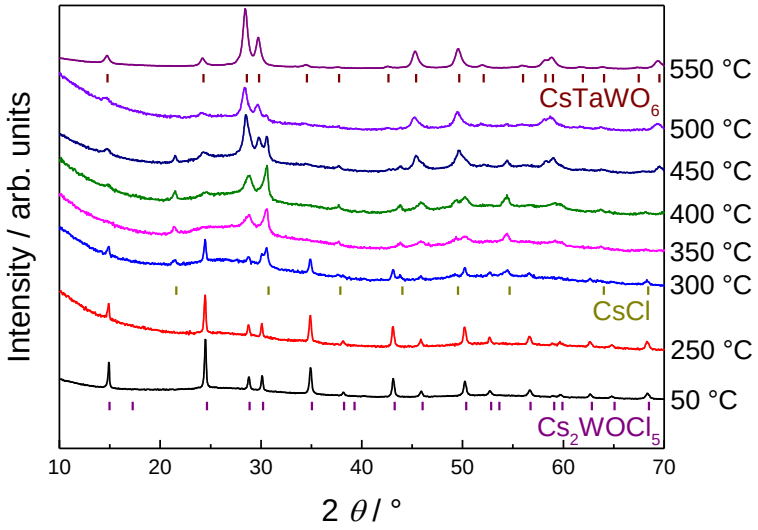

Figure 5.31: *Ex-situ* XRD patterns of the ISO/Cs_2WOCl_5 hybrid during heat treatment (JCPDS reference cards: $CsTaWO_6$ 25-2033, CsCl 02-2173, Cs_2WOCl_5 18-0374).

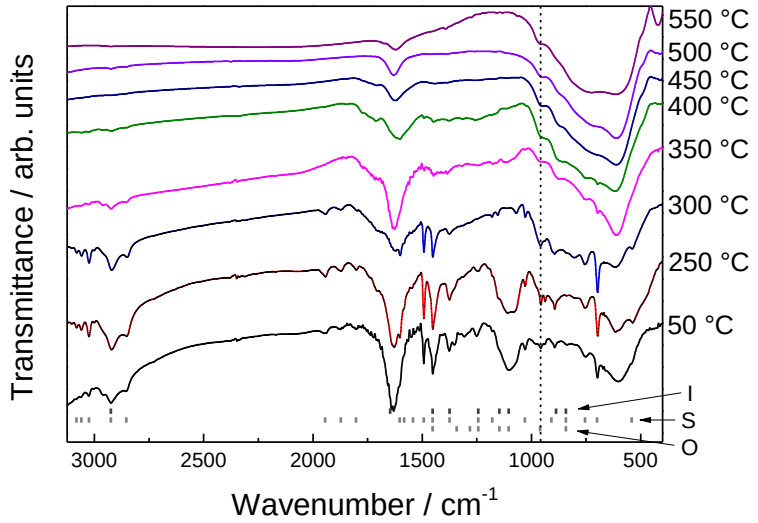

Figure 5.32: *Ex-situ* IR spectra of the ISO/Cs_2WOCl_5 hybrid during heat treatment. Dashed line illustrates the W–O stretching mode; small bars represent the bands of the three polymer blocks.[251-253]

Up to a temperature of 250 °C, no changes can be observed. Beginning at 300 °C, the caesium-containing compound Cs_2WOCl_5 starts to decompose, the intensities of the reflections are getting smaller and reflections of the cubic CsCl phase can be detected in XRD. At the same time, the IR spectrum does not change drastically and all bands of the ISO polymer

are still visible.[249–251] Going to higher temperatures of 300 to 350 °C, the reflections of the Cs_2WOCl_5 further disappear and broad reflections of a cubic structure appear with relative intensities that fit well to the $CsTaWO_6$ compound. IR spectroscopy shows the bands belonging to the ISO polymer start to disappear, indicating the decomposition of the structure directing agent (see also MS data in Figure 5.35 in the next chapter). The broad band at 500-1000 cm^{-1} is based on the formation of the metal-oxygen bonds in $CsTaWO_6$. These observations can be summarized in the following proposed mechanism: at around 300 °C, Cs_2WOCl_5 and tantalum oxychloride form $CsTaWO_6$ under the consumption of oxygen in a redox reaction, whereas oxygen is reduced and tungsten and chlorine are oxidized. The excessive caesium forms CsCl and chlorine is released (or as HCl if further reacted with hydrogen from polymer, water-hydrolyzed educts or moisture).

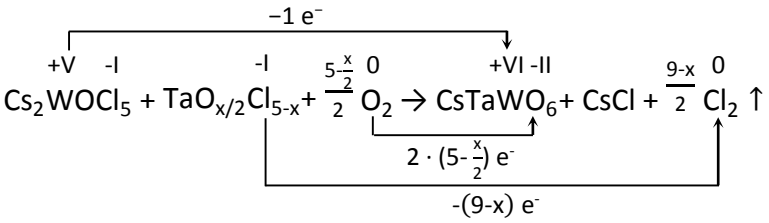

(5.5)

Alternatively, if tantalum is also incorporated as Cs_2MOCl_5 with M = Ta,W the following similar reaction can occur:

$$Cs_2TaOCl_5 + Cs_2WOCl_5 + 2\ O_2 \rightarrow CsTaWO_6 + 3\ CsCl + 3.5\ Cl_2 \qquad (5.6)$$

With increasing temperature and reaction time, the formed CsCl is consumed by residual tantalum and tungsten oxychloride, once again in a redox reaction under the release of chlorine (or HCl):

$$CsCl + (Ta,W)O_yCl_z + \frac{6-y}{2}\ O_2 \rightarrow CsTaWO_6 + \frac{z+1}{2}\ Cl_2 \uparrow \qquad (5.7)$$

At a temperature of around 500 °C, only weak reflections of CsCl are left (*e.g.* at around $2\theta = 30°$) that finally disappear after heating to 550 °C and pure crystalline $CsTaWO_6$ is received. The last temperature step is needed to finally dispose the CsCl and additionally to get a homogenous distribution of tantalum and tungsten (B and B') on the Wyckoff 16c position, observable in the broad band at 500-1000 cm^{-1} in IR spectroscopy, which becomes nearly a plateau. This means, metal-oxygen bonds are statistically distributed and no

accumulation of one species (Ta or W) occurs. In addition, all bands related to the ISO polymer are totally disappeared at this temperature. The total release of chlorine after 550 °C can be also seen in TG-MS measurements that will be shown in the next chapter, in which the decomposition of the polymers during calcination and their influence on pore structure and ordering will be explained in detail.

5.2.2.3 Influence of decomposition of the polymer on the pore structure

The optimum calcination temperature for the mesoporous $CsTaWO_6$ to get a complete removal of polymers was found by thermogravimetric analyses (TG) in combination with mass spectrometry (MS). Figure 5.33a-b shows TG curves for the P123/Cs_2WOCl_5-hybrid and ISO/Cs_2WOCl_5-hybrid, respectively. In both cases, a small mass loss takes place below 100 °C, corresponding to adsorbed water. For the P123 block copolymer, it can be seen that it is burned away between 150 and 350 °C and almost completely removed at this temperature.[238] In contrast, the ISO polymer starts decomposition at around 150 °C with a strong maximum at 320 °C and another local maximum at approximately 450 °C.[252] For both polymers, a complete deletion occurs after a temperature treatment at around 500 °C.

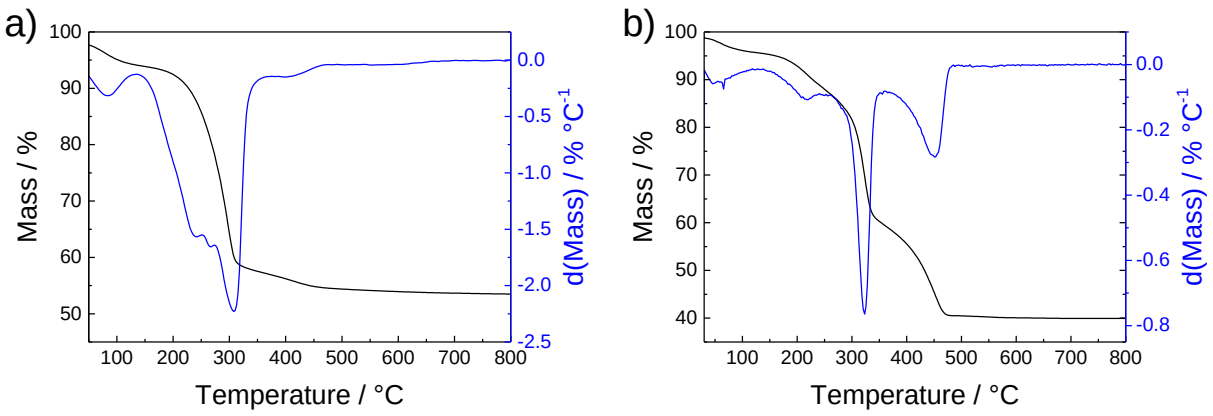

Figure 5.33: TG and DTG data for a) P123-derived and b) ISO-derived mesoporous $CsTaWO_6$.

Figure 5.34 provides a more detailed look into the decomposition products of the P123/Cs_2WOCl_5-hybrid *via* mass spectrometry. At 200 °C, small hydrocarbon fragments can be detected, together with CO_2 and H_2O, all of them can be attributed to the beginning decomposition of P123.[253] HCl with the both mass-to-charge ratios (*m*/*z*) of 36 and 38 due to the two stable isotopes of chlorine (^{35}Cl and ^{37}Cl) also starts to occur at around 200 °C with a maximum at 300 °C. For higher temperatures (above 350 °C), the only mass loss can be

assigned to the *m*/*z* ratio of 44, corresponding to CO_2. This can be a hint for the formation of carbon residues inside the pores, which are burned away at this temperature.

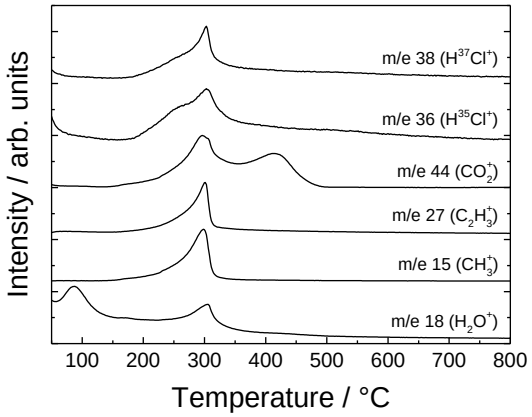

Figure 5.34: MS traces of gaseous products evolving for the P123/Cs_2WOCl_5 hybrid material.

In Figure 5.35, all arising fragments during the thermal treatment of the ISO/Cs_2WOCl_5-hybrid are illustrated. Starting at a temperature of 150 °C, small hydrocarbon fragments with a number of carbon atoms from 1 to 3 can be detected, corresponding to the degradation of the polyisoprene and poly(ethylene oxide) block in the ISO triblock copolymer.[253] The evolution of both HCl species takes place at the same temperature of around 200 °C with a maximum at 300 °C as for the P123-derived $CsTaWO_6$ due to its origin in the chloride precursor/the Cs_2WOCl_5, being the same for both P123 and ISO-derived samples. At around 320 °C, a few strong signals appear and can be assigned to hydrocarbons of the general formula C_4H_x and C_6H_y. These temperature region and mass-to-charge ratios are typical for the decomposition of polystyrene.[254,255] For higher calcination temperatures, smaller fragments are again dominant but with lowering intensities up to a temperature of around 500 °C. Shortly before this temperature is reached, another two maxima can be seen for CO_2^+ and C^+, both giving a hint for the existence of residual carbon inside the pores and its removal at this temperature. Summarized, a weight loss and removal of organic residues can be observed at much higher temperatures for the ISO-derived sample than for the P123-derived one, which can cause a better stabilization of the pore system.[252]

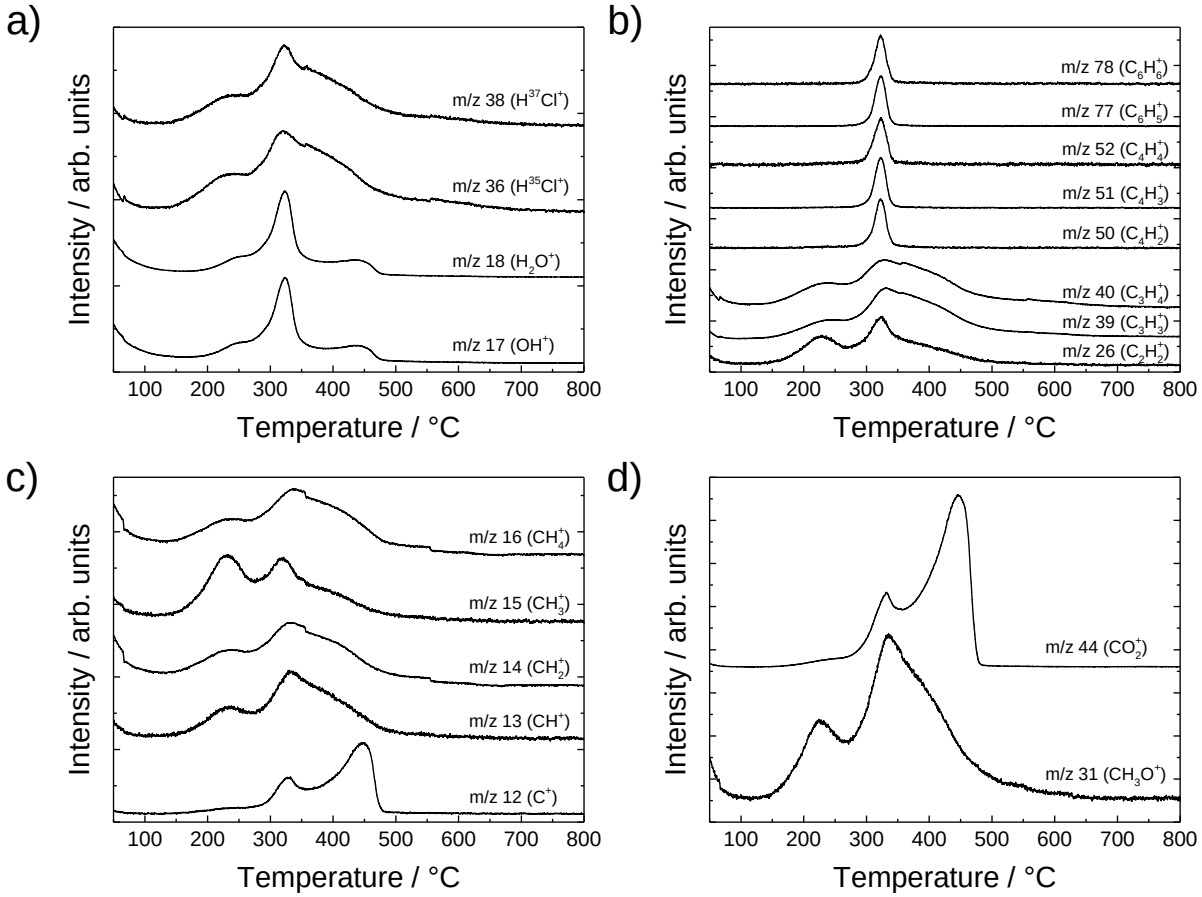

Figure 5.35: MS traces of ISO-derived $CsTaWO_6$: a) water- and chlorine-derived signals, b) bigger organic fragments from polystyrene (PS), c) smaller organic fragments from polyethylene oxide (PEO) and polyisoprene (PI) and d) other fragments, including CO_2, which is released up to 500 °C.[253–255]

5.2.3 P123-derived mesoporous $CsTaWO_6$

5.2.3.1 Influence of porogen and calcination temperature

After the successful preliminary experiments, mesoporous $CsTaWO_6$ powders with P123 as porogen were prepared according to the described synthesis procedure in a Petri dish, located in a climatic chamber with controlled atmosphere (Chapter 3.2.2.1). Figure 5.36a shows XRD patterns of the samples after calcination between 400 and 600 °C and thus after template removal. At 400 °C, besides the amorphous shoulder at around 2 θ = 25−30°, hardly any other reflections can be seen, indicating a mostly X-ray amorphous material. The differences compared to the already visible reflections for the ISO-derived materials (Figure 5.31a) could be explained by the stabilization step at 250 °C for 12 h in these experiments. At 450 °C, all reflections for crystalline $CsTaWO_6$ are already present. That is 150 °C lower in temperature than for non-templated $CsTaWO_6$ powders *via* citrate-route.[30] However, the pattern still

shows amorphous contaminants, belonging to residual organic material from the polymer template (see Figure 5.33 and Figure 5.34). After calcination at 550 °C, the amorphous background was clearly removed and all reflections for crystalline $CsTaWO_6$ were present. These reflections further increased in intensity at 600 °C.

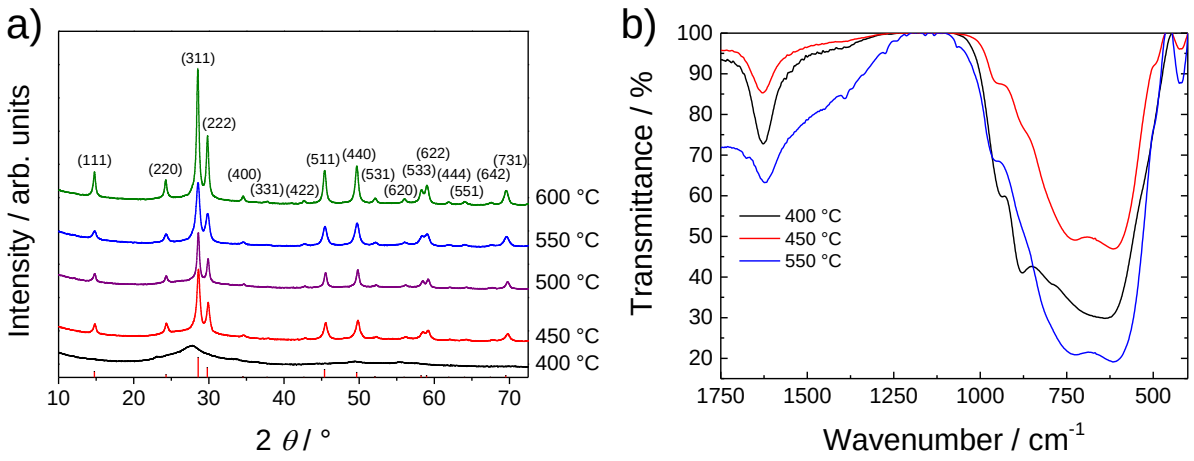

Figure 5.36: a) XRD patterns of the P123-derived mesoporous $CsTaWO_6$, calcined at different temperatures (reference card: JCPDS 25-2033) and b) corresponding IR spectra of the same samples.

IR spectra show a large band dominating the spectrum at around 500-1000 cm^{-1}, originating from W–O and Ta–O bonds, which become more pronounced with increasing calcination temperature indicating the ongoing crystallization. The bands at 1620–1630 cm^{-1} result from surface water. No evidence for any organic residues can be found in IR, indicating a decomposition of the polymer already at 400 °C, as it was predicted by TG-MS (Figure 5.34). However, carbon residues inside the pores cannot be seen in IR.

Figure 5.37 compares N_2 physisorption isotherms of the samples prepared at different calcination temperatures. The shape of the isotherms and the beginning of the hysteresis significantly changes with calcination temperature. Samples at 400 and 450 °C only show interparticle porosity due to an incomplete decomposition of the polymer (compare with Figure 5.33a and Figure 5.34).

The formation of mesopores occurs due to the templating effect, indicated by type V isotherms in Figure 5.37a. With increasing calcination temperature, the crystallinity increases as shown in Figure 5.36a, but at the same time, the surface area decreases. An optimum between crystallinity and surface area could be found at 550 °C, where all template was removed, and the surface area was determined to be 60 $m^2 g^{-1}$, which is approximately

15 times larger than for a non-porous powder prepared *via* citrate route.[30] The corresponding pore volume of this sample was measured to be 0.20 $cm^3\ g^{-1}$. However, already the broad pore size distribution in Figure 5.37b denotes a non-ordered pore system, in contrast to the results for other transition metal oxides like TiO_2 or Ta_2O_5 (Table 2.2),[121,138] prepared with P123. Nevertheless, the sample calcined at 550 °C exhibits a high crystallinity, high surface area and no organic residues, resulting in the first reported highly mesoporous and crystalline quaternary oxide photocatalyst material with defect-pyrochlore structure.[35] The calcination at a lower temperature (500 °C) resulted in samples with a very narrow pore size distribution and nearly the same surface area, but a significantly lower pore volume.

Following XRD, TG-MS and N_2 physisorption results, calcination at 550 °C turned out to be the optimum compromise of good crystallinity, large surface area, high porosity, and no detectable polymer residues.

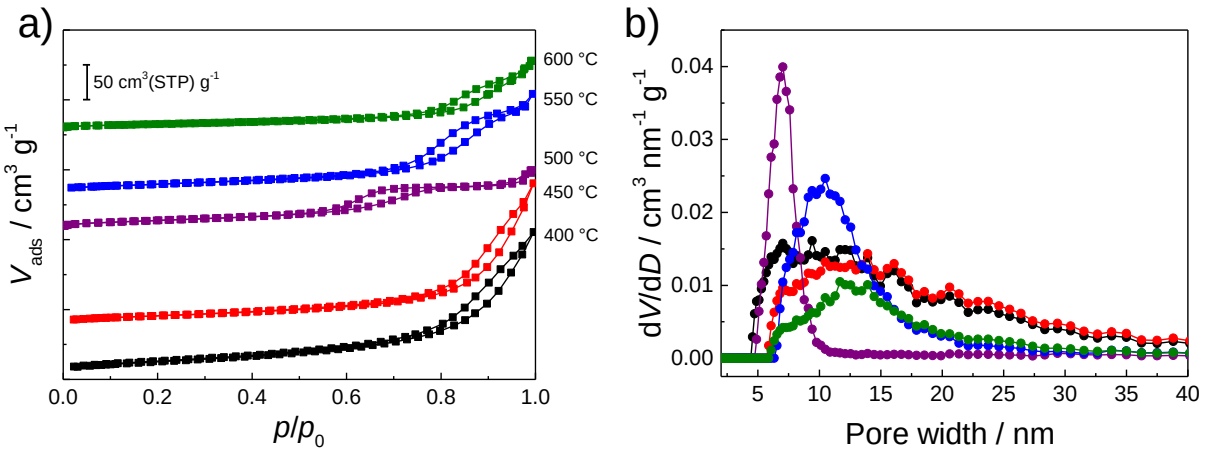

Figure 5.37: a) N_2 physisorption isotherms for mesoporous $CsTaWO_6$ calcined at temperatures of 400 to 600 °C and b) respective pore size distributions.

After finding the optimum calcination temperature to be 550 °C, the best calcination strategy was investigated. As described for the other transition metal oxide Ta_2O_5, WO_3 and Nb_2O_5 (Chapter 5.2.1), the heat treatment of the as-prepared P123/Cs_2WOCl_5-hybrid consisted of two steps, one stabilization step to get a partial decomposition of the polymer and a further condensation of the precursor,[121] and the final calcination step. Other authors did not use a stabilization step for their synthesis of P123-derived mesoporous materials.[21,138] Thus, to prove whether this step is necessary, different heating programs were tested (Figure 5.38). As it can be seen from N_2 physisorption isotherms, no remarkable differences

arise if the stabilization step was left out or the heating rate was decreased. The BET surface area does not change remarkably (around 60 $m^2 g^{-1}$ for all samples). Hence, for a more timesaving calcination, for further experiments of samples dried in a climatic chamber, the heating rate was set to 5 °C min^{-1} and the calcination time to 30 min.

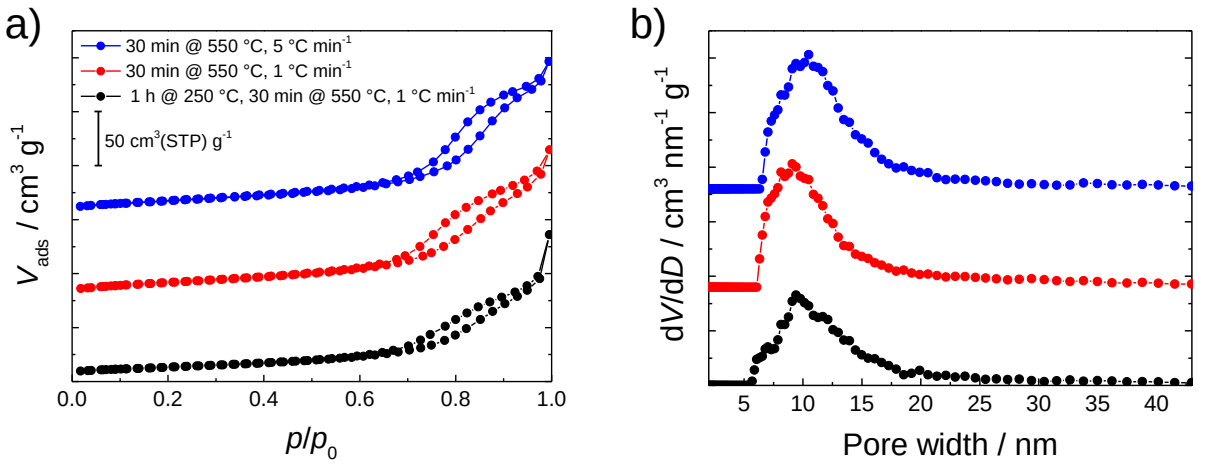

Figure 5.38: a) N_2 physisorption isotherms and b) corresponding pore size distribution from NLDFT adsorption branch model of P123-derived mesoporous $CsTaWO_6$, calcined with different heating rates and with or without an additional stabilization step at 250 °C.

The influence of polymer P123 on the porosity was investigated by changing the amount of P123 from 10 wt% (with respect to the amount of solvent) into both directions to 2.5, 5 and 15 wt%. Additionally, to prove the templating character of the triblock copolymer P123, the precursor solution was dried and calcined at 550 °C without any polymer, and with polyethylene oxide (PEO, M_w = 10000 g mol^{-1}) instead of the diblock copolymer P123.

No formation of pores and only small surface areas of 8 and 14 $m^2 g^{-1}$ could be observed without polymer and with PEO, respectively (Figure 5.39b). A decrease of the P123 content (2.5 and 5 wt%) resulted in the formation of nearly no mesopores and surface areas of only 17 or 20 $m^2 g^{-1}$ (Figure 5.39a) On the other hand, a higher content of P123 (15 wt%) leads to some mesopores, but the surface area does also decrease to 30 $m^2 g^{-1}$, compared to 60 $m^2 g^{-1}$ for the standard synthesis with 10 wt% P123. Therefore, the literature value of 10 wt% in the desired solvent was used in all further experiments with P123 as porogen.[121]

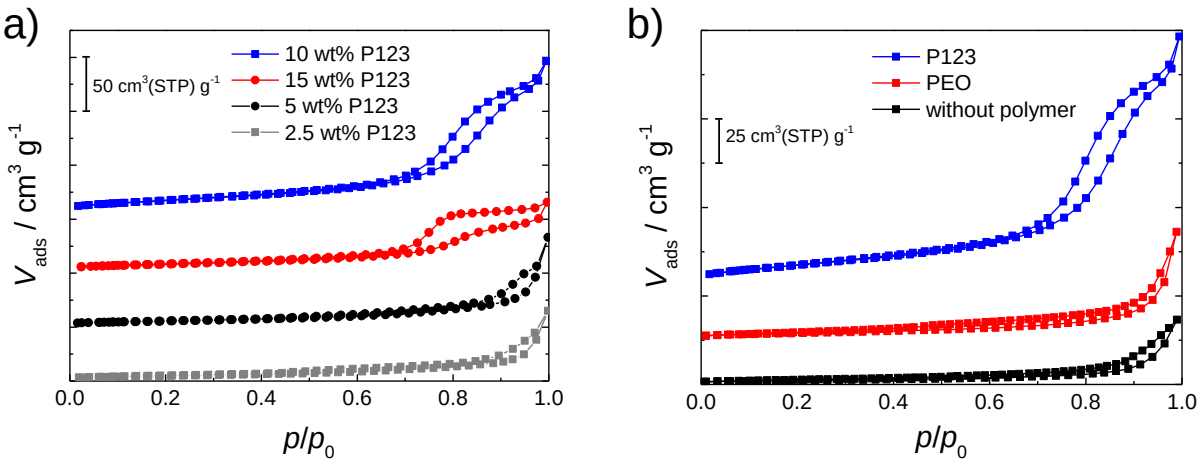

Figure 5.39: Influence of the P123 polymer on the mesoporosity: N_2 physisorption isotherms for a) different amounts of P123 in the synthesis and b) with 10 wt% P123, 10 wt% PEO or no polymer at all.

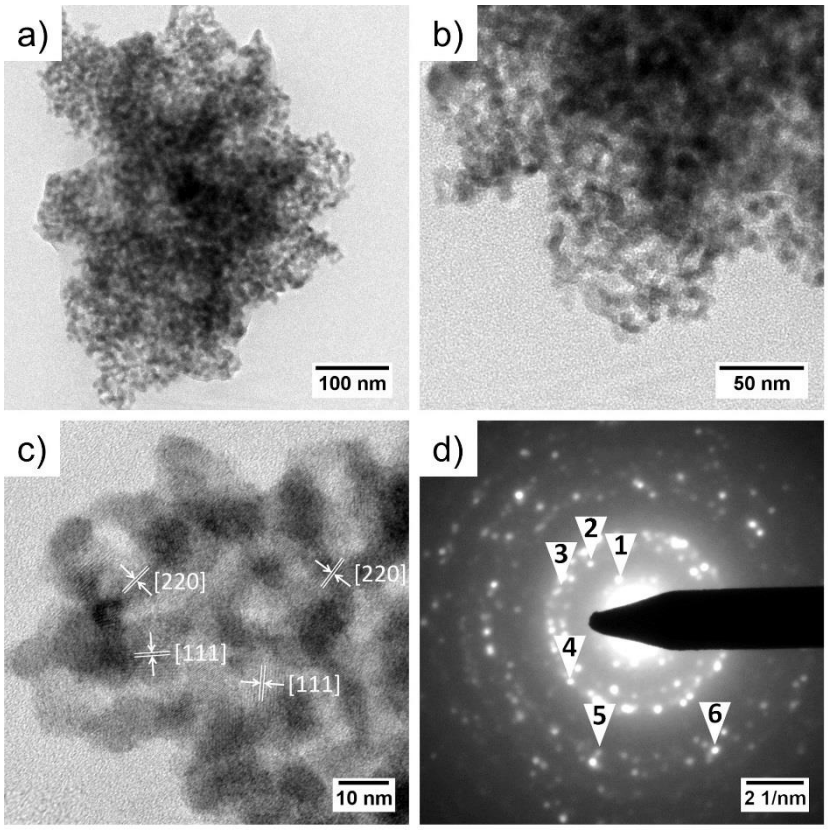

Figure 5.40: TEM images at different magnifications of mesoporous crystalline $CsTaWO_6$, calcined at 550 °C. d_{111} = 0.629 nm, d_{220} = 0.396 nm. The SAED pattern shows rings, which can be assigned to 1: (111), 2: (220), 3: (311), 4: (222), 5: (511) and 6: (440).

TEM images (Figure 5.40a-c) and selected area electron diffraction (SAED, Figure 5.40d) confirm the non-ordered but well-established mesoporous network with a high crystallinity, proved by the Debye-Scherrer ring pattern in SAED and the observable lattice planes in the

material. The band gaps of the sample was calculated to be around 3.6 eV (shown later in Figure 5.43a), which is in good agreement with literature.[30]

A detailed investigation of the oxidation states in the material was done *via* XPS measurements and resulted in oxidation states of tantalum and tungsten being +V and +VI, respectively. An overview spectrum of the P123-derived mesoporous $CsTaWO_6$ is given in Figure 5.41a, and the inset confirms that no residual chlorine from the chloride precursors is left in the material due to the absence of a Cl 2p peak between 195 and 220 eV.[256] High-resolution spectra of the two transition metals tantalum and tungsten are shown in Figure 5.41b. Fits were made using a linear background for the tantalum signal, a Tougaard-background for tungsten and a Gaussian-Lorentzian line shape (GL(30)) in both cases. Spin-orbit splitting leads to two peaks for every transition metal. The resulting energy position for tantalum Ta 4f is 25.8 eV with a splitting of 1.9 eV.[256] The tungsten signal is superimposed with two shake-up satellites of tantalum and can be deconvolved into a W 4f doublet with a splitting of 2.2 eV (35.4 and 37.6 eV) and one line of W 5d (41.0 eV), indicating +VI as the only oxidation state of for tungsten.[256–258] This confirms the results from EPR measurements after calcination at the same temperature (Figure 5.29a). The two remaining caesium and oxygen spectra of $CsTaWO_6$ are in line with this results.

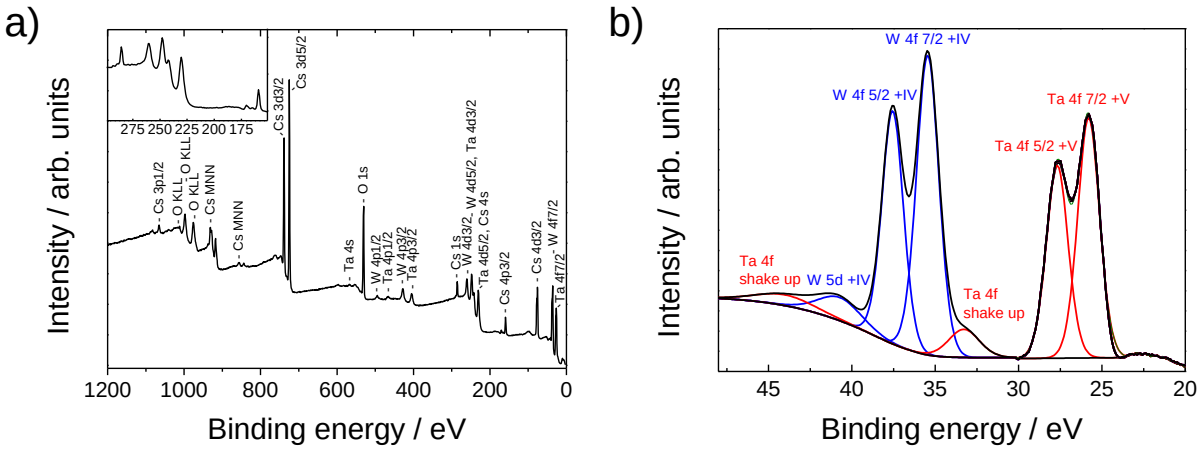

Figure 5.41: a) XPS overview spectrum for the P123-derived mesoporous $CsTaWO_6$. Inset shows the zone at which Cl 2p would occur (~ 200 eV). b) Detail spectrum for the region of the Ta 4f and W 4f orbitals.

5.2.3.2 Influence of different additives

In literature, different ways to tune the pore sizes are known, including the addition of different chemicals into the sol-gel synthesis, *e.g.* citric acid[136] and a mixture of sulfuric acid/hydrochloric acid.[177] The addition of citric acid should probably result in the formation of intermediate carbonate during calcination, strengthen the inorganic network and therefore prevent the porous structure. H_2SO_4/HCl should lead to a carbonization of the polymer matrix under heat treatment in inert gas, whereas the carbon could stabilize the pore network.

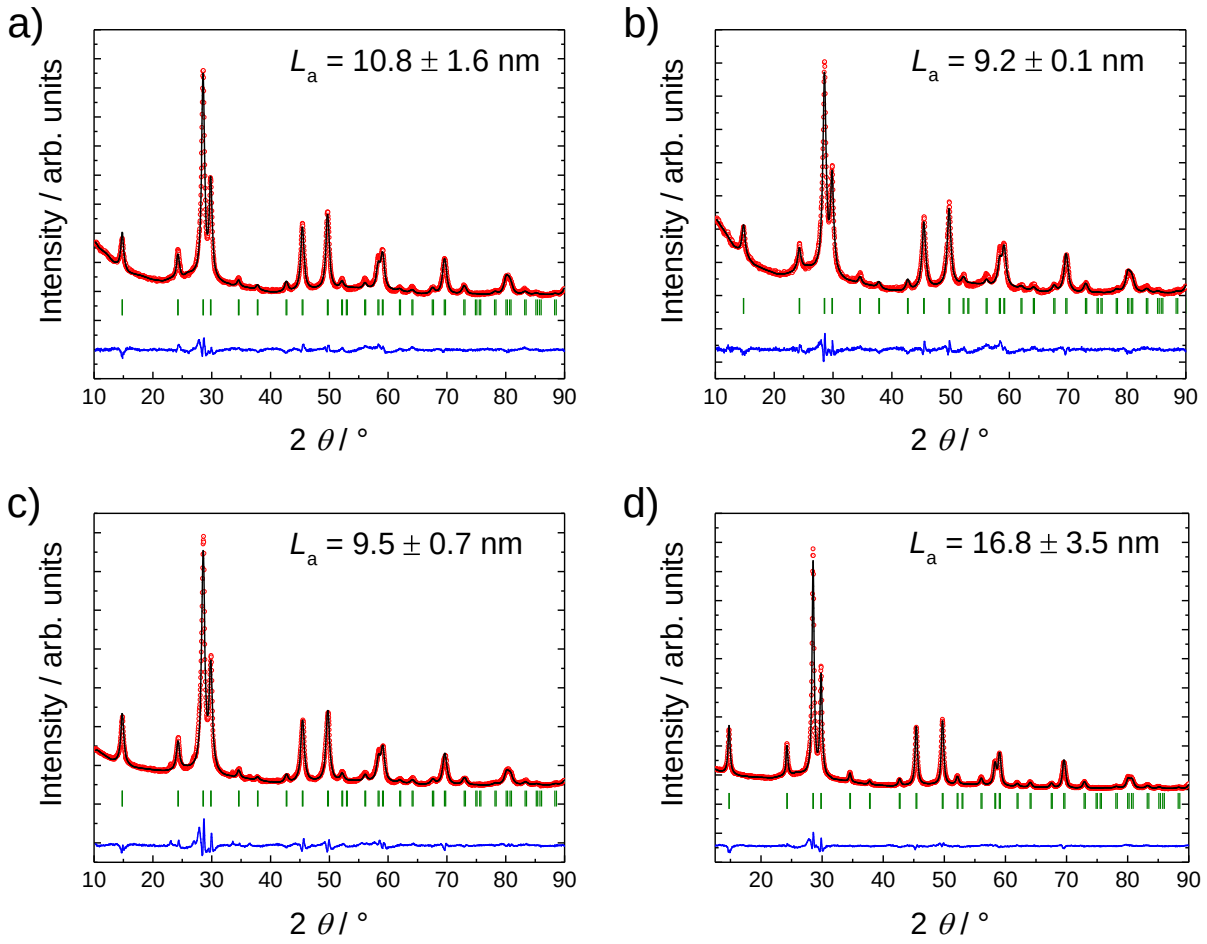

Figure 5.42: Rietveld refinements of mesoporous crystalline $CsTaWO_6$ with a) no additives, b) citric acid, c) H_2SO_4/HCl and d) without additives, but calcined at 600 °C.

Both strategies tested did not influence the crystal structure; phase-pure materials without any by-products could be obtained. Rietveld refinements indicated the crystal structure of $CsTaWO_6$ with cubic lattice (space group $Fd\bar{3}m$) and a lattice constant of $a \approx 10.37$ Å, which fits with the literature value of this compound (10.3768 Å).[33] Figure 5.42 shows the refinements of three different samples, namely the one described in the above chapter

without additives, one with citric acid and one with H_2SO_4/HCl, all calcined at 550 °C. The calculated crystallite sizes were 10.8 nm for mesoporous $CsTaWO_6$ without additives, and 9.2/9.5 nm for mesoporous $CsTaWO_6$ plus citric acid or mesoporous $CsTaWO_6$ plus H_2SO_4/HCl, respectively.

The occupation numbers of Cs, Ta, W, and O atoms in the refinements corresponds to a perfect ratio of 1:1:1:6. Therefore, no dislocation or vacancies for these elements could be detected by X-ray diffraction. Furthermore, the band gap of all three samples was unaffected (Figure 5.43a).

Table 5.5: Obtained parameters from Rietveld refinements of P123-derived mesoporous $CsTaWO_6$, synthesized with or without additives and at different temperatures.

Additive	T_{calc} **/ °C**	L_a **/ nm**	a **/ Å**	**Strain**	X^2	R_{wp} **/ %**
P123	550	10.8	10.375(0)	25.7	4.4	11.4
P123	600	16.8	10.377(2)	17.9	4.6	9.5
+ citric acid	550	9.2	10.368(9)	–*	3.6	12.3
+ H_2SO_4/HCl	550	9.5	10.369(5)	–*	9.8	12.5
+ H_2SO_4/HCl, after H_2 generation	550	9.9	10.370(4)	–*	9.7	12.4

* calculation of strain was not performed for all samples;
T_{calc} = calcination temperature, L_a = average crystallite size, a = lattice constant, χ^2 = goodness of fit, R_{wp} = weighted profile R-factor

Like for the $CsTaWO_6$ nanoparticles, spectroscopic characterization techniques were used to get an insight into possible defects, especially on the surface of mesoporous materials. Raman spectra (Figure 5.43b) confirmed phase purity and a total of nine Raman bands could be observed in the presented region from 100 to 1100 cm^{-1}. All the observed bands could be indexed according to literature (see also Table 5.2 in Section 5.1.1.2 about $CsTaWO_6$ nanoparticles).[220] The two bands corresponding to the B–O vibrations became narrow and more pronounced for the mesoporous materials compared to the non-porous reference, which could be an indication for more bulk vacancies on the B sites (Ta, W). Another remarkable observation was a blue shift of all Raman modes in mesoporous $CsTaWO_6$ compared to the positions of the bands in the non-porous materials. This effect can be

explained by the decrease of the crystallite size into the nanometer scale (9 to 11 nm, see Table 5.5) and hence a phonon confinement.[259–261] XPS measurements for the mesoporous samples including additives (not shown here) exhibit no differences compared to mesoporous $CsTaWO_6$ without any additive (Figure 5.41). Within the limit of accuracy, cation ratios of approximately 1:1:1 can be found, confirming the results from Rietveld refinements.

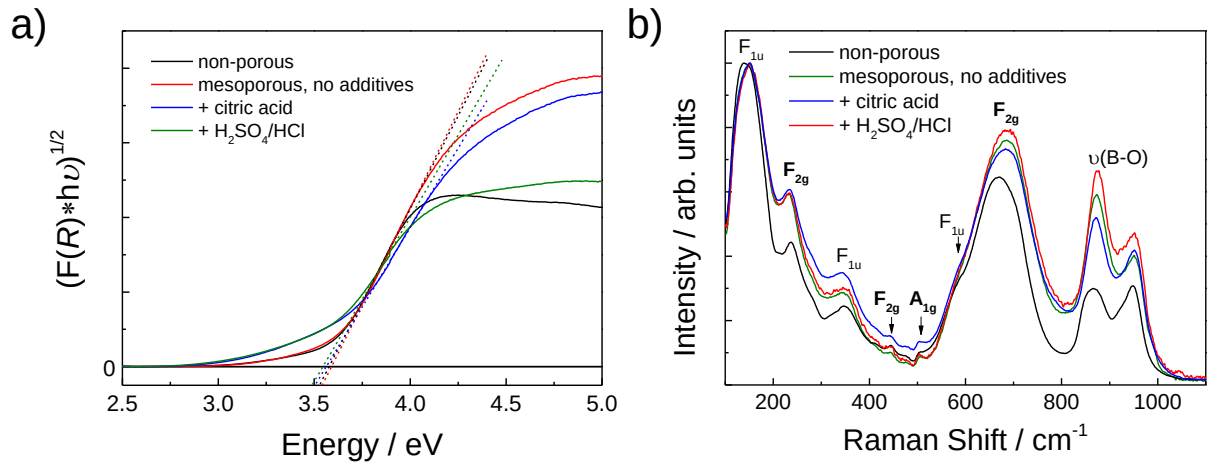

Figure 5.43: a) UV-Vis and b) Raman spectra of differently prepared mesoporous $CsTaWO_6$ powders compared to a non-porous reference, synthesized *via* citrate route.

Isotherms from N_2 physisorption and the corresponding pore size distributions are illustrated in Figure 5.44. The validity of the used NLDFT adsorption model was checked by the fitting comparison and the fitting error was below 1 % (Figure 4.2a). The addition of citric acid leads to an altering of the mesopore morphology, resulting in a narrow pore size distribution of around 5 nm and a reduced pore volume of 0.05 $cm^3\ g^{-1}$. A pore size of around 5 nm is a typical value for the used block copolymer P123, indicating that citric acid prevents the pristine pore size. The surface area slightly decreased from 60 $m^2\ g^{-1}$ for the mesoporous $CsTaWO_6$ without additives down to 47 $m^2\ g^{-1}$. On the other hand, the use of H_2SO_4/HCl as additives results in an increased surface area of 78 $m^2\ g^{-1}$, which is nearly 20 times more compared to the citrate-route material.[30] Moreover, the pore size distribution undergoes a broadening and the pore volume increased to 0.24 $cm^3\ g^{-1}$. These different influences on the pore size and surface area can be explained by the different preparation routes: when using citric acid in the synthesis, an intermediate carbonate formation can strengthen the inorganic sol-gel network before the complete removal of the template.[136] Thus, the porous network is more defined and preserved at the expected value of around 5 nm, which is visible in the pore size

distribution (Figure 5.44b). However, although the pores are getting smaller, the surface area is decreased. In contrast, a preparation with H_2SO_4/HCl as additives results in a carbonization of the polymer under the in this case used inert gas atmosphere, leading to rigid carbon in the sample.[177] That carbon affects a stabilization of the inorganic framework, whereas the carbon oxidation can leave additional voids/pores during the following calcination. This sample exhibited the largest surface area and highest pore volume for all mesoporous $CsTaWO_6$ powders prepared with P123 as porogen and dried in a climatic chamber.

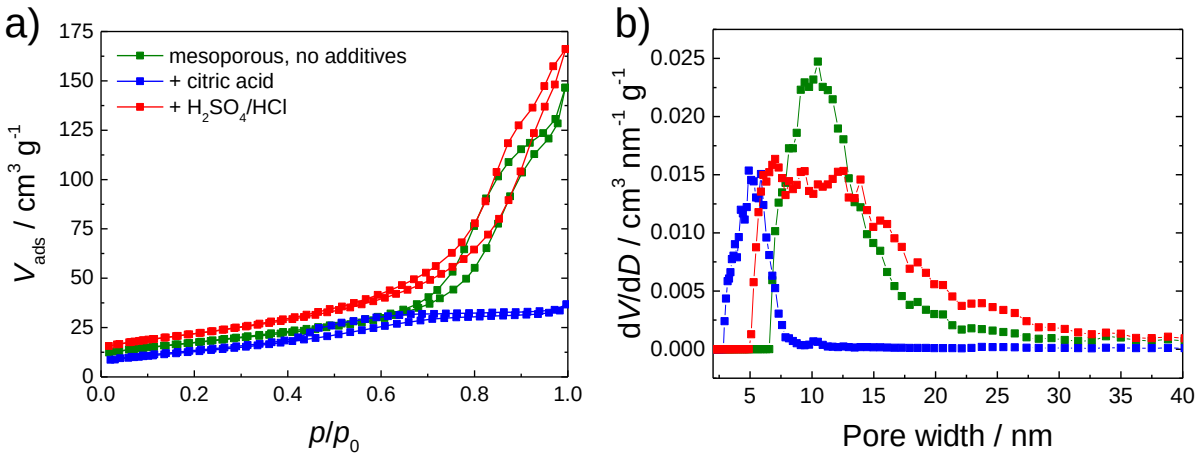

Figure 5.44: a) N_2 physisorption isotherms for mesoporous $CsTaWO_6$ without additive (green), citric acid (blue) and H_2SO_4/HCl (red); b) respective pore size distributions from NLDFT adsorption branch.

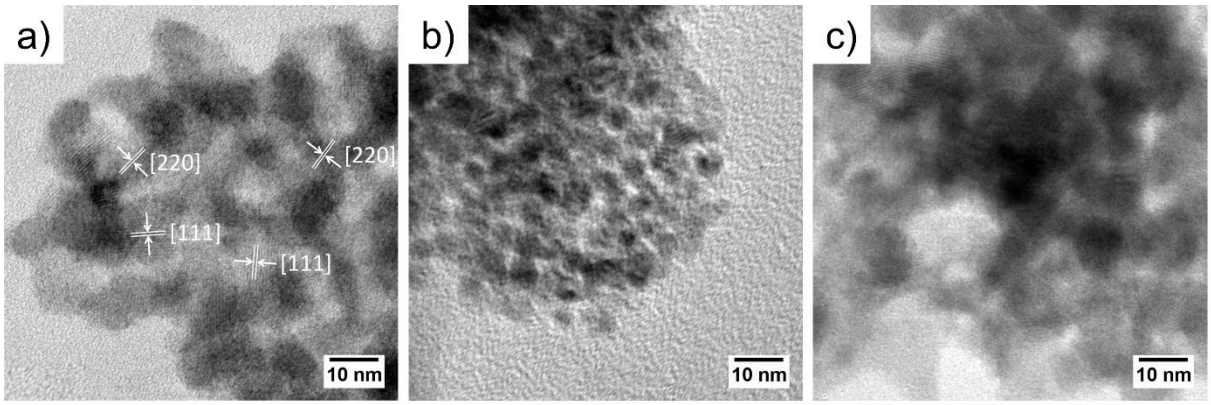

Figure 5.45: TEM images of mesoporous $CsTaWO_6$ a) without additives, b) with citric acid and c) with H_2SO_4/HCl.

TEM images of the three samples confirm the results from N_2 physisorption: mesoporous $CsTaWO_6$ without any additives shows pores with an average size of around 10 nm, while the addition of citric acid leads to much smaller pores of approximately 5 nm. The preparation

with additional H_2SO_4/HCl results in less uniform and mixed small and large pores between crystalline walls (Figure 5.45).

5.2.3.3 Photocatalytic activity

P123-derived mesoporous samples, prepared at different calcination temperatures, were tested regarding their photocatalytic activity from solar simulator irradiation (see Chapter 4.3.1). Furthermore, the three different P123-derived mesoporous $CsTaWO_6$ samples without additive, with citric acid and with a mixture of inorganic acids were compared with each other and a non-porous $CsTaWO_6$ material prepared *via* sol-gel citrate route was used as a reference, calcined at 850 °C.[30] Photocatalytic performances for three different co-catalyst loadings are summarized in Figure 5.46.

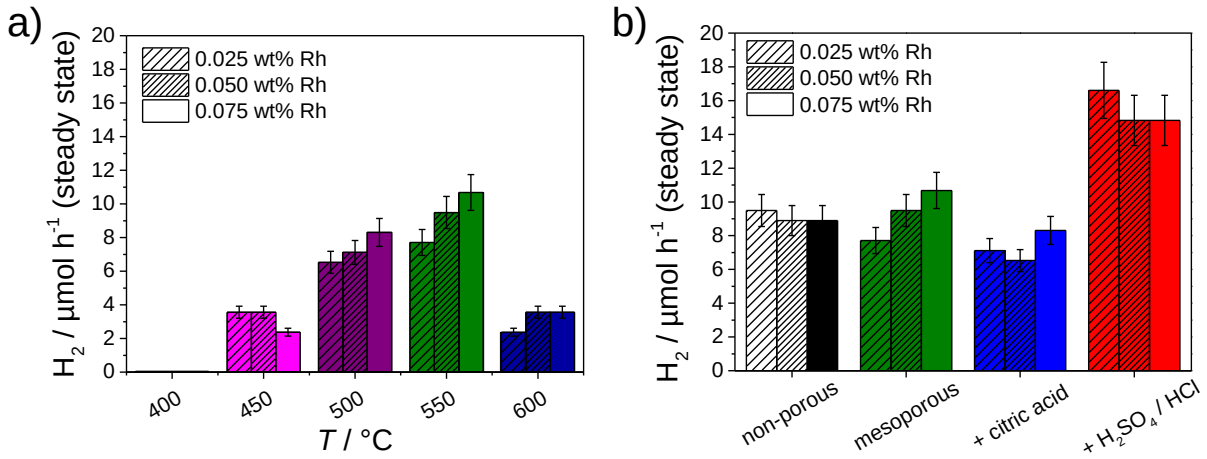

Figure 5.46: Photocatalytic hydrogen evolution from water/methanol mixtures under simulated sun light for a) P123-derived mesoporous $CsTaWO_6$, calcined at different temperatures and b) prepared with and without different additives, and compared with a non-porous reference from citrate route.

Figure 5.46a illustrates photocatalytic activity of almost all mesoporous samples with a strong dependence on the calcination temperature. The sample calcined at 400 °C does not evolve any hydrogen, although it has by far the highest BET surface area (Table 5.6). This can be explained by the missing crystallinity of the material (Figure 5.36a) and the incomplete removal of the polymer (Figure 5.34). With increasing calcination temperature, the crystallinity also increases and the remaining polymer residues are removed, leading to a rise in the activity. After reaching a maximum at 550 °C, the hydrogen evolution rates decrease for the sample calcined at the highest temperature (600 °C). Reasons can be either the breakdown of porosity and surface area in this sample, or the increasing average crystallite

size L_a (Figure 5.42d) being away from the already found optimum crystallite size of around 13 nm in $CsTaWO_6$ nanoparticles (see Chapter 5.1.1.4).

Table 5.6: Properties of P123-derived mesoporous $CsTaWO_6$, prepared at different temperatures and with different additives.

T_{calc} / °C	additive	L_a / nm	S_{BET} / $m^2\ g^{-1}$	D_p / nm	V_p / $cm^3\ g^{-1}$	H_2 / µmol h^{-1}
400	–	–	90	10	0.27	–
450	–		67	12	0.26	2.4
500	–		65	7	0.11	8.3
550	–	10.8	60	10	0.20	10.7
600	–	16.8	35	13	0.14	3.6
550	citric acid	9.2	47	5	0.05	8.3
550	H_2SO_4/HCl	9.5	78	13	0.24	14.9
citrate route	–	42	3.9	–	–	8.9

L_a = crystallite size, S_{BET} = BET surface area, D_p = average pore diameter, V_p = pore volume, H_2 = evolved hydrogen at steady state conditions with 0.075 wt% Rh as co-catalyst.

Further conclusions can be drawn from the listed properties and photocatalytic performances of the mesoporous samples in Table 5.6. First of all, the surface area does not seem to have a major influence on the photocatalytic activity, which can be seen from the samples from 400 to 550 °C, where the complete removal of polymer residues is most important. The samples calcined at 500 and 550 °C exhibit similar surface areas, comparable crystallinity and only minor residues of polymer, as it could be seen from TG-MS (Figure 5.34). Thus, other parameters have to be taken into account. The pore size distribution of the 500 °C samples is much more narrow compared to the sample calcined at 550 °C, also leading to a higher pore volume in the latter case. To exclude the factor of calcination temperature, the mesoporous $CsTaWO_6$ materials prepared with different additives, but at the same temperature, were considered. The sample prepared with the addition of citric acids shows a comparably narrow pore size distribution as the 500 °C sample without additives and showed nearly the same photocatalytic activity, confirming that a narrow pore size distribution is not beneficial. In general, a mesoporous $CsTaWO_6$ prepared with pores smaller than 10 nm gave

even lower activities than the non-porous reference sample. Therefore, one can conclude that mesopores with a size below 10 nm are too small for an efficient hydrogen generation.

Adding H_2SO_4 and HCl to the synthesis, the pore size distribution is very broad, even broader than for the sample calcined at the same temperature without additives, and slightly shifted to higher pore sizes. This material also showed the highest surface area and the best photocatalytic performance. An increase by a factor of two was observed compared to the non-porous reference or the next best mesoporous sample, prepared without the addition of additives at 550 °C. The reasons for this enhanced photocatalytic activity for the generation of hydrogen from water/methanol can be an improved mass transport of methanol into the large and less uniform pores (see also TEM images in Figure 5.45). This causes a better diffusion of the methanol into the bulk of the mesoporous powder and thus a good charge carrier separation throughout the whole photocatalyst.[103]

Summarized, the amount of evolved hydrogen increases with an increase in the median pore diameter, indicating the important aspect of methanol transport in photocatalytic hydrogen production. Marugán *et al.* could also find limited internal diffusion problems and a kinetic control of the reaction by mass transport in their work on mesoporous TiO_2.[262] In their case, a broad pore size distribution led to better performance, too. The enhancement in activity does not scale with the surface area, as it could be also seen for the $CsTaWO_6$ nanoparticles. The higher number of defects due to the lower calcination temperature compared to the non-porous reference material leads to charge carrier traps inside the material.[14] The higher defect concentration could be already assumed from Raman spectra (Figure 5.43b) and the effect will be explained later in more detail when comparing all prepared samples (see Chapter 6).

The stability of the most active mesoporous photocatalyst $CsTaWO_6$ prepared with H_2SO_4/HCl as additives was tested. Post-catalytic TEM, XRD, UV-Vis absorption and physisorption measurements after around 10 h of photocatalytic hydrogen production are illustrated in Figure 5.47. The sample is not altered by the photocatalytic reaction and still offers high crystallinity and mesoporous morphology. BET surface area and pore volume from N_2 physisorption were closed to values before the photocatalytic test reaction, being 67 $m^2\ g^{-1}$ and 0.21 $cm^3\ g^{-1}$, respectively. Slight changes are probably due to the deposition of Rh outside and inside the pore system. Small differences in the absorption spectra can be referred to the

Rh co-catalyst, even if the distribution could not be depicted from TEM images due to the low concentration of Rh.

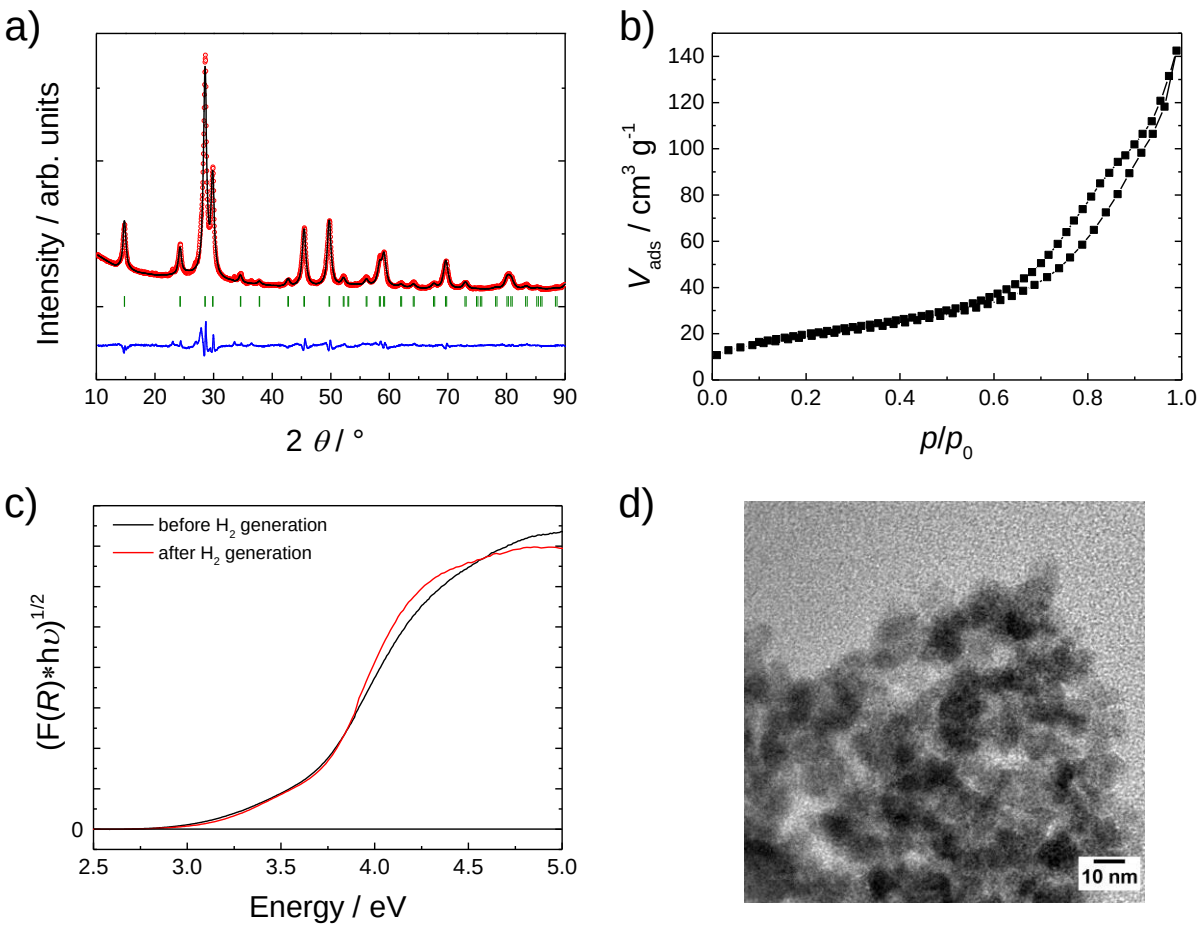

Figure 5.47: Post-catalytic characterization of P123-derived mesoporous $CsTaWO_6$ with H_2SO_4/HCl as additives: a) Rietveld refinement of the sample (parameters can be found in Table 5.5, b) N_2 physisorption isotherm, c) UV-Vis spectra before (black) and after (red) H_2 generation, and d) TEM image of the sample after photocatalysis.

5.2.4 ISO-derived mesoporous $CsTaWO_6$

5.2.4.1 Characterization and assigning the pore geometry

For the synthesis of mesoporous $CsTaWO_6$ with much larger pore sizes compared to P123, the use of ISO polymer as porogen and a drying process on a heating plate was performed. These pores are big enough to have a closer look *via* scanning electron microscopy (SEM). Figure 5.48 illustrates SEM images of different ratios of polymer to precursor with a constant amount of polymer solution (2 mL), but increasing amount of precursor solution, namely 100, 200, 400, 600, 800 and 1000 µL (Cs_2CO_3, $TaCl_5$ and WCl_6 in EtOH; see Table 3.9 in Chapter 3.2.2.2). It could be found that with smaller portions of precursor, highly ordered spherical mesopores could be obtained (Figure 5.48a-b). In contrast, increasing the amount of precursor led to the formation of a non-ordered pore system with a more undefined pore shape (Figure 5.48c-f). All samples were calcined at a temperature of 550 °C because this temperature was already found to be the optimum for the P123-derived samples. Later, also higher calcination temperatures will be tested to have a closer look insight the influence of the calcination temperature on the photocatalytic activity.

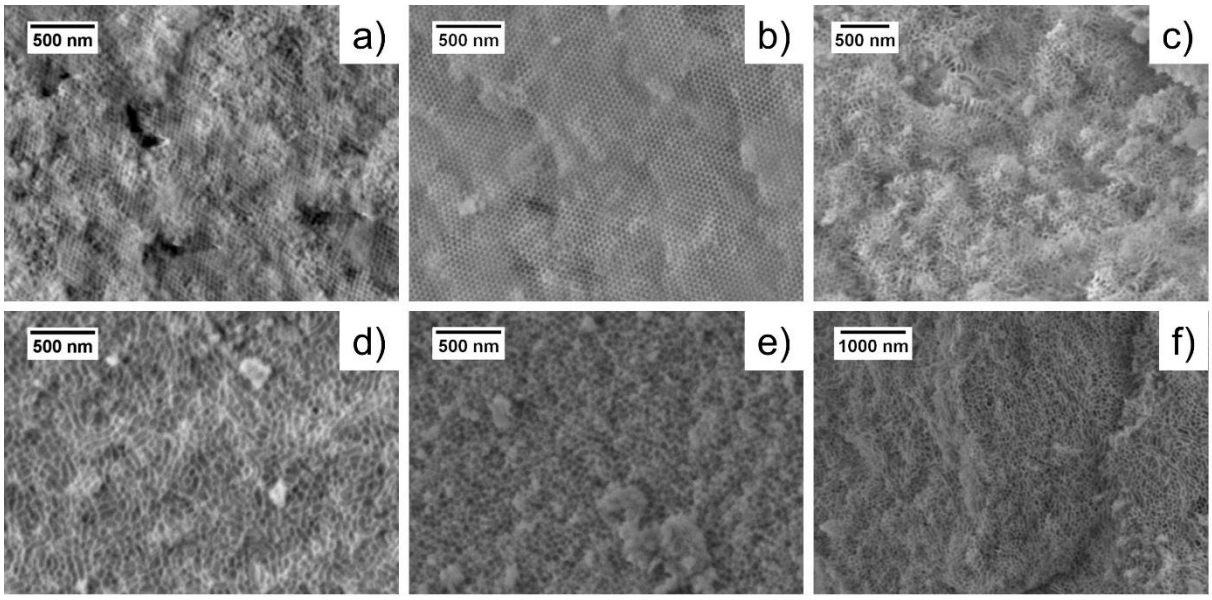

Figure 5.48: SEM images of ISO-derived mesoporous $CsTaWO_6$ with different precursor-to-polymer ratios, resulting in different pore sizes and ordered or non-ordered pore systems. The amounts of precursor solution are a) 100 µL, b) 200 µL, c) 400 µL, d) 600 µL, e) 800 µL and f) 1000 µL, whereas the amount of polymer solution was always set to 2000 µL.

A fine-tuning of the precursor-polymer-ratio showed that even a slightly higher amount of 250 µL precursor solution still results in well-ordered mesopores, raising the yield of the synthesis. SEM images of this sample with higher magnification are presented in Figure 5.49. Highly ordered domains of the mesoporous system can be seen on the entire powder surface. In SEM images, the impression of the kind of ordering is strongly depending on the facets that is caught on picture on the respective image. Figure 5.49d shows the [111] direction,[150,263] giving a view also on the pores behind the first layer, indicating a well penetrating pore system over the whole powder volume. For a more detailed discussion about the different facets in the alternating gyroid (G^A) structure, see the work of Li *et al*. from Cornell University, USA.[264]

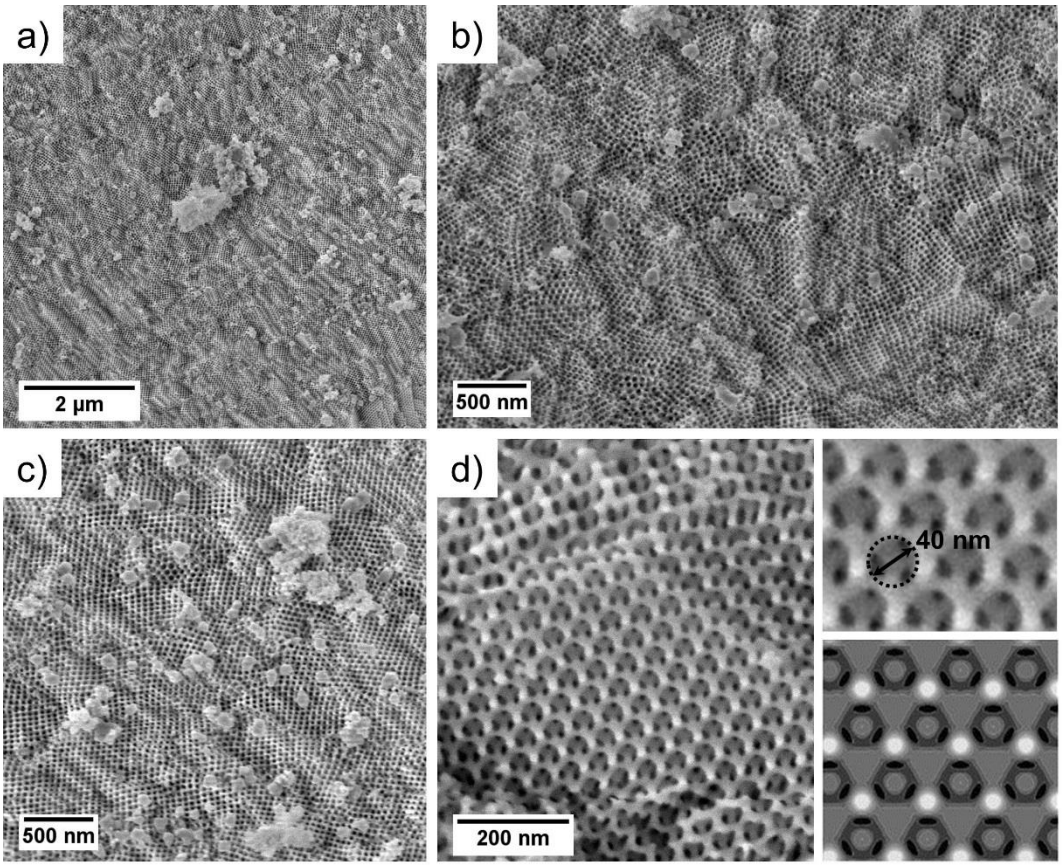

Figure 5.49: SEM images with different magnifications of ISO-derived, highly ordered mesoporous $CsTaWO_6$ (250 µL precursor solution, 2000 µL polymer solution). The insets in d) show a high magnification of the ordered $CsTaWO_6$ (top) and a simulated image of the gyroid structured pore ordering (bottom), fitting perfectly to the observed structure at the [111] direction.[263]

The average pore size from SEM images (inset Figure 5.49d) was measured to be around 40 nm. This value will be compared with other characterization techniques and confirmed later on. TEM images (Figure 5.50) also illustrate the high ordering of the pores and the pore wall can be calculated to be between 10 to 15 nm.

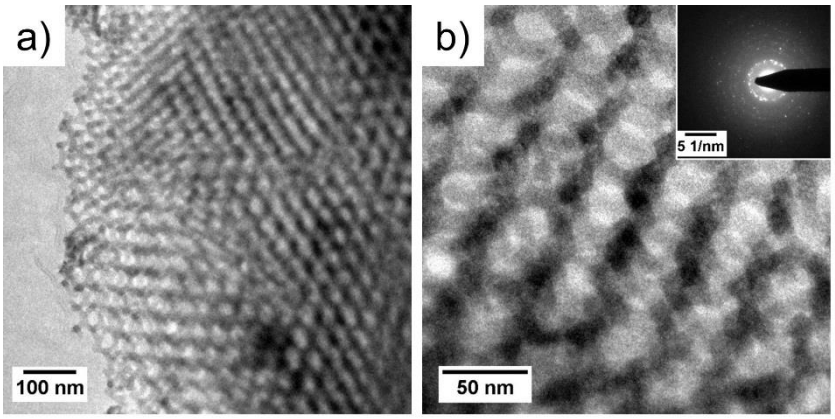

Figure 5.50: TEM images with different magnifications of ISO-derived, highly ordered mesoporous $CsTaWO_6$ (250 µL precursor solution).

Insights into the crystallinity were obtained using XRD. As it was described above, the calcination temperature was set to 550 °C due to the findings with the P123 polymer. As it can be seen from the black curve in Figure 5.51, a holding time of 30 min was too short to get a complete conversion of the precursor into the desired $CsTaWO_6$ product, visible from the high amorphous background around $2\theta = 20–35°$. A fully crystalline product was received by increasing the holding time to 1 h, both for the ordered (250 µL precursor solution, red curve) as well as for the non-ordered sample (1000 µL, blue curve). It can be already seen that the XRD pattern of the non-ordered sample has more pronounced and sharper reflections, indicating a bigger average crystallite size. These sizes will be estimated *via* Rietveld refinements for all samples in the next chapter.

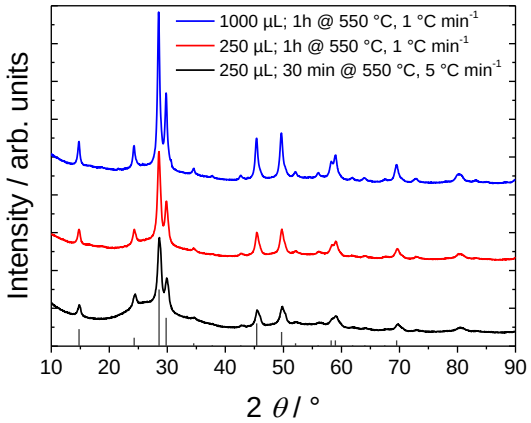

Figure 5.51: XRD patterns of ISO-derived ordered mesoporous $CsTaWO_6$ (250 µL), calcined for 30 min (black) or 1 h at 550 °C (red) and non-ordered mesoporous $CsTaWO_6$ (1000 µL), calcined for 1 h at 550 °C (blue). $CsTaWO_6$ reference card: JCPDS 25-2033.

N_2 physisorption isotherms of the three in Figure 5.51 illustrated samples showed an unique behavior. First of all, the isotherms are identical for the ordered samples with 30 min and 1 h holding time, confirming that a longer holding time just has an influence on the full conversion of the precursor, while the pore size and geometry stays the same (Figure 5.52a). Adsorption and desorption branches were analyzed using the NLDFT adsorption and equilibrium model. The validity of both models was checked by the fitting comparison and the fitting error was 1.3 % for the adsorption and 3.6 % for the equilibrium model (Figure 4.2b). The pore size distributions from NLDFT models reveal different distributions for the adsorption and desorption isotherm, indicating a minor pore blocking effect in this sample due to smaller necks compared to the main pores that have to be emptied before emptying the bigger pores. The maximum of the PSD in the ordered $CsTaWO_6$ is around 39 nm, which is in very good agreement with the value from SEM images (40 nm). The BET surface area for the ordered as well as for the non-ordered sample is 37 $m^2 g^{-1}$. So the samples have the same calcination temperature and the same surface areas, but different pore sizes and crystallite sizes, making it interesting to compare in their photocatalytic activity later on.

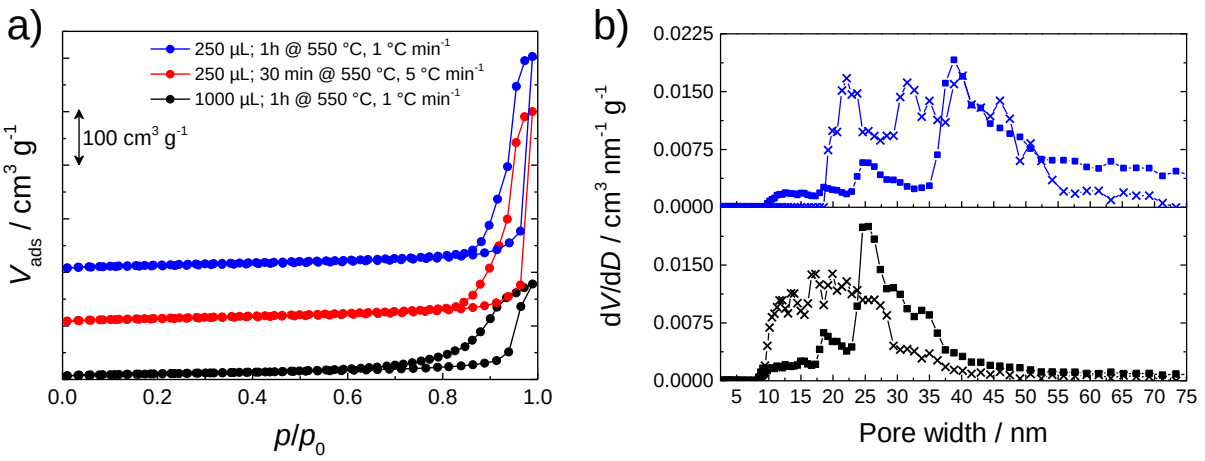

Figure 5.52: a) Corresponding N_2 physisorption isotherms of the in Figure 5.51 shown samples and b) pore size distributions from the adsorption (squares) and desorption branches (crosses) of the ordered and non-ordered $CsTaWO_6$ powders, both calcined for 1 h at 550 °C.

Up to now, the ordering of the pore system was confirmed by SEM images (Figure 5.49). A more powerful technique to get an overall view of an ordering throughout the whole sample are SAXS measurements. These measurements were performed and the results are shown in Figure 5.53 for the ordered (a) and non-ordered (b) mesoporous samples before calcination.

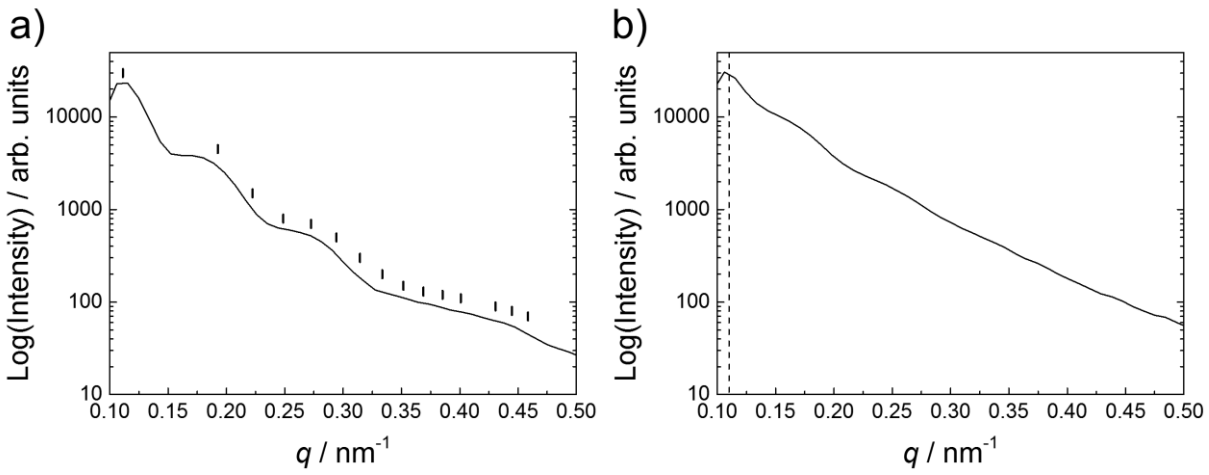

Figure 5.53: SAXS patterns of the ISO/Cs_2WOCl_5-hybrid before calcination of the a) ordered mesoporous sample (250 µL precursor solution) and b) non-ordered mesoporous sample (1000 µL).

The ordered material shows well-defined reflections, which were compared with possible ordered structures of the ISO polymer known in literature (*e.g.* gyroid, lamellar, orthorhombic, hexagonal).[22,143,150,265] The sample before calcination (Figure 5.53a) matches the best with theoretical reflections of the alternating gyroid structure, indicated by solid vertical marks. Therefore, together with the results from SEM images, an alternating gyroid structure seems to be the present ordering in the mesoporous $CsTaWO_6$.[22] However, due to the low resolution of the SAXS data, a final assignement of the mesopore architecture cannot be made. SAXS synchrotron measurements with high resolution are planned to finally solve the structure.

The non-ordered sample only shows one main reflection, whereas other reflections just appear as weak shoulders at higher *q*-values. This is one more indication for a non-ordered pore system. The first main reflection in both SAXS patterns can be consulted to estimate the average value *d* from the middle of one pore to another, including the pore walls. With the relation $q = 4\pi\sin\theta/\lambda$ and under consideration of the Bragg equation (2.13) one can get the relation[150,264,266]

$$d = \frac{2\pi}{q} \tag{5.8}$$

to calculate *d*. This parameter has a value of 80 nm and 82 nm for ordered and non-ordered samples before calcination, respectively. This value for the ISO/Cs_2WOCl_5 hybrid is considerably higher than for comparable mesoporous transition metal oxides like ISO/Nb_2O_5 (62 nm)[265] and ISO/Ta_2O_5 (53 nm).[22] Reasons for the difference can be either the smaller

crystallite sizes and therefore thinner pore walls (7 nm after 700 °C for Nb_2O_5), which also leads to a thinner wall between the pores in the non-calcined sample, or the smaller molecular weight of the ISO polymer. For the preparation of mesoporous Ta_2O_5, an ISO polymer with M_w = 69 kg mol^{-1} was used (compared to 80 kg mol^{-1} in this work), leading to smaller polymer micelles.

The estimated value from SAXS measurements for the pore-pore distance of approximately 80 nm in the ordered ISO/Cs_2WOCl_5-hybrid system before calcination could be confirmed by SEM images with high magnification (Figure 5.54). Here, the distance between two pores was found to be around 85 nm, and the pore walls have a value of 20 nm. It should be noticed that the pore-pore distance and pore walls are measured before calcination and therefore should be more correctly called a micelle-micelle distance and intermediate precursor thickness, respectively.

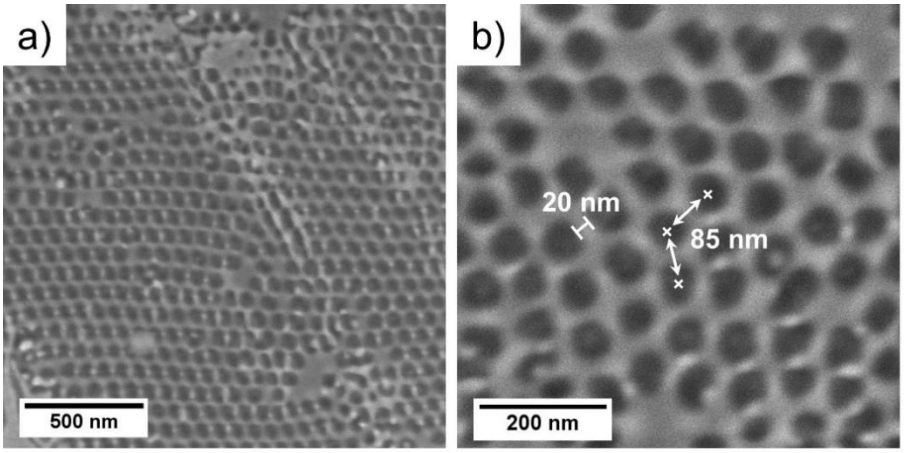

Figure 5.54: SEM images of the ISO/Cs_2WOCl_5-hybrid at two different magnifications, showing highly ordered polymer micelles.

5.2.4.2 Influence of the calcination temperature

The large pores of the ISO-derived mesoporous $CsTaWO_6$ could enable the calcination at higher temperatures without collapsing of the pore structure, as it was the case in the P123-derived samples (see Figure 5.37 and Table 5.6). Two samples with the same synthesis strategy as for the ordered and non-ordered large pore structured $CsTaWO_6$ were calcined for 1 h at 700 °C instead of 550 °C. The corresponding XRD patterns are shown in Figure 5.55. Both samples retain the defect-pyrochlore structure of $CsTaWO_6$ with narrower reflections compared to the samples calcined at 550 °C (Figure 5.51), which indicates larger crystallite sizes. Detailed investigations will be shown later in the Rietveld refinements.

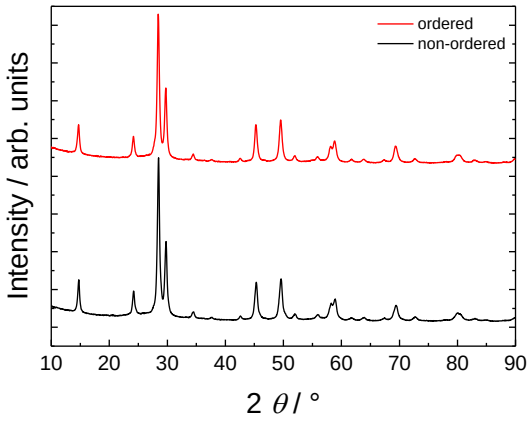

Figure 5.55: XRD patterns of ordered and non-ordered samples, both calcined for 1 h at 700 °C.

The N_2 physisorption isotherms still show a hysteresis, suggesting a preserved pore system (Figure 5.56). The pore size distributions from NLDFT absorption branches confirm this assumption. The BET surface areas and pore volumes are decreased for both the ordered and the non-ordered mesoporous $CsTaWO_6$, resulting in values of 22 $m^2 g^{-1}$, 0.26 $cm^3 g^{-1}$ and 28 $m^2 g^{-1}$, 0.23 $cm^3 g^{-1}$, respectively. The smaller surface area and higher pore volume of the ordered mesoporous sample arise from the slightly larger pores of this sample, with a maximum in the PSD at 40 nm, while the non-ordered sample reveals a maximum at around 25 nm. The decrease in surface area can be also resulting from less roughness of the mesoporous samples after heating to 700 °C. However, two maxima occur in both samples at these two positions of 25 and 40 nm.

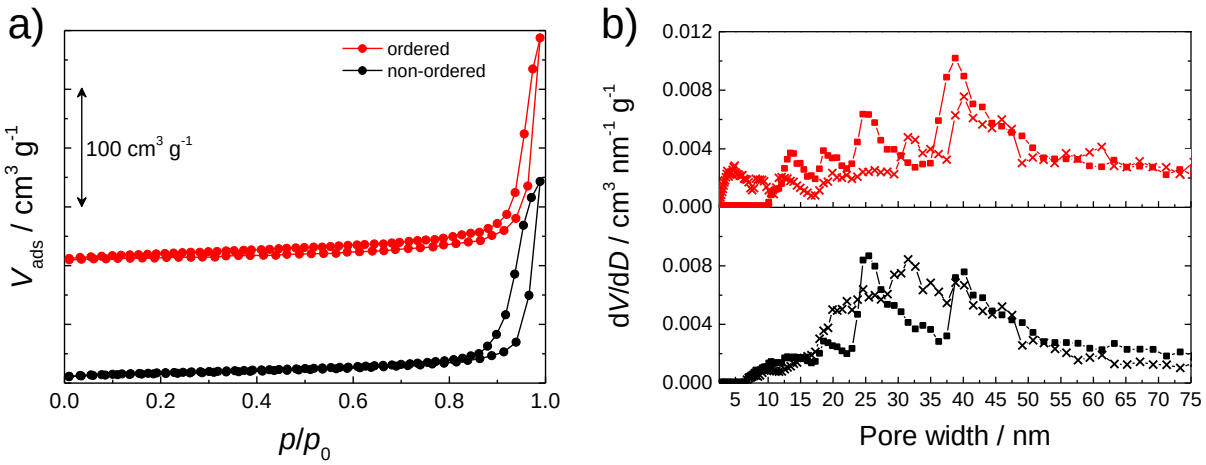

Figure 5.56: a) N_2 physisorption isotherms and b) pore size distributions from the adsorption (squares) and desorption branches (crosses) of the ordered and non-ordered $CsTaWO_6$ powders, both calcined for 1 h at 700 °C.

When comparing the TEM images of both ordered mesoporous $CsTaWO_6$ calcined at 550 and 700 °C, differences can be seen in the pore wall structure (Figure 5.57): at lower temperatures, the pore walls appear not as crystalline as in the sample calcined at a higher temperature. The pore size itself seems to stay the same, confirming the results of the N_2 physisorption data (Figure 5.56). The "darker" looking pore walls in the TEM image of the higher temperature treated sample are also an indicator of the higher crystallinity and/or of thicker pore walls and therefore a longer pass-through way for the electrons in the transmission electron microscopy, resulting in a darker color of these areas. From TEM images, the average pore wall thickness was estimated to be 10 to 15 nm and 15 to 20 nm for ISO-derived ordered mesoporous $CsTaWO_6$, calcined at 550 °C and 700 °C, respectively. The same dimension of increase in the pore wall thickness can be also seen in the average crystallite sizes from Figure 5.59 (growth of around 5−6 nm when going to higher temperatures of 700 °C).

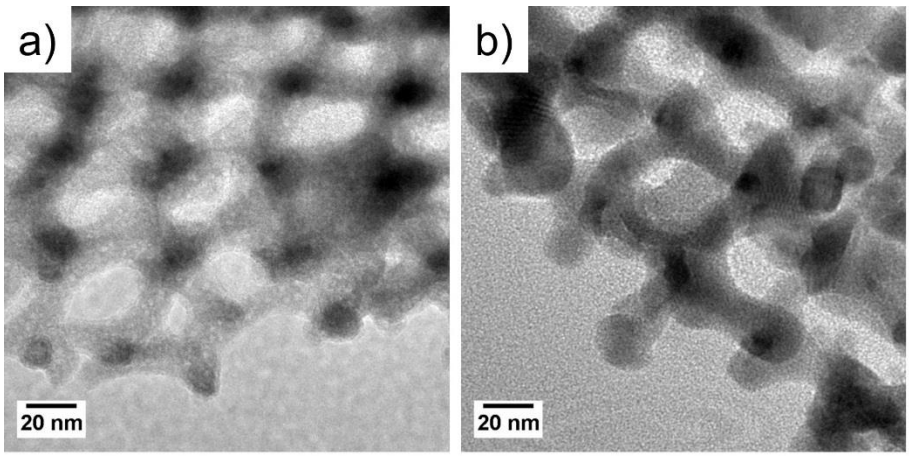

Figure 5.57: Comparison of TEM images with same magnification of ordered mesoporous $CsTaWO_6$ calcined a) for 1 h at 550 °C and b) for 1 h at 700 °C.

Besides the above described samples of ISO-derived mesoporous $CsTaWO_6$ powders, two reference materials were prepared following the same synthesis strategy, but without using any polymer in the solution. The three precursors were dissolved in the same amount of EtOH plus THF and dried under the same conditions (see Chapter 3.2.2.2). Figure 5.58 shows XRD patterns of this materials, calcined for 1 h at 550 °C or 700 °C. Unfortunately, in both cases, the obtained $CsTaWO_6$ was not totally phase-pure. An incomplete conversion of the precursor/the intermediate products (*e.g.*, Cs_2WOCl_5, amorphous condensated Ta/W oxychloride) to $CsTaWO_6$ can be seen. The reference calcined at 550 °C shows small reflections of residual CsCl from the incomplete conversion and a caesium tungsten oxide of $CsW_{1.6}O_6$

stoichiometry and cubic $Fd\bar{3}m$ crystal structure with a lattice constant of 10.213 Å. However, giving an exact composition of the caesium tungsten oxide is not possible, because a number of reference cards have the same crystal structure and positions of the reflections.

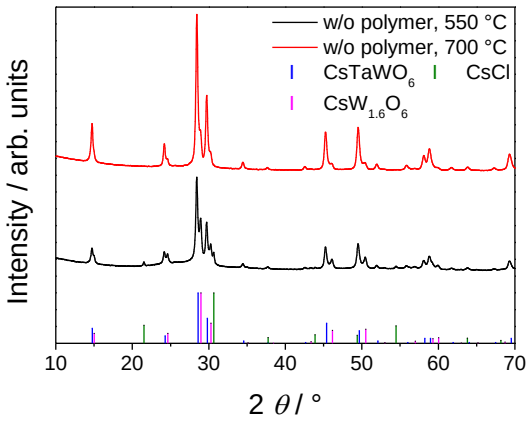

Figure 5.58: XRD patterns of $CsTaWO_6$ materials prepared according to the ISO-derived synthesis method with drying on a heating plate, but without polymer in the synthesis solution. The resulting pattern mainly consist of $CsTaWO_6$ (JCPDS 25-0233), but especially at 550 °C with impurities of $CsW_{1.6}O_6$ (JCPDS 07-1337) and CsCl (JCPDS 02-2173).

The surface areas for these materials are very low (7.7 $m^2\,g^{-1}$ for 550 °C, 3.6 $m^2\,g^{-1}$ for 700 °C). Due to the impurities in these reference materials, they could not be used as non-porous reference materials for the ISO-derived mesoporous $CsTaWO_6$. The formed by-products decrease with increasing temperature. A possible reason for the incomplete conversion at lower temperatures could be the missing porous structure in this material and thus evolving products (Cl_2, HCl, see Equations (5.5) to (5.7)) can hardly leave the material.

5.2.4.3 Crystallite sizes in ISO-derived mesoporous $CsTaWO_6$

Since Rietveld refinements were shown to be a very powerful tool for the characterization of the crystallographic properties of $CsTaWO_6$ samples (as for nanoparticles in Figure 5.3 and P123-derived mesoporous $CsTaWO_6$ in Figure 5.42),[34,35] such refinements were made for the ISO-derived mesoporous $CsTaWO_6$, too (Figure 5.59). For the samples calcined at 550 °C, different values for the average crystallite size can be found with approximately 10 and 12 nm for the ordered and non-ordered materials, respectively. Going to higher temperatures of 700 °C, the crystallite sizes are exactly the same for both samples. In all cases, the whole scattering curve can be refined perfectly and the corresponding crystallite sizes and discrepancy values are shown in Table 5.7

Table 5.7: Obtained parameters from Rietveld refinements of P123-derived mesoporous $CsTaWO_6$, synthesized with or without additives and at different temperatures.

Sample	Precursor solution / µL	T_{calc} / °C	L_a / nm	Strain	X^2	R_{wp} / %
ordered, 550	250	550	9.9	36.3	2.8	7.2
non-ordered, 550	1000	550	12.2	18.3	8.3	11.3
ordered, 700	250	700	16.3	–*	5.7	9.7
non-ordered, 700	1000	700	16.3	–*	4.3	7.9

* calculation of strain was not performed for all samples;
T_{calc} = calcination temperature, L_a = average crystallite size, χ^2 = goodness of fit, R_{wp} = weighted profile R-factor

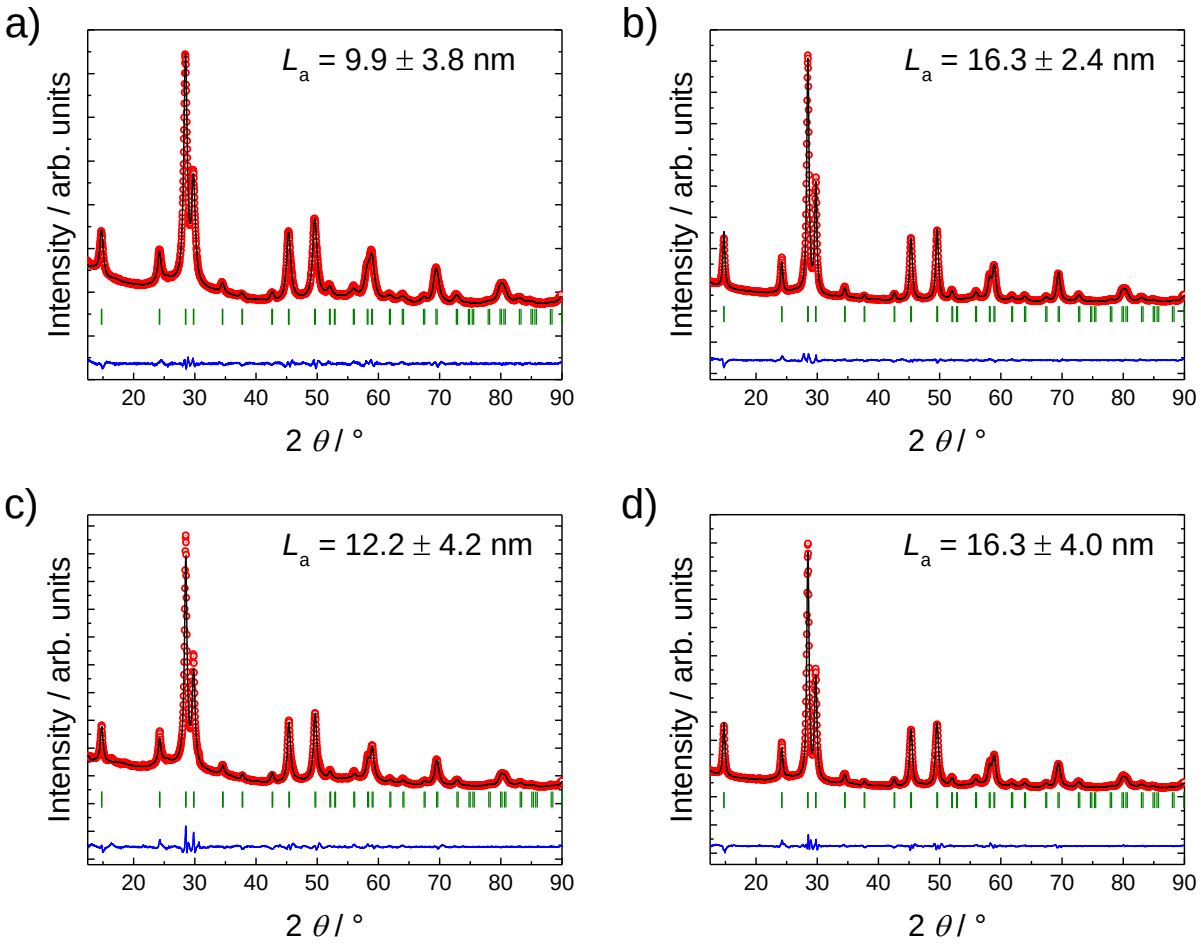

Figure 5.59: Rietveld refinements from XRD patterns of ISO-derived ordered mesoporous $CsTaWO_6$, calcined at a) 550 °C and b) 700 °C and of non-ordered mesoporous $CsTaWO_6$, calcined at c) 550 °C and d) 700 °C and their corresponding crystallite sizes L_a.

The band gaps of all materials were determined *via* Tauc-Plot from diffuse reflectance UV-Vis spectroscopy and illustrated in Figure 5.60a, all having a band gap of around 3.6 eV. This represents the same value as for the P123-derived mesoporous samples (Figure 5.43) or $CsTaWO_6$ reference materials.[30] Raman spectra of all samples, even the samples without polymer, always consist of nine different Raman modes, as they were described in Table 5.2. No remarkable differences between the calcination temperatures or ordered and non-ordered materials can be seen (Figure 5.60b). However, *e.g.* CsCl impurities cannot be seen in Raman spectroscopy because the solid salt does not have any Raman active modes.[219]

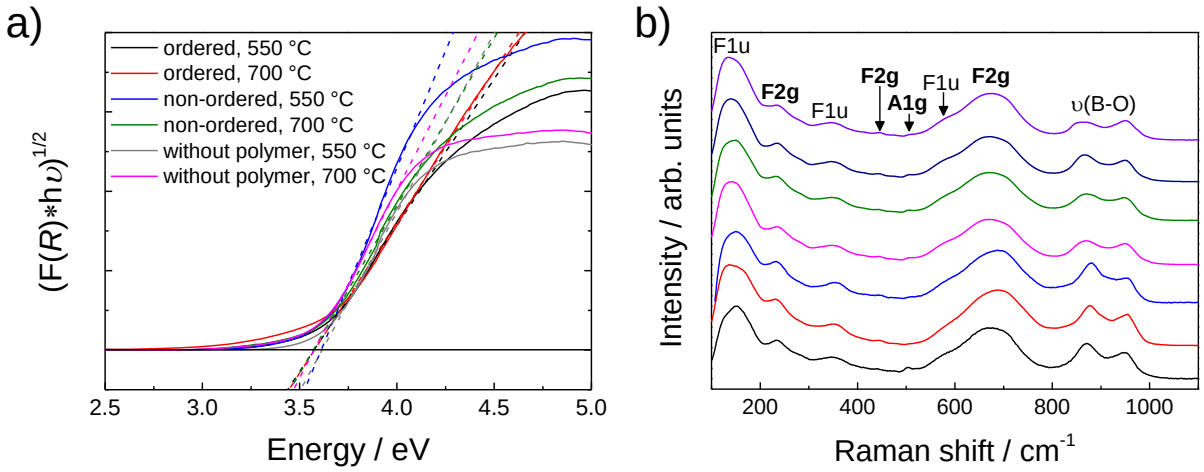

Figure 5.60: a) UV-Vis and b) Raman spectra of ISO-derived mesoporous $CsTaWO_6$ with ordered and non-ordered pore system, calcined at two different temperatures and reference samples with calcination steps at the same temperatures, but without ISO polymer (non-porous references).

A comparison of the most important properties of the ISO-derived mesoporous samples plus a reference material *via* citrate route is given in Table 5.8.

Table 5.8: Properties of ordered and non-ordered ISO-derived mesoporous $CsTaWO_6$, with a reference material prepared *via* citrate route.

Sample	Precursor solution / µL	T_{calc} / °C	L_a / nm	S_{BET} / $m^2\ g^{-1}$	D_p (NLDFT) /nm	V_p / $cm^3\ g^{-1}$
ordered, 550	250	550	10	37	39	0.39
non-ordered, 550	1000	550	12	37	25	0.26
ordered, 700	250	700	16	22	39	0.26
non-ordered, 700	1000	700	16	28	25/40	0.23
sol-gel citrate route	non-porous ref.	850	42	3.9	–	–

T_{calc} = calcination temperature, L_a = average crystallite size, S_{BET} = BET surface area, D_p = average pore diameter, V_p = pore volume.

5.2.4.4 Photocatalytic activity

The photocatalytic performance was measured under UV light irradiation (Chapter 4.3.2). References from citrate route and solid state reaction were also taken into account when comparing the photocatalytic activities. Rh as co-catalyst was stepwise added until the hydrogen rates did not increase remarkably any more. The results of the hydrogen production activities are shown in Figure 5.61 for reference materials (citrate route, SSR, mesoporous route, 13 nm $CsTaWO_6$ nanoparticles) and the ordered and non-ordered samples, calcined at 550 °C or 700 °C. It can be clearly seen that the calcination temperature has a strong influence on the H_2 evolution rates: the samples tempered at lower temperature (550 °C) always exhibit higher rates compared to their direct equivalent, calcined at a higher temperature (700 °C). This is the case although the pore sizes for ordered and non-ordered samples do not change dramatically and BET surface areas are also decreasing not as strong as the activity decreases. Besides this smaller effect of the decreasing surface area on the evolution rates, the main reason for the lower activities seems to be the crystallite size. When comparing the crystallite sizes L_a of the mesoporous materials with the highest activity (Table 5.8), it can be seen that L_a is in the same region as for the best performing $CsTaWO_6$ nanoparticles, which is around

13 nm. This once again indicates that the crystallite size has the major influence on the photocatalytic activity and not the surface area of the investigated material.

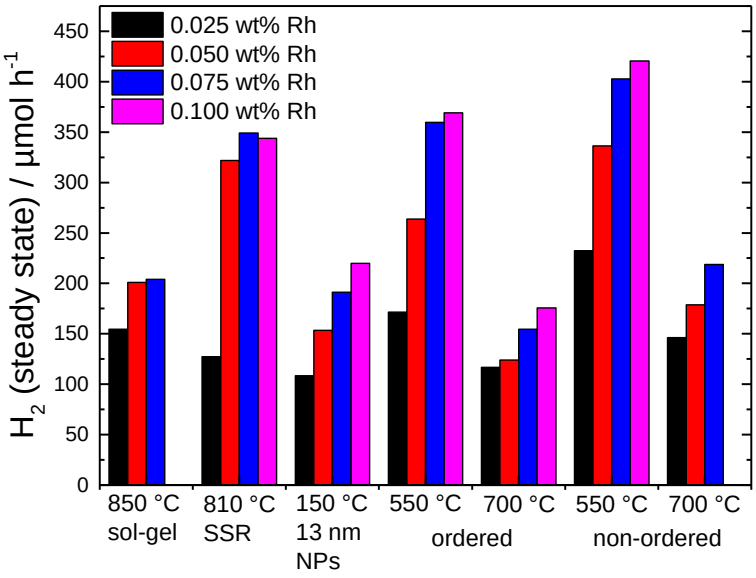

Figure 5.61. Photocatalytic hydrogen production under UV light of ISO-derived mesoporous $CsTaWO_6$ compared to different reference materials.

Another remarkable result of photocatalytic activity studies on the ISO-derived mesoporous $CsTaWO_6$ can be found in the influence of the pore ordering. The obtained hydrogen evolution rates for the highly ordered mesoporous samples with two different calcination temperatures are in both cases slightly lower compared to results for the non-ordered mesoporous materials. This leads to the conclusion that a pore ordering does not have any positive influence on the activity of a photocatalyst.

It is also interesting to see that samples tested under UV light show a different behavior regarding the loading with co-catalyst. Under solar simulator irradiation, the smallest amounts of Rhodium (0.025 wt%) showed the best performances (Figure 5.15 and Figure 5.46), whereas under UV light, a loading of 0.075 wt% was the most active ($CsTaWO_6$ *via* SSR and citrate route) or the activity even slightly increases with further addition of Rh, as for the mesoporous samples. This can be an evidence for 1) materials with a high surface area need comparably more co-catalyst and 2) that the higher number of excited electrons due to the more intensive light irradiation of the UV lamp causes the necessity of more active sites of the co-catalyst to get a migration of all charge carriers to the surface.

5.2.5 Continuative experiments

5.2.5.1 Preparation on a heating plate with P123 as porogen

Due to the successful synthesis of ISO-derived mesoporous $CsTaWO_6$ under a glass dome on a heating plate, the same synthesis strategy was carried out with P123 as porogen instead of the ISO polymer. The procedure described in Chapter 3.2.2.2 stayed exactly the same; only the ISO polymer was replaced by the P123 polymer (conc. 10 wt% in EtOH, THF). As at the beginning of the already shown results for the P123 derived mesoporous $CsTaWO_6$ prepared in a climatic chamber and ISO-derived under a glass dome, the precursor-to-polymer ratio was changed at first. Different ratios led to the in Figure 5.62 shown N_2 physisorption isotherms and corresponding pore size distributions.

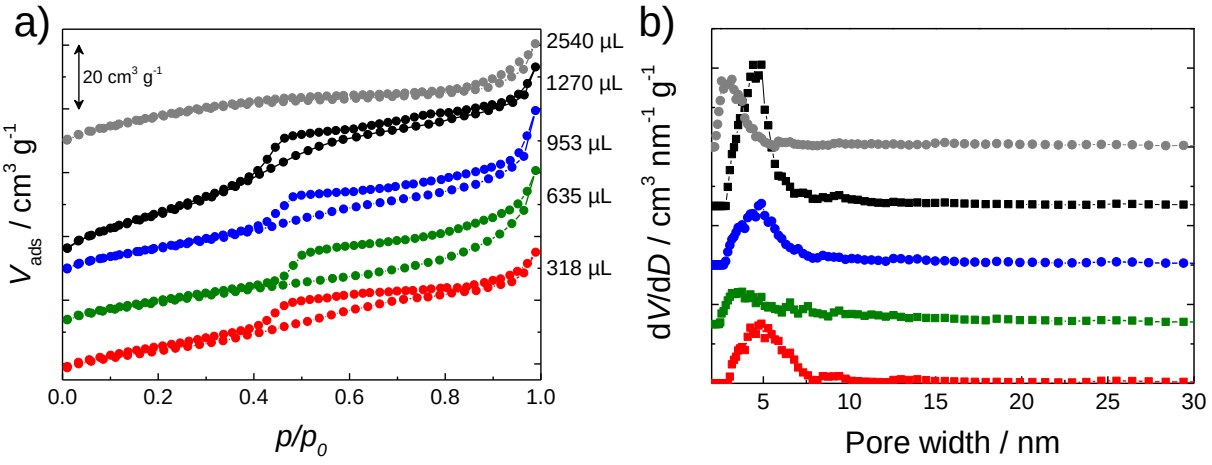

Figure 5.62: a) N_2 physisorption isotherms and b) corresponding NLDFT pore size distributions of P123-derived mesoporous $CsTaWO_6$, dried on a heating plate under a glass dome aperture.

It can be clearly seen that this synthesis procedure resulted in highly porous materials when using volumes of the precursor solution from 318 to 1270 µL, whereas a higher amount led to a less porous material and a decreasing BET surface area (see Figure 5.63a). The highest surface area of around 102 $m^2 g^{-1}$ and a pore size of 5 nm in average can be obtained with 1270 µL of precursor solution. This value of the pore size is the typical one for a preserved pore formation with P123 and without a collapse of the pore system. Corresponding TEM images are shown in Figure 5.63b and confirm a highly mesoporous $CsTaWO_6$ with an average pore size of 5 nm.

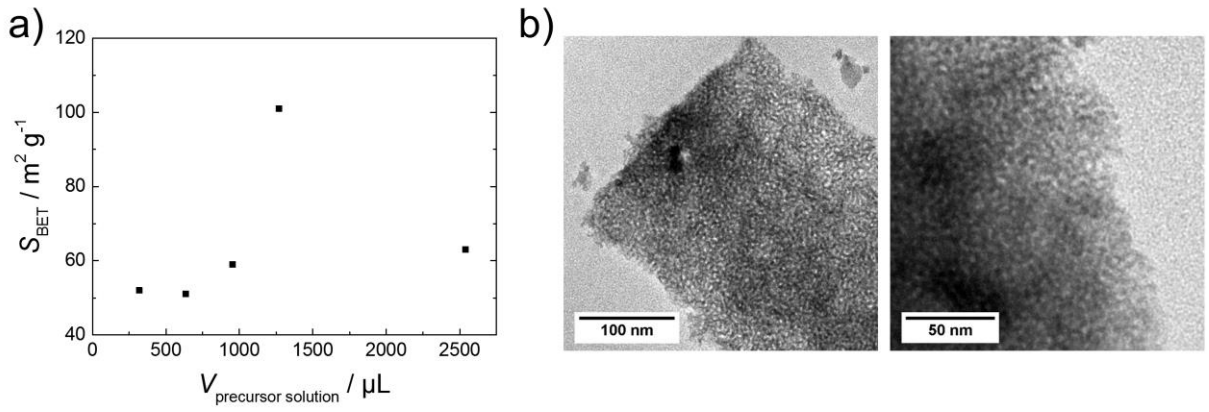

Figure 5.63: a) Dependence of the BET surface area from the amount of precursor solution in the final precursor/polymer-solution and b) TEM images of P123-derived mesoporous $CsTWO_6$ with the highest surface area (1270 µL precursor solution), dried on a heating plate.

However, the crystallinity of the as described synthesized mesoporous $CsTaWO_6$ is still a problem, as it can be seen from XRD measurements (Figure 5.64a). The "normal" calcination procedure with a heating rate of 5 °C min^{-1} for P123-derived samples results in a highly mesoporous material with high surface are (Figure 5.64b), but an amorphous background remains in the XRD pattern. Going to slower heating rates and longer calcination times (with 1 °C min^{-1} to 550 °C for 1 h, as for the ISO-derived materials), the mesoporous $CsTaWO_6$ product is totally crystalline, but the porous structure disappears nearly completely. The differences in the required calcination time between the P123-derived mesoporous $CsTaWO_6$ dried in a climatic chamber and on a heating plate can be the thicker film in the latter case. The obtained pellet after the drying steps on the heating plate and under vacuum (inset in Figure 5.29a) has a thickness of a few millimeter (~ 3 mm), whereas after drying on a Petri dish in the climatic chamber, a fine powder is obtained. During calcination, these two different dimensions can lead to higher calcination times for the pellet to remove all the polymer residues and get a complete crystallization, while, in the case of P123 as porogen, the pore structure can collapse during that process.

So there are different calcination times and heating rates necessary to get a mesoporous product, which is at the same time highly crystalline for the P123-derived samples in a Petri dish, P123-derived samples in a PTFE cup and ISO-derived samples in a PTFE cup. P123-derived mesoporous $CsTaWO_6$ just needs 30 min at 550 °C with a heating rate of 5 °C min^{-1}. At such fast calcination conditions, P123 is a good porogen to form a highly porous product, as it can

be seen in the results of Chapter 5.2.1 and 5.2.3. Using the same synthesis in a PFTE cup results in a much thicker tablet of the P123/Cs_2WOCl_5 hybrid before calcination. To get a fully crystalline product and at the same time a full removal of the polymer, this higher thickness makes it necessary to go to lower heating rates and a longer holding time of 1 °C min^{-1} and 1 h, respectively. However, these low calcination conditions lead to an already composed P123 polymer and therefore a non-preserved pore structure in Figure 5.64. On the other hand, the much more stable ISO polymer can preserve the pore system even with a high ordering at this temperature, as it was shown in Figure 5.49 and Figure 5.50.

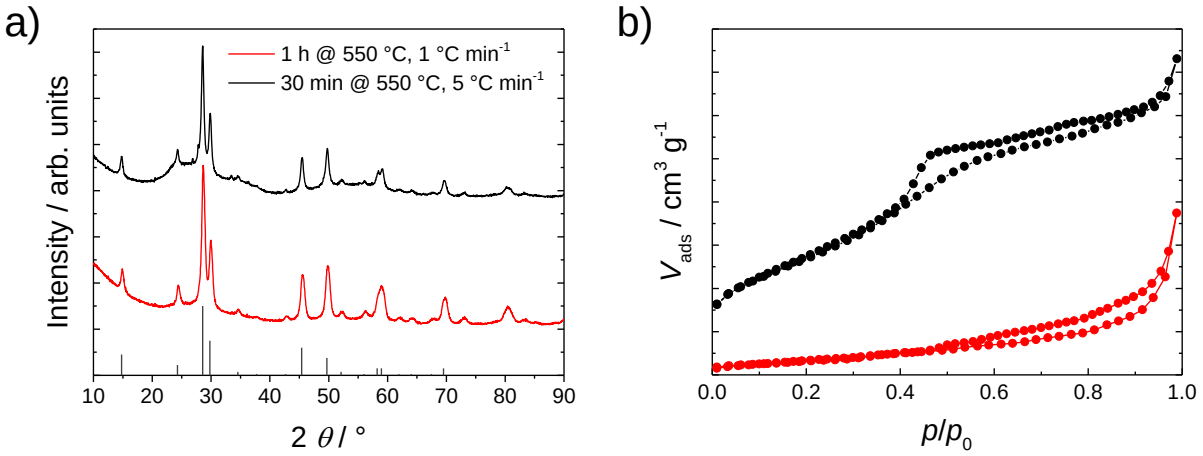

Figure 5.64: a) XRD patterns of P123-derived mesoporous $CsTaWO_6$ with two different calcination programs, prepared on a heating plate (reference card: JCPDS 25-2033) and b) corresponding N_2 physisorption isotherms of the same samples.

5.2.5.2 Preparation on a heating plate with PIB-PEO as porogen

Another polymer that should be more stable and therefore further preserve the pore system is the PIB-PEO block copolymer. Once again, different precursor-to-polymer ratios were tested and results of XRD and N_2 physisorption are shown in Figure 5.65.

Highly mesoporous $CsTaWO_6$ with an average pore size of around 10 nm and surface areas of 37, 64 and 65 m^2 g^{-1} occurred with 200, 400 and 600 µL of precursor solution, respectively (Figure 5.66a). The pore size fits quite well with pore sizes reported in literature for a PIB-PEO polymer with the same molecular weight as used in this work.[153] However, for the synthesis with the more stable PIB-PEO polymer, no phase-pure crystalline $CsTaWO_6$ could be obtained due to less homogenous mixture of precursor and polymer solution. Thus, maybe a change in

the solvents for a complete solvation of the PIB-PEO polymer and the precursor at the same time could lead to better results (*e.g.* a mixture of ethanol and 2-methoxyethanol).[153]

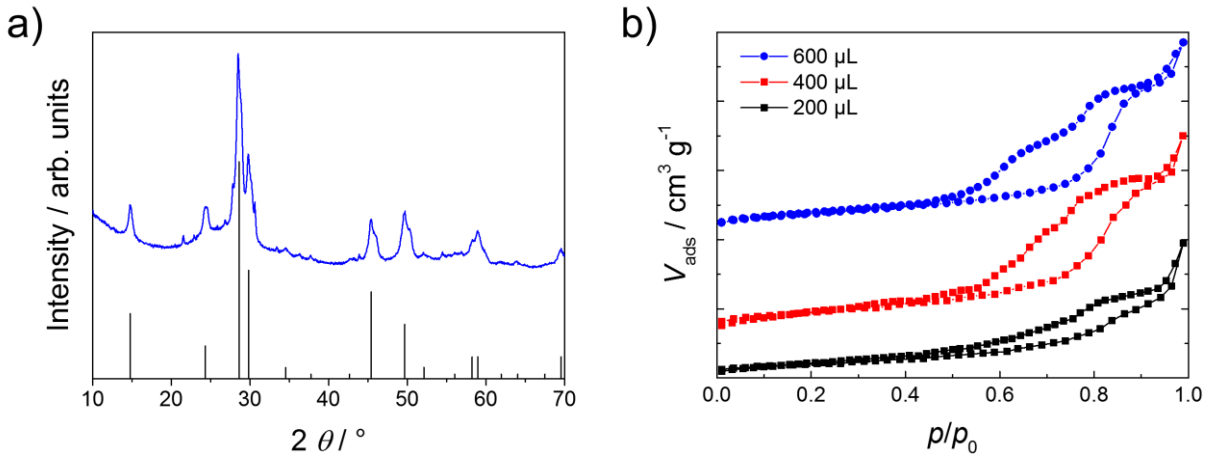

Figure 5.65: XRD pattern of one sample of the PIB-PEO-derived mesoporous $CsTaWO_6$ (600 µL), showing an amorphous background and small reflections from by-products (reference card: JCPDS 25-2033); b) N_2 physisorption isotherms of PIB-PEO-derived mesoporous $CsTaWO_6$ samples, with three different precursor ratios and constant polymer amount.

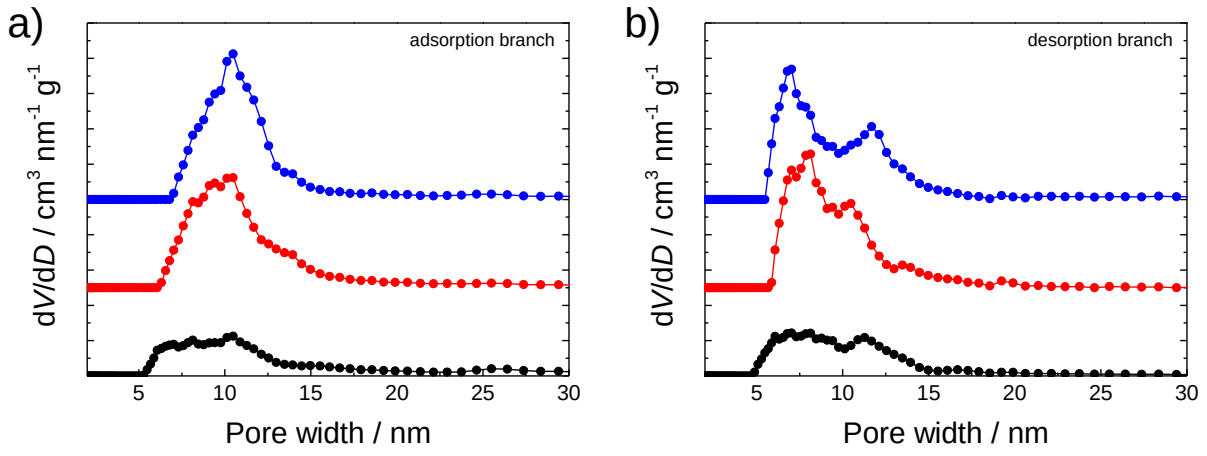

Figure 5.66: NLDFT pore size distributions of PIB-PEO-derived mesoporous $CsTaWO_6$ samples, with three different precursor ratios and constant polymer amount: a) adsorption branch and b) desorption branch.

5.2.5.3 P123-derived mesoporous $KTaWO_6$

After the experiments on mesoporous $CsTaWO_6$, another defect-pyrochlore structured material should be tested for its ability to be synthesized with a mesoporous structure. $KTaWO_6$ was chosen due to two reasons: first, the use of potassium instead of caesium would create a much cheaper material due to its lower cost. Furthermore, the substitution of the A

cation in the general formula $ABB'O_6$ should lead to less synthetic problems compared to the replacement of Ta or W, as it was the case in the preparation of $CsNbWO_6$ and $CsTaMoO_6$ nanoparticles (Chapter 5.1.2). In best case, the potassium cation does not affect the whole process significantly. For the synthesis of mesoporous $KTaWO_6$, potassium acetate (KOAc) was used instead of Cs_2CO_3 in the standard synthesis. XRD patterns of the obtained P123/$KTaWO_6$ hybrid and after calcination to a mesoporous $KTaWO_6$ are shown in Figure 5.67a. Interestingly, the hybrid before calcination is just amorphous without any preformed crystalline oxychlorides as in the case of the synthesis of mesoporous $CsTaWO_6$ (Chapter 5.2.2). After calcination for 30 min at 550 °C, the desired $KTaWO_6$ phase was obtained, indicated by the same reflections as the reference card no. 18-1571.

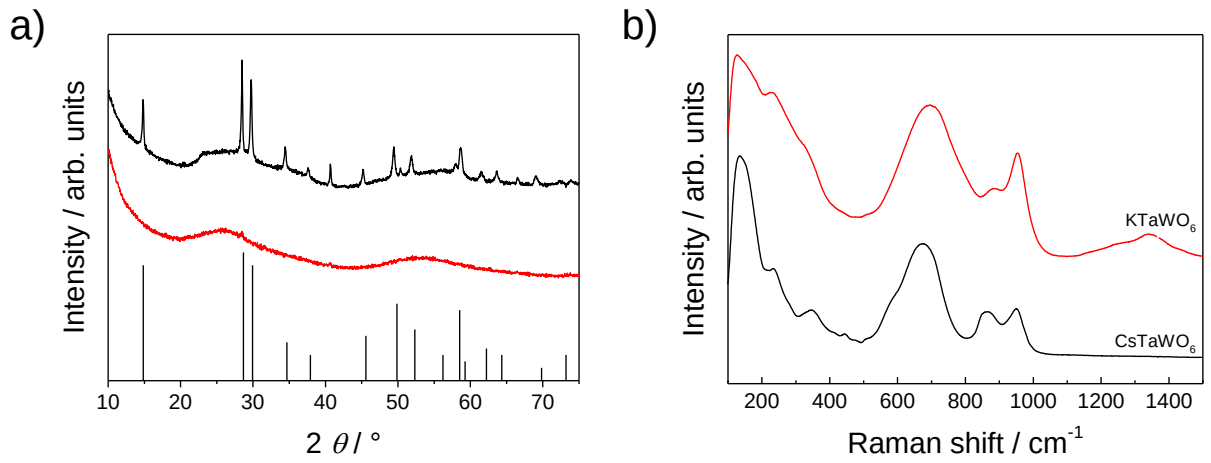

Figure 5.67: a) XRD pattern of the P123/$KTaWO_6$-hybrid (red) and of mesoporous $KTaWO_6$ after calcination for 30 min at 550 °C (black; reference card: JCPDS 25-0684) and b) Raman spectrum of the mesoporous $KTaWO_6$ after calcination and a $CsTaWO_6$ reference spectrum. Bands fit perfectly to the literature values for $KTaWO_6$.[267] The band(s) at 1300-1400 cm^{-1} can be assigned to sp^3-hybridized carbon (residual polymer/polymer decomposition products).[268]

However, an amorphous background can be seen in the XRD pattern at the same positions as in the P123/$KTaWO_6$-hybrid before calcination ($2\theta \approx 20–30°$ and 50–60°), indicating an incomplete conversion of the precursor and/or an incomplete removal of the polymer. From Raman spectra (Figure 5.67b), the same bands as for the $CsTaWO_6$ reference material with the same crystal structure can be seen, just with differing intensities. This was predicted and shown in literature.[267] A broad band at higher wavenumbers of around 1300–1400 cm^{-1} can be assigned to residual organic waste from an incomplete polymer removal.[268]

Nitrogen physisorption was recorded and the results of the isotherms and the pore size distributions are illustrated in Figure 5.68. Also for this compound, a highly mesoporous material could be obtained with a pore size of around 7 nm and a BET surface area of 72 $m^2 g^{-1}$.

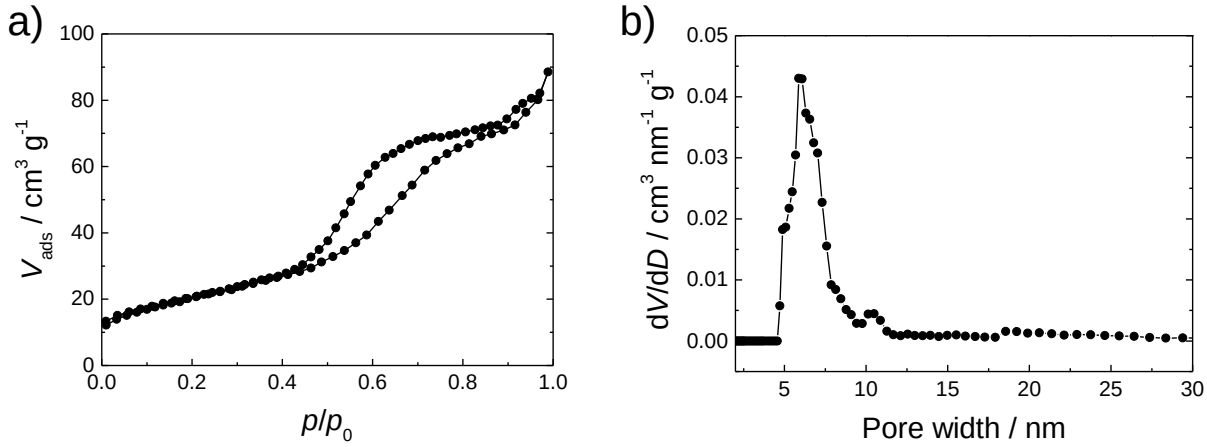

Figure 5.68: a) N_2 physisorption isotherms and b) corresponding NLDFT adsorption model pore size distribution of P123-derived mesoporous $KTaWO_6$, dried on a heating plate under a glass dome.

If compared with mesoporous $CsTaWO_6$, treated at the same conditions (Figure 5.62), it can be seen that the average pore size in mesoporous $KTaWO_6$ is too large for a perfectly preserved P123-derived pore structure. Therefore, probably a longer heating time at a lower calcination temperature (~ 500 °C) would lead to a mesoporous $KTaWO_6$ with preserved pore size of around 5 nm, a high surface area and a total crystalline product due to complete removal of the polymer. Furthermore, the intensities of the reflections in Figure 5.67 are already very sharp at 550 °C, indicating a too high crystallite size, which can be also a reason for the beginning collapse of the pore system. Also this problem could be solved when going to lower calcination temperatures.

5.3 Conclusion

The preparation of $CsTaWO_6$ nanoparticles with a number of different particle sizes offered the conclusion of an optimum particle size (optimum crystallite size) for this compound at around 13 nm. This low-temperature hydrothermal synthesis of nanoparticles was the first reported for a quaternary photocatalyst system and the first report of a quantum size effect with decreasing crystallite size.[34]

It could be shown that the preparation of mesoporous defect-pyrochlore structured materials ($CsTaWO_6$ and $KTaWO_6$) with high surface areas and different pores sizes is possible. The preservation of the porous morphology is the major problem in the synthesis of these complex photocatalyst materials, whereas the used polymer has a strong influence on the possible heating rates and heating times. With P123 as porogen, a highly mesoporous material with surface areas of up to 78 $m^2 g^{-1}$ and variable pore sizes of 5 to 20 nm could be obtained, depending on the used additives. This was the first mesoporous quaternary photocatalyst reported so far and it could be shown that large pores are beneficial for the photocatalytic hydrogen production.[35] However, achievement of a pore ordering was not possible with this polymer. Reasons are the worse templating properties due to the small contrast between hydrophilic and hydrophobic part of the P123 block co-polymer and its lower thermal stability, both leading to a non-ordered pore structure.

In contrast, the pore system derived from the more stable polymers ISO and PIB-PEO can be preserved much better.[151] In the case of the ISO polymer, an ordered mesoporous $CsTaWO_6$ was obtained with alternating gyroid pore geometry, large pore sizes of around 40 nm, and a corresponding surface area of 37 $m^2 g^{-1}$. The ISO-derived mesoporous $CsTaWO_6$ is the first quaternary photocatalyst reported with an ordered pore structure. Changing the precursor-to-polymer ratio during the synthesis led to the formation of a non-ordered mesoporous material with the same surface area and median pore size. The formation mechanism of the synthesis was investigated in detail, and an unusual stable intermediate Cs_2WOCl_5 with tungsten in the uncommon oxidation state +V could be found. Photocatalytic tests showed no advantage of pore ordering; the non-ordered ISO-derived mesoporous $CsTaWO_6$ reached a higher hydrogen evolution rate compared to the ordered sample, and even higher values compared to a $CsTaWO_6$ reference material *via* SSR.

The synthesis strategies could be adapted for other defect-pyrochlore structured materials, such as $CsTaMoO_6$ and $KTaWO_6$ in the case of nanoparticles, and $KTaWO_6$ in the case of P123-derived mesoporous materials.

5.4 Characteristics of nanostructured $CsTaWO_6$

All the above shown photocatalytic measurements (Figure 5.15, Figure 5.46 and Figure 5.61) were carried out with Rhodium loaded in different amounts as co-catalyst. The loading with Rh was always necessary due to an interesting effect in the nanostructured $CsTaWO_6$ materials. During irradiation with a solar simulator, nanostructured materials exhibit a strong blue colorization if not loaded with co-catalyst (Figure 5.69). At the same time, hydrogen evolution rates were relatively low compared to values after Rh deposition. The dark blue color disappears after the addition of Rh, and the dispersion becomes white again, with a light greyish tint due to the deposited Rh. As it was already reported in Chapter 5.2.2.1, a blue color can be an indication for the reduction of W(+VI) to W(+V). This reduction occurs by electrons excited into the conducting band and therefore the W5d orbitals, leading to a partially change in the oxidation state of tungsten. If these electrons are not transferred to the nanostructured $CsTaWO_6$ surface, an accumulation occurs inside the material, leading to the strong colorization. This effect can also explain why the biggest nanoparticles (30 nm) show the highest blue colorization in experiments. Addition of Rh leads to a transfer of these electrons to the surface, their consumption in proton reduction into hydrogen and therefore a decoloration of the photocatalyst and the evolution of hydrogen gas. Such a partially reduction of the conduction band forming transition metal and therefore a storage of electrons was already reported for TiO_2 photocatalysts[269] as well as for carbon nitride, whereas in the latter case, the trapped electrons form highly reductive radicals.[270]

Figure 5.69: Colorization of nanostructured materials during irradiation under a sun simulator due to the reduction of W(+VI) to W(+V). The blue color most probably arises from generated electrons in the conduction band, which do not migrate to the surface due to a missing co-catalyst.

The colorization can be also followed by UV-Vis spectroscopy, as shown in Figure 5.70a, while EPR spectroscopy did not show any stronger signal that could be assigned to W(+V) (Figure 5.70b). Maybe the concentration inside the solution is too low for a clear detection with EPR.

The accumulation of electrons could in theory be used for reduction processes that need a lot of electrons at the same time, like CO_2 reduction into CH_4[63] or N_2 into NH_3.[271] Experiments should be done *e.g.* with $CsTaWO_6$ nanoparticles dispersed in MeOH without deposited Rh plus gaseous CO_2 or N_2. After shining light on the dispersion and a blue colorization, Rh could be added and the evolved gases could be detected with MS. A direct reduction of these gases on a photocatalyst would be a very interesting reaction for the preparation of chemical compounds.

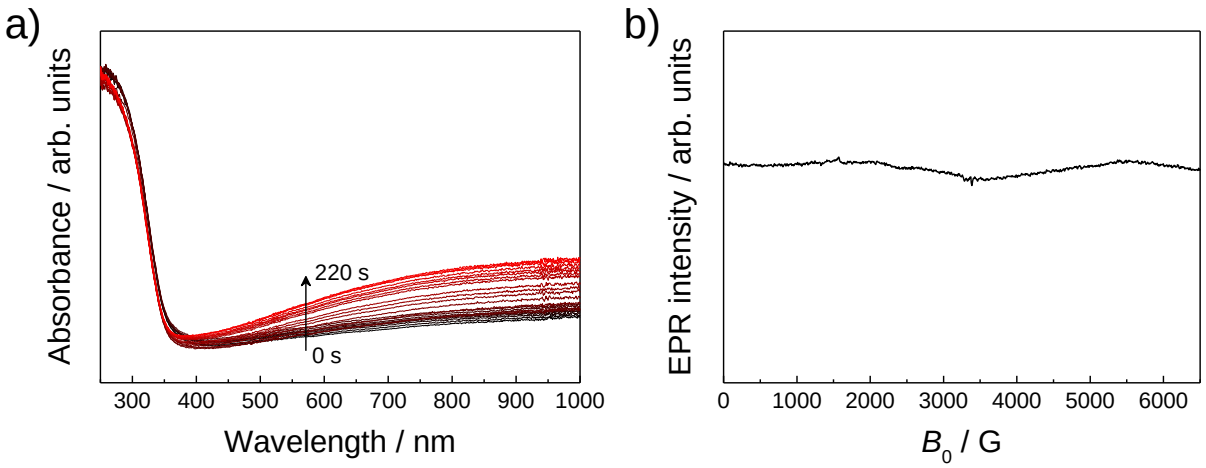

Figure 5.70: a) UV-Vis spectrum of $CsTaWO_6$ nanoparticles during photocatalysis. Changes in the absorption are related to the blue colorization of the dispersion due to the above-mentioned effect of electron accumulation on the W 5d conduction band, leading to a reduction to W(+V). b) EPR spectrum of the same sample after irradiation with light. No clear signal of the W(+V) oxidation state can be seen.

6 Comparison of different morphologies and their influence on photocatalytic activity

To answer the introductive question about the best morphology for a photocatalyst, different nanostructured samples of the defect-pyrochlore structured $CsTaWO_6$ were synthesized and characterized in detail in the above shown chapters. The desired morphologies of non-ordered and ordered mesoporosity and nanoparticulate materials (Figure 2.17)[119] could be prepared and were investigated regarding their photocatalytic activity. A summarizing picture of the morphologies achieved for $CsTaWO_6$ is given in Figure 6.1, here illustrated with the obtained spherical pore geometries for the non-ordered and ordered mesoporous materials.

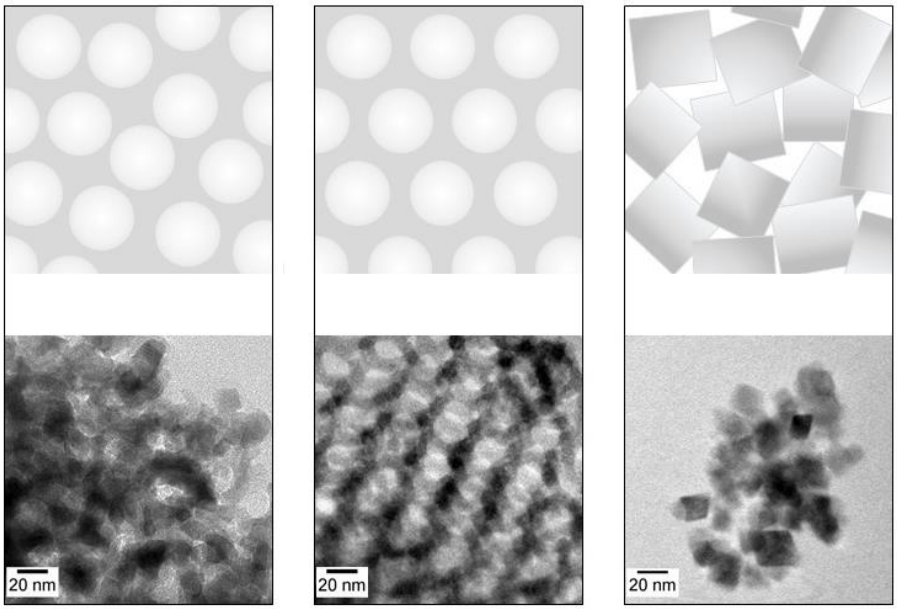

Figure 6.1: Illustration of the different nanostructure morphologies: non-ordered porous materials (left), ordered porous materials (middle) and nanoparticles (right) plus TEM images of the different $CsTaWO_6$ nanostructured samples prepared in this work.[119]

The prepared nanoparticles resulted in the conclusion of the optimum crystallite size for $CsTaWO_6$ to be 13 nm and therefore a diffusion length of the minority charge carriers of about 6−7 nm (Chapter 5.1.1). Additionally, it was found that the surface area is not the main important value in photocatalysis and therefore, an increasing surface area does not directly lead to a better photocatalytic performance (see H_2 evolution results of $CsTaWO_6$ nanoparticles in Figure 5.15).[34] Non-ordered P123-derived mesoporous samples were hinting

to a larger pore size being beneficial compared to small and narrow pores, as it could be seen in Figure 5.46.[35] Hard-templating approaches for $CsTaWO_6$ led to the same assumption (not shown in this work; see reference [128]). Due to this finding, the triblock copolymer ISO was used for the preparation of non-ordered and ordered mesopore systems with large pore sizes. An ordered pore geometry was found to have no advantages compared to a non-ordered pore system (Figure 5.61). Figure 6.2 summarizes the photocatalytic results for a number of samples, including a reference material *via* the sol-gel citrate route,[30] synthesized at a high temperature of 850 °C, and different nanostructured $CsTaWO_6$ materials.

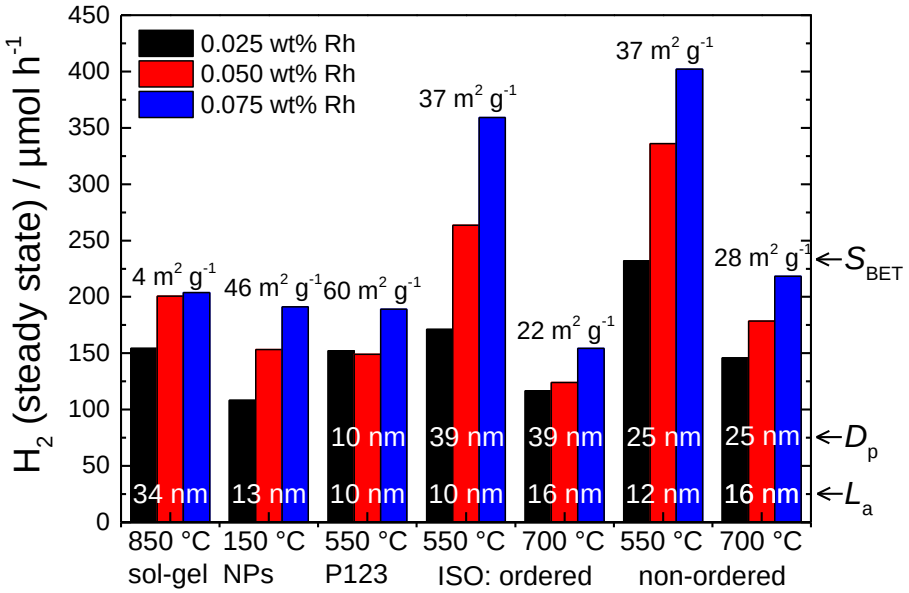

Figure 6.2: Photocatalytic activity of nanostructured $CsTaWO_6$ samples prepared in this work and of a reference material synthesized *via* sol-gel citrate route[30] at comparably high temperatures (850 °C). Average crystallite sizes (L_a), pore diameter (D_p) from NLDFT and BET surface areas (S_{BET}) are also shown.

The highest photocatalytic activity could be found for the ISO-derived non-ordered mesoporous $CsTaWO_6$ with a moderate surface area of around 37 $m^2\ g^{-1}$, where the synergetic effect of a large pore size (20–40 nm) and the optimum crystallite size (12 nm) resulted in the best performing photocatalyst. Unlike in the case of $CsTaWO_6$ nanoparticles, for the ISO-derived mesoporous $CsTaWO_6$ samples no quantum size effect could be seen when looking at the different band gaps of the material (Figure 5.60), all having a value of 3.6 eV. Thus, another parameter has to influence the $CsTaWO_6$ compound at small crystallite sizes L_a. The strain as an indicator for the number of defects in a crystal was found to be highly dependent on the

crystallite size and the used synthesis temperature (Figure 6.3). In the case of a low synthesis temperature as for the $CsTaWO_6$ nanoparticles (150 °C), the strain is at a constantly high value and further increases for the smallest crystallite sizes. This can explain the comparably low activities in hydrogen evolution for all nanoparticles compared to materials prepared *via* other synthesis techniques and therefore higher temperatures. Even the best performing nanoparticles with an average crystallite size of 13 nm are just reaching the value of the sol-gel citrate route sample, although the surface area is more than ten times higher and the crystallite size in the citrate route sample of 34 nm is far away from the found optimum. The formation of a charge separating space charge layer plus the very low strain in this material can probably compensate the disadvantage of the big crystallites.

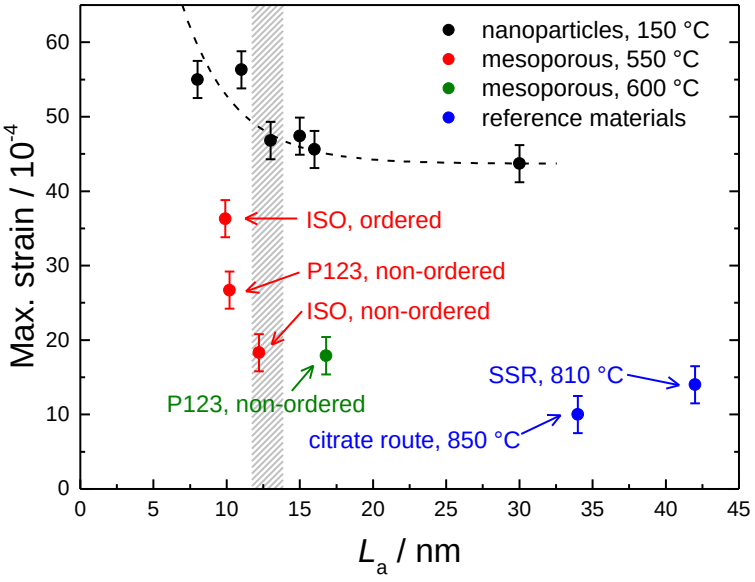

Figure 6.3: Maximum values of strain, determined by Rietveld refinement, of different nanostructured $CsTaWO_6$ and reference $CsTaWO_6$ materials. The strain value can be considered as an estimation of the total amount of structural defects in the particular sample.[193–195] The marked area indicates the region of the optimum crystallite size. The dashed line for the $CsTaWO_6$ nanoparticles is just to guide the eye and is not a result of data fitting.

The mesoporous $CsTaWO_6$ samples also show a trend to higher strain with decreasing crystallite size. That is the conclusive proof for the correctness of the assumption that a crystallite size of around 12 to 13 nm is the optimum for $CsTaWO_6$, because the ISO-derived ordered and non-ordered samples have the same surface area, but exhibit different photocatalytic activity. The better performance of the non-ordered ISO-derived $CsTaWO_6$ is a consequence of the low strain in this product and the crystallite size being close to the

optimum value. ISO-derived mesoporous samples, calcined at 700 °C and thus with Larger crystallites, show worse performance caused by the longer diffusion ways of the charge carriers to the surface (Figure 6.2).

The minor influence of the surface area is illustrated in Figure 6.4a, where a random distribution of the relative activities independent from the BET surface areas can be seen. However, when plotting crystallite size and surface area with relation to their relative activities, a region with the best performing photocatalyst can be found around the assumed optimum crystallite size of 12−13 nm (Figure 6.4b, marked red).

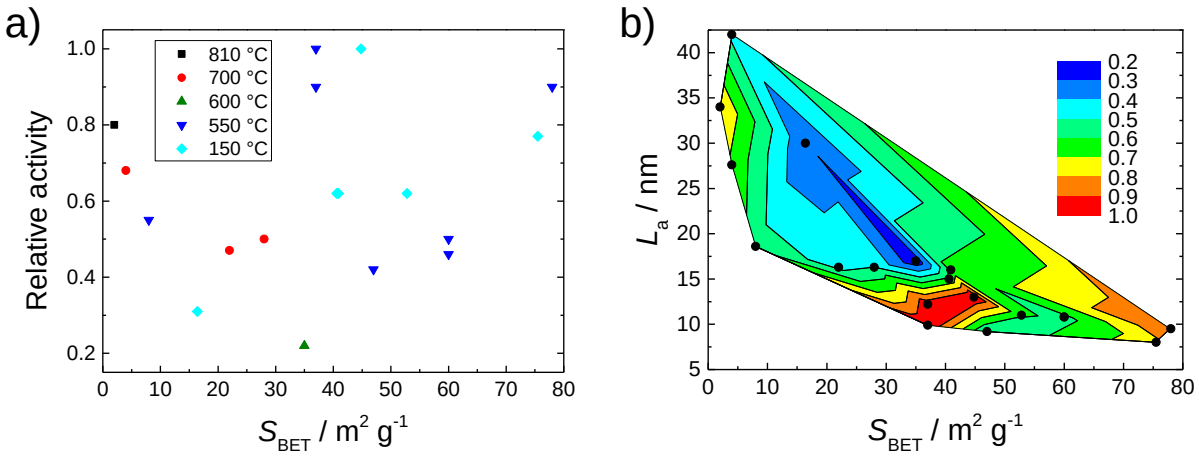

Figure 6.4: a) Relative activities *versus* BET surface areas, showing no clear trend. The most active nanoparticles and mesoporous materials were set to 1; all others were set in relation to these values. b) Crystallite size and BET surface areas with respect to the relative activities, indicating a clear optimum of the crystallite size at around 12−13 nm (marked red).

The properties of the most important photocatalysts and their photocatalytic activities in hydrogen evolution from water/methanol are summarized in Table 6.1.

Table 6.1: Properties and photocatalytic activities under UV light irradiation of several $CsTaWO_6$ samples prepared in this work.

Sample	Pore geometry	T_{calc} / °C	L_a / nm	S_{BET} / $m^2\ g^{-1}$	D_p / nm	V_p / $cm^3\ g^{-1}$	H_2 (0.075 wt% Rh)/ µmol h^{-1}
cit. route	–	850	34	3.9	–	–	204
NPs	–	150	13	46	–	–	191
P123	non-ord.	550	10	60	10	0.20	189
ISO-250	ordered	550	10	37	39	0.39	360
ISO-1000	non-ord.	550	12	37	25	0.26	403
ISO-250	ordered	700	16	22	39	0.26	155
ISO-1000	non-ord.	700	16	28	25/40	0.23	219

T_{calc} = calcination temperature, L_a = average crystallite size, S_{BET} = BET surface area, D_p = average pore diameter, V_p = pore volume and H_2 is the evolved hydrogen at steady state conditions with 0.075 wt% Rh as co-catalyst.

7 Conclusion

A set of new syntheses was established for the preparation of nanostructured $CsTaWO_6$ with increased surface area, decreased calcination time and temperature, and enhanced photocatalytic activity,[34,35] all compared to standard synthesis routes for the defect-pyrochlore structured $CsTaWO_6$ such as SSR[29,31,32] and citrate route.[30]

Single crystal $CsTaWO_6$ nanoparticles were synthesized with different crystallite sizes from 8 to 30 nm *via* a hydrothermal synthesis, and showed surface areas of up to 76 $m^2 g^{-1}$ for the smallest particles.[34] The photocatalytic activity was found to be best for nanoparticles with an average size of 13 nm, which was concluded to be the optimum crystallite size for the $CsTaWO_6$ material, giving a hint for the diffusion length of the minority charge carriers to be around 6 to 7 nm. Higher average crystallite sizes led to a decrease in the photocatalytic performance due to enhanced recombination processes. Furthermore, smaller crystallite sizes resulted in an increased band gap due to the quantum size effect and enlarged strain in the particles.

Mesoporous $CsTaWO_6$ with different pore sizes, pore ordering and non-ordered porosity were prepared using the block copolymers P123[35] and ISO as porogen. It could be found that the major influence in mesoporous materials is the pore size itself and not the surface area of the samples. Small and narrow pores led to no advantage compared to non-porous reference materials, whereas bigger and broader pore size distributions gave rise to an enhanced photocatalytic hydrogen generation, independent of the used polymer and the resulting surface area. An ordered mesopore system showed less activity compared to a non-ordered sample with the same surface area and comparable pore sizes, indicating that pore ordering has no benefits in photocatalysis. The small differences between ISO-derived ordered and non-ordered mesoporous $CsTaWO_6$ are related to the marginally different crystallite sizes of these two samples, leading to a crystallite size in the non-ordered sample close to the optimum value found for $CsTaWO_6$ nanoparticles and therefore enhanced activity. The reason for the disadvantage of a slightly smaller crystallite size in the ordered mesopore system could be attributed to the increased strain parameter in this sample.

It was possible to adapt the introduced synthesis routes for the preparation of nanoparticulate $CsTaWO_6$ and mesoporous $CsTaWO_6$ on other defect-pyrochlore structured

materials, resulting in $KTaWO_6$ and $CsTaMoO_6$ nanoparticles, and mesoporous $KTaWO_6$. The preparation of mesoporous materials on a heating plate under a glass dome was used for first experiments with other polymers than ISO, such as P123 and PIB-PEO, leading to promising results for both polymers.

$CsTaWO_6$ nanoparticles showed a variety of possible further applications, such as starting material for the preparation of $CsTaWO_6$ nanofibers or a good ability of Sn-doping due to the much smaller particle size and increased surface area compared to the citrate route or SSR products. Theoretically, mesoporous $CsTaWO_6$ should also be a good starting material for gas phase doping experiments (*e.g.* with ammonia) due to the high surface area, especially for large pore sizes because of the good exchange and penetration of the doping solution into the entire material.

At the beginning of this work, there had been no systematic investigations on the best morphology of a photocatalyst. Many publications in literature showed confusing results, sometimes contradicting each other or being less comparable, *e.g.* due to the choice of inappropriate reference materials, the formation of by-phases or the variation of more than one parameter at the same time. In this work on a $CsTaWO_6$ photocatalyst as a model system, phase-pure materials were compared with well-known reference materials from literature syntheses and a systematic variation of parameters such as crystallite size, surface area and pore diameter was made. These results can give an answer to the above given question on the best morphology of a photocatalyst. In the best case, a photocatalyst has to provide the optimum crystallite size for the desired compound and a pore size that enables transportation processes throughout the whole sample. At the same time, the synthesis temperature should be as high as possible to avoid strain, but still maintain the optimum crystallite size. For $CsTaWO_6$, these values are found to be 13 nm for the crystallite size and more than 20 nm for the pore diameter. At a calcination temperature of 550 °C, the polymer structure working as a directing agent is burned away completely and a phase-pure and crystalline product with reduced strain can be obtained. Thus, a mesoporous morphology with thin pore walls and large pores gave the best results in photocatalytic hydrogen production. These results should be generally valid for other transition metal oxide photocatalysts, too.

8 Outlook

The morphological influences on the photocatalytic hydrogen production of $CsTaWO_6$ should be in theory valid for other transition metal oxide photocatalysts, such as TiO_2, Ta_2O_5 and Nb_2O_5. Due to its unique properties, $CsTaWO_6$ is a good material for a model photocatalyst. However, the cost-intensive elements, especially caesium, make it a highly expensive material. A first step away from this critical aspect is the substitution of caesium with the earth-abundant element potassium, which is considerably cheaper. As it could be shown in Chapter 5.2.5.3, the preparation of a mesoporous $KTaWO_6$ is also possible and the synthesis of $KTaWO_6$ nanoparticles with the above-described hydrothermal process had been already successful in our group. Microwave-assisted synthesis of the nanoparticles is an even more timesaving synthesis technique and was shown for $CsTaWO_6$ in Chapter 5.1.3. This could be adapted for other defect-pyrochlore structured materials such as $CsTaMoO_6$ or $KTaWO_6$. Due to its similar properties like the defect-pyrochlore structure, comparable band gap and band positions, all the conclusions drawn in this work should be certainly valid for $KTaWO_6$, too.

Both nanostructuring techniques, nanoparticle preparation and mesoporous material synthesis, should be beneficial for a homogenous doping. Although high temperature doping techniques such as N- or S-doping are less useful for nanostructured materials due to their sensitivity against harsh conditions, doping from aqueous solutions showed some promising first results for nanoparticulate systems (Chapter 5.1.3.3). Similar results can be expected for the highly mesoporous materials with large pore sizes because of their good properties for a complete penetration of the doping solution inside the whole material. This would lead to nanostructured, quaternary photocatalysts with activity in the visible light range.

However, there is the general question whether nanostructuring is really necessary in photocatalysis. It could be demonstrated above that nanostructuring can lead to an improved photocatalytic activity even compared to the best-known bulk reference, here $CsTaWO_6$ prepared in a solid-state synthesis. Although the enhancement is just around 20 %, these results show that nanostructuring can indeed be advantageous. This can become very important regarding more complex composite photocatalyst systems, such as Z-scheme structures, where a high contact area is fundamental to obtain the advantage of charge carrier separation on the interfaces of the different compounds. Here, nanostructuring could be

extremely helpful, and the results of this work can give a manual of how to get the best morphology for such a photocatalyst material. One concept for such a high-interface composite photocatalyst could be a second photocatalytically active material, incorporated or even completely filling the pores of the mesoporous host. An incorporation or coating of the mesoporous photocatalyst could lead to a very efficient charge separation and a large surface area simultaneously. A complete filling would decrease the surface area, but the advantage of the well-distributed two-phase system could predominate. The same concept of a coated layer on the nanostructured host can be imagined for the nanoparticulate material, for example as a core-shell system.[272,273]

The preparation of mesoporous materials on a heating plate under a glass dome was found to be a very useful tool to generate compounds even with a complex stoichiometry like $CsTaWO_6$. A wide range of polymers can be chosen, all resulting in highly porous powders of the desired compound. Therefore, it should be possible to synthesize other promising photocatalyst materials with a mesoporous morphology, such as earth-abundant oxides like ferrites with promising band positions ($MgFe_2O_4$, $CaFe_2O_4$, $ZnFe_2O_4$).[274]

9 References

1 H. Rodhe, *Science*, 1990, **248**, 1217.
2 J. Hansen, R. Ruedy, M. Sato and K. Lo, *Rev. Geophys.*, 2010, **48**, RG4004.
3 P. Moriarty and D. Honnery, *Renew. Sustain. Energy Rev.*, 2012, **16**, 244.
4 G. Kopp and J. L. Lean, *Geophys. Res. Lett.*, 2011, **38**, 1.
5 T. Grewe, M. Meggouh and H. Tüysüz, *Chem. - An Asian J.*, 2016, **11**, 22.
6 M. Ni, M. K. H. Leung, D. Y. C. Leung and K. Sumathy, *Renew. Sustain. Energy Rev.*, 2007, **11**, 401.
7 A. O. Ibhadon and P. Fitzpatrick, *Catalysts*, 2013, **3**, 189.
8 R. Marschall, *Adv. Funct. Mater.*, 2014, **24**, 2421.
9 D. Ravelli, D. Dondi, M. Fagnoni and A. Albini, *Chem. Soc. Rev.*, 2009, **38**, 1999.
10 G. Colón, *Appl. Catal. A Gen.*, 2016, **518**, 48.
11 A. Fujishima and K. Honda, *Nature*, 1972, **238**, 37.
12 K. Hashimoto, H. Irie and A. Fujishima, *Jpn. J. Appl. Phys.*, 2005, **44**, 8269.
13 A. Fujishima, T. N. Rao and D. A. Tryk, *J. Photochem. Photobiol. C Photochem. Rev.*, 2000, **1**, 1.
14 J. Schneider, M. Matsuoka, M. Takeuchi, J. Zhang, Y. Horiuchi, M. Anpo and D. W. Bahnemann, *Chem. Rev.*, 2014, **114**, 9919.
15 J. Zhu and M. Zäch, *Curr. Opin. Colloid Interface Sci.*, 2009, **14**, 260.
16 H.-Y. Lin, H.-C. Yang and W.-L. Wang, *Catal. Today*, 2011, **174**, 106.
17 E. J. W. Crossland, N. Noel, V. Sivaram, T. Leijtens, J. A. Alexander-Webber and H. J. Snaith, *Nature*, 2013, **495**, 215.
18 T. Grewe and H. Tüysüz, *ChemSusChem*, 2015, **8**, 3084.
19 X. Li, A. F. Masters and T. Maschmeyer, *ChemCatChem*, 2015, **7**, 121.
20 K. He, C. Zhao, G. Zhao and G. Han, *J. Sol-Gel Sci. Technol.*, 2015, **75**, 557.
21 L. Li, M. Krissanasaeranee, S. W. Pattinson, M. Stefik, U. Wiesner, U. Steiner and D. Eder, *Chem. Commun.*, 2010, **46**, 7620.
22 A. S. Cherevan, S. Robbins, D. Dieterle, P. Gebhardt, U. Wiesner and D. Eder, *Nanoscale*, 2016, **8**, 16694.
23 K. Yu, C. Zhang, Y. Chang, Y. Feng, Z. Yang, T. Yang, L. L. Lou and S. Liu, *Appl. Catal. B Environ.*, 2017, **200**, 514.
24 W.-T. Chen, A. Chan, V. Jovic, D. Sun-Waterhouse, K. Murai, H. Idriss and G. I. N. Waterhouse, *Top. Catal.*, 2015, **58**, 85.
25 K. Kočí, L. Obalová, L. Matějová, D. Plachá, Z. Lacný, J. Jirkovský and O. Šolcová, *Appl. Catal. B Environ.*, 2009, **89**, 494.
26 T. B. Ghosh, S. Dhabal and A. K. Datta, *J. Appl. Phys.*, 2003, **94**, 4577.
27 D. O. Scanlon, C. W. Dunnill, J. Buckeridge, S. A. Shevlin, A. J. Logsdail, S. M. Woodley, C. R. A. Catlow, M. J. Powell, R. G. Palgrave, I. P. Parkin, G. W. Watson, T. W. Keal, P. Sherwood, A. Walsh and A. A. Sokol, *Nat. Mater.*, 2013, **12**, 798.
28 R. Li, Y. Weng, X. Zhou, X. Wang, Y. Mi, R. Chong, H. Han and C. Li, *Energy Environ. Sci.*, 2015, **8**, 2377.
29 S. Ikeda, T. Itani, K. Nango and M. Matsumura, *Catal. Letters*, 2004, **98**, 229.
30 L. Schwertmann, M. Wark and R. Marschall, *RSC Adv.*, 2013, **3**, 18908.
31 L. Schwertmann, A. Grünert, A. Pougin, C. Sun, M. Wark and R. Marschall, *Adv. Funct. Mater.*, 2015, **25**, 905.

32 A. Mukherji, R. Marschall, A. Tanksale, C. Sun, S. C. Smith, G. Q. Lu and L. Wang, *Adv. Funct. Mater.*, 2011, **21**, 126.

33 R. Marschall, A. Mukherji, A. Tanksale, C. Sun, S. C. Smith, L. Wang and G. Q. (Max) Lu, *J. Mater. Chem.*, 2011, **21**, 8871.

34 T. Weller, L. Specht and R. Marschall, *Nano Energy*, 2017, **31**, 551.

35 T. Weller, J. Sann and R. Marschall, *Adv. Energy Mater.*, 2016, **6**, 1600208.

36 T. R. Karl and K. E. Trenberth, *Science*, 2003, **302**, 1719.

37 National Oceanic and Atmospheric Administration, *GISS Surface Temperature Analysis*, http://data.giss.nasa.gov/gistemp/, 6th November, 2016.

38 Pieter Tans and R. Keeling, *Trends in Atmospheric Carbon Dioxide*, Scripps Institution of Oceanography, NOAA/ESRL, http://www.esrl.noaa.gov/gmd/ccgg/trends/data.html, 6th November, 2016.

39 IEA, *Key World Energy Statistics*, International Energy Agency, https://www.iea.org/publications/freepublications/publication/key-world-energy-statistics.html, 6th November, 2016.

40 United Nations Framework Convention on Climate Change, *Adoption of the Paris Agreement*, http://unfccc.int/resource/docs/2015/cop21/eng/l09r01.pdf, 1st December, 2016.

41 S. Rajaambal, K. Sivaranjani and C. S. Gopinath, *J. Chem. Sci.*, 2015, **127**, 33.

42 J. L. Monteith and M. H. Unsworth, *Principles of Environmental Physics Plants, Animals, and the Atmosphere*, Academic Press, 4th edn., 2013.

43 P. J. Mohr, D. B. Newell and B. N. Taylor, *Rev. Mod. Phys.*, 2016, **88**, 35009.

44 D. R. Williams, *Sun Fact Sheet*, NASA Goddard Space Flight Center, http://nssdc.gsfc.nasa.gov/planetary/factsheet/sunfact.html, 6th November, 2016.

45 M. Emilio, J. R. Kuhn, R. I. Bush and I. F. Scholl, *Astrophys. J.*, 2014, **750**, 135.

46 *Resolution B2 on the re-definition of the astronomical unit of length*, Working Group Numerical Standards, https://syrte.obspm.fr/IAU_resolutions/Res_IAU2012_B2.pdf, International Astronomical Union, 2012.

47 H. Moritz, *J. Geod.*, 2012, **74**, 128.

48 S. Zekai, *Solar Energy Fundamentals and Modeling Techniques*, Springer Science & Business Media, 2013, vol. 53.

49 Google, *Google Maps*, https://www.google.de/maps/place/Mitte,+Berlin/@52.5222029,13.362587,13z/data=!3m1!4b1!4m5!3m4!1s0x47a851dfead80d8f:0x26212047581535f2!8m2!3d52.519444!4d13.406667, 6th November, 2016.

50 *Sunrise-and-sunset.com*, 6th November, 2016.

51 T. Khatib and W. Elmenreich, *Int. J. Photoenergy*, 2015, **2015**, 1.

52 *Standard Solar Spectra*, http://www.pveducation.org/pvcdrom/appendices/standard-solar-spectra, 26th January, 2017.

53 W. Bludau, A. Onton and W. Heinke, *J. Appl. Phys.*, 1974, **45**, 1846.

54 F. E. Osterloh and B. A. Parkinson, *Mrs Bull.*, 2011, **36**, 17.

55 U. Eberle, B. Müller and R. von Helmolt, *Energy Environ. Sci.*, 2012, **5**, 8780.

56 M. Jentsch, T. Trost and M. Sterner, *Energy Procedia*, 2014, **46**, 254.

57 X. Chen, S. Shen, L. Guo and S. S. Mao, *Chem. Rev.*, 2010, **110**, 6503.

58 N. Serpone and A. V. Emeline, *J. Phys. Chem. Lett.*, 2012, **3**, 673.

59 H. Pan, *Renew. Sustain. Energy Rev.*, 2016, **57**, 584.

60 H. Kisch, *Angew. Chemie - Int. Ed.*, 2013, **52**, 812.

61 N. S. Lewis and D. G. Nocera, *Proc. Natl. Acad. Sci.*, 2006, **103**, 15729.

62 M. Götz, J. Lefebvre, F. Mörs, A. McDaniel Koch, F. Graf, S. Bajohr, R. Reimert and T.

Kolb, *Renew. Energy*, 2016, **85**, 1371.
63 K. Li, X. An, K. H. Park, M. Khraisheh and J. Tang, *Catal. Today*, 2014, **224**, 3.
64 A. A. Ismail and D. W. Bahnemann, *Sol. Energy Mater. Sol. Cells*, 2014, **128**, 85.
65 G. W. Crabtree, M. S. Dresselhaus and M. V Buchanan, *Phys. Today*, 2004, **57**, 39.
66 T. Yoshida and K. Kojima, *Electrochem. Soc. Interface*, 2015, **24**, 45.
67 J. B. Howard and D. C. Rees, *Chem. Rev.*, 1996, **96**, 2965.
68 S. A. Sherif, F. Barbir and T. N. Veziroglu, *Sol. Energy*, 2005, **78**, 647.
69 P. P. Edwards, V. L. Kuznetsov, W. I. F. David and N. P. Brandon, *Energy Policy*, 2008, **36**, 4356.
70 M. Fischer, M. Werber and P. V. Schwartz, *Energy Policy*, 2009, **37**, 2639.
71 J. A. Turner, *Science*, 1999, **285**, 687.
72 H.-Y. Lin, Y.-W. Chen and C. Li, *Thermochim. Acta*, 2003, **400**, 61.
73 W. K. Jozwiak, E. Kaczmarek, T. P. Maniecki, W. Ignaczak and W. Maniukiewicz, *Appl. Catal. A Gen.*, 2007, **326**, 17.
74 K. P. Brooks, J. Hu, H. Zhu and R. J. Kee, *Chem. Eng. Sci.*, 2007, **62**, 1161.
75 K. Müller, J. Völkl and W. Arlt, *Energy Technol.*, 2013, **1**, 20.
76 T. Ohno, K. Sarukawa, M. Matsumura and D. E. Scaife, *Sol. Energy*, 1980, **125**, 41.
77 J. Luo, J.-H. Im, M. T. Mayer, M. Schreier, M. K. Nazeeruddfn, N.-G. Park, S. D. Tilley, F. Hong Jin and M. Gratzel, *Science*, 2014, **345**, 1593.
78 O. Deutschmann, H. Knozinger, K. Kochloefl and T. Turek, *Heterogeneous Catalysis and Solid Catalysts*, Wiley-VCH Verlag GmbH & Co. KGaA, Weinheim, 2003.
79 P. Zrazhevskiy, M. Sena and X. Gao, *Chem. Soc. Rev.*, 2010, **39**, 4326.
80 A. Rahman, *Am. Sci. Res. J. Eng. Technol. Sci.*, 2014, **7**, 50.
81 H. Raebiger, S. Lany and A. Zunger, *Phys. Rev. B*, 2007, **76**, 45209.
82 V. Parmon, A. V. Emeline and N. Serpone, *Int. J. Photoenergy*, 2002, **4**, 91.
83 A. Goetzberger and C. Hebling, *Sol. Energy Mater. Sol. Cells*, 2000, **62**, 1.
84 T. Jafari, E. Moharreri, A. S. Amin, R. Miao, W. Song and S. L. Suib, *Molecules*, 2016, **21**, 900.
85 L. C. Lau and K. Lee, *Int. J. Res. Eng. Technol.*, 2013, **2**, 195.
86 M. G. Walter, E. L. Warren, J. R. McKone, S. W. Boettcher, Q. Mi, E. A. Santori and N. S. Lewis, *Chem. Rev.*, 2010, **110**, 6446.
87 B. A. Pinaud, J. D. Benck, L. C. Seitz, A. J. Forman, Z. Chen, T. G. Deutsch, B. D. James, K. N. Baum, G. N. Baum, S. Ardo, H. Wang, E. Miller and T. F. Jaramillo, *Energy Environ. Sci.*, 2013, **6**, 1983.
88 L. C. Seitz, Z. Chen, A. J. Forman, B. A. Pinaud, J. D. Benck and T. F. Jaramillo, *ChemSusChem*, 2014, **7**, 1372.
89 K. Maeda, *Chem. Commun.*, 2013, **49**, 8404.
90 C. Colbeau-Justin, M. Kunst and D. Huguenin, *J. Mater. Sci.*, 2003, **38**, 2429.
91 Z.-Y. Zhao, *J. Phys. Chem. C*, 2014, **118**, 24591.
92 K. Ozawa, M. Emori, S. Yamamoto, R. Yukawa, S. Yamamoto, R. Hobara, K. Fujikawa, H. Sakama and I. Matsuda, *J. Phys. Chem. Lett.*, 2014, **5**, 1953.
93 A. J. Cowan, W. Leng, P. R. F. Barnes, D. R. Klug and J. R. Durrant, *Phys. Chem. Chem. Phys.*, 2013, **15**, 8772.
94 R. M. Navarro Yerga, M. Consuelo Álvarez Galván, F. del Valle, J. A. Villoria de la Mano and J. L. G. Fierro, *ChemSusChem*, 2009, **2**, 471.
95 J. Yang, D. Wang, H. Han and C. Li, *Acc. Chem. Res.*, 2013, **46**, 1900.
96 R. Baba, S. Nakabayashi and A. Fujishima, *J. Phys. Chem.*, 1985, **89**, 1902.
97 A. Y. Ahmed, T. A. Kandiel, I. Ivanova and D. Bahnemann, *Appl. Surf. Sci.*, 2014, **319**, 44.

98 W.-C. Lin, W.-D. Yang, I.-L. Huang, T.-S. Wu and Z.-J. Chung, *Energy & Fuels*, 2009, **23**, 2192.
99 J. Schneider and D. W. Bahnemann, *J. Phys. Chem. Lett.*, 2013, **4**, 3479.
100 B. Ohtani, O. O. Prieto-Mahaney, D. Li and R. Abe, *J. Photochem. Photobiol. A Chem.*, 2010, **216**, 179.
101 N. Serpone, E. Borgarello and M. Graetzel, *J. Chem. Soc. Chem. Commun.*, 1984, 342.
102 S. Hotchandani and P. V. Kamat, *J. Phys. Chem.*, 1992, **96**, 6834.
103 T. A. Kandiel, A. A. Ismail and D. W. Bahnemann, *Phys. Chem. Chem. Phys.*, 2011, **13**, 20155.
104 G. R. Bamwenda, S. Tsubota, T. Nakamura and M. Haruta, *J. Photochem. Photobiol. A Chem.*, 1995, **89**, 177.
105 R. F. Weiss, *Mar. Chem.*, 1974, **2**, 203.
106 D. E. Scaife, *Sol. Energy*, 1980, **25**, 41.
107 M. Ahmed and G. Xinxin, *Inorg. Chem. Front.*, 2016, **3**, 578.
108 Mineralogical Society of America, *Handbook of Mineralogy*, http://www.handbookofmineralogy.org/, Chantilly, VA, 2000, vol. 4.
109 B. C. Chakoumakos, *J. Solid State Chem.*, 1984, **53**, 120.
110 A. Jerez, M. L. López, S. García-Martín, M. L. Veiga and C. Pico, *J. Mater. Sci.*, 1991, **26**, 5163.
111 J. Sun, X. Zhao, H. Sun and W. Fan, *J. Solid State Chem.*, 2012, **194**, 352.
112 D. Hollmann, O. Merka, L. Schwertmann, R. Marschall, M. Wark and A. Brückner, *Top. Catal.*, 2015, **58**, 769.
113 B. D. Sharma, *J. Chem. Educ.*, 1987, **64**, 404.
114 M. Al-Mamouri, P. P. Edwards, C. Greaves and M. Slaski, *Lett. to Nat.*, 1994, **369**, 382.
115 M. V. Dozzi, C. D'Andrea, B. Ohtani, G. Valentini and E. Selli, *J. Phys. Chem. C*, 2013, **117**, 25586.
116 Y. Tsujimoto, K. Yamaura, N. Hayashi, K. Kodama, N. Igawa, Y. Matsushita, Y. Katsuya, Y. Shirako, M. Akaogi and E. Takayama-Muromachi, *Chem. Mater.*, 2011, **23**, 3652.
117 M. Weiss, *Optimisation of photocatalytic properties of defectpyrochlores by lattice and band structure engineering*, Master Thesis, Justus-Liebig-University Giessen, Giessen, 2016.
118 G. Leofanti, M. Padovan, G. Tozzola and B. Venturelli, *Catal. Today*, 1998, **41**, 207.
119 T. Weller, P. Voepel and R. Marschall, *Charge Carrier Transfer in Heterogenous Photocatalysis*, ISSN 1611-9479, Bunsenmagazin, 2016, vol. 1.
120 T. Grewe and H. Tüysüz, *J. Mater. Chem. A*, 2016, **4**, 3007.
121 L. Guo, H. Hagiwara, S. Ida, T. Daio and T. Ishihara, *ACS Appl. Mater. Interfaces*, 2013, **5**, 11080.
122 W. Shi, S. Song and H. Zhang, *Chem. Soc. Rev.*, 2013, **42**, 5714.
123 T. Adschiri, Y. Hakuta and K. Arai, *Ind. Eng. Chem. Res.*, 2000, **39**, 4901.
124 D. Gu and F. Schüth, *Chem. Soc. Rev.*, 2014, **43**, 313.
125 Y. Liu, J. Goebl and Y. Yin, *Chem. Soc. Rev.*, 2013, **42**, 2610.
126 W. Li and D. Zhao, *Chem. Commun.*, 2013, **49**, 943.
127 Y. Wan, Y. Shi and D. Zhao, *Chem. Commun.*, 2007, 897.
128 M. Weiss, S. Waitz, R. Ellinghaus, T. Weller and R. Marschall, *RSC Adv.*, 2016, **6**, 79037.
129 R. D. Zhang, P. Li, N. Liu, W. Yue and B. Chen, *J. Mater. Chem. A*, 2014, **2**, 17329.
130 L. Hu, S. Ji, T. Xiao, C. Guo, P. Wu and P. Nie, *J. Phys. Chem. B*, 2007, **111**, 3599.
131 L. Mahoney and R. T. Koodali, *Materials*, 2014, **7**, 2697.
132 X. Cui, S. Mao, M. Liu, H. Yuan and Y. Du, *Langmuir*, 2008, **24**, 10771.

133 C. J. Brinker, Y. Lu, A. Sellinger and H. Fan, *Adv. Mater.*, 1999, **11**, 579.
134 R. Ganguly, M. Kumbhakar and V. K. Aswal, *J. Phys. Chem. B*, 2009, **113**, 9441.
135 P. Alexandridis and T. A. Hatton, *Colloids Surfaces A Physicochem. Eng. Asp.*, 1995, **96**, 1.
136 B. Eckhardt, E. Ortel, D. Bernsmeier, J. Polte, P. Strasser, U. Vainio, F. Emmerling and R. Kraehnert, *Chem. Mater.*, 2013, **25**, 2749.
137 M. Nedelcu, J. Lee, E. J. W. Crossland, S. C. Warren, M. C. Orilall, S. Guldin, S. Hüttner, C. Ducati, D. Eder, U. Wiesner, U. Steiner and H. J. Snaith, *Soft Matter*, 2009, **5**, 134.
138 W. Sun, S. Zhou, B. You and L. Wu, *Chem. Mater.*, 2012, **24**, 3800.
139 Y. Li, W. Luo, N. Qin, J. Dong, J. Wei, W. Li, S. Feng, J. Chen, J. Xu, A. A. Elzatahry, M. H. Es-Saheb, Y. Deng and D. Zhao, *Angew. Chemie - Int. Ed.*, 2014, **53**, 1.
140 L. Mei, H. Zhao and B. Lu, *Adv. Sci.*, 2015, **2**, 1500116.
141 M. Kurahashi, K. Kanamori, K. Takeda, H. Kaji and K. Nakanishi, *RSC Adv.*, 2012, **2**, 7166.
142 A. Pitto-Barry and N. P. E. Barry, *Polym. Chem.*, 2014, **5**, 3291.
143 J. Chatterjee, S. Jain and F. S. Bates, *Macromolecules*, 2007, **40**, 2882.
144 T. H. Epps, E. W. Cochran, T. S. Bailey, R. S. Waletzko, C. M. Hardy and F. S. Bates, *Macromolecules*, 2004, **37**, 8325.
145 H. Sai, K. W. Tan, K. Hur, E. Asenath-Smith, R. Hovden, Y. Jiang, M. Riccio, D. A. Muller, V. Elser, L. A. Estroff, S. M. Gruner and U. Wiesner, *Science*, 2013, **341**, 530.
146 J. Lee, M. C. Orilall, S. C. Warren, M. Kamperman, F. J. DiSalvo and U. Wiesner, *Nat. Mater.*, 2008, **7**, 222.
147 V. K. Mourya, N. Inamdar, R. B. Nawale and S. S. Kulthe, *Indian J. Pharm. Educ. Res.*, 2011, **45**, 128.
148 M. Nedelcu, S. Guldin, M. C. Orilall, J. Lee, S. Hüttner, E. J. W. Crossland, S. C. Warren, C. Ducati, P. R. Laity, D. Eder, U. Wiesner, U. Steiner and H. J. Snaith, *J. Mater. Chem.*, 2010, **20**, 1261.
149 P. Holmqvist, P. Alexandridis and B. Lindman, *J. Phys. Chem. B*, 1998, **102**, 1149.
150 M. Stefik, S. Wang, R. Hovden, H. Sai, M. W. Tate, D. A. Muller, U. Steiner, S. M. Gruner and U. Wiesner, *J. Mater. Chem.*, 2012, **22**, 1078.
151 T. von Graberg, P. Hartmann, A. Rein, S. Gross, B. Seelandt, C. Röger, R. Zieba, A. Traut, M. Wark, J. Janek and B. M. Smarsly, *Sci. Technol. Adv. Mater.*, 2011, **12**, 025005:1.
152 J.-M. Wu, I. Djerdj, T. von Graberg and B. M. Smarsly, *Beilstein J. Nanotechnol.*, 2012, **3**, 123.
153 J. Yue, C. Suchomski, T. Brezesinski and B. M. Smarsly, *ChemNanoMat*, 2015, **1**, 415.
154 N. Pal and A. Bhaumik, *Adv. Colloid Interface Sci.*, 2013, **189–190**, 21.
155 L. Zhao, H. Qin, R. Wu and H. Zou, *J. Chromatogr. A*, 2012, **1228**, 193.
156 F. S. Bates and G. H. Fredrickson, *Phys. Today*, 1999, **52**, 32.
157 J. N. Kondo, M. Uchida, K. Nakajima, L. Daling, M. Hara and K. Domen, *Chem. Mater.*, 2004, **16**, 4304.
158 T. W. Kim and K.-S. Choi, *Science*, 2014, **343**, 990.
159 F. Zou, Z. Jiang, X. Qin, Y. Zhao, L. Jiang, J. Zhi, T. Xiao and P. P. Edwards, *Chem. Commun.*, 2012, **48**, 8514.
160 S. Sun, W. Wang, J. Xu, L. Wang and Z. Zhang, *Appl. Catal. B Environ.*, 2011, **106**, 559.
161 H. Tüysüz and C. K. Chan, *Nano Energy*, 2013, **2**, 116.
162 L. L. Hench and J. K. West, *Chem. Rev.*, 1990, **90**, 33.
163 R. J. P. Corriu and D. Leclercq, *Angew. Chemie - Int. Ed.*, 1996, **35**, 1420.
164 A. E. Danks, S. R. Hall and Z. Schnepp, *Mater. Horiz.*, 2016, **3**, 91.
165 M. Niederberger, *Metal Oxide Nanoparticles in Organic Solvents*, Springer-Verlag

London, 1st edn., 2009.
166 A. Vioux, *Chem. Mater.*, 1997, **9**, 2292.
167 N. Pinna, *SPIE Newsroom*, 2009, 2.
168 M. Niederberger, *Acc. Chem. Res.*, 2007, **40**, 793.
169 V. A. Khodzhemirov, V. A. Yevdokimova and V. M. Cherednichenko, *Polym. Sci. U.S.S.R.*, 1976, **18**, 581.
170 S. Sakka, Ed., *Handbook of Sol-Gel Science and Technology*, Springer US, 1st edn., 2016.
171 F. Fresno, C. Guillard, J. M. Coronado, J.-M. Chovelon, D. Tudela, J. Soria and J.-M. Herrmann, *J. Photochem. Photobiol. A Chem.*, 2005, **173**, 13.
172 E. Filippo, C. Carlucci, A. L. Capodilupo, P. Perulli, F. Conciauro, G. A. Corrente, G. Gigli and G. Ciccarella, *Mater. Res.*, 2015, **18**, 473.
173 E. Masolo, N. Senes, E. Pellicer, M. D. Baró, S. Enzo, M. I. Pilo, G. Mulas and S. Garroni, *Int. J. Hydrogen Energy*, 2015, **40**, 14483.
174 T. Ohno, K. Sarukawa, K. Tokieda and M. Matsumura, *J. Catal.*, 2001, **203**, 82.
175 M. Spitzer, E. Sabadini and W. Loh, *J. Braz. Chem. Soc.*, 2002, **13**, 7.
176 M. Einert, C. Wessel, F. Badaczewski, T. Leichtweiß, C. Eufinger, J. Janek, J. Yuan, M. Antonietti and B. M. Smarsly, *Macromol. Chem. Phys.*, 2015, **216**, 1930.
177 R. Zhang, B. Tu and D. Zhao, *Chem. - A Eur. J.*, 2010, **16**, 9977.
178 R. T. Downs and M. Hall-Wallace, *Am. Mineral.*, 2003, **88**, 247.
179 S. Graulis, D. Chateigner, R. T. Downs, A. F. T. Yokochi, M. Quirós, L. Lutterotti, E. Manakova, J. Butkus, P. Moeck and A. Le Bail, *J. Appl. Crystallogr.*, 2009, **42**, 726.
180 S. Gražulis, A. Daškevič, A. Merkys, D. Chateigner, L. Lutterotti, M. Quirós, N. R. Serebryanaya, P. Moeck, R. T. Downs and A. Le Bail, *Nucleic Acids Res.*, 2012, **40**, D420.
181 S. Gražulis, A. Merkys, A. Vaitkus and M. Okulič-Kazarinas, *J. Appl. Crystallogr.*, 2015, **48**, 85.
182 A. Merkys, A. Vaitkus, J. Butkus, M. Okulič-Kazarinas, V. Kairys and S. Gražulis, *J. Appl. Crystallogr.*, 2016, **49**, 292.
183 P. Scherrer, *Nachrichten von der Gesellschaft der Wissenschaften zu Göttingen, Math. Klasse*, 1918, **2**, 98.
184 A. L. Patterson, *Phys. Rev.*, 1939, **56**, 978.
185 NIST, *Instrument Line Position and Profile Shape Standard for X-ray Powder Diffraction*, Certificat of Analysis, 1989.
186 H. M. Rietveld, *Acta Crystallogr.*, 1967, **22**, 151.
187 H. M. Rietveld, *J. Appl. Crystallogr.*, 1969, **2**, 65.
188 P. Thompson, D. E. Cox and J. B. Hastings, *J. Appl. Cryst.*, 1987, **20**, 79.
189 J. Rodríguez-Carvajal, *An Introduction to the Program Fullprof 2000*, 2001.
190 L. B. McCusker, R. B. Von Dreele, D. E. Cox, D. Louër and P. Scardi, *J. Appl. Crystallogr.*, 1999, **32**, 36.
191 B. H. Toby, *Powder Diffr.*, 2006, **21**, 67.
192 J. G. M. van Berkum, R. Delhez, T. H. de Keijser and E. J. Mittemeijer, *Acta Crystallogr.*, 1996, **A52**, 730.
193 A. R. Stokes and A. J. C. Wilson, *Proc. Phys. Soc.*, 1944, **56**, 174.
194 G. K. Williamson and W. H. Hall, *Acta Metall.*, 1953, **1**, 22.
195 Y. T. Prabhu, K. V. Rao, V. S. S. Kumar and B. S. Kumari, *World J. Nano Sci. Eng.*, 2014, **4**, 21.
196 K. S. W. Sing, *Adv. Colloid Interface Sci.*, 1998, **76–77**, 3.
197 M. Thommes, K. Kaneko, A. V. Neimark, J. P. Olivier, F. Rodriguez-Reinoso, J. Rouquerol and K. S. W. Sing, *Pure Appl. Chem.*, 2015, **87**, 1051.

198 K. S. W. Sing, D. H. Everett, R. A. W. Haul, L. Moscou, R. A. Pierotti, J. Rouquérol and T. Siemieniewska, *Pure Appl. Chem.*, 1985, **57**, 603.
199 S. Brunauer, P. H. Emmett and E. Teller, *J. Am. Chem. Soc.*, 1938, **60**, 309.
200 S. Brunauer, L. S. Deming, W. E. Deming and E. Teller, *J. Am. Chem. Soc.*, 1940, **62**, 1723.
201 K. Sing, *Colloids Surfaces A Physicochem. Eng. Asp.*, 2001, **187–188**, 3.
202 E. P. Barrett, L. G. Joyner and P. P. Halenda, *J. Am. Chem. Soc.*, 1951, **73**, 373.
203 M. Thommes and K. A. Cychosz, *Adsorption*, 2014, **20**, 233.
204 P. I. Ravikovitch and A. V. Neimark, *Colloids Surfaces A Physicochem. Eng. Asp.*, 2001, **187–188**, 11.
205 P. I. Ravikovitch, G. L. Haller and A. V. Neimark, *Adv. Colloid Interface Sci.*, 1998, **76–77**, 203.
206 A. V Neimark and P. I. Ravikovitch, *Microporous Mesoporous Mater.*, 2001, **44–45**, 697.
207 T. A. Kandiel, I. Ivanova and D. W. Bahnemann, *Energy Environ. Sci.*, 2014, **7**, 1420.
208 J. Tauc, R. Grigorovici and A. Vancu, *Phys. Status Solidi*, 1966, **15**, 627.
209 A. V. Knyazev, N. G. Chernorukov, N. N. Smirnova, N. Y. Kuznetsova and A. V. Markin, *Thermochim. Acta*, 2008, **470**, 47.
210 S. S. H. Rizvi and R. A. Heidemann, *J. Chem. Eng. Data*, 1987, 183.
211 M. Conde Engineering, *Thermophysical Properties of {NH3+H2O} Solutions for the Industrial Design of Absorption Refrigeration Equipment*, http://www.mie.uth.gr/ekp_yliko/nh3_h2oproperties_1.pdf, 2004.
212 M. Popescu, R. Piticescu, E. Vasile, D. Taloi, M. Petriceanu, M. Stoiciu and V. Badilita, *Zeitschrift fur Naturforsch. - Sect. B A J. Chem. Sci.*, 2010, **65**, 1024.
213 R. C. Warner, *J. Biol. Chem.*, 1942, **142**, 705.
214 F. Rafat, *Arch. Appl. Sci. Res.*, 2014, **6**, 75.
215 P. M. Schaber, J. Colson, S. Higgins, D. Thielen, B. Anspach and J. Brauer, *Thermochim. Acta*, 2004, **424**, 131.
216 S. Tsunekawa, K. Ishikawa, Z.-Q. Li, Y. Kawazoe and A. Kasuya, *Phys. Rev. Lett.*, 2000, **85**, 3440.
217 A. Y. Kuznetsov, R. Machado, L. S. Gomes, C. A. Achete, V. Swamy, B. C. Muddle and V. Prakapenka, *Appl. Phys. Lett.*, 2009, **94**, 193117.
218 W. H. Qi, M. P. Wang and Y. C. Su, *J. Mater. Sci. Letts*, 2002, **21**, 877.
219 F. A. Miller and C. H. Wilkins, *Anal. Chem.*, 1952, **24**, 1253.
220 M. Mączka, A. V Knyazev, A. Majchrowski, J. Hanuza and S. Kojima, *J. Phys. Condens. Matter*, 2012, **24**, 195902.
221 L. E. Brus, *J. Chem. Phys.*, 1984, **80**, 4403.
222 L. E. Brus, *J. Phys. Chem.*, 1986, **90**, 2555.
223 T. Vossmeyer, L. Katsikas, M. Giersig, I. G. Popvie, K. Diesner, A. Chemseddine, A. Eychmuller and H. Weller, *J. Phys. Chem.*, 1994, **98**, 7665.
224 S. Monticone, R. Tufeu and A. V Kanaev, *J. Phys. Chem. B*, 1998, **102**, 2854.
225 K. Zhu, J. Shi and L. Zhang, *Solid State Commun.*, 1998, **107**, 79.
226 M. A. Malik, P. O'Brien, S. Norager and J. Smith, *J. Mater. Chem.*, 2003, **13**, 2591.
227 N. Satoh, T. Nakashima, K. Kamikura and K. Yamamoto, *Nat. Nanotechnol.*, 2008, **3**, 106.
228 H. Lin, C. P. Huang, W. Li, C. Ni, S. I. Shah and Y.-H. Tseng, *Appl. Catal. B Environ.*, 2006, **68**, 1.
229 Y. Zhang, Y. Chen, P. Westerhoff, K. Hristovski and J. C. Crittenden, *Water Res.*, 2008, **42**, 2204.
230 S. Hilaire, M. J. Süess, N. Kränzlin, K. Bieńkowski, R. Solarska, J. Augustyński and M. Niederberger, *J. Mater. Chem. A*, 2014, **2**, 20530.

231 N. Le Houx, G. Pourroy, F. Camerel, M. Comet and D. Spitzer, *J. Phys. Chem. C*, 2010, **114**, 155.

232 J. Buha, D. Arčon, M. Niederberger and I. Djerdj, *Phys. Chem. Chem. Phys.*, 2010, **12**, 15537.

233 M. Einert, C. Wessel, F. Badaczewski, T. Leichtweiß, C. Eufinger, J. Janek, J. Yuan, M. Antonietti and B. M. Smarsly, *Macromol. Chem. Phys.*, 2015, **216**, 1930.

234 A. S. Cherevan, P. Gebhardt, C. J. Shearer, M. Matsukawa, K. Domen and D. Eder, *Energy Environ. Sci.*, 2014, **7**, 791.

235 M.-R. Gao, X. Cao, Q. Gao, Y.-F. Xu, Y.-R. Zheng, J. Jiang and S.-H. Yu, *ACS Nano*, 2014, **8**, 3970.

236 Z. Mou, Y. Wu, J. Sun, P. Yang, Y. Du and C. Lu, *ACS Appl. Mater. Interfaces*, 2014, **6**, 13798.

237 N. Kemnade, C. J. Shearer, D. J. Dieterle, A. S. Cherevan, P. Gebhardt, G. Wilde and D. Eder, *Nanoscale*, 2015, **7**, 3028.

238 M. B. Zakaria, N. Suzuki, N. L. Torad, M. Matsuura, K. Maekawa, H. Tanabe and Y. Yamauchi, *Eur. J. Inorg. Chem.*, 2013, 2330.

239 V. C. Gibson, T. P. Kee and A. Shaw, *Polyhedron*, 1988, **7**, 579.

240 D. Brown, *J. Chem. Soc.*, 1964, 4944.

241 P. Wang, W. Xu and Y.-Q. Zheng, *Z. Krist. NCS*, 2003, **218**, 25.

242 C. C. Alves, T. B. C. Campos and W. A. Alves, *Spectrochim. Acta - Part A Mol. Biomol. Spectrosc.*, 2012, **97**, 1085.

243 O. J. Klejnot, *Inorg. Chem.*, 1965, **4**, 1668.

244 O. Collenberg, *Zeitschrift fur Anorg. und Allg. Chemie*, 1914, **102**, 247.

245 H. Kon and N. E. Sharpless, *J. Phys. Chem.*, 1966, **70**, 105.

246 P. Hrobárik, O. L. Malkina, V. G. Malkin and M. Kaupp, *Chem. Phys.*, 2009, **356**, 229.

247 A. Sabatini and I. Bertini, *Inorg. Chem.*, 1966, **5**, 204.

248 A. Takase and K. Miyakawa, *Jpn. J. Appl. Phys.*, 1991, **30**, L1508.

249 C. Y. Liang and S. Krimm, *J. Polym. Sci.*, 1958, **27**, 241.

250 T. Miyazawa, K. Fukushima and Y. Ideguchi, *J. Chem. Phys.*, 1962, **37**, 2764.

251 J. L. Binder, *J. Polym. Sci. Part A*, 1963, **1**, 37.

252 K. W. Tan, H. Sai, S. W. Robbins, J. G. Werner, T. N. Hoheisel, S. A. Hesse, P. A. Beaucage, F. J. DiSalvo, S. M. Gruner, M. Murtagh and U. Wiesner, *RSC Adv.*, 2015, **5**, 49287.

253 S. Han, C. Kim and D. Kwon, *Polymer*, 1997, **38**, 317.

254 P. Pfaffli, A. Zitting and H. Vainio, *Scand. J. Work. Environ. Heal.*, 1978, **4**, 22.

255 J. L. Gurman, L. Baier and B. C. Levin, *Fire Mater.*, 1987, **11**, 109.

256 J. F. Moulder, W. F. Stickle, P. E. Sobol and K. D. Bomben, *Handbook of X-ray Photoelectron Spectroscopy*, Physical Electronic Inc., Eden Prairie, MN, 1992.

257 D. D. Sarma and C. N. R. Rao, *J. Electron Spectros. Relat. Phenomena*, 1980, **20**, 25.

258 J. N. Yao, P. Chen and A. Fujishima, *J. Electroanal. Chem.*, 1996, **406**, 223.

259 D. Bersani, P. P. Lottici and X.-Z. Ding, *Appl. Phys. Lett.*, 1998, **72**, 73.

260 K.-R. Zhu, M.-S. Zhang, Q. Chen and Z. Yin, *Phys. Lett. A*, 2005, **340**, 220.

261 X. Xue, W. Ji, Z. Mao, H. Mao, Y. Wang, X. Wang, W. Ruan, B. Zhao and J. R. Lombardi, *J. Phys. Chem. C*, 2012, **116**, 8792.

262 J. Marugán, D. Hufschmidt, M. J. López-Muñoz, V. Selzer and D. Bahnemann, *Appl. Catal. B Environ.*, 2006, **62**, 201.

263 M. W. Matsen, *J. Chem. Phys.*, 1998, **108**, 785.

264 Z. Li, K. Hur, H. Sai, T. Higuchi, A. Takahara, H. Jinnai, S. M. Gruner and U. Wiesner, *Nat. Commun.*, 2014, **5**, 3247.

265 S. W. Robbins, P. A. Beaucage, H. Sai, K. W. Tan, J. G. Werner, J. P. Sethna, F. J. DiSalvo, S. M. Gruner, R. B. Van Dover and U. Wiesner, *Sci. Adv.*, 2016, **2**, e1501119.
266 S. W. Robbins, H. Sai, F. J. DiSalvo, S. M. Gruner and U. Wiesner, *ACS Nano*, 2014, **8**, 8217.
267 A. V. Knyazev, M. Mączka and N. Y. Kuznetsova, *Thermochim. Acta*, 2010, **506**, 20.
268 P. K. Chu and L. Li, *Mater. Chem. Phys.*, 2006, **96**, 253.
269 H. H. Mohamed, R. Dillert and D. W. Bahnemannt, *J. Phys. Chem. C*, 2011, **115**, 12163.
270 V. W. Lau, D. Klose, H. Kasap, F. Podjaski, M.-C. Pignié, E. Reisner, G. Jeschke and B. V. Lotsch, *Angew. Chemie Int. Ed.*, 2017, **56**, 510.
271 D. Zhu, L. Zhang, R. E. Ruther and R. J. Hamers, *Nat. Mater.*, 2013, **12**, 836.
272 W. Fu, H. Yang, M. Li, L. Chang, Q. Yu, J. Xu and G. Zou, *Mater. Lett.*, 2006, **60**, 2723.
273 D. Wang, T. Hisatomi, T. Takata, C. Pan, M. Katayama, J. Kubota and K. Domen, *Angew. Chemie - Int. Ed.*, 2013, **52**, 11252.
274 D. H. Taffa, R. Dillert, A. C. Ulpe, K. C. L. Bauerfeind, T. Bredow, D. W. Bahnemann and M. Wark, *J. Photonics Energy*, 2016, **7**, 12009.

10 List of abbreviations

’ = arcminute (unit)

” = arcsecond (unit)

% = percent (unit)

° = degree (unit)

°C = degree Celcius (unit)

θ = scattering angle

λ = wavelength

µ = *micro-*, prefix of units donating a factor of 10^{-6}

μ_B = Bohr magneton

ν = frequency

π = ratio of a circle's circumference to its diameter

ρ = density

σ = Stefan-Boltzmann constant

χ^2 = goodness of fit

2D = two-dimensional

a = lattice constant

A = acceptor

A = ampere (unit)

Å = Ångstrom (unit)

A_{N_2} = contact surface area of one molecule nitrogen

Acac = acetylacetonate

AM = air mass coefficient

arb. units = arbitrary units

at% = atomic percent (unit)

au = astronomical unit

B = Debye Waller factor *or* FWHM

B_0 = magnetic induction

bar = unit of pressure, 1 bar equals 10^5 Pa or 0.987 atm

BET = Brunauer-Emmett-Teller model

BJH = Barrett-Joyner-Halenda model

n-BuOH = butan-1-ol

c = *centi-*, prefix of units donating a factor of 10^{-3}

C = BET constant

CB = conduction band

CoPi = cobalt phosphate

cos = cosine

cps = counts per second

$CsNbWO_6$ = caesium niobium tungstate

$CsTaMoO_6$ = caesium tantalum molybdate

$CsTaWO_6$ = caesium tantalum tungstate

CTAB = hexadecyltrimethyl-ammonium bromide

D = diameter, distance *or* diffusion length

D_p = pore diameter

d = day (unit)

d = distance between parallel lattice planes

D = donor

DFT = density functional theory

DLS = dynamic light scattering

DMF = dimethylformamid

DOS = density of states

Dr. = Doctor

Dr. rer. nat. = Doctor rerum naturalium

DR-UV-Vis = diffuse reflectance UV-Vis (spectroscopy)

DST = daylight saving time

e^- = electron

e = elementary charge

E = east

E = energy

e.g. = *exempli gratia*, for example

E_{CB} = conduction band energy

E_F = Fermi energy, Fermi level

E_g = band gap energy

E_{VB} = valence band energy

EDX = energy-dispersive X-ray spectroscopy

EISA = evaporation-induced self-assembly

EPR = electron paramagnetic resonance (spectroscopy)

et al. = *et alii*, and others

etc. = *et cetera*, and so on

EtOH = ethanol

EU-28 = European union with its 28 member states

eV = electronvolt (unit)

$Fd\bar{3}m$ = space group 227

$Fm\bar{3}m$ = space group 225

FTIR = Fourier transform infrared spectroscopy

g = gram (unit)

g = *g*-factor, dimensionless magnetic moment

G = Gauss (unit)

ΔG^0 = Gibbs free energy

GC = gas chromatograph

h = hour (unit)

h = Planck constant

h^+ = hole

H^+ = proton

H_2 = hydrogen

H_2O = water

HAc = acetic acid

HER = hydrogen evolution reaction

hkl = Miller indices

Hz = Hertz (unit)

IR = infrared, infrared spectroscopy

I_{sc} = average solar irradiation

ISO = polyisoprene-*b*-polystyrene-*b*-poly(ethylene oxide)

IUPAC = International Union of Pure and Applied Chemistry

J = Joule (unit)

JCPDS = Joint Committee on Powder Diffraction Standards

k = *kilo*-, prefix of units donating a factor of 10^3

k = wave vector

K = Kelvin (unit)

K = Bragg constant

K_α = electron transition from L shell to K shell

KOAc = potassium acetate

$KTaWO_6$ = potassium tantalum tungstate

L = liter (unit)

L = diffusion length

L_a = (average) crystallite size

m = meter (unit)

m = *milli*, prefix of units donating a factor of 10^{-3}

m = mass

M = molar concentration (unit)

M = molecular weight

M. Sc. = Master of Science

m/z = mass-to-charge ratio

MeOH = methanol

MFC = mass flow controller

min = minute (unit)

mol = mole (unit)

MS = mass spectrometer

M_W = molecular weight

n = *nano*-, prefix of units donating a factor of 10^{-9}

N = north

N_A = Avogadro constant

$Nb(OEt)_5$ = niobium ethoxide

NLDFT = non-local density functional theory

no. = number

NP = nanoparticle(s)

O_2 = oxygen

OER = oxygen evolution reaction

p = pressure

p_0 = saturation pressure

PEO-PPO-PEO = poly(ethylene oxide)-*b*-poly(propylene oxide)-*b*-poly(ethylene oxide); Pluronic

P123 = PEO_{20}-PPO_{70}-PEO_{20}

P25 = titanium dioxide nanopowder, 21 nm primary particle size, trademark of Evonik Degussa GmbH

PAN = polyacrylonitrile

PEG, PEO = poly(ethylene oxide)

PEO-PS = poly(ethylene oxide)-*b*-polystyrene

pH = potential of hydrogen

PI = polyisoprene

PIB-PEO = poly(isobutylene)-*b*-poly(ethylene oxide)

PI-PEO = polyisoprene-*b*-poly(ethylene oxide)

PI-PS-PEO = polyisoprene-*b*-polystyrene-*b*-poly(ethylene oxide); ISO

ppm = parts per million (unit)

PPG, PPO = polypropylene oxide

Prof. = Professor

PS = polystyrene

PSD = pore size distribution

PTFE = polytetrafluoro-ethylene (Teflon)

q = scattering vector (SAXS)

QSDFT = quenched solid density functional theory

QSE = quantum size effect

R = gas constant

R = radius *or* reflectance (in UV-Vis spectroscopy)

R_{wp} = weighted profile R-factor

rpm = revolution per minute (unit)

s = second (unit)

S = scattering vector (WAXS)

S_{BET} = surface area from BET equation

SAED = selected area electron diffraction

SAXS = small-angle X-ray scattering

SEM = scanning electron microscopy

SHE = standard hydrogen electrode

sin = sine

SSR = solid-state reaction

t = time

T = *tera-*, prefix of units donating a factor of 10^{12}

T = Tesla (unit)

T = temperature

T_{calc} = calcination temperature

$Ta(OEt)_5$ = tantalum ethoxide

TCD = thermal conductivity detector

TDOS = total density of states

TEM = transmission electron microscopy

TEOS = tetraethyl orthosilicate

TG, TGA, TG-MS = thermogravimetric analysis with mass spectrometry

THF = tetrahydrofuran

TMOS = tetramethyl orthosilicate

UV = ultraviolett

UV-Vis = ultraviolet-visible (spectroscopy)

V = volt (unit)

V = volume

V_{ads} = volume adsorbed

V_{mono} = volume to cover one monolayer

V_p = pore volume

VB = valence band

vol% = volume percent (unit)

W = Watt (unit)

WAXS = wide-angle X-ray scattering

w/o = without

wt% = weight percent (unit)

x, y, z = positions to describe a three dimensional system

XPS = X-ray photoelectron spectroscopy

XRD, PXRD = (powder) X-ray diffraction

z = angle between incoming radiation and the ground

11 List of publications, contributions and research visits

11.1 Publications in peer-reviewed journals

- **T. Weller**, L. Specht and R. Marschall, "Single crystal $CsTaWO_6$ nanoparticles for photocatalytic Hydrogen production", *Nano Energy*, 2017, **31**, 551; DOI: 10.1016/j.nanoen.2016.12.003, Impact factor (2015): 11.553

- M. Einert, R. Ostermann, **T. Weller**, S. Zellmer, G. Garnweitner, B. M. Smarsly and R. Marschall, "Hollow α-Fe_2O_3 Nanofibres for Solar Water Oxidation: Improving the Photoelectrochemical Performance by Formation of α-Fe_2O_3/ITO-Composite Photoanodes", *J. Mater. Chem. A*, 2016, **4**, 18444; DOI: 10.1039/C6TA06979G, Impact factor (2015): 8.262

- M. Weiß, S. Waitz, R. Ellinghaus, **T. Weller** and R. Marschall, "Highly Mesoporous $CsTaWO_6$ *via* Hard-Templating for Photocatalytic Hydrogen Production", *RSC Adv.*, 2016, **6**, 79037; DOI: 10.1039/C6RA16016F, Impact factor (2015): 3.289

- **T. Weller**, J. Sann and R. Marschall, "Pore Structure Controlling the Activity of Mesoporous Crystalline $CsTaWO_6$ for Photocatalytic Hydrogen Generation", *Adv Energy Mater.*, 2016, **6**, 1600208; DOI: 10.1002/aenm.201600208, Impact factor (2015): 15.230

- I. Djerdj, J. Popović, S. Mal, **T. Weller**, M. Nuskol, Z. Jagličić, Ž. Skoko, D. Pajić, C. Suchomski, P. Vöpel, R. Marschall, B. Kozlevčar and B. M. Smarsly, "Aqueous Sol−Gel Route toward Selected Quaternary Metal Oxides with Single and Double Perovskite-Type Structure Containing Tellurium", *Cryst. Growth Des.*, 2016, **16**, 2535; DOI: 10.1021/acs.cgd.5b01558, Impact factor (2015): 4.425

- H. A. Hopper, J. Lea, J. Cheng, **T. Weller**, R. Marschall, J. Z. Bloh, D. E. Macphee, A. Folli and A. C. Mclaughlin, "An Investigation of the Optical Properties and Water Splitting Potential of the Coloured Metallic Perovskites $Sr_{1-x}Ba_xMoO_3$", *J. Solid State Chem.*, 2016, **234**, 87; DOI: 10.1016/j.jssc.2015.12.002, Impact factor (2015): 2.265

- M. Möller, S. Urban, P. Cop, **T. Weller**, R. Ellinghaus, M. Kleine-Boymann, C. Fiedler, J. Sann, J. Janek, L. Chen, P. J. Klar, D. M. Hofmann, J. Philipps, P. Dolcet, S. Gross, H. Over and B. M. Smarsly, "Synthesis and Physicochemical Characterization of $Ce_{1-x}Gd_xO_{2-\delta}$: A Case Study on the Impact of the Oxygen Storage Capacity on the HCl Oxidation Reaction", *Chem. Cat. Chem.*, 2015, **7**, 3738; DOI: 10.1002/cctc.201500712, Impact factor (2015): 4.724

11.2 Publications without review process

- **T. Weller**, P. Vöpel and R. Marschall, "Charge Carrier Transfer in Heterogeneous Photocatalysis", *Bunsenmagazin*, 2016, **1**, 24; ISSN: 1611-9479.

11.3 Talks and poster contributions

- "Morphological Influences on the Photocatalytic Activity of $CsTaWO_6$", **T. Weller**, L. Specht, R. Marschall, *21st International Conference on Photochemical Conversion and Storage of Solar Energy (IPS-21)*, St. Petersburg, Russia, 24th to 29th July 2016, **oral presentation**.

- "Mesoporous and Nanoparticulate Crystalline $CsTaWO_6$ – Influence of the Nanostructure on the Photocatalytic Hydrogen Generation", **T. Weller**, L. Specht, R. Marschall**,** *9th European meeting on Solar Chemistry and Photocatalysis: Environmental Applications (SPEA-9)*, Strasbourg, France, 13th to 17th July 2016, poster contribution.

- "Soft-Templated Mesoporous $CsTaWO_6$ for Photocatalytic Hydrogen Production", **T. Weller**, J, Sann, R. Marschall, *28. Deutsche Zeolith Tagung (28. DZT)*, Giessen, Germany, 02nd to 04th March 2016, poster contribution.

- "Soft-Templated Mesoporous $CsTaWO_6$ for Photocatalytic Hydrogen Production", **T. Weller**, J. Sann, R. Marschall, *25. Diskussionstagung Anorganisch-Technische Chemie (ATC)*, Frankfurt am Main, Germany, 25th to 26th February 2016, poster contribution.

- "Soft-Templated Mesoporous $CsTaWO_6$ for Photocatalytic Hydrogen Production", **T. Weller**, R. Marschall, *9th International Mesostructured Materials Symposium (IMMS-9)*, Brisbane, Australia, 17th to 20th August 2015, poster contribution, awarded with the ***Journal of Materials Chemistry A Runner up Prize***.

- "Soft-Templated Mesoporous $CsTaWO_6$ for Photocatalytic Hydrogen Production", **T. Weller**, R. Marschall, *Materialforschungstag 2015*, Marburg, Germany, 09th July 2015, poster contribution.

- "Soft-Templated Mesoporous $CsTaWO_6$ for Photocatalytic Hydrogen Production", **T. Weller**, R. Marschall, *27. Deutsche Zeolith Tagung (27. DZT)*, Oldenburg, Germany, 25th to 27th February 2015, poster contribution.

11.4 Research visits

- Four-week stay at the research group of Prof. Dr. Dominik Eder, Institute of Materials Chemistry, Vienna University of Technology, Vienna, Austria, 09th May to 03rd June 2016.

- Four-week stay at the research group of Prof. Dr. Lianzhou Wang, Australian Institute for Bioengineering and Nanotechnology (AIBN), The University of Queensland, Brisbane, Australia, 06th August to 03rd September 2015.

- One-week stay at the research group of Prof. Dr. Igor Djerdj, Division of Materials Physics, Rudjer Boskovic Institute, Zagreb, Croatia, 03rd to 08th November 2014.